Universidade do Minho
Escola de Engenharia

Paulo Jorge da Silva Santos

Wave-based sensor, actuator and optimizer

outubro de 2023

UMinho | 2023

Paulo Jorge da silva santos

Wave-based sensor, actuator and optimizer

Universidade do Minho
Escola de Engenharia

Paulo Jorge da Silva Santos

Wave-based Sensor, Actuator and Optimizer

Tese de Doutoramento
Programa Doutoral em
Sistemas Avançados de Engenharia para a Indústria (AESI)

Trabalho efetuado sob a orientação do
Professor Doutor Jorge Miguel Nunes dos Santos Cabral
Doutor Filipe Manuel Serra Alves

outubro de 2023

DIREITOS DE AUTOR E CONDIÇÕES DE UTILIZAÇÃO DO TRABALHO POR TERCEIROS

Acknowledgements

I would like to express my sincere and special thanks to my advisor and friend, Dr. Professor Jorge Cabral. His exceptional guidance, dedication, and wisdom have profoundly influenced my academic and personal development throughout this journey. His constant support and encouragement to challenge myself were fundamental to the successful completion of this thesis. I am deeply grateful.

I would also like to express my deep gratitude to my other two supervisors, Dr. Filipe Serra alves and Dr. José Azevedo Gonçalves, for their support and guidance throughout my research journey.

I would like to thank the Fundação para a Ciência e Tecnologia (FCT) and Bosch Car Multimedia for funding my PhD (grant PD/BDE/142901/2018).

I would like to extend a special and heartfelt thanks to João Carvalho, who has been a friend and a constant source of support, encouragement, and inspiration throughout my thesis. His unwavering presence, insightful advice, and genuine interest in my academic and personal development were truly invaluable. I am deeply grateful. Also, I would like to extend my sincere thanks to my dear friends Miguel Esteves, Francine Oliveira, Rodrigo Marinho, Eduardo Mendes, and Luís Novais, for their unwavering support and friendship during this challenging journey. Your encouragement, understanding, and ongoing support were crucial in helping me navigate the ups and downs of this research endeavor.

To my two brothers, Pedro Santos and Tiago Santos, thank you for always being by my side and providing me with the motivation and inspiration to keep going.

Finally, I would like to thank my parents, Maria Silva and Álvaro Santos, for their unconditional love, unwavering support, and endless encouragement. Their sacrifices and belief in me were fundamental in making this thesis a reality.

Paulo Jorge da Silva Santos

October 16th, 2023

STATEMENT OF INTEGRITY

I hereby declare having conducted this academic work with integrity. I confirm that I have not used plagiarism or any form of undue use of information or falsification of results along the process leading to its elaboration.

I further declare that I have fully acknowledged the Code of Ethical Conduct of the University of Minho.

Resumo

A presente tese explora a utilização de ondas para abordar dois desafios significativos na indústria automóvel. O primeiro desafio consiste no desenvolvimento de um sistema de cancelamento ativo de ruído (ANC) que possa reduzir os ruídos não estacionários no compartimento de passageiros de um veículo. O segundo desafio é criar uma metodologia de conceção ótima para sensores de posição indutivos capazes de medir deslocamentos lineares, rotacionais e angulares.

Para abordar o primeiro desafio, foi desenvolvido de um sistema ANC onde *wavelets* foram combinadas com um banco de filtros adaptativos. O sistema foi implementado em uma FPGA, e testes demonstraram que o sistema pode reduzir o ruído não estacionário em um ambiente acústico aberto e não controlado em 9 dB. O segundo desafio foi abordado através de uma metodologia que combina um algoritmo genético com um método numérico rápido para otimizar um sensor de posição indutivo. O método numérico foi usado para simular o campo eletromagnético associado à geometria do sensor, permitindo a maximização da corrente induzida nas bobinas recetoras e a minimização da não-linearidade no sensor. A minimização da não-linearidade foi conseguida através do desenho (layout) das bobinas que compõem o sensor. Sendo este otimizado no espaço de Fourier através da adição de harmónicos apropriados na geometria. As melhores geometrias otimizadas apresentaram uma não-linearidade inferior a 0,01% e a 0,25% da escala total para os sensores de posição angular e linear, respetivamente, sem calibração por software.

O sistema ANC proposto tem o potencial de melhorar o conforto dos ocupantes do veículo, reduzindo o ruído indesejado dentro do compartimento de passageiros. Isso poderia reduzir o uso de materiais de isolamento acústico no veículo, levando a um veículo mais leve e, em última análise, a uma redução no consumo de energia. A metodologia desenvolvida para sensores de posição indutivos contribui para o estado da arte de sensores de posição eficientes e económicos, o que é crucial para os requisitos complexos da indústria automóvel. Essas contribuições têm implicações para o desenho de sistemas automotivos, com requisitos de desempenho e considerações ambientais e económicas.

Palavras-chave: Cancelamento ativo de ruído, otimização, sensor de posição indutivo

Abstract

This thesis explores the use of waves to tackle two major engineering challenges in the automotive industry. The first challenge is the development of an Active Noise Cancelling (ANC) system that can effectively reduce non-stationary noise inside a vehicle's passenger compartment. The second challenge is the optimization of an inductive position sensor design methodology capable of measuring linear, rotational, and angular displacements.

To address the first challenge, this work designs an ANC system that employs wavelets combined with a bank of adaptive filters. The system was implemented in an FPGA, and field tests demonstrate its ability to reduce non-stationary noise in an open and uncontrolled acoustic environment by 9 dB. The second challenge was tackled by proposing a new approach that combines a genetic algorithm with a fast and lightweight numerical method to optimize the geometry of an inductive position sensor. The numerical method is used to simulate the sensor's electromagnetic field, allowing for the maximization of induced current on the receiver coils while minimizing the sensor's non-linearity. The non-linearity minimization was achieved through its unique sensor's coils design optimized in the Fourier space by adding the appropriate harmonics to the coils' geometry. The best optimized geometries exhibited a non-linearity of less than 0.01% and 0.25% of the full scale for the angular and linear position sensors, respectively. Both results were achieved without the need for signal calibration or post-processing manipulation.

The proposed ANC system has the potential to enhance the comfort of vehicle occupants by reducing unwanted noise inside the passenger compartment. Moreover, it has the potential to reduce the use of acoustic insulation materials in the vehicle, leading to a lighter vehicle and ultimately reducing energy consumption. The developed methodology for inductive position sensors represents a state-of-the-art contribution to efficient and cost-effective position sensor design, which is crucial for meeting the complex requirements of the automotive industry.

Keywords: Active Noise Cancelling (ANC), inductive position sensor, optimization

Table of Contents

List of Figures

List of Tables

List of Algorithms

List of Acronyms

ABS Antilock Braking System.

AI Artificial Intelligence.

AM Amplitude Modulation.

AMR Anisotropic Magnetoresistance.

ANC Active Noise Cancellation.

APS Angular Position Sensor.

BCLK Bit Clock.

BRAM Block of Random-Access Memory.

CEM Computational Electromagnetism.

CIC Cascaded Integrator-Comb.

DFT Discrete Fourier Transform.

DSP Digital Signal Processor.

DWT Dyadic Wavelet Transform.

EA Evolutionary Algorithm.

EMF Electromotive Force.

ESP Electronic Stability Program.

FDTD Finite Difference Time Domain.

FEM Finite Element Method.

FFT Fast Fourier Transform.

FHM Fast Harmonic Method.

FIR Finite Impulse Response.

FLANN Functional Link Artificial Neural Network.

FMM Fast Multipole Method.

FPGA Field Programmable Gate Array.

FxLMS Filtered-x Least Mean Square.

FxNLMS Filtered-x Normalized Least Mean Square.

GA Genetic Algorithm.

GMR Giant Magnetoresistance.

GMRES Generalized Minimum Residue.

I^{2}S Inter-IC Sound.

IDFT Inverse Discrete Fourier Transform.

IIR Infinite Impulse Response.

LIPS Linear Position Sensor.

LMS Least Mean Square.

LRCLK Left/Right Clock.

LU Lower–Upper.

MEMS Microelectromechanical System.

MIMO Multiple-Input Multiple-Output.

MLFMM Multilevel Fast Multipole Method.

MoM	Method of Moments.
NLMS	Normalized Least Mean Square.
PCB	Printed Circuit Board.
PCM	Pulse Code Modulation.
PDM	Pulse Density Modulation.
PL	Programmable Logic.
PS	Processing System.
PSO	Particle Swarm Optimization.
RAM	Random-Access Memory.
RCGA	Real-Coded Genetic Algorithm.
SA	Simulated Annealing.
SD	Serial Data.
SISO	Single-Input Single-Output.
SNR	Signal-to-Noise Ratio.
TCS	Traction Control System.
TDM	Time-Division Multiplexing.
TMR	Tunnel Magnetoresistance.
UWPT	Undecimated Wavelet Packet Transform.
WPT	Wavelet Packet Transform.
WS	Word Select.

Chapter 1

Introduction

Waves are a fundamental aspect of the natural world and play a crucial role in our ability to sense our surroundings. We see and hear because of the existence of waves, electromagnetic and mechanical. Electromagnetic waves do not require a medium to propagate as they can travel through a vacuum, such as space. They range in frequency from radio waves through infrared and visible light to X-rays and gamma rays. Unlike electromagnetic waves, mechanical waves, such as sound waves, require a medium to propagate. They are created by the vibration of an object, such as a vocal cord, guitar string, or drumskins, which creates a pressure change or disturbance in the medium through which they travel. This pressure change travels through the medium as a wave, and we perceive these waves as sound. We can hear sound waves propagating through the air (or water, if we are in a dive) from around 20 Hz to 20 kHz.

A sensor is a device designed to detect or measure physical properties or changes in the environment, converting this information into a signal that can be analyzed or monitored [1]. Essentially, sensors serve as an interface between the physical world and a system that processes the data they gather. In particular, sensors can detect or measure several types of waves, such as acoustic or radio waves. They play a critical role in numerous fields, including engineering and physics, as they enable the measurement of diverse physical quantities. For instance, a microphone, a specific type of sensor, transforms acoustic waves into electrical signals, allowing for the measurement of acoustic pressure—even those outside the audible range, such as ultrasound and infrasound. Moreover, electromagnetic or mechanical waves can be indirectly used to measure other physical quantities, such as position, distance, and velocity. As demonstrated in this thesis, linear or angular positions can be indirectly measured through electromagnetic waves. A coil generates an electromagnetic wave, a conductive target modulates it based on its position, and another coil subsequently detects it.

An actuator is a component or device that converts input energy, such as electrical, hydraulic, or pneumatic, into mechanical motion or action, thereby facilitating control and movement in systems or processes [1]. Actuators perform the opposite function of sensors by typically converting a signal, often electrical, into a physical quantity like generating an electromagnetic or mechanical wave. A common example is a speaker, which transforms an electrical signal, typically an audio signal, into an acoustic wave that we perceive as sound. Both sensors and actuators are widely used in machinery, robotics, automation, and automotive systems to execute specific actions or tasks, and can be considered transducers since they generally convert energy from one form to another.

Sensors and actuators are essential components in the rapidly-evolving automotive industry. As new challenges arise, such as electric and autonomous vehicles, increased environmental concerns, and the need for more efficient and reliable technology, there is a growing demand for high-performance, low-cost sensors and actuators. An emerging technology in the automotive industry that uses sensors and actuators is Active Noise Cancellation (ANC). ANC systems use sensors (microphones) and actuators (loudspeakers) to replace bulky and heavy noise-reduction materials, thus reducing consumption and weight, and ultimately resulting in improved passenger comfort. This way, passengers can enjoy a quieter and more comfortable ride in their electric and autonomous vehicles. Another example can be seen in the evolving positioning sensor technologies. Traditional permanent magnet-based sensors, composed of rare raw materials, are replaced by more economical and environmentally friendly inductive technologies immune to constant magnetic fields. This is particularly important for electric cars due to the strong magnetic fields caused by high currents.

Overall, the automotive industry is constantly evolving, and sensors and actuators play a vital role in meeting new challenges and demands. They are essential components that enable the development of electric and autonomous vehicles, as well as improve the efficiency and performance of traditional vehicles. As technology advances, we can expect to see even more innovative uses of sensors and actuators in the automotive industry, resulting in improved safety, performance, and environmental sustainability.

1.1 Motivation

The University of Minho and Bosch Car Multimedia Braga established a research and technology development collaboration back in 2013. During the first phase (2012-2015), *HMIExcel* (Human Machine Interface Excellence) was conducted, focusing on developing multimedia solutions for automobiles in the man-machine interface. Building on this success, in 2015, the University of Minho and Bosch Car Multimedia Portugal launched a new initiative called *INNOVATIVE Car HMI*, which aimed to generate knowledge and technologies that transfer into global advancements in future car solutions.

In July 2018, the partnership moved into its third phase with the Sensible Car Program, further concentrating on developing smart critical sensors to meet the capabilities required of autonomous vehicles. Driven by their impressive track record in innovative automotive technology and research, I opted to work in this partnership with Bosch Car Multimedia and the University of Minho. This collaboration allowed me to contribute to cutting-edge advancements in the field while benefiting from their extensive knowledge and resources, and provided the opportunity to work alongside industry experts and researchers, fostering a stimulating environment for learning and professional growth.

As a result of my involvement in the partnership, I explored two emerging technologies in the automotive industry. The first was the ANC system, which enhances vehicle occupant comfort by reducing unwanted noise inside the passenger compartment. This technology also has the potential to reduce the use of acoustic insulation materials, leading to lighter vehicles and ultimately reducing energy consumption. However, current ANC systems in the automotive industry mainly focus on reducing stationary noise, leaving non-stationary noise unaddressed. This gap in the technology motivated research into finding possible solutions using spectral methods, making the development of an ANC system for reducing non-stationary noise one of this thesis's main goals.

The other main goal was the inductive position sensor technology based on planar coils printed directly on Printed Circuit Boards (PCBs), which has been gaining attention in the research community in recent years. These sensors offer several advantages, most notably their robustness in the presence of an external continuous magnetic field, crucial for applications in electric vehicles, among others. Furthermore, their production is relatively low-cost, as the coils can be printed directly onto the PCB, eliminating the need for magnets. Despite these strengths, the performance of these sensors depends on the coil geometry, and the current development process often involves time-consuming trial-and-error methods. To address this issue, the development of a methodology to obtain an optimal solution in a reasonable time became another goal of this thesis.

My personal motivation for this work was driven by my interest in signal processing and radio technologies, allowing me to not only expand my knowledge in these fields but also apply them in practical scenarios.

1.2 Scope

The scope of this thesis focused on two primary emerging technologies in the automotive industry, namely the ANC systems and inductive position sensors.

The research on ANC systems encompassed a comprehensive literature review to understand the current state of ANC systems in the automotive industry. The scope included identifying the limitations of existing ANC systems in addressing non-stationary noise and exploring potential solutions using spectral methods. Furthermore, the development and validation of an improved ANC system that effectively reduced non-stationary noise was covered.

Regarding inductive position sensors, the scope of the thesis covered a review of recent advancements in inductive position sensor technology, focusing on planar coils printed directly on PCBs. The analysis included the advantages and challenges associated with these sensors, such as coil geometry dependencies. The research involved developing an electromagnetic simulation tool to simulate the sensor's coils' geometry and assess the sensor's performance, as well as designing an optimization algorithm to efficiently search for optimal coil geometries within a reasonable time frame. The validation of the developed methodology was also included in the scope of this thesis.

Throughout the research process, the collaboration with the University of Minho and Bosch Car Multimedia Braga was maintained to facilitate access to necessary resources, expertise, and industry insights. The scope of this thesis aimed to address practical challenges associated with ANC systems and inductive position sensors, willing to contribute to the ongoing development of future electric and autonomous vehicles.

1.3 Research questions

In order to guide this research and achieve the objectives mentioned above, the following research questions were formulated:

- RQ1: What are the current advancements in research on ANC systems and inductive position sensors?
- RQ2: What spectral methods are most suitable for addressing each of the two engineering problems presented?
- RQ3: Are the methods selected as solutions viable and effective?

To progressively attain the main purposes of this thesis while answering the aforementioned research questions, the following objectives were defined:

- O1: Conduct a comprehensive review of the current state-of-the-art research on both topics, ANC systems and inductive position sensors;
- O2: Propose solutions for both problems using spectral methods;
- O3: Develop an ANC prototype using an Field Programmable Gate Array (FPGA) to implement the proposed ANC system;
- O4: Evaluate the proposed ANC prototype through measurements and tests;
- O5: Develop a methodology for the optimal design of inductive position sensors;
- O6: Evaluate the methodology solution by designing inductive position sensors with optimized non-linearity.

1.4 Research methodology

A range of research methodologies, from RM1 to RM6, were used to achieve the proposed objectives (O1 to O6) and answer the formulated research questions (RQ1 to RQ3). These methodologies served as a guide to direct and organize the research activities throughout the process.

RM1–State-of-the-art of ANC systems in the automotive industry: This state-of-the-art review aimed to analyze the current state of ANC systems in the automotive industry through a detailed examination of several techniques. The study covered a range of techniques, from those based exclusively on Filtered-x Least Mean Squares (FxLMS) to wavelet-based systems, evaluating their operational requirements, advantages, and drawbacks. This in-depth analysis provided a comprehensive understanding of the capabilities and limitations of ANC systems in the automotive industry. This study addressed vital aspects of research question RQ1 and focused on a specific part of objective O1, providing essential insights to address the remaining research questions.

RM2-Develop of FPGA-based ANC system prototype capable of reducing non-static noises: After assessing the current state of ANC technologies, the study and development of an ANC system capable of effectively reducing non-stationary signals was initiated. This process involved exploring different algorithms, control strategies, and signal-processing techniques, followed by their implementation in MATLAB® software and assessing them using both simulated and real-world signals. Based on their performance and ease of implementation, the most promising solutions were selected and implemented in FPGA. This methodology addresses an essential aspect of research question RQ2, it is part of objective O2, and fulfils completely de objective O3.

RM3-Evaluate FPGA-based ANC system: Experiments were executed to evaluate the performance of the implemented FPGA-based ANC architecture and determine its effectiveness in reducing non-stationary noise. These experiments were conducted in a spacious and uncontrolled acoustic environment using a loudspeaker as the noise source. The ANC system used two loudspeakers to generate the anti-phase signal, and noise and error microphones to close the algorithm feedback loop. Various signals were used as noise sources to assess the system's performance, including urban street noise, crowded restaurant ambient noise, and pink noise. These signals were used for their unpredictability, realism, and ability to test the system's dynamic range. The evaluation aimed to address part of the research question RQ3 and fulfil objective O4.

RM4-State-of-the-art of inductive position sensors: This state-of-the-art review focused on the study of PCB-based inductive position sensors and other position-sensing technologies through a comprehensive analysis of the current state-of-the-art of these technologies. This study analyzed at various position-sensing technologies, such as inductive, magnetic, capacitive and optical sensors, assessing their operational requirements, strengths, and limitations. It provided a comprehensive understanding of the capabilities and constraints of PCB-based inductive position sensors. This knowledge was essential for addressing part of research question RQ1, and partially achieve objective O1, which is to gain an in-depth understanding of PCB-based inductive position sensor technology and its current advancements in the field.

RM5-Develop an optimization methodology for inductive position sensors: By examining the current state-of-the-art of inductive position sensor technologies, the study and development of an inductive position sensor design methodology capable of optimizing the sensor's response was initiated. This process involved exploring different PCB-based designs, electromagnetic simulations, and optimization techniques to improve overall sensor linearity, maximize induced current, and achieve other performance improvements. The PCB design exploration and electrical simulations were evaluated using MATLAB® software. This methodology addresses an essential aspect of research question RQ2, part of objective O2, and fulfils objective O5 completely.

RM6-Evaluate the proposed optimization methodology for inductive position sensors: In order to validate the developed optimization methodology for inductive position sensors and determine its effectiveness, the methodology was applied to optimize two sensor geometries: an Angular Position Sensor (APS) and a Linear Position Sensor (LIPS). These sensors were designed to measure the full range. The optimized sensors were then characterized in terms of linearity and induced current, and the results were compared with the ones obtained from non-optimized versions (current state-of-the-art). Through this methodology, it is possible to address an essential aspect of research question RQ3 and fully achieve objective O6.

1.5 Thesis structure

The structure of this thesis is as follows, the next chapter of the thesis provides the theoretical foundation necessary to understand the research conducted in later chapters. The chapter is structured into three main sections, beginning with signal processing, which covers the properties of signals, including linearity, time invariance, impulse response, causality, and stability. The second section covers Fourier analysis, including transfer functions, Fourier transforms in $L^1(\mathbb{R})$ and $L^2(\mathbb{R})$, convergence, regularity, decay, uncertainty principle, and compact support. The last section covers wavelets. The chapter then moves into Computational Electromagnetism (CEM), discussing Maxwell's equations in both integral and differential forms, time-harmonic fields, constitutive relations, vector wave equations, scalar and vector potentials, and boundary conditions. It also covers the Method of Moments (MoM) and the Fast Multipole Method (FMM). The final section of the chapter covers global optimization techniques, specifically Simulated Annealing (SA), Particle Swarm Optimization (PSO), and Genetic Algorithm (GA).

The ANC system capable of leading with non-stationary noises in open spaces is covered in chapter 3. The chapter begins by providing a comprehensive overview of the current state-of-the-art of ANC systems, discussing their operational requirements, main advantages, and drawbacks. The chapter then describes a classical feedback ANC system and introduces a proposed hardware-accelerated ANC system that uses FPGA technology. The proposed system includes an overview of its design, an arrangement for random noise cancellation, and an in-depth examination of the implementation of various modules, such as the Finite Impulse Response (FIR) filter module, the Undecimated Wavelet Packet Transform (UWPT) module, and the Filtered-x Normalized Least Mean Square (FxNLMS) module. The chapter concludes with an evaluation of the system, outlining the methodology used for testing, presenting the results obtained, and providing a thorough discussion of the findings.

In chapter 4 a methodology for optimizing inductive position sensors is proposed. The chapter starts by providing an overview of the current state-of-the-art of position sensor technologies, including magnetic, optical, capacitive, and inductive sensors. The chapter then moves into the specifics of inductive-based position sensors and introduces a methodology for their design optimization. The chapter also includes a section on the Fast Harmonic Method (FHM), a modified version of the MoM developed during this thesis. The chapter concludes with an evaluation of the proposed methodology, outlining the methodology used for testing, presenting the obtained results, and providing a thorough discussion of the findings. The evaluation includes optimization using the MoM, the FHM, and the FMM, focusing on peak-to-peak induced current optimization, non-linearity optimization, and harmonic content optimization.

Finally, chapter 5 concludes this thesis by providing the conclusions, highlighting the contributions, identifying the limitations, and proposing future work to address the identified limitations.

Chapter 2

Theoretical context

This chapter outlines the theoretical foundations necessary for understanding the research in this thesis. It begins with the signal processing, covering Fourier analysis and wavelets. The chapter then delves into Computational Electromagnetism (CEM), including Maxwell's equations, the Method of Moments (MoM), and the Fast Multipole Method (FMM). Finally, it addresses global optimization techniques, such as Simulated Annealing (SA), Particle Swarm Optimization (PSO), and Genetic Algorithm (GA).

2.1 Signal processing

Signal processing is a field that involves transforming and manipulating signals to extract useful information. It typically includes techniques such as data transformation, information extraction, pattern recognition, decision-making, statistical analysis, and signal modelling. These techniques are used in many fields, including speech enhancement, speaker identification, speech recognition, object tracking, sonar and radar systems, medical imaging, automated control systems, robotics, broadcasting, compression, encoding, and music synthesis [2–4].

One of the fundamental concepts in signal processing is the analysis of the frequency content of a signal. Fourier analysis is a mathematical tool that enables examining the frequency components of a signal. It is based on the idea that any signal can be represented as a sum of simple harmonic functions, such as sine and cosine waves, which allows for the analysis of signals in the frequency domain [2–4].

Another important tool in signal processing is wavelets [4]. They are similar to Fourier analysis but offer a more localized analysis of signals in both the time and frequency domains. This makes wavelets helpful in analyzing signals that are not stationary or that change over time, with applications such as image compression, noise reduction, and feature extraction [4].

Fourier analysis and wavelets are widely-used and essential mathematical tools in signal processing. They are employed in various fields to extract useful information from signals. Both have advantages and disadvantages and are often used together for comprehensive signal analysis.

It is important to note that signal processing is a vast and complex field with many different tools that can be used to extract useful information from signals. Fourier analysis and wavelets are just two examples of the many tools used in signal processing. Understanding the basics of these two tools provides a foundation for understanding decisions and implementations throughout this thesis.

2.1.1 Signal Properties

In this section, some of the properties of signals are introduced. These properties are an essential base for the discussion the Fourier integrals further ahead in the chapter.

2.1.1.1 Linearity

An operator, L, is said to be linear if the superposition theorem applies; that is, if the input, $f\left(t\right)$, is a weighted sum of multiple signals, the output, $Lf\left(t\right)$, will also be defined by a weighted sum of responses to each of the inputs [2, 3]. Analytically, if $Lf_1\left(t\right)$ is the output of $f_1\left(t\right)$, and $Lf_2\left(t\right)$ is the output of $f_2\left(t\right)$, then:

$$af_1\left(t\right) + bf_2\left(t\right) \Rightarrow aLf_1\left(t\right) + bLf_2\left(t\right) \tag{2.1}$$

where in the above equation, a and b are constants that can be complex numbers.

2.1.1.2 Time invariance

Linear time-invariant operators are used to implement signal processing operations like signal transmission, stationary denoising, and predictive coding. An operator is said to be time-invariant if a time shift in the input $f\left(t\right)$ results in the same exact time shift in the output signal [2, 3].

$$g\left(t\right)=Lf\left(t\right)\Rightarrow g\left(t-\tau\right)=Lf\left(t-\tau\right) \tag{2.2}$$

2.1.1.3 Impulse response

Linear time-invariant systems can be characterized entirely by their response to a Dirac impulse. If $f\left(t\right)$ is continuous, its value at t can be given by Equation 2.3, where $\delta\left(t-u\right)$ is the Dirac impulse located at time u [2, 3].

$$f\left(t\right)=\int_{-\infty}^{+\infty}f\left(u\right)\delta\left(t-u\right)du \tag{2.3}$$

Because of L's continuity and linearity, the system's output, $Lf\left(t\right)$, is the convolution of the input of the system, $f\left(t\right)$, with the system's impulse response, Equation 2.4, where h is the impulse response of L ($h\left(t\right)=L\delta\left(t\right)$).

$$Lf\left(t\right)=\int_{-\infty}^{+\infty}f\left(u\right)h\left(t-u\right)du \tag{2.4}$$

The time-invariance demonstrates that $L\delta\left(t-u\right)=h\left(t-u\right)$, resulting in:

$$\begin{aligned}Lf\left(t\right)&=\int_{-\infty}^{+\infty}f\left(u\right)h\left(t-u\right)du\\&=\int_{-\infty}^{+\infty}h\left(u\right)f\left(t-u\right)du\\&=h\left(t\right)*f\left(t\right)\end{aligned} \tag{2.5}$$

A linear time-invariant filter is comparable to a convolution with the impulse response $h\left(t\right)$, not requiring that $f\left(t\right)$ be continuous. This formula is true for every signal $f\left(t\right)$ for which the convolution integral converges [4].

2.1.1.4 Causality

A filter is said to be *causal* if its output depends only on the current and past input values. If the filter depends on future values, it is *non-causal* [2, 3]. Equation 2.5, represents a convolution between an input signal, $f\left(t\right)$, with an impulse response, $h\left(t\right)$. In this example if $Lf\left(t\right)$ does not depend on the values $f\left(u\right)$ for $u > t$, meaning that $h\left(u\right) = 0$ for $u < 0$. This impulse response, $h\left(t\right)$, is said to be *causal* [4].

2.1.1.5 Stability

A *stable* operator, L, is one in which the output, $Lf\left(t\right)$, does not diverge for small inputs of $f\left(t\right)$, or more specifically, one whose output's amplitude is limited for limited input's amplitude. Basically, the *stability* property ensures that $Lf\left(t\right)$ is bounded if $f\left(t\right)$ is bounded [4]. Since:

$$\left|Lf\left(t\right)\right| \leq \int_{-\infty}^{+\infty} \left|h\left(u\right)\right| \left|f\left(t-u\right)\right| du \leq \sup_{u\in\mathbb{R}} \left|f\left(u\right)\right| \int_{-\infty}^{+\infty} \left|h\left(u\right)\right| du \tag{2.6}$$

It is sufficient that $\int_{-\infty}^{+\infty} \left|h\left(u\right)\right| du < +\infty$, even if $h\left(u\right)$ is an unbound function. Thus, $h\left(u\right)$ is said to be *stable* if it is absolutely integrable [4].

2.1.2 Fourier Transform

In this subsection, to prevent problems with convergence, the Fourier integral is first defined in space $L_1\left(\mathbb{R}\right)$. Then, it is expanded to the space $L_2\left(\mathbb{R}\right)$.

2.1.2.1 Transfer functions

Eigenvectors of convolution operators are complex exponentials $e^{j\omega t}$.

$$\begin{aligned} Le^{j\omega t} &= \int_{-\infty}^{+\infty} h\left(u\right) e^{j\omega\left(t-u\right)} du \\ &= e^{j\omega t} \int_{-\infty}^{+\infty} h\left(u\right) e^{-j\omega u} du \\ &= H\left(\omega\right) e^{j\omega t} \end{aligned} \tag{2.7}$$

Where the eigenvalue:

$$H\left(\omega\right)=\int_{-\infty}^{+\infty}h\left(u\right)e^{-j\omega u}du \tag{2.8}$$

is the Fourier transform of $h\left(u\right)$ [4]. Because complex sinusoidal waves, $e^{j\omega t}$, are eigenvectors of time-invariant linear operators, it is tempting to decompose any function $f\left(t\right)$ as a sum of these eigenvectors. The eigenvalues $H\left(\omega\right)$ can then be used to express $Lf\left(t\right)$ [4].

2.1.2.2 Fourier transform in $L^1\left(\mathbb{R}\right)$

The Fourier integral, Equation 2.9, is an integral that measures *how much* of a particular frequency ω is present in a given function $f\left(t\right)$. If $f\left(t\right)\in L^1\left(\mathbb{R}\right)$, then the integral converges, and $f\left(t\right)$ is an absolutely integrable signal, Equation 2.11 [4]. Similarly, it may be possible to reconstruct the original signal $f(t)$ by applying the Inverse Fourier Transform, Equation 2.10. If $f\left(t\right)\in L^1\left(\mathbb{R}\right)$ and $F\left(\omega\right)\in L^1\left(\mathbb{R}\right)$ then one can apply the Inverse Fourier Transform to recover the original signal $f\left(t\right)$ [4]. For example, if $f\left(t\right)=e^{-|t|}$ is absolutely integrable (Equation 2.11), then $F\left(\omega\right)=2/\left(1+\omega^2\right)$ is also absolutely integrable, so the Inverse Fourier Transform (Equation 2.10) works. However, if $f\left(t\right)=\delta\left(t\right)$, is absolutely integrable as well, then $F\left(\omega\right)$ is equal to 1 in the entire domain, so it is not absolutely integrable, and the Inverse Fourier Transform fails to recover the original signal.

$$F\left(\omega\right)=\int_{-\infty}^{+\infty}f\left(t\right)e^{-j\omega t}dt \tag{2.9}$$

$$f\left(t\right)=\frac{1}{2\pi}\int_{-\infty}^{+\infty}F\left(\omega\right)e^{j\omega t}d\omega \tag{2.10}$$

$$\left|F\left(\omega\right)\right|\leq\int_{-\infty}^{+\infty}\left|f\left(t\right)\right|dt<+\infty \tag{2.11}$$

The Inverse Fourier Transform, Equation 2.10, recovers $f\left(t\right)$ by integrating an infinite set of sinusoids $e^{j\omega t}$ against the Fourier Transform of the function, $F\left(\omega\right)$. By doing so, one can prove that the hypothesis $F\left(\omega\right)\in L^1\left(\mathbb{R}\right)$ implies that $f\left(t\right)$ is continuous [4]. Therefore, the reconstruction (Equation 2.10) is not proved for discontinuous functions. To extend the Fourier Transform to hold any function $f(t) \in L^2(\mathbb{R})$, it is necessary to extend the definition of the Fourier transform from $L^1(\mathbb{R})$ to $L^2(\mathbb{R})$ [4].

One of the most important properties of the Fourier Transform is that for any two functions $f(t)$ and $h(t)$ that are elements of $L^1(\mathbb{R})$, the function $g(t)$ resulting from the convolution $f(t) * h(t)$ is also an element of $L^1(\mathbb{R})$ [4]. This can also be expressed as complex sinusoidal waves, $e^{j\omega t}$, being eigenvalues of convolution operators. Furthermore, the response $Lf(t) = g(t) = f(t) * h(t)$ of a linear time-invariant system can be calculated from its Fourier Transform $G(\omega) = F(\omega) H(\omega)$. By converting $G(\omega)$ into the original domain using the Inverse Fourier Transform, Equation 2.10, one can obtain the $Lf(t)$. This implies that each frequency component $e^{j\omega t}$ of amplitude and phase $F(\omega)$ is amplified or attenuated, and phase shifted, by $H(\omega)$. As a result, such a convolution is known as *frequency filtering*, and the filter's *transfer function* is $H(\omega)$ [4].

2.1.2.3 Fourier transform in $L^2(\mathbb{R})$

The Fourier transform of the indicator function $f = 1_{[-T,T]}$ that has discontinuities at $t = \pm T$, therefore, its Fourier Transform is not integrable:

$$F(\omega) = \int_{-T}^{T} e^{-j\omega t} dt = 2\frac{\sin(T\omega)}{\omega} \tag{2.12}$$

Thus, the Inverse Fourier Transform, Equation 2.10, does not apply in this case. This prompts the expansion of the Fourier Transform to the space $L^2(\mathbb{R})$ of functions $f(t)$ with finite energy, as shown in Equation 2.13. By doing so, one can access all of the resources offered by the presence of an inner product in the Hilbert space $L^2(\mathbb{R})$ [4]. The inner product of $f(t) \in L^2(\mathbb{R})$ and $g(t) \in L^2(\mathbb{R})$ is given by Equation 2.14, where $*$ denotes complex conjugate, and the norm of $f(t) \in L^2(\mathbb{R})$ is given by Equation 2.15.

$$|F(\omega)|^2 \leq \int_{-\infty}^{+\infty} |f(t)|^2 dt < +\infty \tag{2.13}$$

$$\langle f, g\rangle = \int_{-\infty}^{+\infty} f(t) g^*(t) dt \tag{2.14}$$

$$\|f\|^2 = \langle f, f\rangle = \int_{-\infty}^{+\infty} |f(t)|^2 \, dt \tag{2.15}$$

If $f(t)$ and $h(t)$ are in $L^1(\mathbb{R}) \cap L^2(\mathbb{R})$, then:

$$\int_{-\infty}^{+\infty} f(t)\, h^*(t)\, dt = \frac{1}{2\pi} \int_{-\infty}^{+\infty} F(\omega)\, H^*(\omega)\, d\omega \tag{2.16}$$

Also, the resulting norm of $f(t) \in L^1(\mathbb{R}) \cap L^2(\mathbb{R})$ is:

$$\int_{-\infty}^{+\infty} |f(t)|^2 \, dt = \frac{1}{2\pi} \int_{-\infty}^{+\infty} |F(\omega)|^2 \, d\omega \tag{2.17}$$

Equations 2.16 and 2.17 are called the Parseval and Plancherel formulas, respectively [4].

2.1.2.4 Convergence

In the last two sections, the fundamental concepts have been described, enabling the determination of the class of signals for which the Fourier integrals, Equations 2.9 and 2.10, converge. Additionally, this ensures that $\hat{f}(t)$, the result of applying the Inverse Fourier Transform to $F(\omega)$, is a valid representation of $f(t)$. For $\hat{f}(t)$ to be a valid representation of $f(t)$, $f(t)$ must be either square integrable (Equation 2.13) or absolutely integrable (Equation 2.11). In the latter case, $f(t)$ must also be continuous.

2.1.2.5 Regularity and decay

$|F(\omega)|$ decay is determined by $f(t)$'s worst single behaviour. For instance, because $f(t) = 1_{[-T,T]}$ is discontinuous at $t = \pm T$, $F(\omega)$ decays like $|\omega|^{-1}$. In this case, it is also worth mentioning that $f(t)$ is a normal function for $t \neq \pm T$. The decay of $|F(\omega)|$ does not provide this information. Therefore, to determine the local regularity of a signal $f(t)$, it is necessary to decompose it using time-localized waveforms rather than sinusoidal waves $e^{j\omega t}$ [4].

2.1.2.6 Uncertainty principle

Due to the Heisenberg uncertainty principle, it is well known that it is impossible to know a particle's position and momentum simultaneously with arbitrary precision [4]. One can only measure one of them.

Similarly, the uncertainty principle does not permit the existence of a function $f\left(t\right)$ with highly localized energy in time that has a Fourier Transform $F\left(\omega\right)$ with energy concentrated in a low-frequency interval. For example, the Dirac $\delta\left(t-u\right)$ has a support limited to $t=u$, but its Fourier Transform $e^{-j\omega u}$ has an energy distribution that is uniform across all frequencies. It is known that only if $f\left(t\right)$ has regular temporal variations does $\left|F\left(\omega\right)\right|$ decay fast at high frequencies. As a result, the energy of $f\left(t\right)$ must be dispersed over a relatively broad domain.

In order to reduce the time spread of $f\left(t\right)$, it can be scaled by $s<1$ while maintaining the overall energy unchanged [4]:

$$f_s\left(t\right)=\frac{1}{\sqrt{s}}f\left(\frac{t}{s}\right) \tag{2.18}$$

The Fourier transform $F_s\left(\omega\right)=\sqrt{s}F\left(s\omega\right)$ is dilated by $1/s$, meaning that what was gained in time localization was lost in frequency localization. It can be seen as a trade-off between time and frequency localization [4].

The Heisenberg uncertainty principle restricts time and frequency energy concentrations [4].

2.1.2.7 Compact support

If a signal, $f\left(t\right)$, which is not identically null has a compact support (is zero outside a finite interval), its Fourier Transform, $F\left(\omega\right)$, cannot be zero on an entire interval. Again, if $F\left(\omega\right)$, which is not identically null, has a compact support, then $f\left(t\right)$ cannot be zero on a whole interval, which shows that a function of compact support, whose Fourier Transform has a compact support, does not exist [4]. It is impossible to know an event's time and frequency simultaneously with arbitrary precision.

2.1.3 Wavelet Transform

The wavelet transform is a signal processing technique that computes the signal spectrum over time, like the windowed Fourier transform. However, the wavelet transform uses a compact support basis function called wavelet. This compact support makes them particularly suitable for handling non-stationary signals. There are several wavelet-based functions, such as Haar (see Equation 2.19) and Daubechies [5]. The Haar wavelet is also known as a particular case of the Daubechies wavelet and is the simplest possible wavelet.

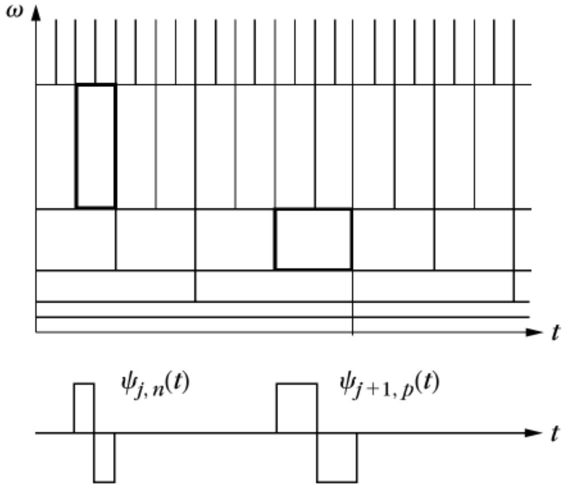

Figure 2.1: Translation-scale boxes in Gabor space

$$\Psi(t) = \begin{cases} 1 & if\; 0 \leq t < 1/2 \\ -1 & if\; 1/2 \leq t < 1 \\ 0 & otherwise \end{cases} \tag{2.19}$$

The wavelet function (Ψ) is scaled and translated (represented as *s* and *u* in Equation 2.20) before being convoluted with the signal of interest $f\,(t)$ (see Equation 2.21). This translation and scaling in wavelet transform plays similar roles to time and frequency in the windowed Fourier transform.

Unlike the windowed Fourier transform that has the same resolution for all time-frequency boxes, the wavelet transform has different *time-frequency* (translation-scale) resolutions (Figure 2.1), making it more suitable to analyze the frequency-temporal dynamics of the signal of interest.

$$\Psi_{u,s}(t) = \frac{1}{\sqrt{s}}\Psi\left(\frac{t-u}{s}\right) \tag{2.20}$$

$$Wf(u,s) = \int_{-\infty}^{+\infty} f(t)\Psi^{*}_{u,s}(t)dt \tag{2.21}$$

The wavelet transform can be computed using a bank of filters. The filter banks' technique [6–8], also known as the fast wavelet transform algorithm, decomposes a discrete signal (e.g., *f[n]*) into two half-sized signals using a filtering and subsampling procedure. This procedure is cascaded as shown in Figure 2.2,

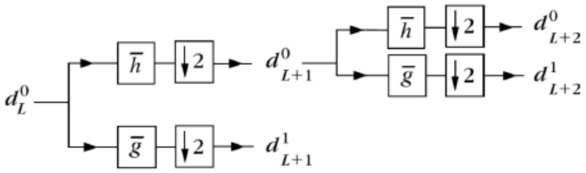

Figure 2.2: Dyadic wavelet transform

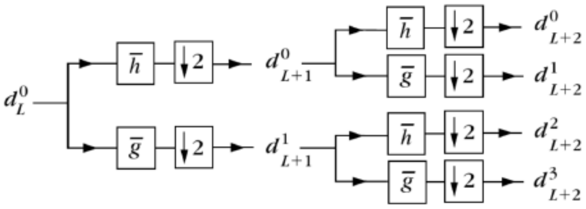

Figure 2.3: Packet wavelet transform

where $\overline{h}$ is a low-pass filter and $\overline{g}$ is a high-pass filter, d^0 is the wavelet approximation coefficient, and d^1 is the wavelet detail coefficient.

Figure 2.2 illustrates the Dyadic Wavelet Transform (DWT) in which the wavelet approximation coefficient is cascaded as opposed to the wavelet detail coefficient. This wavelet transform results in translation-scale boxes illustrated in Figure 2.1 [4] (higher temporal resolution at high *frequencies*, but with low spectral resolution; and low temporal resolution at low *frequencies*, but with high spectral resolution). Figure 2.3 depicts a Wavelet Packet Transform (WPT) where both the approximation coefficient and the detail coefficient of the wavelet are decomposed, resulting in translation-scale boxes with the same resolution.

There is a variant of the WPT called Undecimated Wavelet Packet Transform (UWPT) [9]. As the name suggests, this approach does not perform decimation after filtering; instead, the wavelet's filter coefficients are upsampled.

Using this technique, the wavelet coefficients are doubled at each level of decomposition, in contrast to the WPT, where the number of wavelet coefficients is equal to the number of samples of the input signal. Figure 2.4 illustrates the UWPT where the dilated filters, $\overline{h}$ and $\overline{g}$, are upsampled.

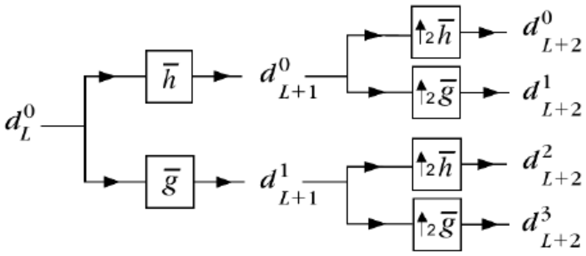

Figure 2.4: Undecimated wavelet packet transform

Equations 2.22 and 2.23 represents the filter upsampling process by inserting zeros between each pair of coefficients of $\overline{h}(l)$ and $\overline{g}(l)$, where *j* is the decomposition level, and *L* is the total number of coefficients of the original filters $\overline{h}(l)$ and $\overline{g}(l)$.

$$\overline{h}_j[l] = \left[\overline{h}[0], \underbrace{0, ..., 0}_{2^j-1}, \overline{h}[1], \underbrace{0, ..., 0}_{2^j-1}, ..., \overline{h}[L-1], \underbrace{0, ..., 0}_{2^j-1}\right] \tag{2.22}$$

$$\overline{g}_j[l] = \left[\overline{g}[0], \underbrace{0, ..., 0}_{2^j-1}, \overline{g}[1], \underbrace{0, ..., 0}_{2^j-1}, ..., \overline{g}[L-1], \underbrace{0, ..., 0}_{2^j-1}\right] \tag{2.23}$$

2.2 Computational Electromagnetism

In this section, the exploration of fundamental principles of Computational electromagnetics (CEM) is undertaken, with a focus on designing optimal inductive position sensors. The goal is to develop a customized simulation tool for streamlining the optimization process. The insights provided are essential for creating an efficient tool that can perform thousands of electromagnetic simulations within a reasonable timeframe.

CEM is a technology that applies numerical methods in the field of electromagnetics, allowing for the modeling of electromagnetic field interactions with matter using Maxwell's equations [10, 11]. Numerous numerical methods have been widely adopted in CEM, such as the Finite Difference Time Domain (FDTD) method [12–14], the Finite Element Method (FEM), the Method of Moments (MoM), and the Fast Multipole Method (FMM) [15]. The FDTD and FEM methods are based on differential equations, while MoM and FMM rely on integral equations.

To introduce CEM, one first explores Maxwell's equations, which consist of four fundamental equations describing the behavior of electric and magnetic fields. These equations serve as the foundation of classical electromagnetism and offer a mathematical framework for comprehending various electromagnetic phenomena.

Subsequently, the MoM and FMM methods are presented among the four mentioned methods, as they offer greater advantages in terms of speed and computational resources for the needs of the inductive position sensors optimization process.

2.2.1 Maxwell's equations

James Clerk Maxwell (1831-1879) established Maxwell's equations in 1861, which provide a comprehensive description of all macroscopic electromagnetic phenomena. These equations consolidate the work of several notable figures in electromagnetism, including Coulomb (1736-1806), Ampère (1775-1836), Oersted (1777-1851), Faraday (1791-1867), and Maxwell himself, into a set of four equations that can be expressed in both integral and differential forms. Considered fundamental in the study of electromagnetism, these equations have a wide range of applications in fields such as electrical engineering, electronics, and optics.

2.2.1.1 Integral form

The law of magnetic induction established by Faraday is the foundation for Maxwell's first equation. This law states that a time-varying magnetic flux induces an Electromotive Force (EMF), Equation 2.24, meaning that if a closed-loop conductor is immersed in this time-varying magnetic flux ($\frac{d\Phi}{dt}$) an EMF (ε) emerges at its terminals [16–18].

$$\varepsilon = -\frac{d\Phi_M}{dt} \tag{2.24}$$

The EMF can also be expressed in terms of the electric field, Equation 2.25. According to this equation, if a conductor is immersed in an electric field, $\vec{E}$, an EMF appears at its terminals [16–18].

$$\varepsilon = \int_C \vec{E} \cdot d\vec{l} \tag{2.25}$$

The magnetic flux inside a closed path C is given by Equation 2.26, by replacing this quantity in Equation 2.24 and combining Equation 2.25 yields the first Maxwell's equation, Equation 2.27, Faraday's law [16–18].

$$\Phi_M = \iint_S \vec{B} \cdot d\vec{S} \tag{2.26}$$

The second Maxwell's equation, Equation 2.28, is Ampère's law with the additional term $-\frac{d}{dt}\iint_S \vec{D} \cdot d\vec{S}$ added by Maxwell. This additional term similarly to the first Maxwell's equation but with the fields exchanged, describes that a time-varying electric flux generates a magnetic field [16–18].

The third equation of Maxwell, Equation 2.29, is derived from electrostatic Gauss's law, which states that the displacement vector flux across a closed surface equals its internal charge [16–18].

Maxwell's fourth equation, Equation 2.30, describes how magnetic flux density field lines behave. Experimental observations demonstrated that these lines are closed, meaning the total number of lines that enters a closed surface equals the total number of lines that leaves it. For this reason, the magnetic flux over a closed surface S is null, preventing the existence of isolated magnetic poles [16–18].

$$\oint_C \vec{E} \cdot d\vec{l} = -\frac{d}{dt}\iint_S \vec{B} \cdot d\vec{S} \qquad \text{(Faraday's law)} \qquad (2.27)$$

$$\oint_C \vec{H} \cdot d\vec{l} = -\frac{d}{dt}\iint_S \vec{D} \cdot d\vec{S} + \iint_S \vec{J} \cdot d\vec{S} \qquad \text{(Ampère-Maxwell law)} \qquad (2.28)$$

$$\oiint_S \vec{D} \cdot d\vec{S} = \iiint_V \rho dV \qquad \text{(Gauss's law–electric)} \qquad (2.29)$$

$$\oiint_S \vec{B} \cdot d\vec{S} = 0 \qquad \text{(Gauss's law–magnetic)} \qquad (2.30)$$

In Maxwell's equations above:

$\vec{E}$ is the electric field intensity (V/m);

$\vec{D}$ is the electric flux density (C/m^2);

$\vec{H}$ is the magnetic field intensity (A/m);

$\vec{B}$ is the magnetic flux density (T);

$\vec{J}$ is the electric current density (A/m^2);

$\vec{\rho}$ is the electric charge density (C/m^3).

Another essential equation is the equation of continuity that can be derived from Equations 2.28 and 2.29 [16–18]:

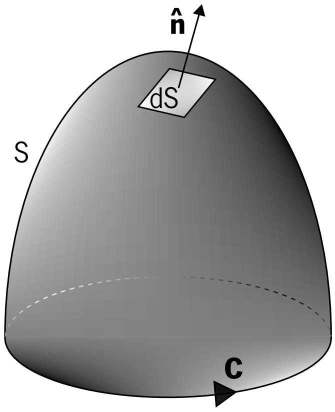

Figure 2.5: Stokes theorem illustration

$$\oiint_S \vec{J} \cdot d\vec{S} = -\frac{d}{dt} \iiint_V \rho dV \qquad \text{(Equation of continuity)} \tag{2.31}$$

This equation is the mathematical representation of the law of the conservation of charges [16–18].

2.2.1.2 Differential form

Maxwell's equations in differential form can be derived from Stokes's theorem, Equation 2.32, and Gauss's theorem, Equation 2.33 [16–18].

$$\oint_C \vec{F} \cdot d\vec{l} = \iint_S \nabla \times \vec{F} \cdot \hat{n}\, dS \tag{2.32}$$

Stokes's theorem, also known as the divergence theorem, states that the integral of a closed loop line C of a vector field is equal to the flux of its curl through the enclosed surface S (see Figure 2.5) [16–18]. By applying this theorem to the first two integral Maxwell's equations, Equations 2.27 and 2.28, their differential forms are obtained, which are Equations 2.34 and 2.35.

$$\oiint_S \vec{F} \cdot \hat{n}\, dS = \iiint_V \nabla \cdot \vec{F}\, dV \tag{2.33}$$

The third and fourth Maxwell's equations and the equation of continuity in the differential form, Equations 2.36 to 2.38, are derived by applying Gauss's theorem to their integral forms (Equations 2.29 to 2.31). This theorem states that the flux of the vector field $\vec{F}$ through the closed surface S that limits the volume

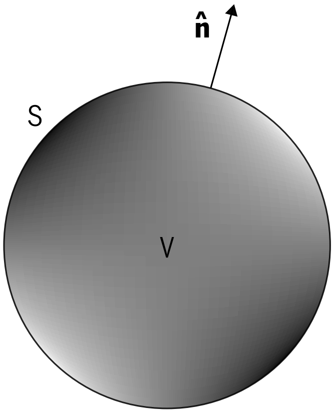

Figure 2.6: Gauss-Ostrogradski theorem illustration

V, with the normal vector $\hat{n}$ pointing to the exterior, equals the volume integral of the divergence over the region inside the surface of the vector $\vec{F}$ (see Equation 2.33 and Figure 2.6) [16–18].

$$\nabla \times \vec{E} = -\frac{\partial \vec{B}}{\partial t} \qquad \text{(Faraday's law)} \qquad (2.34)$$

$$\nabla \times \vec{H} = \frac{\partial \vec{D}}{\partial t} + \vec{J} \qquad \text{(Ampère-Maxwell law)} \qquad (2.35)$$

$$\nabla \cdot \vec{D} = \rho \qquad \text{(Gauss's law–electric)} \qquad (2.36)$$

$$\nabla \cdot \vec{B} = 0 \qquad \text{(Gauss's law–magnetic)} \qquad (2.37)$$

In a manner analogous to the integral form, the equation of continuity (Equation 2.38) can also be derived from Maxwell's equations in the differential form (Equations 2.35 and 2.36) [16–18].

$$\nabla \cdot \vec{J} = -\frac{\partial \rho}{\partial t} \qquad \text{(Equation of continuity)} \qquad (2.38)$$

In the time-harmonic fields, only three of the five equations (Equations 2.34 to 2.38) are independent; the remaining two can be derived from these three independent equations. The independent equations can be Equations 2.34 through 2.36 or Equations 2.34, 2.35, and 2.38 [16–18].

2.2.1.3 Time-harmonic fields

When the fields are oscillating harmonically at a single frequency, Maxwell's Equations 2.34 and 2.35, as well as the equation of continuity, Equation 2.38, can be formulated more conveniently by utilizing the complex phasor notation as follows [16–18]:

$$\nabla \times \vec{E} = -j\omega\vec{B} \qquad \text{(Faraday's law)} \qquad (2.39)$$

$$\nabla \times \vec{H} = j\omega\vec{D} + \vec{J} \qquad \text{(Ampère-Maxwell law)} \qquad (2.40)$$

$$\nabla \cdot \vec{J} = -j\omega\rho \qquad \text{(Equation of continuity)} \qquad (2.41)$$

where

$$j\omega = \frac{\partial}{\partial t} \qquad (2.42)$$

in which $j^2 = -1$, and ω is the angular frequency.

The time-harmonic fields are not as restricted as they initially appear; utilizing the Fourier analysis and knowing the field for any ω, it is straightforward to convert the time-harmonic fields into time-varying fields using the inverse Fourier transform, Equation 2.10.

2.2.1.4 Constitutive relations

From the set of four Maxwell's equations plus the equation of continuity, only three equations are independent. However, there are four unknowns: $\vec{E}$, $\vec{B}$, $\vec{D}$, and $\vec{H}$, which exceed the number of independent equations. It becomes definite when the macroscopic properties of the medium are considered. These properties are the constitutive relation between pairs of vector fields:

$$\vec{D} = [\epsilon]\,\vec{E} \qquad (2.43)$$

$$\vec{B} = [\mu]\,\vec{H} \qquad (2.44)$$

$$\vec{J} = [\sigma]\,\vec{E} \qquad (2.45)$$

where:

ϵ is the electric permittivity (F/m);

μ is the magnetic permittivity (H/m);

σ is the conductivity (S/m).

Those quantities are tensors in their general form. Still, they can be reduced into scalers in the case of isotropic media and even into constants if the media is both isotropic and homogeneous [16–18]. In this last circumstance, the constitutive relations are position-independent.

2.2.1.5 Vector wave equations

Maxwell's equations are a set of first-order differential equations that describe the behavior and interactions between two fields, the electric and magnetic. However, in the case of isotropic media, these first-order differential equations can be converted into a second-order equation involving just one of the fields [16–18]. For the electric field $\vec{E}$, the second-order differential equation can be obtained by substituting the $\vec{H}$ field in Equation 2.40 with the expression $-\frac{1}{j\omega\mu}\nabla \times \vec{E}$, which is derived by applying Equation 2.44 into Equation 2.39. By doing this, the following equation is obtained:

$$\nabla \times \left(\frac{1}{\mu}\nabla \times \vec{E}\right) - \omega^2\epsilon\vec{E} = -j\omega\vec{J} \tag{2.46}$$

Similarly, a second-order differential equation for the $\vec{H}$ field can be obtained:

$$\nabla \times \left(\frac{1}{\epsilon}\nabla \times \vec{H}\right) - \omega^2\mu\vec{H} = \nabla \times \left(\frac{1}{\epsilon}\vec{J}\right) \tag{2.47}$$

These equations are called inhomogeneous vector wave equations [16–18]. However, the solution of the above equations (Equations 2.46 and 2.47) still needs to satisfy the third and fourth Maxwell's equations, Equations 2.36 and 2.37, respectively. For the particular case where the media is isotropic and homogeneous, the vector wave equations can be simplified as follows:

$$\nabla^2 \vec{E} + k^2 \vec{E} = -j\omega\mu\vec{J} \tag{2.48}$$

$$\nabla^2 \vec{B} + k^2 \vec{B} = -\mu\nabla \times \vec{J} \tag{2.49}$$

This is done by applying the vector calculus identity 2.50. In the case of Equation 2.48, it was assumed that there are no charges ($\nabla \cdot \vec{E} = 0$) [16–18].

$$\nabla \times \left(\nabla \times \vec{F}\right) = \nabla \left(\nabla \cdot \vec{F}\right) - \nabla^2 \vec{F} \tag{2.50}$$

2.2.1.6 Scalar and vector potentials

Maxwell's equations provide all the knowledge required for fully identifying an electromagnetic phenomenon, but they can offer difficulties when the solutions are more complex. To make it easier to find a solution, auxiliary functions known as potentials (electric scaler potential and magnetic vector potential) are defined, simplifying the search of a solution in some situations [16–18].

$$\nabla \cdot \left(\nabla \times \vec{F}\right) = 0 \tag{2.51}$$

$$\nabla \times (\nabla \phi) = 0 \tag{2.52}$$

The magnetic vector potential, $\vec{A}$, can be introduced through Maxwell's Equations 2.37. By considering the vector calculus identity 2.51, the following is obtained:

$$\vec{B} = \nabla \times \vec{A} \tag{2.53}$$

Similarly, via Maxwell's Equation 2.39 and applying the vector calculus identity 2.52, the function of the electric scaler potential, ϕ, is presented as:

$$\vec{E} = -\nabla\phi - j\omega\vec{A} \tag{2.54}$$

Magnetic vector potential ($\vec{A}$) and electric scaler potential (ϕ) are not well-defined functions [16–18]. This is demonstrated by introducing an arbitrary function, ψ, to create a new pair of potentials, $\left(\vec{A}', \phi'\right)$, where:

$$\vec{A}' = \vec{A} - \nabla\psi \tag{2.55}$$

$$\phi' = \phi + j\omega\psi \tag{2.56}$$

By applying Equations 2.53 and 2.54 to the new potentials defined by Equations 2.55 and 2.56, and considering the vector calculus identity 2.52, the following is obtained:

$$\vec{B} = \nabla \times \vec{A}' = \nabla \times \vec{A} - \nabla \times \nabla\psi = \nabla \times \vec{A} \tag{2.57}$$

$$\vec{E} = -j\omega\vec{A}' - \nabla\phi' = -j\omega\vec{A} + j\omega\nabla\psi - \nabla\phi - j\omega\nabla\psi = -j\omega\vec{A} - \nabla\phi \tag{2.58}$$

The differential equations that must be satisfied for the potentials in isotropic media are direct consequences of Maxwell Equations 2.36 and 2.40. By applying Equations 2.53 and 2.54, along with the constitutive relations, Equations 2.43 and 2.44, the following is obtained:

$$\nabla \times \left(\frac{1}{\mu}\nabla \times \vec{A}\right) = \omega^2\epsilon\vec{A} - j\omega\epsilon\nabla\phi + \vec{J} \tag{2.59}$$

$$j\omega\nabla \cdot \left(\epsilon\vec{A}\right) + \nabla \cdot (\epsilon\nabla\phi) = -\rho \tag{2.60}$$

For isotropic and homogeneous media, it can be further simplified by applying the vector calculus identity 2.50 [16–18]:

$$\nabla^2\vec{A} + k^2\vec{A} - \nabla\left(\nabla \cdot \vec{A} + j\omega\mu\epsilon\phi\right) = -\mu\vec{J} \tag{2.61}$$

$$\nabla^2\phi + j\omega\nabla \cdot \vec{A} = -\frac{\rho}{\epsilon} \tag{2.62}$$

Gauge invariance is a concept that applies to many areas of physics, and several authors have proposed restrictions on this degree of freedom [16]. In this work, the Lorentz gauge condition has been utilized:

$$\nabla \cdot \vec{A} + j\omega\mu\epsilon\phi = 0 \tag{2.63}$$

Imposing the Lorentz gauge condition (Equation 2.63), the differential equations for the potentials, Equations 2.61 and 2.62, are simple:

$$\nabla^2 \vec{A} + k^2 \vec{A} = -\mu \vec{J} \tag{2.64}$$

$$\nabla^2 \phi + k^2 \phi = -\frac{\rho}{\epsilon} \tag{2.65}$$

2.2.1.7 Boundary conditions

For a given problem, there are many solutions that satisfy Maxwell's equations. However, just one of them is the solution to the real-world problem. To obtain it, in addition to knowledge of differential equations, it is required to know the boundary conditions associated with the domain. Those conditions can be deduced from the integral form of Maxwell's equations (Equations 2.27 to 2.30). Where in its general form at the interface between two media, given by:

$$\hat{n} \times \left(\vec{E}_1 - \vec{E}_2\right) = 0 \tag{2.66}$$

$$\hat{n} \cdot \left(\vec{D}_1 - \vec{D}_2\right) = \rho_s \tag{2.67}$$

$$\hat{n} \times \left(\vec{H}_1 - \vec{H}_2\right) = \vec{J}_s \tag{2.68}$$

$$\hat{n} \cdot \left(\vec{B}_1 - \vec{B}_2\right) = 0 \tag{2.69}$$

where $\hat{n}$ is the unit vector normal to the interface, as depicted in Figure 2.7. Also, only two equations, one from Equations 2.66 and 2.69, and the other from Equations 2.67 and 2.68, are independent.

The boundary conditions can be simplified in a particular case where one of the media is a perfect conductor [17]. Since an ideal conductor cannot sustain internal fields, Equations 2.66 and 2.69 becomes:

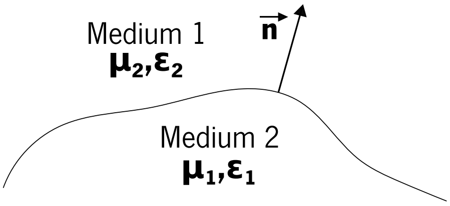

Figure 2.7: Interface between two media

$$\hat{n} \times \vec{E} = 0 \tag{2.70}$$

$$\hat{n} \cdot \vec{B} = 0 \tag{2.71}$$

where $\vec{E}$ and $\vec{B}$ are the outside fields to the conductor, and $\hat{n}$ points away from the conductor [17].

2.2.2 Method of moments

MoM [19] was designed to solve the integral field equations, and it is frequently employed to analyze antenna devices because the antennas are typically thin wires and thin sheets. The MoM discretizes the *3D* devices by decomposing them into a *2D* surface mesh and, similarly, decomposes the thin wire devices into a straight *1D* segment mesh. This discretization and the open domain nature of the MoM (meaning that the specification of boundary conditions is not required) are the main reasons for being applied in the antenna domain. The basis and test functions are then applied to each element [20, 21]. The choice of these functions is central, as errors can occur due to this decision [22]. Pulse, triangular, and sinusoidal functions are the most commonly used basis and test functions for thin wires.

Green's functions, the core of MoM, are the impulse response of an inhomogeneous linear differential operator, which aids in analyzing the current on each element and the strength of each moment. Typically, there are many issues associated with MoM, such as low-frequency breakdown and singularities [23]. However, by employing singularity extraction, the accuracy of calculating Green's function integral is enhanced. Also, MoM discretization results in a large and dense matrix, making it time-consuming and unsuitable for significant problems. Nevertheless, this could be overcome by employing preconditioners and iterative approaches [24]. In this thesis MoM was used to model thin-wire structures with speed, precision, stability, and versatility by using triangular functions as basis and test functions [10].

The MoM has several strengths over other methods, namely FDTD and FEM, which are methods based on differential equations. The main strengths are: i) the open domain, meaning that it does not require boundary conditions in the domain edge in contrast with the FDTD and FEM, which requires it to be closed domain methods; ii) the discretization of thin wires devices with unidimensional segments, which in contrast with FDTD and FEM that require the discretization of the entire volume where the device is in; iii) the memory usage that is much less than in FDTD and FEM; and iv) the processing time that is also shortened compared to the processing time needed by FDTD and FEM.

The derivation of the terms used in the MoM to form the matrix equation (manipulated to solve the thin-wire-based inductive sensors) starts with the imposition of the Lorenz gauge in the potential formulation of the electromagnetic field equations. In which the imposed Lorenz gauge, Equation 2.72, yields Equation 2.73. Where, ∇ is the vector differential operator, $j^2 = -1$, ω is the angular frequency, μ is the magnetic permeability, ϵ is the electric permittivity, ϕ is the electric scalar potential, $\vec{A}$ is the magnetic vector potential, $\vec{J}$ is the current density, and k is the wavenumber.

$$\nabla \cdot \vec{A} = -j\omega\mu\epsilon\phi \tag{2.72}$$

$$\nabla^2 \vec{A} + k^2 \vec{A} = -\mu \vec{J} \tag{2.73}$$

In the context of Green's functions, one can solve the non-homogeneous linear equation, Equation 2.73, which can be represented generically by Equation 2.74. In this equation, $\mathcal{L}$ is a linear operator, Φ is an unknown function, and g is a force function. As a result, for Equation 2.74, a solution can be expected in the form of Equation 2.75, where the core of this integral operator, G, is the Green's function. In this case, Green's function has the form of Equation 2.76 due to the $\mathcal{L}$ operator being $\nabla^2 + k^2$ and because it is a three-dimensional problem. Moreover, the integral operator in Equation 2.75 can be seen as the sum of the influences produced by all sources (at r' positions) in the Ω domain at the r position. In the case of Equation 2.73, where the unknown function Φ is the magnetic vector potential $\vec{A}$ and the known force function g is $\mu\vec{J}$, making the respective substitutions in Equation 2.75 leads to Equation 2.77 [19]. Furthermore, because μ, in most cases, defines the permeability of a linear, isotropic, and homogeneous medium that a scalar can represent, μ can be extracted from the integral, as shown in Equation 2.77.

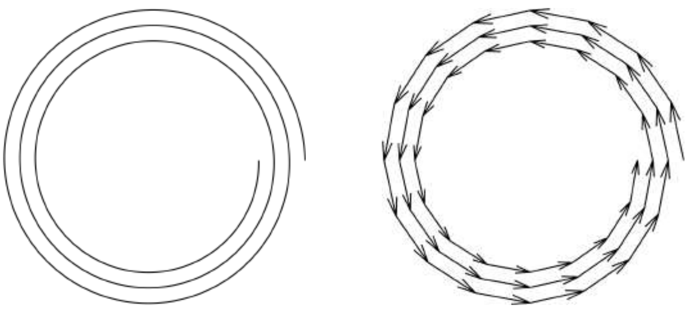

(a) Curved thin wire **(b)** Discretization

Figure 2.8: Curved thin wire discretization

$$\mathcal{L}\Phi = g \tag{2.74}$$

$$\Phi(r) = \int_{\Omega} G(r, r')g(r')dr' \tag{2.75}$$

$$G(\vec{r}, \vec{r'}) = \frac{e^{-jk|\vec{r}-\vec{r'}|}}{4\pi|\vec{r}-\vec{r'}|} \tag{2.76}$$

$$\vec{A}(\vec{r}) = -\mu \int_{\Omega} G(\vec{r}, \vec{r'})\vec{J}(\vec{r'})d\vec{r'} \tag{2.77}$$

Using the potential formulation of the electromagnetic field equations, the electric field $\vec{E}$ can be obtained through Equation 2.78a. By rearranging this equation, Equation 2.78a, the term $-j\omega\mu\epsilon\phi$ can be replaced with $\nabla \cdot \vec{A}$ from Equation 2.72, which leads to Equation 2.78b. Equation 2.78c is obtained by replacing the magnetic vector potential $\vec{A}$ with the right-hand side of Equation 2.77.

$$\vec{E} = -j\omega\vec{A} - \nabla\phi \tag{2.78a}$$

$$= -\frac{j}{\omega\mu\epsilon}\left(k^2 - \nabla\nabla\cdot\right)\vec{A} \tag{2.78b}$$

$$= \frac{j}{\omega\epsilon}\left(k^2 - \nabla\nabla\cdot\right)\int_{\Omega} G(\vec{r}, \vec{r'})\vec{J}(\vec{r'})d\vec{r'} \tag{2.78c}$$

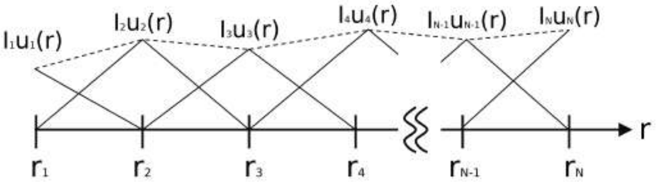

Figure 2.9: Triangle functions with *half triangle* on first and last segment

Figure 2.8a depicts a thin curved wire, and Figure 2.8b shows this thin curved wire subdivided into N segments with $N+1$ endpoints. Although the segments, in this example, are the same length, they can be of different lengths. However, because the tangent vector is a piecewise continuous function, the segments must be small enough not to disturb (distort) the curvature of the wire. Since the wire is very thin, it can be assumed that the current $\vec{J}$ is a filamentary current $\vec{I}$. This current $\vec{I}$ is expanded using base functions ($\vec{u}_n$), Equation 2.79, where I_n are the unknown coefficients and $\vec{u}_n$ is an arbitrary basis, but most frequently is a pulse, triangular or sinusoidal function. Among the three, the triangular function, Equation 2.80, is the most used, being depicted in Figure 2.9 [19]. As represented in Figure 2.9, the first and last segments are assigned a *"half triangle"*, allowing the solution to take any value at the ends. Otherwise, if a *"full triangle"* is assigned, the solution will be zero at the ends, which is the case of an antenna.

$$\vec{I}(\vec{r}) = \sum_{n=1}^{N} I_n \vec{u}_n(\vec{r}) \tag{2.79}$$

$$\vec{u}_n(\vec{r}) = \begin{cases} \dfrac{\vec{r}-\vec{r}_n}{|\vec{r}_{n+1}-\vec{r}_n|} & ,\vec{r} \in \overline{\vec{r}_n, \vec{r}_{n+1}} \\ \\ \dfrac{\vec{r}_{n+2}-\vec{r}}{|\vec{r}_{n+2}-\vec{r}_{n+1}|} & ,\vec{r} \in \overline{\vec{r}_{n+1}, \vec{r}_{n+2}} \end{cases} \tag{2.80}$$

In the inductive sensor design, the excitation coil is sourced by a delta-gap source, as shown in Figure 2.10a [19]. The delta-gap source treats the source as if the field exists only between the coil terminals, having zero value outside. Whenever it is assumed that the field exists on a single wire segment and is zero on the others, it means that the resulting excitation vector will only have non-zero elements for basis functions supported on that segment. This sourcing method typically yields less accurate results for input impedance simulation, but it does very well at simulating radiation patterns, which is one of the reasons

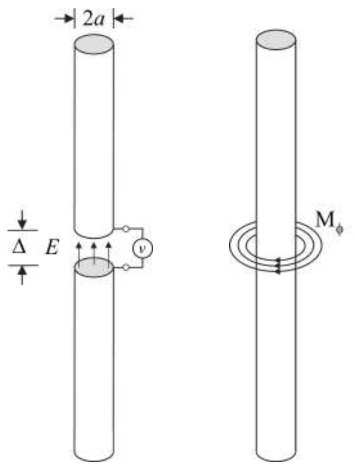

(a) Delta-Gap **(b)** Frill

Figure 2.10: MoM's thin wire feeding techniques

for its selection. The other reasons are its implementation simplicity and reduced computational cost, when compared to other techniques, namely frill (Figure 2.10b [19]).

Equation 2.81a is obtained by applying thin-wire discretization to Equation 2.78c. This is accomplished by substituting the current density $\vec{J}$, in Equation 2.78c, with the discretized filamentary current $\vec{I}$ in Equation 2.79. Also, since I_n is independent of the integration variable $\vec{r}'$ and the order of operations can be changed, $\sum_{n=1}^{N} I_n$ can be moved outside the integral, leading to Equation 2.81b (or Equation 2.81c, where $\vec{g}_m$ is given by Equation 2.82).

$$\vec{E}(\vec{r}_m) \approx \frac{j}{\omega\epsilon}\left(k^2 - \nabla\nabla\cdot\right)\int_{\Delta\vec{r}'_n} G(\vec{r}_m,\vec{r}')\sum_{n=1}^{N} I_n\vec{u}_n(\vec{r}')d\vec{r}' \tag{2.81a}$$

$$= \sum_{n=1}^{N} I_n\frac{j}{\omega\epsilon}\left(k^2 - \nabla\nabla\cdot\right)\int_{\Delta\vec{r}'_n} G(\vec{r}_m,\vec{r}')\vec{u}_n(\vec{r}')d\vec{r}' \tag{2.81b}$$

$$= \sum_{n=1}^{N} I_n\vec{g}_m \tag{2.81c}$$

$$\vec{g}_m = \frac{j}{\omega\epsilon}\left(k^2 - \nabla\nabla\cdot\right)\int_{\Delta\vec{r}'_n} G(\vec{r}_m,\vec{r}')\vec{u}_n(\vec{r}')d\vec{r}' \tag{2.82}$$

To solve the unknown current amplitudes I_n, N equations must be obtained from Equation 2.81c by multiplying Equation 2.81c with weight (or test) functions $\vec{v}_n$, and integrating them along the wire's length.

As a result, the inner product of each weighting function and $\vec{g}_m$ is formed, which leads to Equation 2.83b. In this way, a set of N simultaneous equations written in matrix form are obtained, as shown in Equation 2.84 or 2.85, where Z_{mn}, the impedance matrix, is given by Equation 2.86, and V_m, the source vector, is given by Equation 2.87. The unknown current's value is then calculated by solving the matrix equation, Equation 2.84 or 2.85 [19].

$$\left\langle \vec{v}_n, \sum_{n=1}^{N} I_n \vec{g}_m \right\rangle = \left\langle \vec{v}_n, \vec{E} \right\rangle \Leftrightarrow \tag{2.83a}$$

$$\sum_{n=1}^{N} I_n \left\langle \vec{v}_n, \vec{g}_m \right\rangle = \left\langle \vec{v}_n, \vec{E} \right\rangle \tag{2.83b}$$

$$\begin{bmatrix} \langle \vec{v}_1, \vec{g}_1 \rangle & \cdots & \langle \vec{v}_1, \vec{g}_N \rangle \\ \vdots & \ddots & \vdots \\ \langle \vec{v}_N, \vec{g}_1 \rangle & \cdots & \langle \vec{v}_N, \vec{g}_N \rangle \end{bmatrix} \begin{bmatrix} I_1 \\ \vdots \\ I_N \end{bmatrix} = \begin{bmatrix} \left\langle \vec{v}_1, \vec{E}_1 \right\rangle \\ \vdots \\ \left\langle \vec{v}_N, \vec{E}_N \right\rangle \end{bmatrix} \tag{2.84}$$

$$[Z]\,[I] = [V] \tag{2.85}$$

$$\begin{aligned} Z_{mn} = j\omega\mu \int_{\Delta\vec{r}_m} \vec{v}_m(\vec{r}) \cdot \int_{\Delta\vec{r}'_n} \vec{u}_n(\vec{r}') G(\vec{r}, \vec{r}') d\vec{r}' d\vec{r} \\ -\frac{j}{\omega\epsilon} \int_{\Delta\vec{r}_m} \nabla \cdot \vec{v}_m(\vec{r}) \int_{\Delta\vec{r}'_n} \nabla' \cdot \vec{u}_n(\vec{r}') G(\vec{r}, \vec{r}') d\vec{r}' d\vec{r} \end{aligned} \tag{2.86}$$

$$V_m = \int_{\Delta\vec{r}_m} \vec{v}_m(\vec{r}) \cdot \vec{E}(\vec{r}) d\vec{r} \tag{2.87}$$

In the matrix elements, Equation 2.86, the calculations are carried out using an *M*-point numerical Gauss-Legendre quadrature formula, resulting in Equation 2.89 [19], where w_p and w_q are the quadrature weights. Additionally, Equation 2.89 includes Δ_p and Δ_q, which are related to the divergence operation. This is because the divergence of a triangular function is $1/\Delta_l$ or $-1/\Delta_l$ on a segment of length Δl when used as a basis and test function, depending on whether it is the first or second segment of the element, as demonstrated in Equation 2.88. It is important to mention that Equation 2.89 only applies to non-overlapping elements because a division by zero occurs when applying it to overlapping elements. For this reason, singularity extraction must be applied for these overlapping elements, leading to Equation 2.92, where $S1$ and $S2$ are given by Equations 2.90 and 2.91, respectively, with a being the wire radius. Equations 2.92 and 2.89 provide the elements for the impedance matrix, Z, for the overlapping and non-overlapping segments, respectively.

$$
\begin{aligned}
\nabla \cdot \vec{u}_n &= \begin{cases} \nabla \cdot \dfrac{\vec{r} - \vec{r}_n}{|\vec{r}_{n+1} - \vec{r}_n|}, \vec{r} \in \overline{\vec{r}_n, \vec{r}_{n+1}} \\ \\ \nabla \cdot \dfrac{\vec{r}_{n+2} - \vec{r}}{|\vec{r}_{n+2} - \vec{r}_{n+1}|}, \vec{r} \in \overline{\vec{r}_{n+1}, \vec{r}_{n+2}} \end{cases} \\
&= \begin{cases} \nabla \cdot \dfrac{\vec{r} - \vec{r}_n}{\Delta_l} \\ \\ \nabla \cdot \dfrac{\vec{r}_{n+2} - \vec{r}}{\Delta_l} \end{cases} = \begin{cases} \dfrac{1}{\Delta_l} \nabla \cdot (\vec{r} - \vec{r}_n) \\ \\ \dfrac{1}{\Delta_l} \nabla \cdot (\vec{r}_{n+2} - \vec{r}) \end{cases} \\
&= \begin{cases} \dfrac{1}{\Delta_l} \left[\dfrac{\partial (r_x - r_{x_n})}{\partial x} + \dfrac{\partial (r_y - r_{y_n})}{\partial y} + \dfrac{\partial (r_z - r_{z_n})}{\partial z} \right] \\ \\ \dfrac{1}{\Delta_l} \left[\dfrac{\partial \left(r_{x_{n+2}} - r_x\right)}{\partial x} + \dfrac{\partial \left(r_{y_{n+2}} - r_y\right)}{\partial y} + \dfrac{\partial \left(r_{z_{n+2}} - r_z\right)}{\partial z} \right] \end{cases} \\
&= \begin{cases} \dfrac{1}{\Delta_l} \left[\dfrac{\partial r_x}{\partial x} + \dfrac{\partial r_y}{\partial y} + \dfrac{\partial r_z}{\partial z} \right] \\ \\ \dfrac{1}{\Delta_l} \left[-\dfrac{\partial r_x}{\partial x} - \dfrac{\partial r_y}{\partial y} - \dfrac{\partial r_z}{\partial z} \right] \end{cases} = \begin{cases} \dfrac{1}{\Delta_l} \\ -\dfrac{1}{\Delta_l} \end{cases}
\end{aligned}
\tag{2.88}
$$

$$
\begin{aligned}
Z_{mn} = &\frac{1}{4\pi} \sum_{p=1}^{M} \sum_{q=1}^{M} w_p(\vec{r}_p) w_q(\vec{r}'_q) \\
&\left[j\omega\mu \vec{v}_m(\vec{r}_p) \cdot \vec{u}_n(\vec{r}'_q) \pm \frac{j}{\omega\epsilon\Delta_p\Delta_q} \right] \frac{e^{-jk\vec{r}_p - \vec{r}'_q|}}{|\vec{r}_p - \vec{r}'_q|}
\end{aligned}
\tag{2.89}
$$

$$\begin{aligned} S_1(r) &= \frac{1}{\Delta_l}\sqrt{a^2+(r-\Delta_l)^2} - \frac{1}{\Delta_l}\sqrt{a^2+r^2} \\ &+ \frac{r}{\Delta_l} log\left[\frac{r+\sqrt{a^2+r^2}}{r-\Delta_l+\sqrt{a^2+(r-\Delta_l)^2}}\right] - \frac{jk\Delta_l}{2} \end{aligned} \tag{2.90}$$

$$S_2(r) = \pm\frac{1}{\Delta_l^2}\left[log\left[\frac{r+\sqrt{a^2+r^2}}{r-\Delta_l+\sqrt{a^2+(r-\Delta_l)^2}}\right] - jk\Delta_l\right] \tag{2.91}$$

$$Z_{mn} = \frac{1}{4\pi}\sum_{p=1}^{M} w_p(r_p)\left[j\omega\mu v_m(r_p)S_1(r_p) - \frac{j}{\omega\epsilon}S_2(r_p)\right] \tag{2.92}$$

2.2.3 Fast multipole method

The FMM was first introduced by Barnes [25] to reduce the computational complexity of the classic N-body problem. The most common example of an N-body problem is the gravitational interaction of the celestial bodies. When the gravitational interaction is merely between two bodies, it is simple to calculate, analytically, the location and velocity of the two bodies through past and future time. However, when the gravitational interaction is between three or more celestial bodies, it is inevitable to use numerical methods. The N-body problem involves the computation of $\frac{1}{2}N(N-1)$ gravitational forces between all pairs, where the N is the total number of celestial bodies. When N is small, it is trivial to solve it using computers. However, when N becomes very large, the calculations may grow so large that it becomes impractical or impossible. To reduce the complexity of the N-body problem, Greengard and Rokhlin [26] provided a theoretical breakthrough. In its most potent multi-level form, the asymptotic cost per iteration is reduced from $O(N^2)$ to $O(NlogN)$ [25], and it is one of the most popular of the fast methods today.

The FMM, in a nutshell, is a method that exploits the fact that the amplitude of the interaction between the basis (*radiated* field) and testing (*received* field) functions diminish quickly over distance. As a result, a group of closely spaced thin-wire elements can be simplified at a distance as a single function that represents the entire group's potential [19]. It is accomplished by rewriting the interaction of the basis and test functions in terms of their multipole expansions. In addition, the multipole expansion can be truncated at some finite order without significantly compromising the result. For the inductive sensor, the interaction between nearby thin-wire elements is done using MoM.

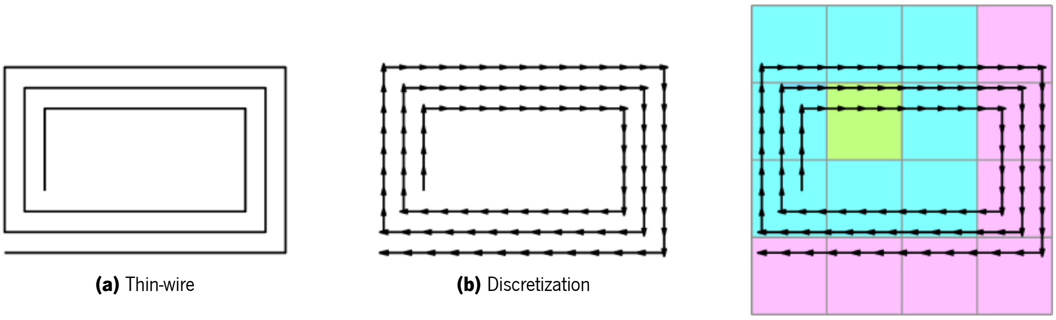

(a) Thin-wire **(b)** Discretization **(c)** Spatial subdivision

Figure 2.11: Thin-wire discretization

Figure 2.11a depicts a thin-wire conductor with a rectangular shape. In Figure 2.11b, the conductor is discretized similarly to the thin-wire MoM, where each element consists of two straight segments, and two consecutive elements share the same middle segment. This segment sharing means that the total number of elements is one less than the total number of straight segments. Additionally, each element has its own test and basis function, both triangular functions in this work, represented by $\vec{v}_n$ and $\vec{u}_n$, respectively, throughout the remainder of this document. Finally, these thin-wire elements are grouped into square cells to be used in the FMM by dividing the space around each basis function into two regions: the *near-field* and *far-field* regions, as depicted in Figure 2.11c. From the perspective of one local group (e.g., the group in light-green in Figure 2.11c), the so-called *near-field* region encompasses all groups with strong-field interactions with this group. In the case of Figure 2.11c, these are the local group and all nearby groups colored in light-blue. The regions having weaker interactions with the local group are called *far-field* regions, and in the example of Figure 2.11c, these are all light-red cubes.

In Equation 2.85, a matrix-vector product is presented within the context of MoM. Here, Z represents the impedance matrix, which accounts for the interactions between the basis and test functions. The right-hand side vector I represents the excitation of each basis function and can be seen as a filamentary current due to the use of thin wires. The left-hand side vector V is the sum of the fields *received* by each test function as a result of the fields *radiated* by all basis functions. All elements that compose the impedance matrix Z are given by Equation 2.86 where, $j^2 = -1$, ω is the angular frequency, μ is the magnetic permeability, ϵ is the electric permittivity, $G(\vec{r}, \vec{r'})$ is the Green's function, and r' and r are the source and field points, respectively. Equation 2.76 is Green's function for the wave equation in a *3D* space, where k is the wavenumber. The elements that compose the vector V are given by Equation 2.87, where $\vec{E}$ is the electrical field.

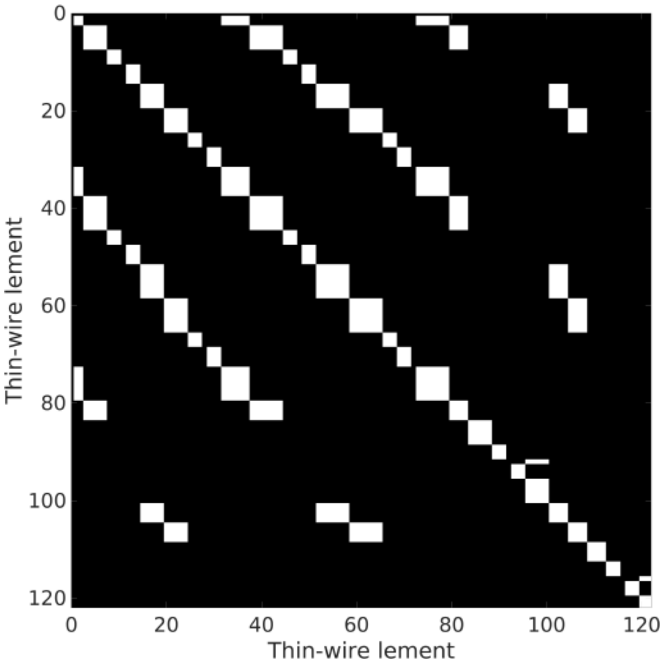

Figure 2.12: FMM Z_{near} mask of the thin-wire discretization

Because some basis functions are in the near region of a specific testing function and others are in the far region, the vectors V and I can be divided into V^{near}, V^{far}, I^{near}, and I^{far} as shown in Equation 2.93 [19]. As a result, the impedance matrix Z is divided into two sparse matrices, Z^{near} and Z^{far} (Equation 2.94). This allowed to divide the electromagnetic problem into two independent equations, $\left[Z^{near}\right]\left[I^{near}\right] = \left[V^{near}\right]$ and $\left[Z^{far}\right]\left[I^{far}\right] = \left[V^{far}\right]$. In the FMM, both equations are solved at a time and independently, with the near region equation explicitly solved, as in the MoM, and the far region equation solved differently on the fly (described further in this section). Figure 2.12 depicts the Z^{near} matrix for the Figure 2.11c example, where matrix elements with values other than zero are represented in white. One of the primary advantages of this approach is that the Z^{near} matrix is extremely sparse, as illustrated in Figure 2.12. As a result, the memory required to store this matrix is significantly reduced, as is the processing time required to solve the near region equation.

$$[V] = \left[V^{near}\right] + \left[V^{far}\right] = \left[Z^{near}\right][I] + \left[Z^{far}\right][I] \tag{2.93}$$

$$[Z] = \left[Z^{near}\right] + \left[Z^{far}\right] \tag{2.94}$$

As previously stated, the near region equation is solved numerically, as in the MoM. The far region equation,

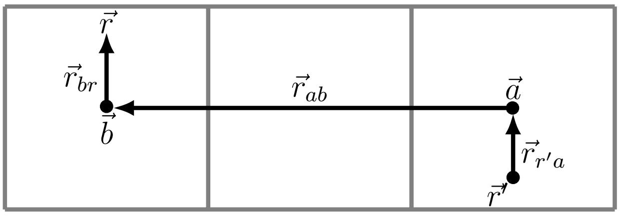

Figure 2.13: Wave translation in the context of the FMM

on the other hand, is solved on the fly using an algorithm. As mentioned, this algorithm begins by dividing the *3D* space where the thin-wire device is located into cubic cells (see Figure 2.11c, where each square cell is, in reality, a cube seen from above). All thin wires within the same cube cell belong to the same local group (light-green in Figure 2.11c), which, when combined with all thin wires within adjacent cubic cells (light-blue in Figure 2.11c), forms the near region. The algorithm solves all far interactions between the local group and the far region, which are all groups outside the near region (light-red in Figure 2.11c). These interactions are solved by translating each thin-wire element's source and field points in each cubic cell to the centre of the corresponding cube. Figure 2.13 depicts it, with the source point $\vec{r'}$ translated to the centre of the correspondent cube, point $\vec{a}$, and the observation point $\vec{r}$ translated to the centre of the correspondent cube, point $\vec{b}$. Both cubes with centre points $\vec{a}$ and $\vec{b}$ are in the far region of each other. This translation acts as the wave radiating from a distant point where being radiated from a point nearby. Throughout the observation of Figure 2.13, the vector $\vec{r}-\vec{r'}$ can be written as the sum of three vectors, $\vec{r}_{r'a}$, $\vec{r}_{ab}$, and $\vec{r}_{br}$ (see Equation 2.95). Consequently, Green's function can be rewritten accordingly, where $\vec{r}-\vec{r'}$ is replaced by the sum of the three vectors, Equation 2.96 [19].

$$\vec{r}-\vec{r'}=\vec{r}_{r'a}+\vec{r}_{ab}+\vec{r}_{br}=\left(\vec{a}-\vec{r'}\right)+\left(\vec{b}-\vec{a}\right)+\left(\vec{r}-\vec{b}\right) \tag{2.95}$$

$$\frac{e^{-jk|\vec{r}-\vec{r'}|}}{4\pi|\vec{r}-\vec{r'}|}=\frac{e^{-jk|\vec{r}_{ab}+(\vec{r}_{r'a}+\vec{r}_{br})|}}{4\pi\left|\vec{r}_{ab}+(\vec{r}_{r'a}+\vec{r}_{br})\right|} \tag{2.96}$$

By using the addition theorem for spherical waves ([19]) and knowing that $|\vec{r}_{r'a}+\vec{r}_{br}|<|\vec{r}_{ab}|$ due to the $\vec{r'}$ and $\vec{r}$ being very close to the $\vec{a}$ and $\vec{b}$ cubic cell centre points, Green's function can be rewritten in terms of multipoles, Equation 2.97 [19]. Where j_l is a spherical Bessel function of the first kind, P_l is a Legendre polynomial of order l, and $h_l^{(2)}$ is a spherical Hankel function of the second kind given by Equation 2.98. Where in Equation 2.98, $H^{(2)}$ is the Hankel function of the second kind, and n_l is the spherical Bessel function of the second kind.

$$\frac{e^{-jk|\vec{r}_{ab}+(\vec{r}_{r'a}+\vec{r}_{br})|}}{4\pi\,|\vec{r}_{ab}+(\vec{r}_{r'a}+\vec{r}_{br})|} = -\frac{jk}{4\pi}\sum_{l=0}^{\infty}(-1)^l(2l+1)$$
$$j_l(k|\vec{r}_{r'a}+\vec{r}_{br}|)h_l^{(2)}(k|\vec{r}_{ab}|)P_l\left(\frac{\vec{r}_{r'a}+\vec{r}_{br}}{|\vec{r}_{r'a}+\vec{r}_{br}|}\cdot\vec{r}_{ab}\right) \tag{2.97}$$

$$h_l^{(2)}(x) = \sqrt{\frac{\pi}{2x}}H_{l+1/2}^{(2)}(x) = j_l(x) - jn_l(x) \tag{2.98}$$

Using Equation 2.99 ([19]), Equation 2.97 can be converted to a surface integral on the unit sphere and Equation 2.100 is thus obtained ([19]), where $\hat{k}$ is the unit vector radially oriented on the unit radius sphere. Note that the integration and summation operations have been exchanged.

$$4\pi(-j^l)j_l(k|\vec{r}_{r'a}+\vec{r}_{br}|)P_l\left(\frac{\vec{r}_{r'a}+\vec{r}_{br}}{|\vec{r}_{r'a}+\vec{r}_{br}|}\cdot\vec{r}_{ab}\right) =$$
$$\oint_1 e^{-jk\hat{k}\cdot(\vec{r}_{r'a}+\vec{r}_{br})}P_l(\hat{k}\cdot\vec{r}_{ab})dS \tag{2.99}$$

$$\frac{e^{-jk|\vec{r}_{ab}+(\vec{r}_{r'a}+\vec{r}_{br})|}}{4\pi\,|\vec{r}_{ab}+(\vec{r}_{r'a}+\vec{r}_{br})|} = \frac{k}{(4\pi)^2}\oint_1 e^{-jk\hat{k}\cdot(\vec{r}_{r'a}+\vec{r}_{br})}$$
$$\sum_{l=0}^{\infty}(-j)^{l+1}(2l+1)h_l^{(2)}(k\,|\vec{r}_{ab}|)P_l(\hat{k}\cdot\vec{r}_{ab})dS \tag{2.100}$$

For the far interactions on the FMM algorithm, the summation can be truncated at some level, depending on how far away are source and the observation point. In other words, the greater the distance between the source and the observation point, the fewer the number of multipoles required to achieve satisfactory results. In Equation 2.101, the same equation as in Equation 2.100 is used but written in a more friendly way, where $T(\vec{r'},\hat{k})$ and $R(\vec{r},\hat{k})$ are the *radiation* and *receive* functions, Equations 2.102 and 2.103 respectively, and $H(k,\hat{k},\vec{r}_{ab})$ is the *transfer* function (Equation 2.104) truncated at some level L [19]. The *transfer* function can be thought of as a method for converting outgoing spherical waves from a far group to incoming spherical waves in the local group. It should be noted that the *transfer* function is independent of the positions of $\vec{r}$ and $\vec{r}'$ and only depends on $\vec{r}_{ab}$. Due to that, if the geometry of the thin-wire changes in a way that does not require a change in the structure of the cubic cells, the *transfer* functions does not need to be recalculated.

$$\frac{e^{-jk|\vec{r}-\vec{r}'|}}{4\pi|\vec{r}-\vec{r}'|} = \oint_1 R(\vec{r},\hat{k})H(k,\hat{k},\vec{r}_{ab})T(\vec{r}',\hat{k})dS \tag{2.101}$$

$$T(\vec{r}',\hat{k}) = e^{jk\hat{k}\cdot\vec{r}_{r'a}} \tag{2.102}$$

$$R(\vec{r},\hat{k}) = e^{jk\hat{k}\cdot\vec{r}_{br}} \tag{2.103}$$

$$H(k,\hat{k},\vec{r}_{ab}) = \frac{k}{(4\pi)^2}\sum_{l=0}^{L}(-j)^{l+1}(2l+1)h_l^{(2)}(k\,|\vec{r}_{ab}|)P_l(\hat{k}\cdot\hat{r}_{ab}) \tag{2.104}$$

The Z^{far} matrix is given by the function $L(\vec{v}_m,\vec{u}_n)$ (Equation 2.105), in Equation 2.106 [19]. This function is the same as the one used in Equation 2.86 to form the impedance matrix on the MoM. However, it is written differently, with both differential operators operating only on the Green's function.

$$Z_{mn}^{far} = L(\vec{v}_m,\vec{u}_n) \tag{2.105}$$

$$L(\vec{v}_m,\vec{u}_n) = \\ j\omega\mu\int_{\Delta\vec{r}_m}\vec{v}_m(\vec{r})\cdot\int_{\Delta\vec{r}'_n}\vec{u}_n(\vec{r}')\left[1-\frac{1}{k^2}\nabla\nabla'\right]G(\vec{r},\vec{r}')d\vec{r}'d\vec{r} \tag{2.106}$$

Equation 2.107 is obtained by substituting the Green's function in Equation 2.106 with its multipole representation equivalence in Equation 2.101 and rearranging the integral operators. It is important to note that the rearrangement of the integral operators was possible due to the *radiation* function being independent of $\vec{r}$, the *receive* function being independent of $\vec{r}'$, and the *transfer* function being independent of both. In

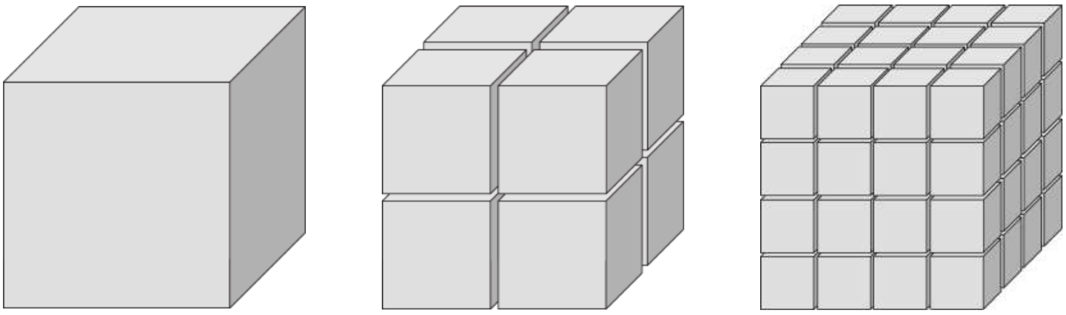

(a) Octree level 1 **(b)** Octree level 2 **(c)** Octree level 3

Figure 2.14: Octree levels 1 to 3

Equation 2.107, $T(\vec{u}_n, \hat{k})$, $H(k, \hat{k}, \vec{r}_{ab})$, and $R(\vec{v}_m, \hat{k})$ are, respectively, the *radiation*, *transfer*, and *receive* functions, depicted in Equations 2.108, 2.102, and 2.109. In the *radiation* function, Equation 2.108, the term $[1 - \hat{k}\hat{k}]$ is included, which is applied to the vector resulting from the integral term. Suppose the resulting vector is called $\vec{x}$, and applying the term $[1 - \hat{k}\hat{k}]$ on it results in $\vec{x} - \hat{k}(\hat{k} \cdot \vec{x})$. Analyzing this reveals that this term operates by removing the $\hat{k}$ component from the vector $\vec{x}$, leaving only the $\hat{\theta}$ and $\hat{\phi}$ components. Consequently, when pre-computing the *radiation* and *receive* functions, only the $\hat{\theta}$ and $\hat{\phi}$ components are stored [19].

$$L(\vec{v}_m, \vec{u}_n) = \oint_1 R(\vec{v}_m, \hat{k}) \cdot H(k, \hat{k}, \vec{r}_{ab}) T(\vec{u}_n, \hat{k}) dS \tag{2.107}$$

$$T(\vec{u}_n, \hat{k}) = \left[1 - \hat{k}\hat{k}\right] \cdot \int_{\Delta \vec{r}'_n} \vec{u}_n(\vec{r}') e^{jk\hat{k}\cdot\vec{r}_{r'a}} d\vec{r}' \tag{2.108}$$

$$R(\vec{v}_m, \hat{k}) = j\omega\mu \int_{\Delta \vec{r}_m} \vec{v}_m(\vec{r}) e^{jk\hat{k}\cdot\vec{r}_{br}} d\vec{r} \tag{2.109}$$

The integration on the sphere in Equation 2.107 ([19]) was computed using the Gauss-Legendre quadrature rule in θ and Simpson's rule in ϕ, where the quadrature weights $w_s(\hat{k})$ were pre-multiplied with the *transfer* functions.

2.2.3.1 Multilevel Fast Multipole Method

The complexity of the one-level FMM is $O(N^{\frac{3}{2}})$, but it can be extended and applied recursively, leading to Multilevel Fast Multipole Method (MLFMM) [27], which has a complexity of $O(NlogN)$. In a nutshell,

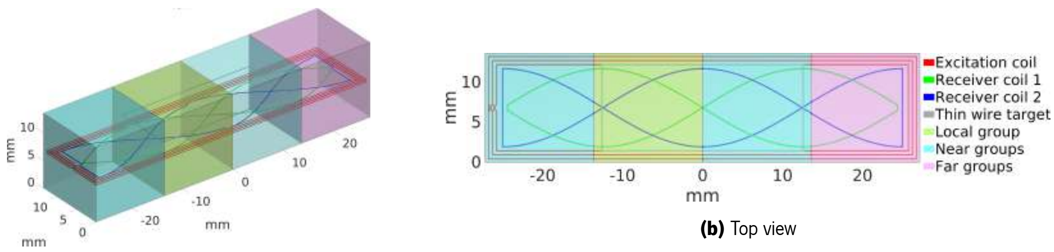

(a) 3D view

(b) Top view

Figure 2.15: Linear Position Sensor (LIPS) on octree level 3

the MLFMM is an octal tree structure of L levels that house the device. This octal tree structure's first level is a single cubic box recursively divided into eight identical child boxes at subsequent levels. Figure 2.14 (adapted from [19]) shows it on a three-level octal tree, with the first level's box divided into eight identical child boxes on the second level. Each second-level box is subdivided into eight smaller child boxes on the third level.

The near and far regions are delimited similarly to one-level FMM. Like in the one-level FMM, in MLFMM, all neighbour boxes at level l that share at least one vertice with the local group box are considered to be part of the near group, and there are a maximum of $3^3 = 27$ near group boxes, including the local group. The far group boxes at level l are all the child boxes of all parent boxes at level $l-1$, which are neighbours (that share at least one vertice) of the local group parent box and do not belong to the near group zone at level l. Meaning there are a maximum of $6^3 - 3^3 = 189$ far group boxes. Furthermore, because the *transfer* function (Equation 2.104) is a function of only k, $\hat{k}$, and $\vec{r}_{ab}$, where k and $\hat{k}$ have the same values across the entire octal tree level, it is clear that there are only $7^3 - 3^3 = 316$ different possible values of $\vec{r}_{ab}$ in a particular level of the octal tree. In other words, on each level of the octal tree, it is only, required to compute a maximum of 316 unique *transfer* functions.

On the MLFMM, the Z^{near} matrix is assembled according to the thin-wire elements inside each near region at the highest level only. In other words, this octal tree's highest level dictates how sparse the Z^{near} will be, meaning that the highest number of levels the octal tree has, the more sparse the Z^{near} matrix will be. However, a higher sub-division level comes at a cost. The closer the centre boxes of a local group and a far group are, the higher multipoles are required to compute the far interactions accurately. Nevertheless, a higher number of multipoles could potentially present numerical issues. Due to the spherical Hankel function, $h_l^{(2)}(k\,|\vec{r}_{ab}|)$ on the *transfer* function of Equation 2.104, becomes highly oscillatory for fixed $k\,|\vec{r}_{ab}|$ and increasing l, [19]. Due to that, using MLFMM to simulate significantly small devices' in comparison to their operation wavelength can be challenging.

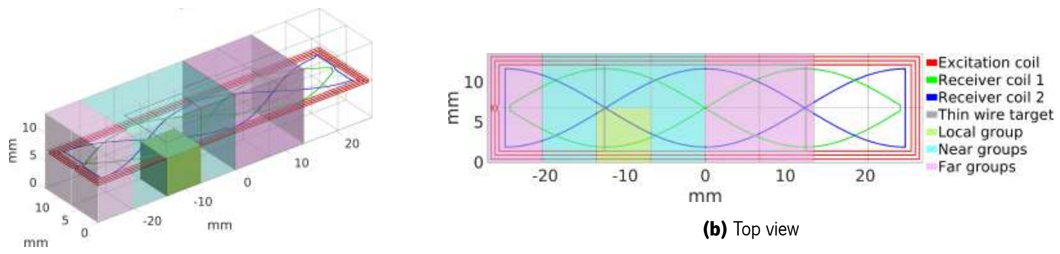

(a) 3D view

(b) Top view

Figure 2.16: LIPS on octree level 4

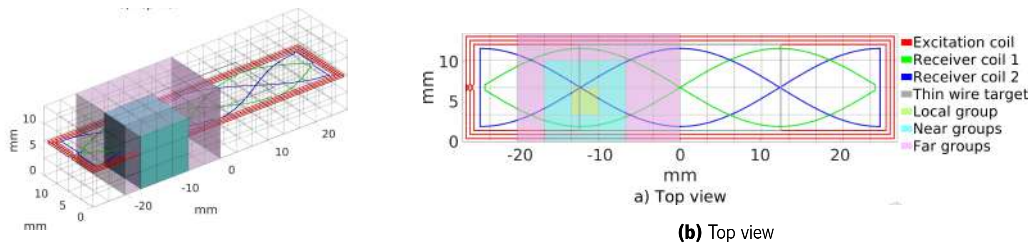

(a) 3D view

(b) Top view

Figure 2.17: LIPS on octree level 5

Figures 2.15, 2.16 and 2.17 show an inductive sensor inserted on an octal tree cubic structure. The octal tree in this example has five levels ($L = 5$), with levels 1 and 2 omitted and levels 3, 4, and 5 depicted in Figures 2.15, 2.16 and 2.17, respectively. In light-green is a local group, and in light-blue and light-red are the near and far regions, respectively, in the correspondent level.

The MLFMM algorithm has three stages: aggregation, translation, and disaggregation (see Figure 2.19, adapted from [28] and Algorithm 1). The aggregation phase is the first to be executed and starts at the highest level on the octal tree. It begins by combining the radiation patterns of all basis functions inside each box at the highest level, following steps 5-8 in Algorithm 1. Where t^{θ} and t^{ϕ} are the aggregated field vectors on the $\hat{\theta}$ and $\hat{\phi}$ components vector in the unit sphere, T^{θ} and T^{ϕ} are the *radiation* functions (see Equation 2.108), I is the current vector where Z^{far} matrix is multiply by using this algorithm, and $W_{l,L}$ is an interpolation matrix. This interpolation matrix upsamples the result of multiplication of the *transfer* function with the current vector to the rate needed at the highest level on the octal tree. The use of interpolation is explained further in the current subsection. As the algorithm progress into the lowers levels of the octal tree (upward pass), the radiation fields of the child boxes are aggregated and passed up to their parents using interpolation and phase shift, steps 14-17 in Algorithm 1. Where $W_{n+1,n}$ is the interpolation matrix that upsamples from the rate at level $n+1$ to the rate at level n, and $e^{jk\hat{k}_n\cdot(\vec{r}_c-\vec{r}_p)}$ is the phase shift term that shifts the phase of the aggregated child field vectors, $t^{\theta}_{c,n+1}$ and $t^{\phi}_{c,n+1}$, that irradiates at child's box centre's position, $\vec{r}_c$, as it radiates at parent's box centre's position, $\vec{r}_p$. The

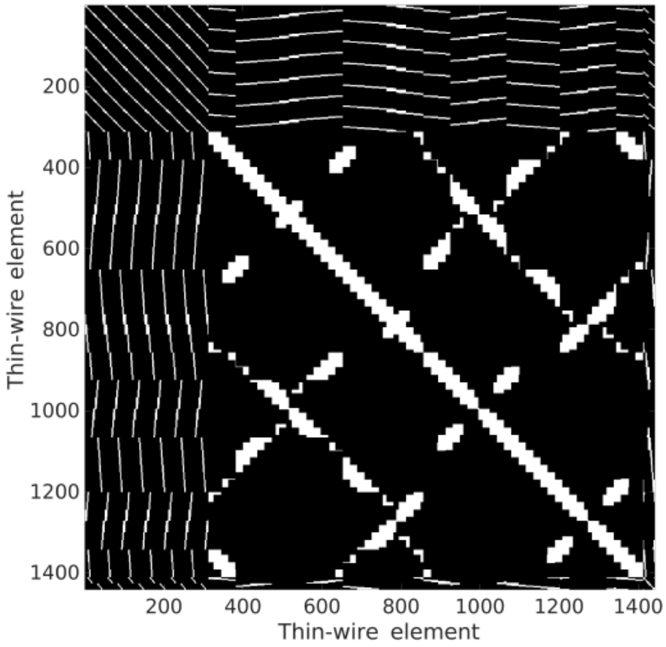

Figure 2.18: LIPS on octree Z_{near} mask (white square means 1 and black square means 0)

operation ($\odot$) in lines 15 and 16 denotes term-wise multiplication. Note that levels one and two do not have far groups, so the aggregation phase ends at level three.

In the translation phase, the aggregated fields are translated into incoming fields in the downward pass, starting at level 3 and ending at the highest level of the octal tree. This is accomplished by performing all transfers between all far groups at each level of the octal tree, as shown in steps 26, 27, 35, and 36 of Algorithm 1. Where s^{θ} and s^{ϕ} are the local field vectors, and H represents the *transfer* function depicted in Equation 2.104. The local fields are then passed down to the child boxes in the so-called disaggregation phase, steps 32 and 33 in Algorithm 1, which is done simultaneously with the translation phase. In this phase, the parents' local fields are phase-shifted, $e^{-jk\hat{k}_n\cdot(\vec{r}_c-\vec{r}_p)}$, and downsampled, $W^T_{n,n-1}$, where T denotes matrix transpose. Finally, steps 40-49 of Algorithm 1 disaggregate the local fields s^{θ} and s^{ϕ} at the highest level of the octal tree using the *receive* functions R^{θ} and R^{ϕ} from Equation 2.109. This disaggregation is done by downsampling the local fields (steps 41 and 42) and multiplying them with the appropriate *receive* function (step 46). As previously stated, the unit sphere surface integral is computed using the Gauss-Legendre quadrature in the θ dimension and Simpson's rule in the ϕ dimension, where the quadrature weights $w_s(\hat{k})$ were pre-multiplied with the *transfer* function. As a result, the integration is performed by simply adding all discretized points in the unit sphere, as shown in step 46 of Algorithm 1.

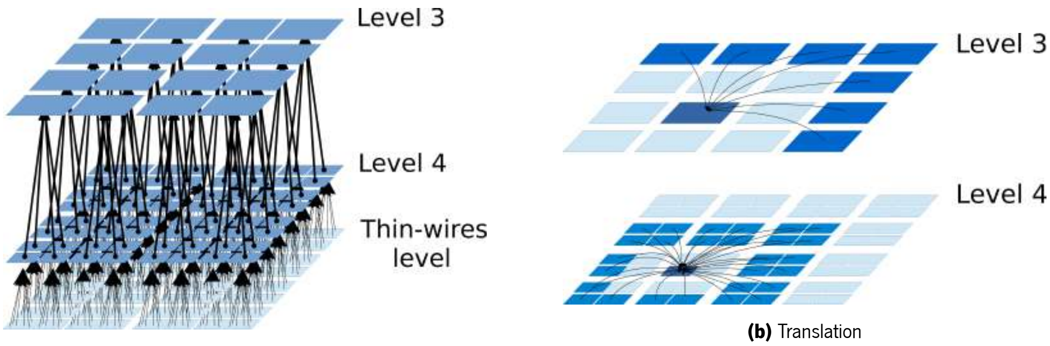

(a) Aggregation

(b) Translation

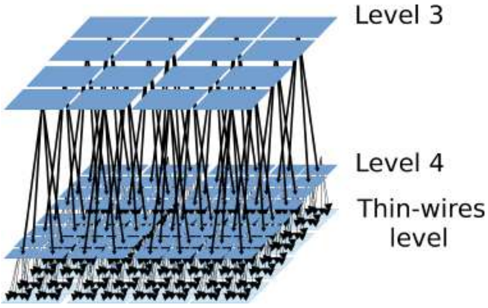

(c) Disaggregation

Figure 2.19: MLFMM algorithm

The interpolation matrices, $W_{l,L}$ in steps 6 and 7 and $W_{n+1,n}$ in steps 15 and 16, are used to save memory by storing the *transfer* functions and the aggregated field vectors at a lower sampling rate, meeting the Nyquist rate, and upsampling them to the higher rate as the process progresses into the lower levels on the octal tree. This bandwidth increase is due to the bandwidth of the product being the sum of the individual bandwidths. In the disaggregation phase, these interpolation matrices W are transposed to act as downsampling. The interpolation matrices are formed using Lagrange Polynomials, where the weights are calculated using Equation 2.110, with x representing the position of the points to upsample and x' representing the position of the upsampled points.

$$W_{mn} = \prod_{\substack{k=1 \\ k\neq n}}^{N} \frac{x'_m - x_k}{x_n - x_k} \tag{2.110}$$

Algorithm 1 MLFMM Algorithm

```
{Aggregation Phase}
for all non-empty cubes c in level L do
    Initialize all elements in vector $t^{\theta}_{c,L}$ to zero
    Initialize all elements in vector $t^{\phi}_{c,L}$ to zero
    for all thin-wire elements e in cube c do
        $t^{\theta}_{c,L} = t^{\theta}_{c,L} + W_{l,L}\left(T^{\theta}_{e,c} I_e\right)$
        $t^{\phi}_{c,L} = t^{\phi}_{c,L} + W_{l,L}\left(T^{\phi}_{e,c} I_e\right)$
    end for
end for
for n = L-1 to 3 do
    for all non-empty cubes p in level n do
        Initialize all elements in vector $t^{\theta}_{p,n}$ to zero
        Initialize all elements in vector $t^{\phi}_{p,n}$ to zero
        for all child cubes c in parent cube p do
            $t^{\theta}_{p,n} = t^{\theta}_{p,n} + e^{jk\hat{k}_n\cdot(\vec{r}_c-\vec{r}_p)} \odot \left(W_{n+1,n} t^{\theta}_{c,n+1}\right)$
            $t^{\phi}_{p,n} = t^{\phi}_{p,n} + e^{jk\hat{k}_n\cdot(\vec{r}_c-\vec{r}_p)} \odot \left(W_{n+1,n} t^{\phi}_{c,n+1}\right)$
        end for
    end for
end for
```

```
{Disaggregation Phase}
for all non-empty cubes c in level 3 do
    Initialize all elements in vector $s^{\theta}_{c,3}$ to zero
    Initialize all elements in vector $s^{\phi}_{c,3}$ to zero
    for all non-empty cubes f far from c do
        $s^{\theta}_{c,3} = s^{\theta}_{c,3} + H(k, \hat{k}_3, \vec{r}_{fc}) \odot t^{\theta}_{f,3}$
        $s^{\phi}_{c,3} = s^{\phi}_{c,3} + H(k, \hat{k}_3, \vec{r}_{fc}) \odot t^{\phi}_{f,3}$
    end for
end for
for n = 4 to L do
    for all non-empty cubes c in level n do
        $s^{\theta}_{c,n} = W^T_{n,n-1} \left( e^{-jk\hat{k}_n \cdot (\vec{r}_c - \vec{r}_p)} \odot s^{\theta}_{c,n-1} \right)$
        $s^{\phi}_{c,n} = W^T_{n,n-1} \left( e^{-jk\hat{k}_n \cdot (\vec{r}_c - \vec{r}_p)} \odot s^{\phi}_{c,n-1} \right)$
        for all non-empty cubes f far from c do
            $s^{\theta}_{c,n} = s^{\theta}_{c,n} + H(k, \hat{k}_n, \vec{r}_{fc}) \odot t^{\theta}_{f,n}$
            $s^{\phi}_{c,n} = s^{\phi}_{c,n} + H(k, \hat{k}_n, \vec{r}_{fc}) \odot t^{\phi}_{f,n}$
        end for
    end for
end for
for all non-empty cubes c in level L do
    $s^{\theta}_{c,f} = W^T_{f,L} s^{\theta}_{c,L}$
    $s^{\phi}_{c,f} = W^T_{f,L} s^{\phi}_{c,L}$
    for all thin-wires elements e in cube c do
        $V_e = 0$
        for all unit sphere points p do
            $V_e = V_e + s^{\theta}_{c,f} R^{\theta}_{p,e,c} + s^{\phi}_{c,f} R^{\phi}_{p,e,c}$
        end for
    end for
end for
```

2.3 Global optimization

Global optimization is a technique used to obtain the best or one of the best solutions from a set of possible solutions. It is particularly beneficial when dealing with complex, non-linear problems that have multiple local optima, such as the optimization of inductive position sensors. A variety of global optimization algorithms are available, each with its unique strengths and weaknesses. Examples of popular global optimization algorithms include Simulated Annealing (SA), Particle Swarm Optimization (PSO), and Genetic Algorithm (GA).

SA is a global optimization algorithm that draws inspiration from the physical annealing process employed in metallurgy. This algorithm simulates the gradual cooling of a material to enhance the quality of its structure. Similarly, the SA algorithm gradually reduces the temperature of the search space to find the global optimum [29].

PSO is a global optimization algorithm that imitates the collective behaviour of a swarm of birds or a school of fish. Each particle in PSO represents a candidate solution that moves through the search space and updates its position based on the best solution found so far [30].

GA is a global optimization algorithm based on the principles of natural selection and genetics. This algorithm simulates the process of evolution by generating a population of candidate solutions and iteratively improving them using a set of genetic operations, including selection, crossover, and mutation [31].

These algorithms are widely used in various engineering and scientific fields. This section discusses the aforementioned global optimization algorithms: SA, PSO, and GA, keeping in mind the optimization of inductive position sensors. Ultimately, only one of these algorithms is selected and employed in the optimization tool.

2.3.1 Simulated Annealing algorithm

SA [32] is a simple and general algorithm for finding a global minimum inspired by an analogy to physical systems. It is a Monte Carlo search method named from the heating-cooling methodology of metal annealing.

SA operates by modeling a random walk on the domain of interest, Ω space. The random walk steps represent the states of the system and its elements $\omega \in \Omega$. This algorithm searches the state space

Algorithm 2 Simulated Annealing Algorithm

```
{Initialize state}
$\omega = \omega_0$
{Initialize temperature}
$T = T_0$
for $n_{temp} = 1$ to $N_{temps}$ do
    for $n_{step} = 1$ to $N_{steps}$ do
        Select at random a neighbour $\omega' \in \eta(\omega)$
        $\triangle E = E(\omega') - E(\omega)$
        {Evaluate the change in energy, $\triangle E$}
        if $\triangle E \leq 0$ then
            {Downhill move}
            $\omega = \omega'$
        else
            Generate a random number $R$ uniform on $[0, 1]$
            if $R < e^{-\triangle E/T}$ then
                {Uphill move}
                $\omega = \omega'$
            end if
        end if
    end for
    {Next lowest temperature}
    $T = Temp\left[n_{temp}\right]$
end for
```

for low-energy states. At each moment during the search, there is only one current state ω, unlike PSO and GA described further, which search multiple states simultaneously. Based on this current state, the algorithm randomly selects a neighbor $\omega' \in \eta(\omega)$, where $\eta(\omega)$ are the neighbors of ω. Then, a bias is incorporated in favor of motions that reduce energy. This is achieved by calculating the energy of ω', $E(\omega')$, and comparing it to the energy of the current state ω, $E(\omega)$. Let $\triangle E = E(\omega') - E(\omega)$; when $\triangle E > 0$, the walk is considered as going uphill, and when $\triangle E \leq 0$, the walk is considered as going downhill. To influence the bias, downhill moves are always accepted, while uphill moves are accepted only occasionally. This approach is essential to prevent the system from becoming trapped in local minima. Uphill moves of size $\triangle E$ are allowed with $x^{\triangle E}$ probability, where $x \in [0, 1]$ is a control parameter. It is important to note that when $x = 1$, all moves are approved; however, when $x = 0$, only downhill moves are accepted. For intermediate x values, the likelihood of accepting an uphill move decreases as x lowers. A random walk is used in SA to decrease x from an initial value around one to a final value near zero. As the algorithm progresses, less time is spent traveling uphill.

In more conventional physical notation, the parameter x is specified in terms of the temperature T by

$x = e^{-1/T}$, mimicking a state with variable temperatures where the temperature affects the decision-making probability at each step [29]. Algorithm 2 resumes all the above described.

2.3.2 Particle Swarm Optimization

PSO was initially proposed by Eberhard and Kennedy [33–35] as an alternative to traditional optimization techniques, such as gradient descent and SA. PSO draws inspiration from the social behaviour of bird flocks, fish schools, and insect swarms, and aims to mimic the collective intelligence of these animals.

The PSO algorithm simulates the movement of particles (individuals) in an n-dimensional search space, where each particle (individual) represents a candidate solution to a particular problem. In the initial iteration, the particle positions and velocities are randomly initialized in the search space. Subsequently, in the following iterations, the velocity of each particle is determined by the best position achieved by any neighbouring member of the swarm, the best position achieved by the particle, and the particle's previous position. The best position found by any member of the swarm is referred to as the global best position. The algorithm terminates when the quality of the current solution is satisfactory or when the maximum number of iterations is reached. Otherwise, the velocities and positions of the particles are updated, and the next iteration begins. The updated formulas for the velocity and position of the particle are given below:

$$V_n\left(t+1\right) = w \cdot V_n\left(t\right) + c_1\varphi_1\left(X_n^{best} - X_n\right) + c_2\varphi_2\left(X^{best} - X_n\right) \tag{2.111}$$

$$X_n\left(t+1\right) = X_n\left(t\right) + V_n\left(t+1\right) \tag{2.112}$$

Where c_1 and c_2 are positive constants, and φ_1 and φ_2 are two random variables with a uniform distribution between zero and unity. The Equation 2.111 incorporates the inertia weight w, which represents the impact of the previous velocity vector, $V_n\left(t\right)$, on the new velocity vector, $V_n\left(t+1\right)$. To prevent particles from moving too quickly from one area in the search space to another, the velocity is restricted by an upper bound limit V_{max}. At each iteration, the best solution value, P_n^{best}, and its corresponding position, X_n^{best}, are updated for each particle when a better solution is found. Similarly, the best swarm solution,

P^{best}, and its corresponding position, X^{best}, are updated when a better solution is found for the whole swarm [30].

Social interaction is the key feature driving the PSO algorithm [30]. Particles in the swarm learn from one another, and based on the information acquired, they move closer to the best solution obtained previously by themselves and their neighbours. The communication among particles within a neighbourhood topology can be defined in various ways. For example, the star topology presented in Algorithm 3 allows each particle to communicate with all members in the swarm, forming a fully connected social network. In this case, each particle is drawn towards the best solution found by any member of the whole swarm [30].

The PSO algorithm was originally designed for continuous spaces. However, several problems have a discrete space where the input is always a set of discrete values. To address this issue, Kennedy and Eberhart proposed the first PSO algorithm that could be generalized for discrete-valued spaces [36]. In binary PSO, each particle represents its state as a binary value of 0 or 1. A particle's value can then be changed from one state to another. In binary PSO, a particle's velocity represents the probability that the particle may change its state.

Algorithm 3 Particle Swarm Optimization Algorithm

```
{Initialize the best global performance}
$P^{best} = \infty$
for $n = 1$ to $N_{particles}$ do
    {Initialize particle position and velocity}
    Randomly initialize the particle position $X_n$
    Randomly initialize the particle velocity $V_n$, such that $\|V_n\| \leq V_{max}$
    {Evaluate the performance of this particle}
    $P_n = fitness\_function(X_n)$
    {Initialize the best performance of this particle}
    $P_n^{best} = P_n$
    $X_n^{best} = X_n$
    {Compare the performance of this particle with the best one and update it}
    if $P_n^{best} < P^{best}$ then
        $P^{best} = P_n^{best}$
        $X^{best} = X_n^{best}$
    end if
end for
for $i = 1$ to $N_{interactions}$ do
    for $n = 1$ to $N_{particles}$ do
        {Compute new velocity}
        Generate two random numbers, $\varphi_1$ and $\varphi_2$, uniform on $[0, 1]$
        $V_n(t+1) = w \cdot V_n(t) + c_1\varphi_1 \left(X_n^{best} - X_n\right) + c_2\varphi_2 \left(X^{best} - X_n\right)$
        {If velocity is higher than $V_{max}$, then clip it}
        if $\|V_n(t+1)\| > V_{max}$ then
            $V_n(t+1) = \hat{V}_n(t+1) \cdot V_{max}$
        end if
        {Compute new position}
        $X_n(t+1) = X_n(t) + V_n(t+1)$
        {Evaluate performance}
        $P_n = fitness\_function(X_n)$
        {Update new best of this particle}
        if $P_n < P_n^{best}$ then
            $P_n^{best} = P_n$
        end if
        {Update new best of sworm}
        if $P_n < P^{best}$ then
            $P^{best} = P_n$
        end if
    end for
end for
```

2.3.3 Genetic algorithm

Biological sciences underwent a revolution in the second half of the 19th century when Charles Darwin identified how nature chooses and optimizes living beings [37]. With computers and advanced computational tools, applying GAs in optimization processes became possible. The Evolutionary Algorithms (EAs), to which the GA belongs, are algorithms inspired by natural behaviour and the evolution of living organisms [38]. They try to emulate the Darwinian model of natural evolution on a computer. GA, PSO, SA and other algorithms of this class are all global optimizers. They have been widely used in electromagnetic optimization [39–41]. Basically, GAs evolve a population of candidate designs for a particular purpose, and each individual has a chromosome where vector parameters are encoded in several genes. In addition, GAs work with the entire population of chromosomes for a generation rather than one chromosome at a time, facilitating their parallelization if necessary. Essentially, the GA is composed of genetic operators that generate a series of populations whose members will evolve to satisfy the general purpose.

The first step of the GA is to generate, randomly, the chromosomes of the first generation. Then, it executes the fitness function for each chromosome to compute its corresponding fitness value. Subsequently, it enters the algorithm's main loop, where the new and subsequent generations are generated through the genetic operators of selection, crossover and mutation. This process is iterated until no improvement is observed, a defined goal is reached, or a defined number of generations is achieved. Algorithm 4 schematizes the above mentioned steps.

By *selecting* the best chromosomes, the initial stage in population genetic modification is used to probabilistically advance the best solutions to the next generation and reject less-fitting solutions according to the objective function being optimized [41]. This operator controls the algorithm's convergence, and different strategies can be used to make this selection, but the roulette-wheel, ranking and tournament selection are the most frequent. Tournament selection frequently has the fastest convergence among the three selection methods mentioned.

The tournament selection algorithm is depicted in Algorithm 5. Essentially, the algorithm randomly selects two chromosomes from the population and performs a tournament amongst them; the winner is the one with the highest fitness value, and the price is that their genes will be crossed with another winner. This process repeats until the desired number of chromosomes is achieved to be crossed by the next genetic operator: *crossover*.

Algorithm 4 Genetic Algorithm

```
{Generation 1}
Randomly set the genes of the chromosomes
Calculate the fitness value of all individuals using the fitness function
for generation 2 to the total number of generations do
    {Tournament Selection}
    Perform a Tournament Selection over the previous generation
    {Crossover}
    Cross the genes of the Tournament Selection winners
    {Gaussian Mutation}
    Mutate some genes
    Calculate the fitness value of all individuals of the current generation using the fitness function
    {Elitism}
    Select individuals from previous and present generations to be members of the next generation
end for
```

Algorithm 5 Tournament Selection Algorithm

```
for 1 to the total number of individuals in the population do
    {Opponent 1}
    Select randomly one individual as the first opponent that has not been selected as the first opponent before
    {Opponent 2}
    Select randomly one individual as the second opponent that has not been selected and as the second opponent before
    {Winner}
    From the two opponents, select the one with the best fitness value as the winner
end for
```

The *crossover* operator is the primary search tool for GA since it combines chromosomes with relevant genetic information, creating a new population. The simplest type of crossover is a one-point crossover, in which the new individual inherits genes from both parents. One parent supplies the genes before the cut point, and the other supplies the remaining genes. Two-point and N-point crossover are two alternative processes that have been proposed. In the two-point crossover, the parents' chromosomes to be crossed are separated into three sections, with one parent providing the core set of genes and the other providing the remaining ones. In N-point crossover, the gene from each parent is switched with a certain probability and inherited by the new individual. Like binary-encoding, GAs have a crossover operator to deal with binary-coded chromosomes, Real-Coded Genetic Algorithms (RCGAs) [42–44] have a crossover operator specially designed to deal with real-coded chromosomes. In Algorithm 6 an example of a potential crossover operator implementation is given. In this example, the algorithm randomly selects the genes from parent 1 to be inherited by child 1, while the remaining ones come from parent 2. In turn,

Algorithm 6 Crossover Algorithm

```
for $n$ = 1 to the total number of individuals in the population in increments of 2 do
    {Parent 1}
    Select several genes randomly from individual $n$
    {Parent 2}
    Select the remaining genes randomly from individual $n+1$
    {Child 1}
    The first child receives the selected genes from each parent
    {Child 2}
    The second child receives the non-selected genes from each parent
end for
```

Algorithm 7 Gaussian Mutation Algorithm

```
for $n$ = 1 to the total number of individuals in the population do
    for $g$ = 1 to the total number of genes in the individual do
        Generate a random bit $p$ based on the mutation probability value
        if $p$ is equal to 1 then
            Generate a random value $u_i$ between 0 and 1
            Using Equation 2.113, apply a gaussian mutation to the gene $g$ of the individual $n$
        end if
    end for
end for
```

Child 2 inherits both parents' rejected genes.

The subsequent genetic operator is the *mutation*. It is introduced to prevent early convergence and to ensure variety. The mutation disrupts genes at random, resulting in a new population that serves as the starting point for the following generation. Because mutation affects chromosomes arbitrarily, it is not considered a research tool.

Mutation in RCGAs is similar to binary-encoding GAs, except it is usually a slight random perturbation of the initial value. Algorithm 7 depicts an implementation of a gaussian mutation. In this example, the algorithm disrupts genes at random by changing their real value in accordance with a gaussian curve (Equation 2.113 [45]), resulting in a new individual.

$$x_i' = x_i + \sqrt{2}\sigma(b_i - a_i)\,\mathrm{erf}^{-1}(u_i') \tag{2.113}$$

Algorithm 8 Elitism Algorithm

```
Sort the individuals from the previous generation by their fitness value from best to worst
Sort the individuals from the current generation by their fitness value from best to worst
Select the first individuals from the previous generation's sorted list based on the elitism ratio value
Select the first individuals from the current generation's sorted list based on the elitism ratio value
Create a new generation with the selected individuals
```

$$u_i' = \begin{cases} \text{erf}\left(\frac{a_i - x_i}{\sqrt{2}(b_i - a_i)\sigma}\right) \cdot (1 - 2u_i) & , if\ u_i \leq 0.5 \\ \\ \text{erf}\left(\frac{b_i - x_i}{\sqrt{2}(b_i - a_i)\sigma}\right) \cdot (2u_i - 1) & , if\ u_i > 0.5 \end{cases} \tag{2.114}$$

$$\text{erf}(x) = \frac{2}{\sqrt{\pi}} \int_0^x e^{-t^2} dt \tag{2.115}$$

In conjunction with mutation, the elitism operator is frequently employed to guarantee that the best preview members are included in the following generation. Without this, the most refined member of the previous generation would not be present in the next. Moreover, the new generation could be potentially further away from the optimal solution than the previous one and make it longer to find a possible optimal solution. The employed elitism, Algorithm 8, essentially replaces the worst individuals from the current generation with the best ones from the previous generation in accordance with the elitism ratio.

2.4 Summary

This chapter has provided an overview of the theoretical foundations necessary for understanding the research presented in this thesis. The discussion began with an introduction to signal processing, focusing on Fourier analysis and wavelets, which are crucial tools for analyzing the frequency content of signals. The properties of signals and the Fourier transform were also explored in depth, highlighting the significance of these concepts in signal processing applications.

Next, the chapter delved into CEM, keeping in mind the design of optimal inductive position sensors. The fundamental principles of CEM were outlined, introducing Maxwell's equations as the basis of classical electromagnetism. Among the various numerical methods in CEM, the MoM and the FMM were highlighted for their speed and computational efficiency, which are essential for the optimization process of inductive position sensors.

Finally, global optimization techniques were discussed, focusing on SA, PSO, and GA. These algorithms were examined having in mind the optimization of inductive position sensors, and only one of them would be selected for use in the optimization tool developed in this thesis.

In conclusion, this chapter has provided the necessary theoretical background for the development of an Active Noise Cancellation (ANC) based on wavelets and a customized simulation tool aimed at optimizing inductive position sensors. The concepts and methods introduced in this chapter will be applied and further explored in the subsequent chapters of this thesis.

Chapter 3

Mechanical waves application – ANC

An Active Noise Cancellation (ANC) system is used to reduce unwanted noises, either periodic or random [46]. There are many applications for these systems, ranging from headphones for aviation or general usage [47] to the automotive sector. The latter uses ANC systems to eliminate stationary noises originating from the engine, road, or the external environment [48].

The working principle consists of a transducer, usually a speaker that reproduces a cancellation signal, which is a sound wave (Mechanical wave) with the same amplitude as the signal to be cancelled, but with an inverted phase. The two sound waves (the signal to be cancelled and the cancellation signal) combine to form a new wave, in a process called interference, resulting in destructive interference as the two signals cancel each other out [46].

3.1 State-of-the-art

Over recent years, ANC systems have been extensively researched and several systems were developed for the automotive industry to improve the acoustic comfort of vehicle occupants by reducing engine, road, and wind noise [49–55]. These systems work by analyzing and identifying the frequency components of unwanted ambient noise and generating an opposing *anti-noise* signal to cancel it out.

The most common type of ANC system used in automotive applications is the feedback ANC system, which uses microphones to measure the ambient noise and speakers to generate an opposing *anti-noise* signal to cancel it out. These systems are typically based on adaptive filtering algorithms such as the Least Mean Square (LMS) [56] and the Normalized Least Mean Square (NLMS) [57, 58], which continuously adapt the filter coefficients in real-time to reduce the noise. However, these systems estimate the secondary path, the acoustic path from the microphones to the speakers, only during the calibration phase. If the acoustic properties change for some reason, such as a change in vehicle interior layout or the introduction of new materials that affect the sound transmission, the performance of the ANC system can drop significantly, and in some cases, it can even become unstable and generate additional noise. To overcome this problem, some researchers, such as Padhi et al., propose a technique for evaluating the secondary path during the ANC activity [59].

Recent advancement in ANC systems uses frequency-domain techniques, such as wavelets, to decompose the noise signal into its frequency components, allowing for the developing of more targeted and effective control algorithms. Wavelet-based ANC systems are able to reduce noise in specific frequency ranges more effectively and provide the ability to separate noise sources and treat them individually [52, 60–66]. This is an alternative to the popular frequency-domain filtering method based on the Fast Fourier Transform (FFT) algorithm.

Another trend in recent ANC systems is using artificial neural networks to improve their performance. This results in a more effective noise reduction than traditional ANC systems. Studies have shown that this approach can be more effective than methods such as LMS, NLMS, and others [60, 67–72]. Researchers proposed using hybrid systems that combine different ANC methods to achieve better performance [59, 73]. These hybrid systems usually consist of a sinusoidal noise cancellers subsystem, narrowband ANC subsystem and broadband ANC subsystem. The conventional hybrid ANC system is capable of suppressing mixed noise. However, in non-linear environments, the attenuation performance of the conventional hybrid ANC system can be significantly weakened due to its lack of non-linear components. An improved hybrid ANC system, the hybrid Functional Link Artificial Neural Network (FLANN) system, has been proposed to overcome this limitation [70, 72]. This system adds the FLANN structure to the conventional hybrid ANC system.

The use of smart materials, such as piezoelectric materials, is another area of research in ANC systems. These materials can actively change their properties in response to external stimuli, creating active noise cancellation systems that can adapt to changing noise levels in real-time, providing a more effective and efficient noise reduction [53].

Another aspect of ANC systems is the number of microphones and loudspeakers. A Single-Input Single-Output (SISO) ANC system works well in attenuating noise at a specific point in space, such as headphones, but is less effective in large areas like the passenger compartment of a vehicle. In such cases,

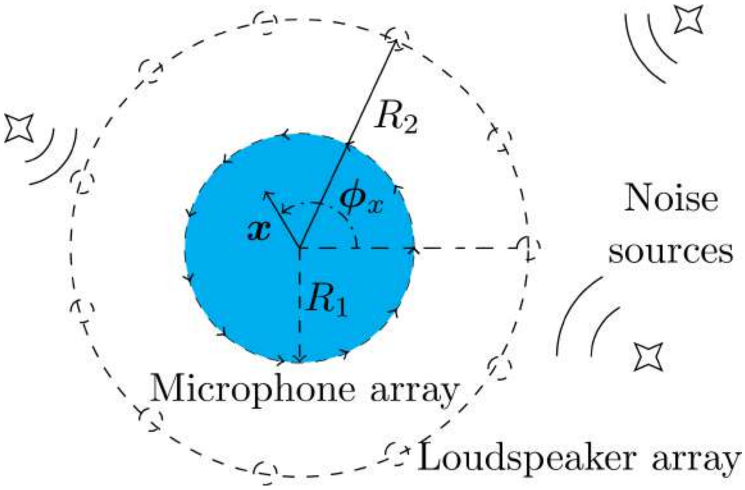

(a) An ANC region defined by its spatial boundaries, represented by a black area, comprises a circular array of microphones with a radius R1 and a circular array of loudspeakers with a radius R2

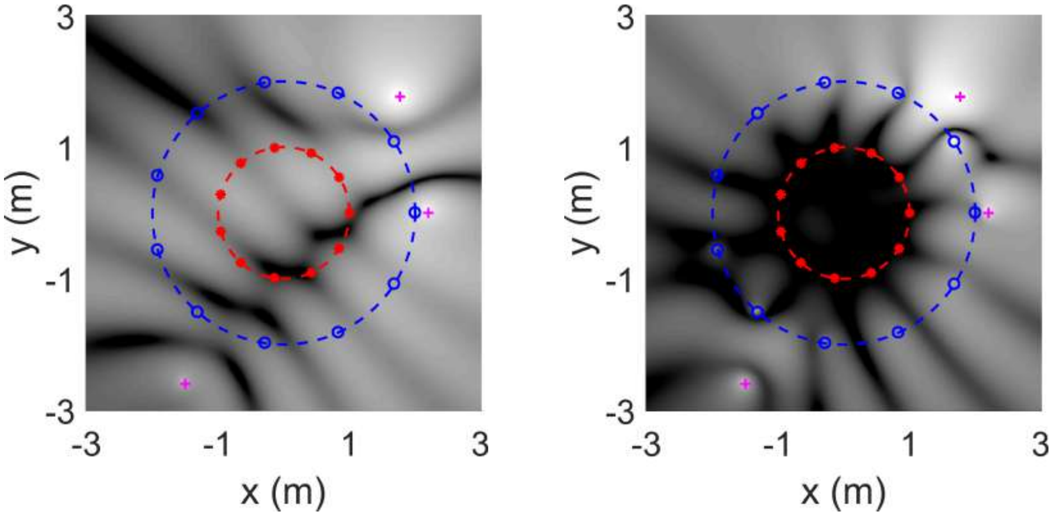

(b) Primary noise field in free-field (200 Hz)

(c) Noise field after ANC activation (free-field)

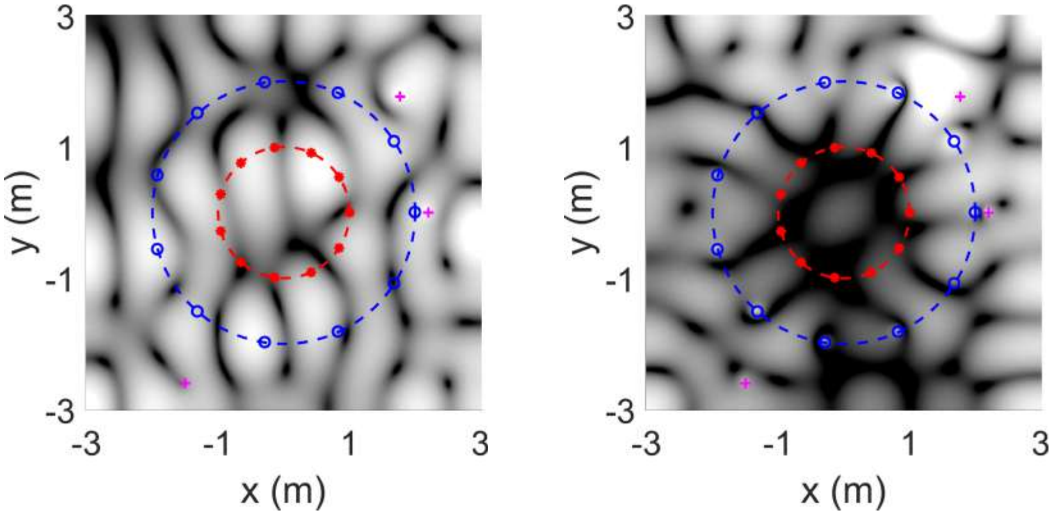

(d) Primary noise field in the reverberant environment (200 Hz)

(e) Noise field after ANC activation (reverberant environment)

Figure 3.1: Noise cancellation performance of a Multiple-Input Multiple-Output (MIMO) ANC system, studied by Zhang et al.

a MIMO ANC system is needed. This system uses a constellation of microphones and loudspeakers to capture and cancel out unwanted noise. In a study by Zhang et al., an ANC system composed of eight microphones and eight loudspeakers arranged in a circular configuration was proposed [74]. The researchers evaluated the system's performance in both a free-field and reverberant environment, with and without the ANC system activated. The results (Figure 3.1 [74]) showed that the proposed MIMO ANC system effectively reduced noise in both environments, with a noticeable noise reduction when the ANC system was activated.

Recent studies have proposed using global optimization algorithms to design and identify the optimal configuration of an ANC system. For example, Long et al. used a Genetic Algorithm (GA) to find an optimal solution for a sub-band ANC system for broadband noise cancellation [75], and Porghoveh et al. developed an ANC system for reducing engine noise within smart cubic vehicle enclosures using a global optimization framework based on Particle Swarm Optimization (PSO) [49].

Overall, ANC technology is constantly evolving to meet new challenges and demands in the automotive industry to provide a more comfortable and pleasant ride for the passengers while also reducing the need for bulky and heavy acoustic insulation materials, which contributes to a more lightweight and fuel-efficient vehicle consequently reducing the environmental impact.

3.2 Classical feedback ANC system

In a typical ANC system, an adaptive filter called FxLMS [56] is used. The core of this algorithm is the LMS method [76–79]. Equation 3.1 is used to calculate the coefficients ($\hat{\boldsymbol{w}}$) for the LMS Finite Impulse Response (FIR) filter, which approximates the response of the primary path (from the noise source to the error microphone, see Figure 3.2) to minimize the error signal (*e[n]*). Where $\hat{\boldsymbol{w}}$*[n]* is the current LMS FIR filter coefficient vector, μ is the step size, ***xs****[n]* is the delayed signal reference, *e[n]* is the error signal, *T* denotes matrix transpose, and $\hat{\boldsymbol{w}}$*[n+1]* is the LMS FIR filter coefficients vector for the new iteration. The error signal results from the sum of the noise signal (*d[n]*) with the anti-phase signal (*y'[n]*) (see Equation 3.2). The FIR filter output signal, *y[n]*, is the outcome of transforming the reference signal (***x****[n]*) accordingly to the LMS's calculated coefficients, as described by Equation 3.3. Then, the anti-phase signal is obtained by multiplying the filter output signal (*y[n]*) by -1. The error signal will converge to zero as the FIR filter response converges to that of the primary path (acoustic environment).

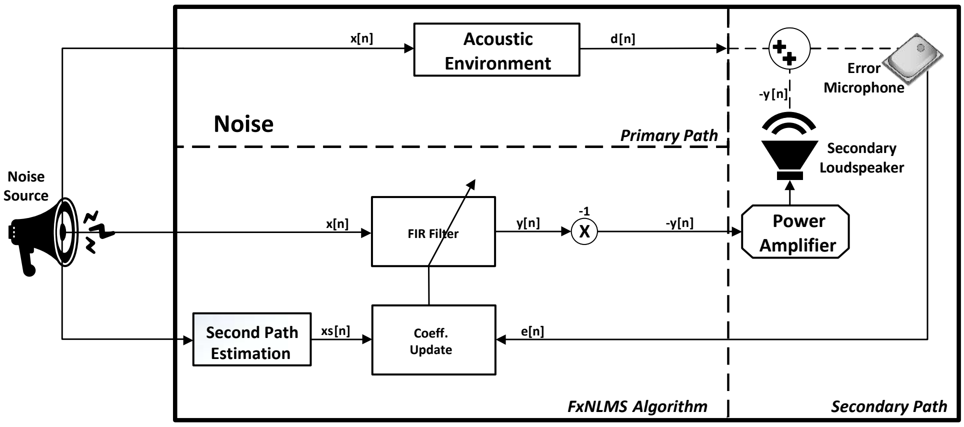

Figure 3.2: Filtered-x Least Mean Square (FxLMS) block diagram

The LMS algorithm has the limitation of requiring virtually no delay between the emitted anti-phase signal and the input of the coefficients update algorithm. This path is commonly referred to in the literature as a secondary path. For that reason, Widrow et al. [56] proposed the FxLMS to account for the secondary path's delays. By considering the effect of the secondary path on the system, the algorithm can correctly calculate the coefficients that minimize the error. For this reason, the same delay must be created in the reference signal that feeds the coefficients update algorithm.

$$\hat{\boldsymbol{w}}[n+1] = \hat{\boldsymbol{w}}[n] + \mu \boldsymbol{xs}[n] e^T[n] \tag{3.1}$$

$$e[n] = d[n] - y'[n] \tag{3.2}$$

$$y[n] = \hat{\boldsymbol{w}}^T \boldsymbol{x}[n] \tag{3.3}$$

The adaptive filter LMS is susceptible to the input power changes of the reference signal. For example, a sudden volume change may turn the algorithm unstable [80]. To solve this problem, one common solution is the normalization of the reference signal before using it to calculate the coefficients. Using this method, called NLMS, the estimation of the learning rate is much more effective, which allows the error to converge to zero. Equation 3.4 is the formula for updating the NLMS coefficients.

$$\hat{\boldsymbol{w}}[n+1] = \hat{\boldsymbol{w}}[n] + \frac{\mu}{\|\boldsymbol{xs}[n]\|^2}\boldsymbol{xs}[n]e^T[n] \tag{3.4}$$

3.3 Proposed hardware accelerated ANC system

The present section describes the system overview of the wavelet-based ANC system proposed in this thesis, and the arrangement of the various constituent elements (secondary loudspeakers, noise and error microphones). The positioning of the elements was crucial for the overall performance of the proposed ANC system.

3.3.1 System overview

The block diagram depicted in Figure 3.3 represents a MIMO approach, with two error microphones, two secondary loudspeakers, and one reference microphone. The Microelectromechanical System (MEMS) based microphones used have a Pulse Density Modulation (PDM) output signal. This justifies the need for the PDM to Pulse Code Modulation (PCM) converter right after the microphones. The noise source is entirely independent of the system.

The error (***e****[n]*) and reference (*x[n]*) signals are processed and divided into several sub-band channels using Undecimated Wavelet Packet Transform (UWPT). Each channel is an input for a dedicated Filtered-x Normalized Least Mean Square (FxNLMS) algorithm. Four FIR filters apply the secondary path estimation to the reference signal, one for each secondary loudspeaker and error microphone combination. In addition, there are two other FIR filters to apply the third path estimation (the path from the secondary loudspeakers to the reference microphone) to the anti-phase signal (***y****[n]*). The goal is to eliminate the presence of the anti-phase signal on the reference signal (as the reference microphone shares the same space as the secondary loudspeakers) and obtain a signal that contains almost only information from the noise source. Finally, the outputs of all FxNLMS algorithms are added and then shifted to obtain the anti-phase signal.

To further elaborate, each output channel of the UWPT is directly connected to the input of a distinct FxNLMS module, which processes the sub-bands of the input signal derived from the UWPT outputs in parallel. The number of FxNLMS modules running in parallel influences the system's efficiency. The higher the number of modules running, the better the cancellation of the noise will be. However, since each

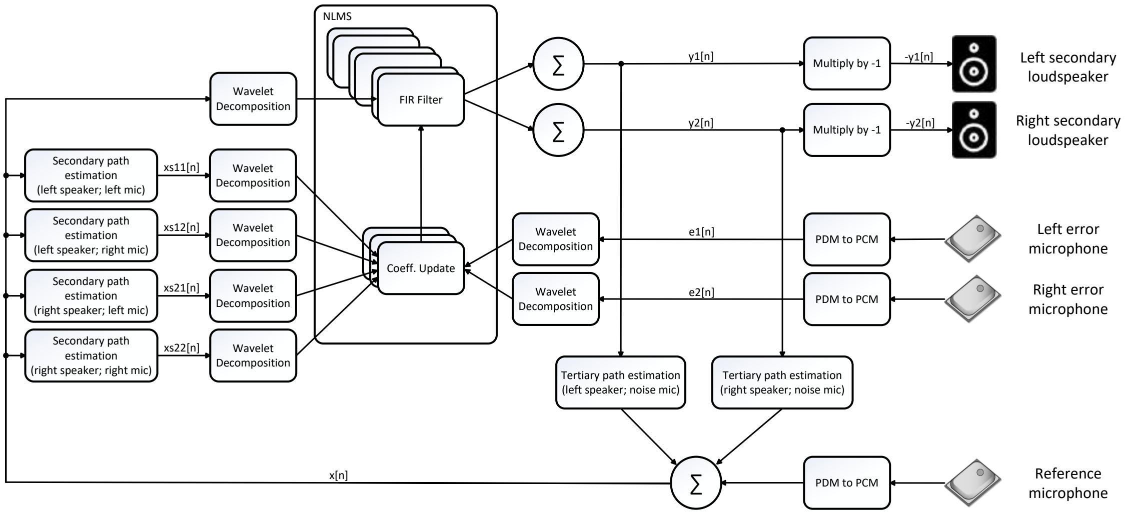

Figure 3.3: ANC block diagram with wavelets

reference signal channel has its unique power, it is necessary to normalize each channel independently. In this way, all error signals from all channels converge to zero at almost the same rate.

It was decided to implement the UWPT rather than the Dyadic Wavelet Transform (DWT) or Wavelet Packet Transform (WPT). These techniques have drawbacks that limit their usage. As an example, the DWT has two limitations: *i)* the output rates on each output channel are different and; *ii)* there is an output channel that contains half of the spectrum of the input signal (i.e., higher frequencies). For that reason, the FxLMS algorithm will operate with a high bandwidth input, and consequently, this would result in lower performance. In the case of the WPT, the drawback is the low output sampling rate. The FxLMS algorithm requires an adequate sampling rate of the input signal (which is related to the update of the coefficients). This sampling rate is particularly important to actuate on the higher spectral components of the input signal. A lower sampling rate means that the FxLMS will not be able to cope with such fast-transitioning signals. For those reasons, the UWPT was the selected wavelet implementation. It has all outputs with the same sample rate and with the same rate as the input signal. Also, the input signal's bandwidth is equally divided by all outputs. In this way, the FxNLMS algorithm is constantly fed with an adequate sampling rate, thus improving its overall performance.

3.3.2 Arrangement for random noise cancellation

One way to interpret the FxNLMS algorithm is to bear in mind that its objective is to constantly search for the coefficients (of the FIR filter) that estimate the response of the primary path. Nevertheless, it

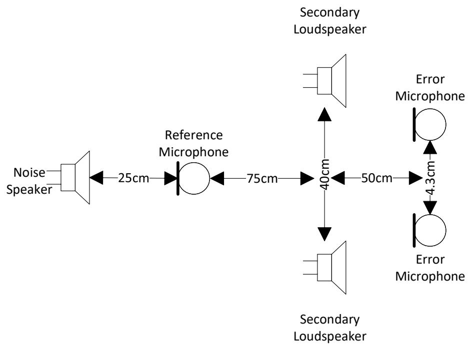

Figure 3.4: Example of ANC components arrangement

is not always possible to find a physically realistic solution. For example, the delay of the primary path could be smaller than the delay of the secondary path. Such a particular solution would not represent a typical geometry of an ANC system. To improve the stability of the system, the constituent components were arranged, as illustrated in Figure 3.4. The delay of the primary path (the distance of the reference microphone to the error microphone) is larger than the secondary path (distance from the secondary loudspeaker to the error microphone).

3.3.3 Field Programmable Gate Array (FPGA) implementation

The implementation of the ANC system comprises several distinct modules, with the primary focus on five key components: the PDM to PCM converter, the FIR filters, the UWPT, the FxNLMS, and the Inter-IC Sound (I^2S) output module. The PDM to PCM converter module transforms the output signal from the MEMS microphones, in PDM format, into a PCM format that the implemented ANC system can process. The FIR filter modules serve multiple purposes (see block diagram of Figure 3.3), such as applying second path estimations to the reference signal (*Second path estimation* blocks in the block diagram) ($x\left[n\right]$), third path estimations (*Third path estimation* blocks in the block diagram) to the anti-phase signals ($y_1\left[n\right]$ and $y_2\left[n\right]$), and, within the FxNLMS module, primary path estimations to each sub-band of the $x\left[n\right]$ signal. The UWPT module (identified as *Wavelet Decomposition* in the block diagram) decomposes error signals ($e_1\left[n\right]$ and $e_2\left[n\right]$), and reference signals ($x\left[n\right]$, $xs_{11}\left[n\right]$, $xs_{12}\left[n\right]$, $xs_{21}\left[n\right]$, and $xs_{22}\left[n\right]$) into several sub-bands. The FxNLMS module continuously estimates the primary path, with one module dedicated to each sub-band decomposition. Since the overall system performance primarily depends on the number of parallel FxNLMS algorithms, the modules have been designed to optimize the balance between FPGA logic

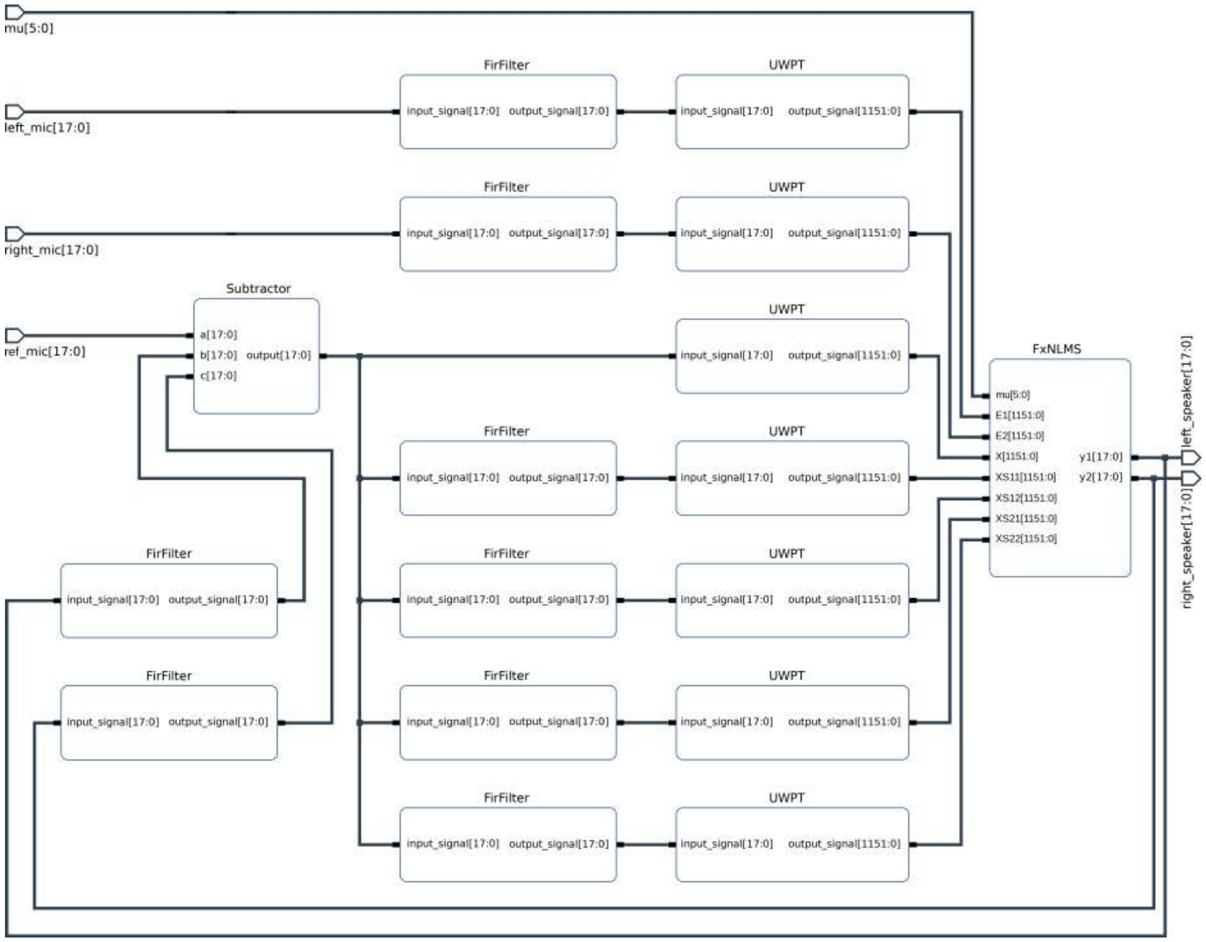

Figure 3.5: FPGA implementation block diagram

resource usage and performance. The I^{2}S output module supplies an I^{2}S amplifier with the anti-phase signals ($-y_1[n]$ and $-y_2[n]$).

Given the requirement for a considerable number of modules running in parallel, an FPGA is a suitable choice, as it enables hardware acceleration and promotes hardware parallelization. It is also crucial to select an FPGA with enough resources to implement the ANC system. Furthermore, these resources must accommodate all the FxNLMS modules necessary for achieving effective random noise reduction, as previously mentioned in Section 3.3.1. To optimize random noise cancellation through a larger number of parallel FxNLMS modules, the *XILINX* FPGA *XC7Z045* was chosen. This FPGA offers one of the highest numbers of Digital Signal Processors (DSPs) available on the market within its family.

Figure 3.5 depicts the FPGA ANC implementation block diagram. In this block diagram, the PDM to PCM conversion and the I^{2}S output modules are not present for simplicity. Here, the diagram inputs, *mu*, *left_mic*, *right_mic*, and *noise_mic* are respectively the step size μ, the left error microphone signal in PCM format, the right error microphone signal in PCM format, and the reference microphone signal in PCM format. The outputs *y1* and *y2* are the left and right anti-phase loudspeaker signals (already multiplied by -1) in PCM format, ready to be sent to the I^{2}S amplifier through the I^{2}S output module.

The remainder of this section will describe in more detail the implementation of the five main modules mentioned above, providing a comprehensive understanding of their individual functions and interactions within the overall system. By outlining these modules and their roles in the ANC system, a clearer picture of the system's design and operation will emerge.

3.3.3.1 PDM to PCM converter module

In this ANC implementation, all three microphones (the two error microphones and the reference microphone) are MEMS microphones with a PDM interface. Since the implemented ANC algorithm requires a PCM signal, a conversion is necessary. To address this need, a conversion module was implemented in the ANC system. The PCM to PDM module implementation was designed to minimize conversion delay and avoid DSP usage. Reducing the conversion delay is crucial, as any extra delay in the signal can adversely affect the ANC performance, specifically the convergence speed.

A common implementation of a PDM to PCM conversion involves using a decimation filter, typically a Cascaded Integrator-Comb (CIC) filter, followed by a FIR filter for additional alias rejection and signal shaping. This approach allows for the efficient conversion of high-bit-rate PDM signals to lower-bit-rate PCM signals while maintaining signal integrity and minimizing the overall computational complexity. However, one drawback of this strategy is the high group delay associated with the conversion process, which can negatively impact the performance of real-time systems, such as active noise cancellation, where low-latency signal processing is essential.

To illustrate the potential impact of group delay, consider the following example: suppose a CIC filter with $N = 3$ stages has a differential delay of $M = 1$ and a decimation factor of $R = 16$. Additionally, assume two half-band decimating FIR filters and one FIR decimating by 2 filter connected in series, with each filter having an order of 100. In this configuration, the PDM microphone signal is downsampled from 3.072 MHz to 48 kHz. The total group delay, D, for the CIC filter can be calculated as $D = N\left(RM - 1\right)/2 = 22.5$ samples. For the FIR filters, the group delay for each filter can be calculated as half of the filter order, which is 50 samples per filter. With two decimating by 2 half band FIR filters and one decimating by 2 FIR filter in series, the total group delay is $50 + 2 \times 50 + 4 \times 50 = 350$ samples. Thus, the overall group delay for the entire conversion process is $22.5 + 350 = 372.5$ samples or $395/3.072 \times 10^6 = 129\mu s$, where the 3.072×10^6 is the PDM sample rate in Hz. This added latency could degrade the performance of the noise cancellation system, as it may not be able to respond quickly enough to rapidly changing noise conditions.

Another possibility is the use of Infinite Impulse Response (IIR) filters, as they are less complex than FIR filters. However, they introduce some phase distortion, which might not be a significant problem for the ANC system, as it could adapt to this distortion. Nonetheless, the IIR filter, like the FIR filter, requires a DSP to perform the multiplications. With a limited number of these resources available in the FPGA, an algorithm that does not require a DSP would be more preferable. As a result, a moving-average filter was chosen for the PDM to PCM converter, as it offers a simpler and more resource-efficient solution for the conversion process. Nevertheless, the moving-average filter is considered one of the least effective filters because of its limited capability to distinguish between different frequency bands. Dispait this, the moving-average filter has a lower group delay compared to more complex FIR filters, which is advantageous in real-time applications like ANC systems where low-latency signal processing is crucial. Equation 3.5 describes the implemented moving-average filter, in which $x\left[n\right]$ represents the input signal, $y\left[n\right]$ indicates the output signal, and M denotes the number of points employed in the moving average.

$$y\left[n\right] = \frac{1}{M} \sum_{m=0}^{M-1} x\left[n-m\right] \tag{3.5}$$

In the implemented PDM to PCM conversion module, a series of four moving-average filters is used, each incorporating $M = 64$ points in the moving average computation. These filters are connected in series, with the first filter receiving the 1-bit PDM signal from the microphone as input, where 0 represents -1 and 1 indicates 1. During each filtering stage, six bits are added to the word size ($log_2\left(M\right)$), resulting in a 25-bit word size signal at the end of the process. As a piece of information, the division operation by M depicted in Formula 3.5 was not implemented, as it can be viewed as a gain factor. By avoiding the division by M, the system is simplified. Lastly, the 25-bit word size is reduced to an 18-bit word size by discarding the 3 least significant bits and the 4 most significant bits.

In the context of the implemented PDM to PCM conversion module, the group delay for each stage is calculated to be $(M-1)/2 = 31.5$ samples. Taking into account all four stages, the total group delay amounts to 126 samples. This corresponds to a time delay of $128 \times 3.072 \times 10^6 = 41\mu s$.

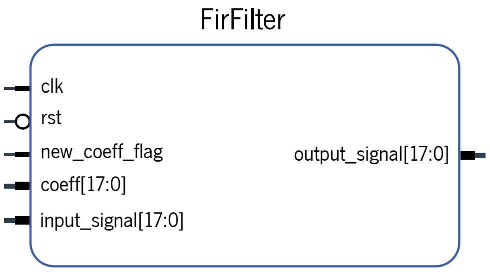

Figure 3.6: FIR filter module interface

3.3.3.2 FIR filter module

The FIR filter implements the mathematical convolution operation, featuring two distinct implementations. The first implementation is employed to apply the impulse responses of the second and third paths, while the second implementation resides within the FxNLMS module for applying the first path estimation. A crucial distinction between these implementations pertains to the filter coefficients: for the second and third path impulse response applications, the static coefficients are established at system boot, whereas the FIR filter within the FxNLMS module has coefficients that change dynamically. Consequently, the FIR filter with static coefficients can be optimized further in comparison to its dynamic counterpart. In the following paragraphs, the discussion focus on the FIR filter implementation that uses static coefficients.

This filter has 2048 coefficients, each of 18-bit. Its values are pre-processed during the environment's impulse response detection and stored in a dedicated Block of Random-Access Memory (BRAM). The input signal is received and acquired via the *input_signal* port (18-bit), with incoming samples also stored in a BRAM. This BRAM is managed as a circular buffer, where each new sample is stored in the next address, and upon reaching full capacity, the first stored sample is overwritten with the newest sample.

Resource optimization was a key consideration for this module, which operates at a system clock of 116.667 MHz. The large system clock allows the convolution operation's multiplications to be executed serially in a pipeline fashion when compared to the input signal's sample rate of 47.97 kHz. As a result, only one DSP is needed to perform all the multiplications.

For each incoming sample, the module has 2432 clock cycles to complete all calculations, with approximately 2048 clock cycles required to perform all 2048 multiplications, one for each coefficient. Considering that the master clock is set to 116.667 MHz (which is 2432 times higher than the audio sample rate of 47.97 kHz) and the coefficient calculations are performed using an FFT that necessitates 2^n coefficients where $n \in \mathbb{N}$, the value of 2048 was chosen. This is the highest value of the form 2^n where $n \in \mathbb{N}$ that is less than 2432.

A higher number of coefficients is necessary for handling non-stationary signals, which allows for increased distance between the error microphones and the anti-phase loudspeakers, as well as the placement of the reference microphone farther away. The additional coefficients sufficiently accommodate signal delays in this context, ultimately enhancing overall performance.

Lastly, the division operation of the convolution is performed by bit-shifting the final result. The result is divided by a power of two value ($2^{11} = 2048$). This choice for the total number of coefficients was also influenced by this concept, as 2048 is the power of two value closest to 2432.

3.3.3.3 UWPT module

The wavelet transform is executed through a cascade of filters in this implementation. This cascade produces n outputs, with each output consisting of m levels of filters (see Figure 2.4). In this implementation, six levels ($m = 6$) of filters were used, which was the maximum allowed by the resources available on the chosen FPGA. If more resources were available, a higher level would have been employed, since a greater decomposition of the error and reference signals leads to improved ANC performance. It should be noted that increasing the level of m by 1 effectively doubles the resources needed for implementation, as the number of FxNLMS modules also doubles.

In this implementation, the nature of the Haar wavelet basis function was exploited. Instead of using a set of filters, the convolution of six levels of the wavelet was implemented within a single FIR filter. This was accomplished by convoluting all filters associated with a specific output.

Consider Figure 2.4, which presents two levels of decomposition ($m = 2$) resulting in $n = 4$ outputs. The first output signal, labeled $d^0L + 2$, is derived by convoluting the input signal with the filter coefficients $\bar{h}$ from the first decomposition level. Then, the resulting signal is convoluted with the filter coefficients $\uparrow 2\bar{g}$ from the second decomposition level. Due to the associative property of convolution operations, they can be performed in any order, making $(d^0L\bar{h}) \uparrow 2\bar{g}$ equivalent to $d_L^0(\bar{h} \uparrow 2\bar{g})$. This method allows filters that produce a specific output to be convoluted in advance and saved in memory.

Furthermore, the Haar wavelet has filter coefficients for the $\bar{h}$ (low-pass) as $[1, 1]$ and for the $\bar{g}$ (high-pass) as $[1, -1]$ at the first decomposition level. For the second decomposition level, as described in 2.1.3 for the UWPT (see Equations 2.22 and 2.23), the filters $\bar{h}$ and $\bar{g}$ are upsampled by 2, inserting a zero between

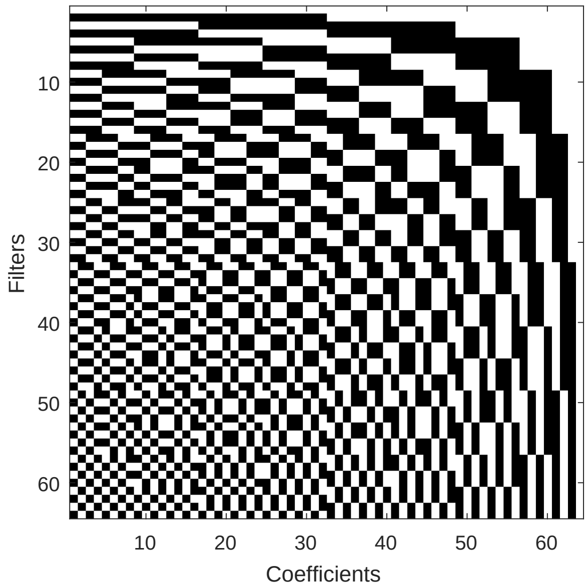

Figure 3.7: Wavelet Haar module coefficients (white square means 1 and black square means -1)

coefficients ($\bar{h}_1 = [1, 0, 1, 0]$ and $\bar{g}_1 = [1, 0, -1, 0]$). By convoluting $\bar{g}$ with $\bar{g}_1$, for example, a filter with coefficients $[1, -1, -1, 1, 0]$ is obtained. Subsequent convolution with $\bar{g}_2$ (at decomposition level 3) results in $[1, -1, -1, 1, -1, 1, 1, -1, 0, 0, 0, 0]$.

In this thesis, the ANC implementation involved convoluting filters from the first to the 6th level of decomposition. In the end, the entire cascade consisted of 64 (2^m where $m = 6$) independent filters (see Figure 3.7), where each filter is composed of 64 coefficients, were precalculated and stored in the BRAMs using initialization files. Each coefficient is represented by one bit, where 0 means -1 and 1 denots 1, Note that, consecutive zeros at the right end of the coefficients were discarded to save memory and facilitate one-bit coefficient representation.

The input signal (18-bit) is filtered in parallel by these filters, and at the output, the module generates 64 translation-scale sub-bands channels operating at the same sample rate as the input signal. Each of these channels represents a spectral sub-band of the input signal. The acquisition and storage of the input signals are made in a similarly way (as explained for the FIR filter).

The convolution operation in this module does not perform any multiplications, since the nature of the Haar wavelet is explored to perform only additions and subtractions, so that there is no need to use the FPGA's DSPs. In this way, if the coefficient is 1, an addition is performed. If the coefficient is -1 (bit with the value zero in memory), a subtraction is done. Similarly, as in the FIR filter module, the division is performed by simply shifting the bits 6 positions to the right.

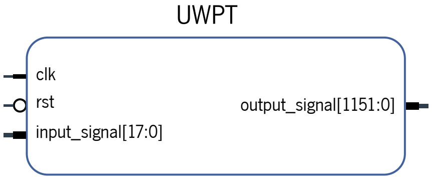

Figure 3.8: UWPT module interface

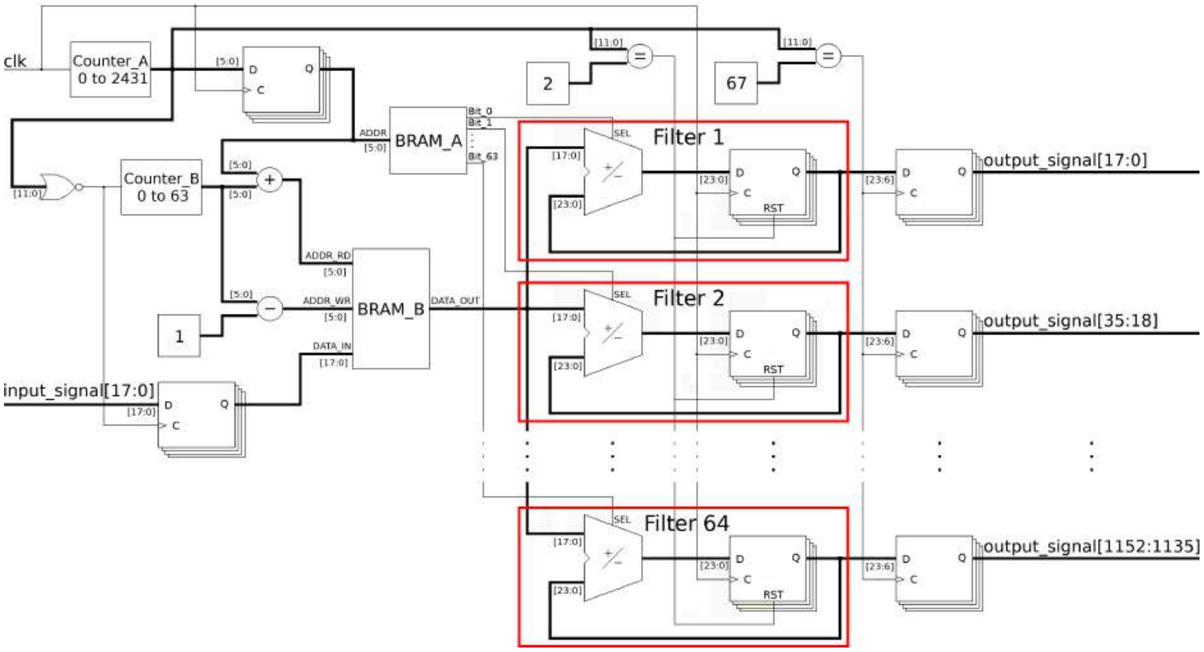

Figure 3.9: Wavelet Haar module implementation diagram

In Figure 3.9 is depicted the Wavelet Haar module implementation diagram. Each filter is composed by an arithmetic unit (containing an adder and a subtractor) and an accumulator. The accumulator is represented by the flip-flop connected to the arithmetic unit output. The reason for having the convolution operation done without any multiplication is mainly to save DSP resources, allowed by the nature of the Haar wavelet, as explained in sub-section 3.3.3.3. Similar to the implementation of the FIR filter described in sub-section 3.3.3.2, the filtering is done at a rate much higher (2432 times higher) than the acquisition frequency. This enables the convolution operation to be performed sequentially, allowing for pipeline-like optimization.

The arithmetic unit has two operand inputs, the input signal and the feed output of the accumulator, and one control line, the *SEL* bit. The first operand input, containing the input signal, is 18-bit wide, and since 64 additions or subtractions are made, six extra bits are needed in the accumulator to store the result. This explains why the second operand input is 24-bit wide. The operation to be performed (addition or subtraction) is selected by the *SEL* bit of the arithmetic unit, which is also connected to the output data port of the *BRAM_A*, where each bit represents the value of a given coefficient for the associated filter. The final result of the filter is *truncated* (the 18 most significant bits).

In the *BRAM_A* the coefficients of the 64 filters are stored, having 1-bit wide word, being its content depicted in Figure 3.7. As already mentioned, the output of the *BRAM_A* is directly connected to the *SEL* bit of the arithmetic unit. The access to the BRAM's content is done at the system clock, being the read address port (*ADDR_RD*) managed by the six least significative bits of the *Counter_A*, required to address the 64 coefficients.

The acquisition of the input signal (18-bit) happens when the *Counter_A* (incrementing at the system clock) overflow to 0 value. When the overflow occurs, the input signal is fetched by a flip-flop in order to be stored on the *BRAM_B*, implemented as a circular buffer of 64 elements. The write address port (*ADDR_WR*) is updated at the input sampling frequency and its value corresponds to $Counter_B - 1$, which is the address where the incoming samples will be stored. Note that this counter is also working at the input signal's frequency, 47.97 kHz. Whenever the end of the *BRAM_B* is reached, the incoming sample overwrites the oldest stored sample. Reading samples from the *BRAM_B* is done through the read address port (*ADDR_RD*). The *Counter_B* value is used as a reference for the first value to be read (write address value plus one). To the reference, an offset is added, which is related to the sequential nature of the filtering process. Since the reading is done at the system clock, all the samples stored in memory are read from the oldest to the newest (in this order) for the filtering process.

On the filters accumulator flip-flop, there is a reset signal. This is needed for the convolution of each new input sample. Moreover, the BRAMs elements work as a pipeline system, but two clock cycles are required to output the memory requested content. For this reason, the reset signal of the accumulator flip-flop is set when *Counter_A* is equal to 2. This delay and the internal delay of 1 clock cycle of the accumulator flip-flop result in a final clock count of 67. It takes 67 system clocks to obtain a processed sample.

3.3.3.4 FxNLMS module

The FxNLMS module interface is depicted in Figure 3.10 and features 11 inputs and 2 outputs. The *anc_on* input enables or disables the output's anti-phase signals, *y1* and *y2*. The *mu* input governs the convergence speed of the FxNLMS algorithm, while inputs *E1* and *E2* correspond to the error microphone signals. The reference signal is represented by *X*, and the inputs *XS11*, *XS12*, *XS21*, and *XS22* are the reference signal filtered by the second path estimation coefficients.

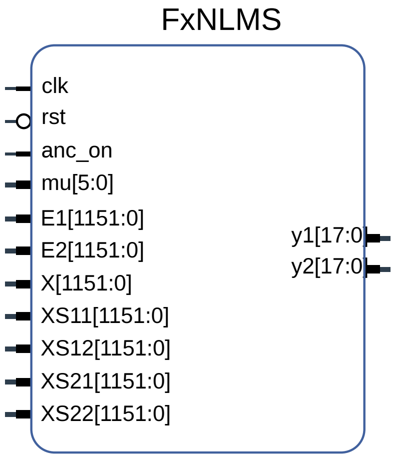

Figure 3.10: FxNLMS module interface

The module has two main components, as illustrated in Figure 3.3: the FIR filters and the coefficient update. In the first stage at the coefficients update block, there is a normalization operation. This normalization was crafted to avoid mathematical divisions, thus saving DSP resources (details can be found later in this section). Each UWPT outputs 64 channels and each channel is processed by a single FxNLMS module. As such, there are 64 FxNLMS per UWPT, and since a MIMO configuration was used, two FIR filters are needed for each FxNLMS algorithm (one for each cancelling speaker). In total are required the instantiation of 128 FIR blocks to filter the reference signal, $x\left[n\right]$, using the on-line primary path estimation coefficients, $\hat{w}\left[n\right]$.

Each FIR filter has 1000 coefficients of 48-bit. The number of coefficients was limited to the available resources of the FPGA. The implementation of FIR filters inside the FxNLMS module is similar to the one described in the FIR filter module section. The coefficients are stored in BRAMs as well as the last 1000 samples of the reference signal $x\left[n\right]$. The storage of the input signal is done as described in the FIR filter module section. As the FPGA's DSPs have *18+25* bit inputs and 48-bit outputs each and the coefficients are 48-bit, three DSPs per filter are required.

As previously mentioned, the total number of coefficients, 1000, was determined by the available resources of the FPGA, which has a total of 545 BRAMs with a capacity of 36 kbit each. These BRAMs can be configured as memory of various sizes, such as 32K of 1-bit word, 16K of 2-bit word, 8K of 4-bit word, 4K of 9-bit (or 8-bit) word, 2K of 18-bit (or 16-bit) word, 1K of 36-bit (or 32-bit) word, or 512 of 72-bit (or 64-bit) word. Additionally, each BRAM can be divided into two completely independent 18 Kb BRAMs. Given these restrictions and the 48-bit word size of the coefficients, one complete BRAM was configured as 1k of 32-bit word, and half a BRAM as 1k of 16-bit word, necessitating the use of 1.5 BRAMs. Moreover,

Table 3.1: Computing a very rough approximation to the inverse of a number by reversing the order of the bits

Number		Inverse	
Decimal	**Binary**	**Binary**	**Decimal**
1	00000001.0000000	00000001.0000000	1.0000000
2	00000010.0000000	00000000.1000000	0.5000000
4	00000100.0000000	00000000.0100000	0.2500000
8	00001000.0000000	00000000.0010000	0.1250000
16	00010000.0000000	00000000.0001000	0.0625000
32	00100000.0000000	00000000.0000100	0.0312500
64	01000000.0000000	00000000.0000010	0.0156250
100	01100100.0000000	00000000.0000010	0.0156250

storing the last 1000 samples of the reference signals, $x\left[n\right]$, $xs_{11}\left[n\right]$, $xs_{12}\left[n\right]$, $xs_{21}\left[n\right]$, and $xs_{22}\left[n\right]$, which have an 18-bit word size, required 2.5 BRAMs, configured as five halves of $1k$ of 18-bit word. Altogether, this amounted to 1.5 BRAMs per FIR filter per FxNLMS module, plus 2.5 BRAMs, resulting in 5.5 BRAMs per FxNLMS module. When accounting for the 64 FxNLMS modules running in parallel, a total of 352 BRAMs out of the available 545 were needed.

The NLMS coefficients update block implements Equation 3.4. The algorithm starts by calculating the noise signal energy, $||\boldsymbol{xs}[n]||^2$, of the last 1000 samples. This is done by adding all the 1000 elements after being multiplied by themselves (see Equation 3.6). For this operation, the same strategy as described in the FIR filter module section was used, the multiplications are performed serially (pipeline) to minimize the DSPs number.

$$||\boldsymbol{xs}[n]||^2 = \sum \boldsymbol{xs}[n]^2 \tag{3.6}$$

After calculating the energy of the ***xs[n]*** signal, it is necessary to invert the result. To avoid the division operation, the order of the bits was reversed around the decimal point, followed by a shift of one bit to the left, as shown in Table 3.1. Then, all bits to the left of the first 1, counting from right to left, are set to be zero. In this way, a very rough approximation of the inverse of a number is obtained.

Once the inverse calculation of the ***xs[n]*** signal energy is done, the next step is to multiply it by the constant μ (see Equation 3.4), which is always a power of two. This multiplication is done by shifting $log_2(\mu)$ bits to the left.

The rest of the calculations are done serially to use as few DSPs as possible.

Table 3.2: FPGA resources utilization

Resource	Utilization	Available	Utilization
LUT	82061	218600	37.54 %
LUTRAM	4855	70400	6.90 %
FF	108629	437200	24.85 %
BRAM	365	545	66.97 %
DSP	900	900	100.00 %
IO	26	250	10.40 %
BUFG	3	32	9.38 %

To conclude, Table 3.2 shows the total resources used by the proposed ANC in a *XILINX* FPGA *XC7Z045*.

3.3.3.5 I^{2}S output module

The output module represents the final stage of the ANC system and is responsible for transmitting the processed PCM signal to an external I^{2}S stereo amplifier.

The I^{2}S interface is a serial communication protocol explicitly designed for transmitting digital audio data between devices. It has gained widespread use in audio systems due to its simplicity, synchronization capabilities, and low jitter characteristics. The I^{2}S protocol necessitates three signals for operation:

- Bit Clock (BCLK): Provides the clock signal for synchronizing data transmission between the output module and the I^{2}S stereo amplifier.
- Word Select (WS): Also known as the Left/Right Clock (LRCLK), this signal indicates whether the current data sample belongs to the left or right audio channel.
- Serial Data (SD): Transmits the actual audio data in a Time-Division Multiplexing (TDM) format.

The output module obtains the processed PCM signal from the previous stage of the ANC system (FxNLMS module) and formats the PCM signal in accordance with the I^{2}S protocol requirements. This process involves organizing the data into left and right audio channels and ensuring the correct bit depth and sample rate.

In this particular ANC system, the external I^{2}S stereo amplifier is designed to accept a bit depth of 20 bits and supports various sample rates, such as 44.1 kHz, 48 kHz, 96 kHz, and 192 kHz. However, for this specific implementation, an 18-bit bit depth is employed, accompanied by a sample rate of 47.97 kHz, which is close to the accepted 48 kHz. The amplifier can accommodate this sample rate due to the synchronization capabilities inherent in the I^{2}S protocol.

3.3.3.6 Second and third path impulse responses

The impulse responses of the second and third paths (see Figure 3.2 and Subsection 3.3.1, respectively) are calculated in the Processing System (PS). First, the PS plays a wave file on the left secondary loudspeaker that contains a pre-recorded swept-frequency sine. At the same time, the signals captured by all three microphones, the reference microphone and the two error microphones, are recorded. Next, the same procedure is repeated for the right secondary loudspeaker, and three more captured microphone signals are stored. Then, the PS calculates all the six impulse responses using the reproduced signal and the six recorded signals. Finally, it sends all six impulse responses to the respective FIR filter modules on the Programmable Logic (PL) side.

The procedure described here, in this sub-section, is the first operation that the ANC system does when it is turned on.

3.4 System evaluation

This section starts with the presentation of the methodology used to assess the ANC system developed during this research, followed by the results and a brief discussion.

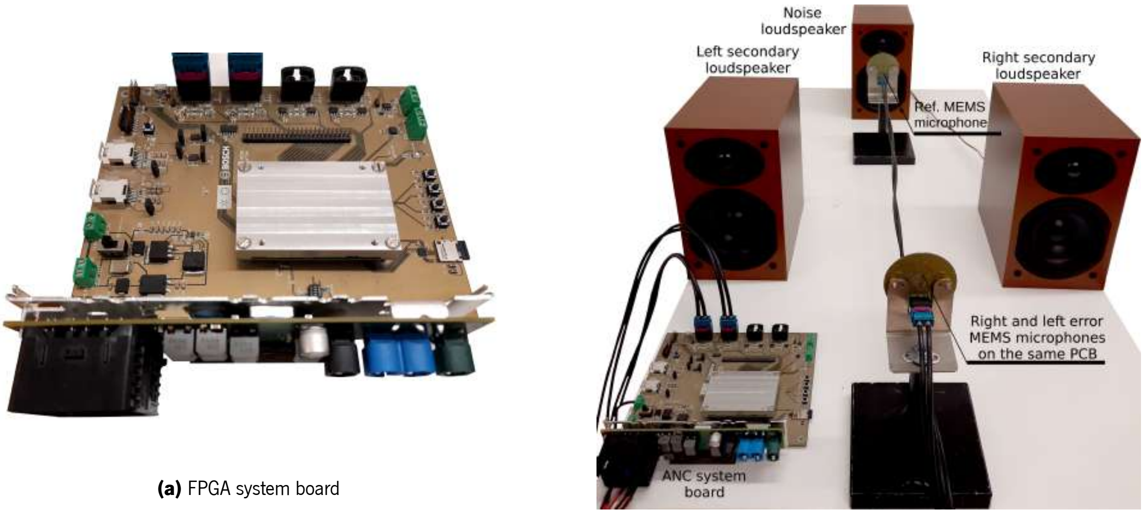

(a) FPGA system board

(b) System hardware

Figure 3.11: Hardware accelerated ANC system

3.4.1 Test methodology

The tests of this ANC system were done in a spacious and uncontrolled acoustic environment, more concretely an academic auditorium (Figure 3.12), where a loudspeaker was used as the noise source. This loudspeaker, including its amplifier and controller, are entirely independent of the ANC system. The ANC system controls two loudspeakers to generate the anti-phase signal and uses the reference microphone and the two error microphones to close feedback path. These elements were disposed as illustrated in Figure 3.4. As the source of ”noise”, four signals were selected to evaluate the system’s performance: *O Fortuna*, a piece of classical music composed by Carl Orff and directed by André Rieu; an urban street environment sound captured in a busy city; an ambient noise of a crowded restaurant; and pink noise. *O Fortuna* was chosen because it has a rich spectrum and a high dynamic range, suitable for showing the performance of this ANC system. Urban street and crowded restaurant ambient noises were selected because they are unpredictable and are more realistic use cases, and pink noise because it is random and has a full spectrum that fades along with the frequency, suitable for evaluating the system’s dynamic range.

Figure 3.12: ANC in the academic auditorium

3.4.2 Results

The results are organized as follows. For each source of ”noise” (*O Fortuna*, urban street, crowded restaurant, and pink noise) there are four associated graphics (Figures 3.13, 3.14, 3.15 and 3.16). The first graphic (top) depicts the noise (time representation) captured by one of the two error microphones: the red curve was captured when the ANC system was *off* and the blue curve when the ANC system was turned *on*. Note that the temporal signals were time-shifted so that they became overlaid. The calculation of the gain was done using these signals values. The second and third graphics (central) are spectrograms of the time domain signals. To draw the spectrograms (exclusively), a WPT up to level 9 with the Daubechies wavelet having two vanishing moments (*db2*) was used. This allowed a good translate-scale resolution, being the scale ordered by its frequency dominance. The fourth and last graphic shows the noise spectrum (FFT) when the ANC system is *off* (blue curve) and when the ANC system is *on* (red curve).

Figure 3.13 shows the results obtained when the ”noise” source is the classical piece, *O Fortuna*. Using the data of the time domain curves, the ANC system was able to reduce an average of 9.45 dB of ”noise”. The central spectrograms depict the spectral noise evolution over time, when the system is *on* and when the system is *off*, respectively. As can be seen, the ANC system was capable of reducing an entire band and working with the same performance in low and high amplitude noise. The bottom graphic shows the FFT of the time domain curves for their entire duration (15s). There was a decrease in intensity for almost all frequencies below 7 kHz. The system does not show any cancellation effect above this frequency.

Figure 3.14 depicts the result obtained when urban environment was used to generate the noise signal. In this case, the attenuation gain was, on average, 9.09 dB. Considering the time-domain signals, the noise's attenuation is noticeable when the ANC system is working. Regarding the spectrograms, an attenuation in the whole spectrum is visible along with the entire signal FFT, as expected. Between the 8th to 10th second, an engine of a car sound was present, and it is visible that the system attenuated this high-intensity sound. Looking at the FFT, the system reduced almost all frequencies up to 7 kHz, as was already observed in the previous result.

Figure 3.15 illustrates the ANC system response to the noise of a quotidian sound of a crowded restaurant. The trend from the previous results remains present. There is a noticeable reduction of the noise (temporal signals), more precisely 9.06 dB on average. The spectrograms show an attenuation for the entire lower part of the spectrum, and the FFT support this.

The last result (Figure 3.16) examines the ANC system's response to pink noise. By analyzing the time domain of the spectrograms, it is evident that the noise was attenuated, though to a lesser degree compared to the previously discussed results. In this instance, the average attenuation reached 6.34 dB. By inspecting both the spectrogram and the FFT graphics in Figure 3.16, it becomes clear that the system was particularly effective in reducing frequencies below 7 kHz. Consistent with the responses observed for the other three noise sources, nearly all frequencies up to 7 kHz experienced a reduction.

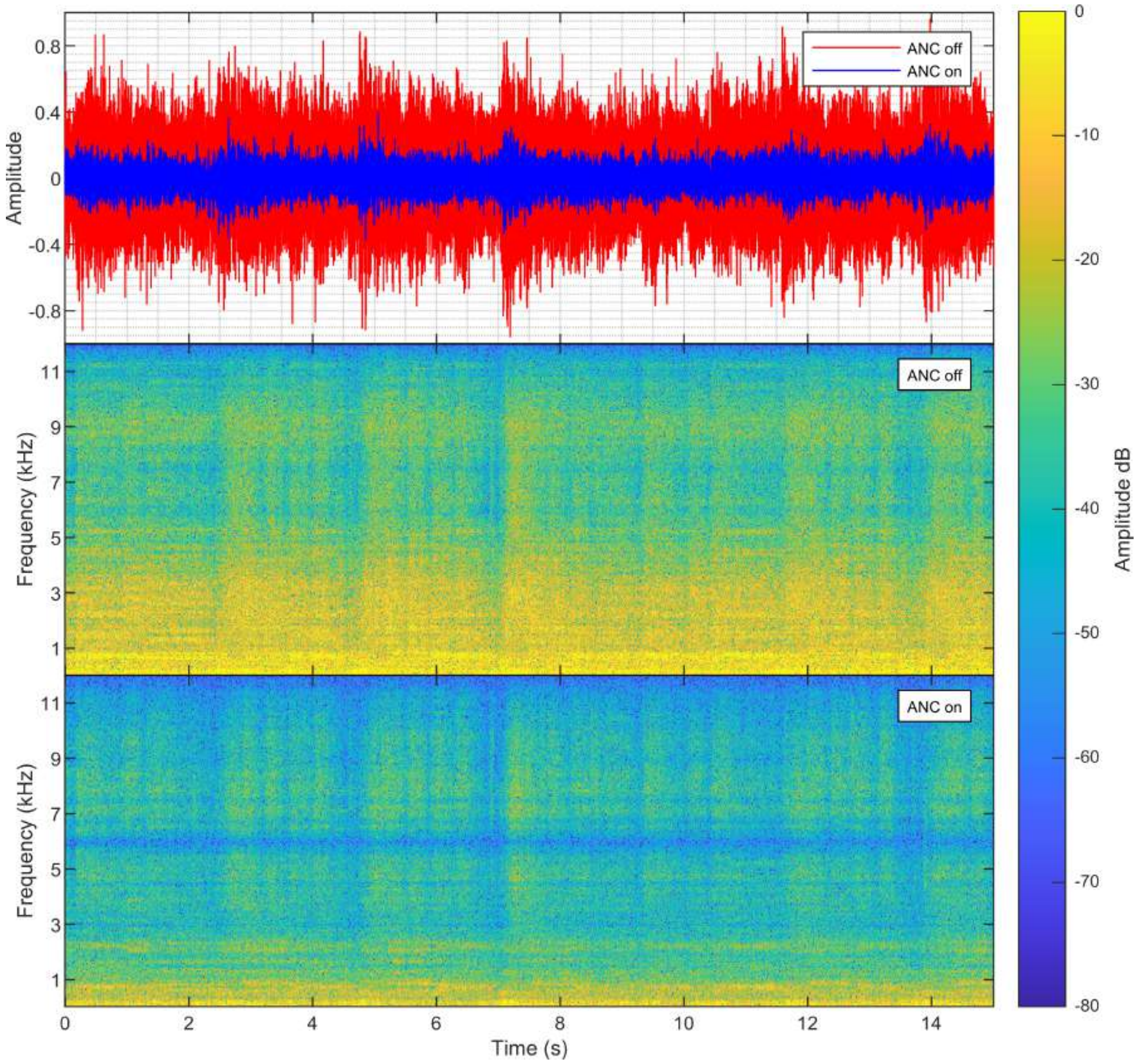

(a) Time domain and spectrogram of the error microphone's signal

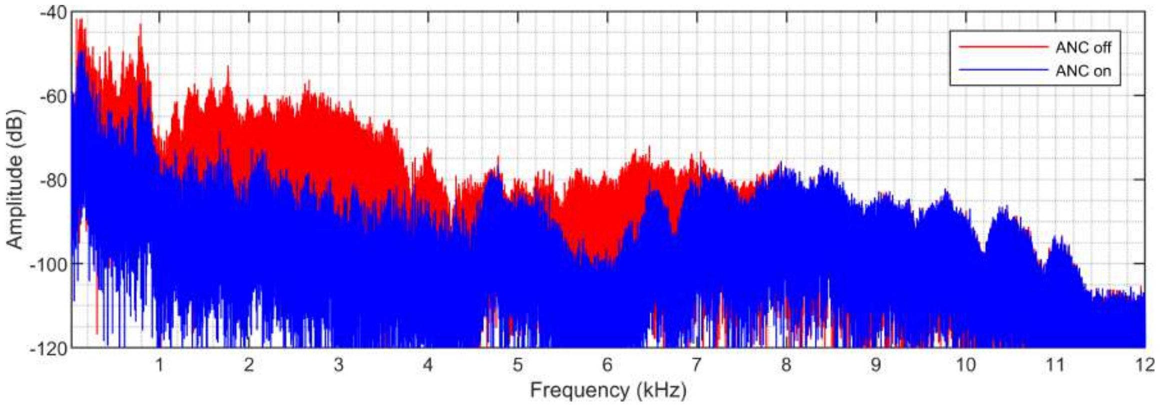

(b) Frequency domain of the error microphone's signal

Figure 3.13: Experimental results of the proposed ANC system - classical music as a "noise" source

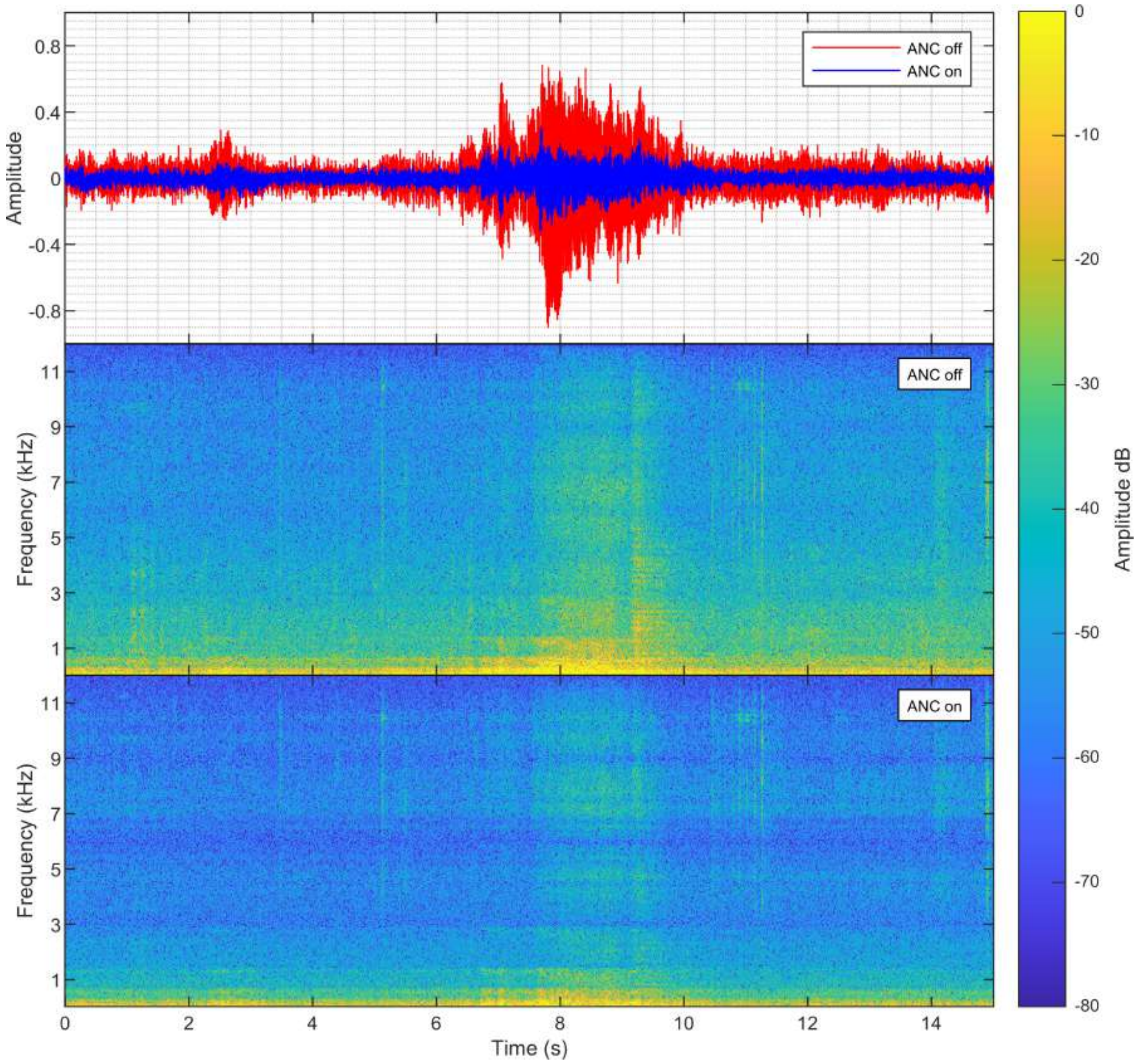

(a) Time domain and spectrogram of the error microphone's signal

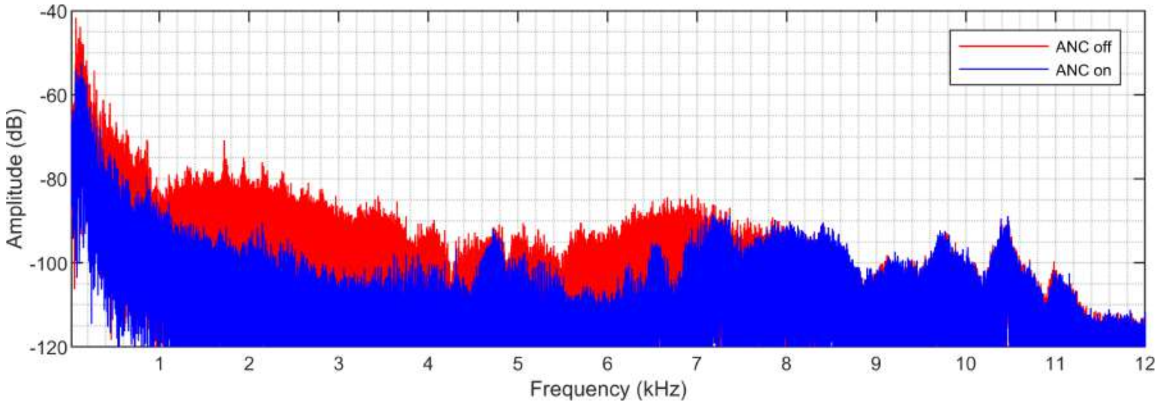

(b) Frequency domain of the error microphone's signal

Figure 3.14: Experimental results of the proposed ANC system - city ambient sound as a noise source

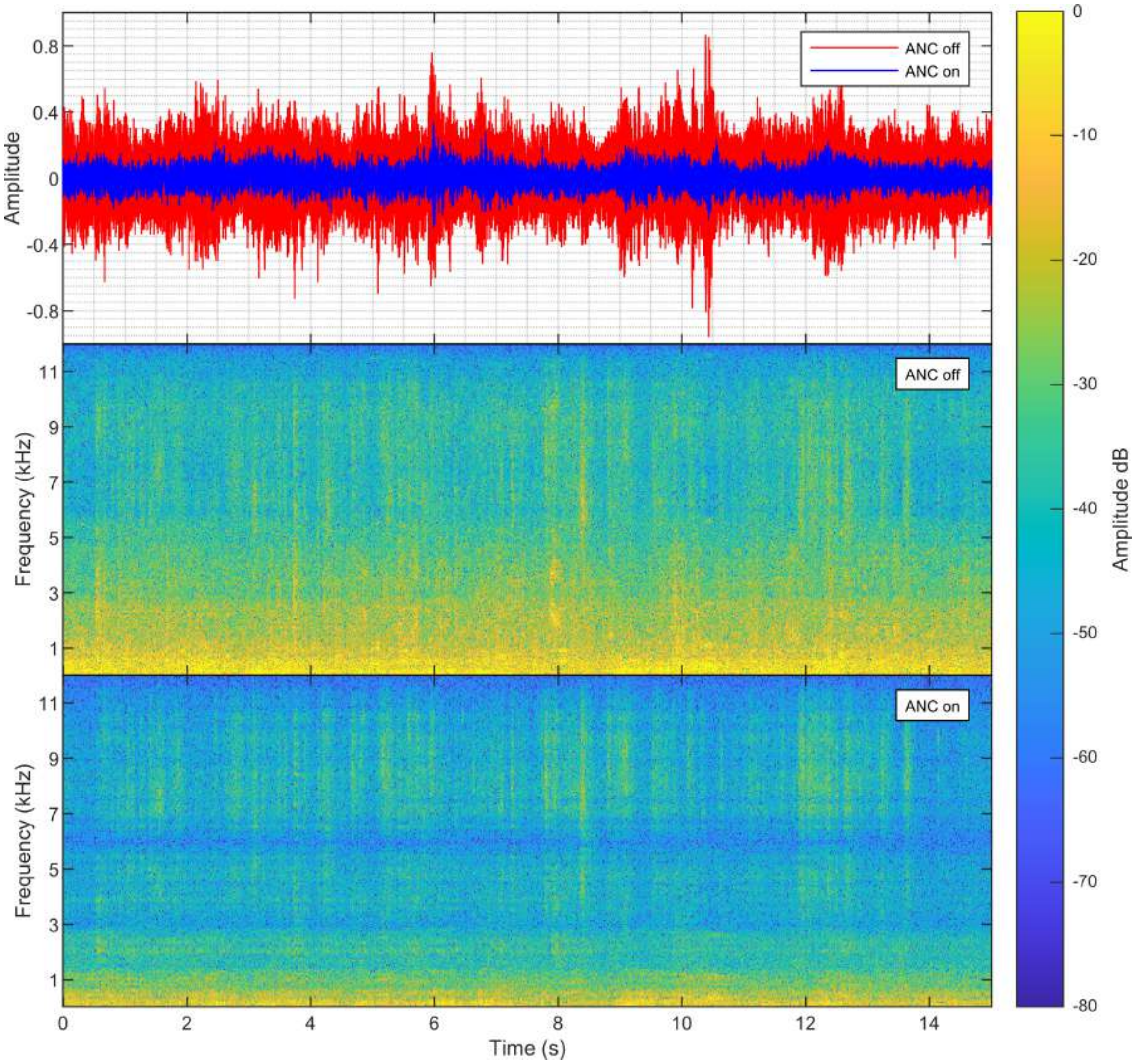

(a) Time domain and spectrogram of the error microphone's signal

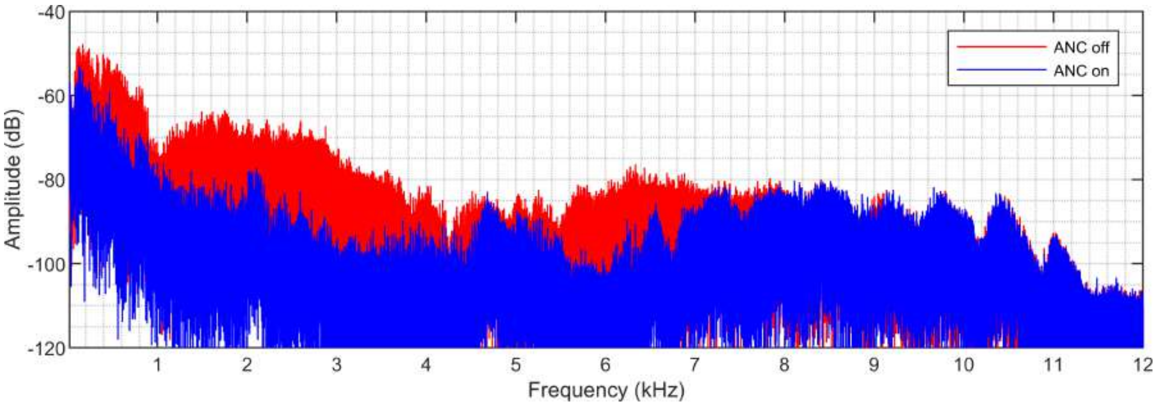

(b) Frequency domain of the error microphone's signal

Figure 3.15: Experimental results of the proposed ANC system - crowded restaurant ambient sound as a noise source

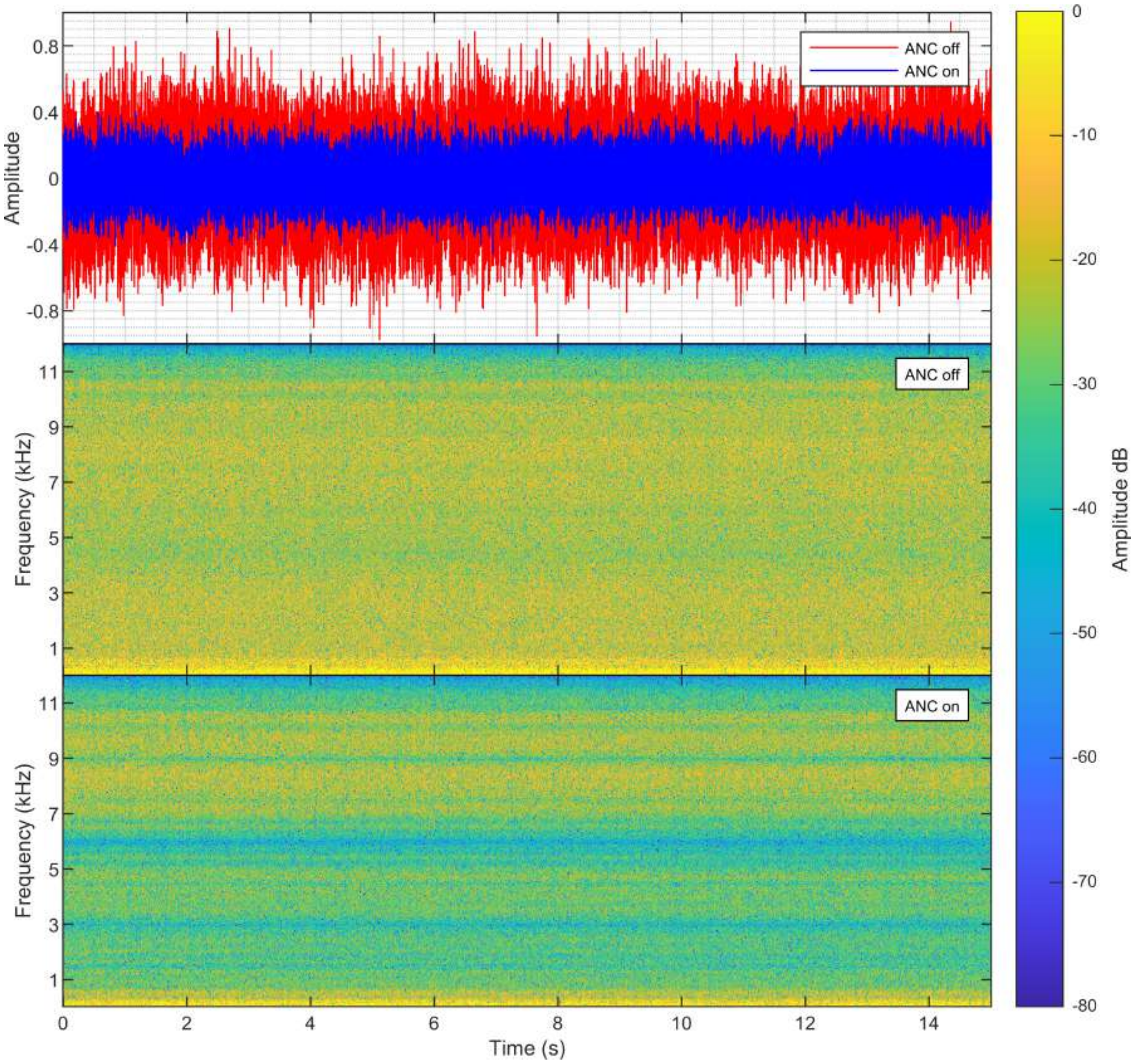

(a) Time domain and spectrogram of the error microphone's signal

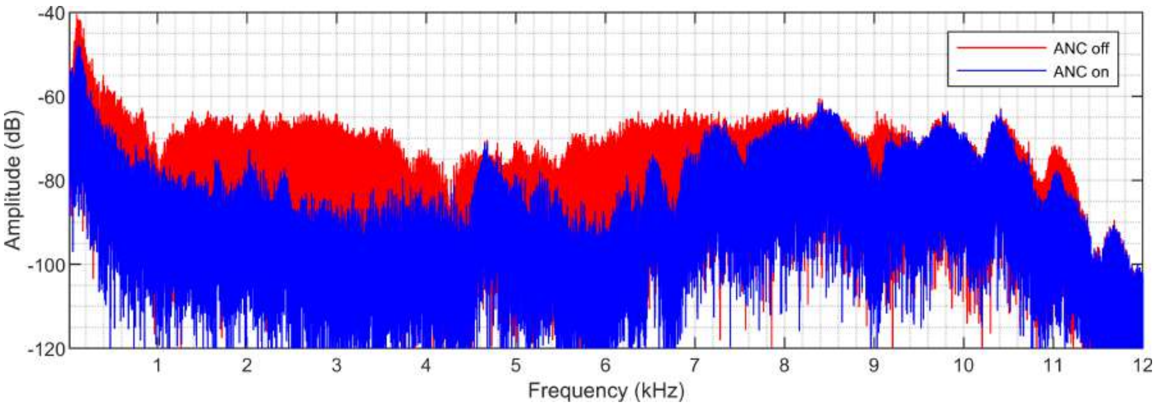

(b) Frequency domain of the error microphone's signal

Figure 3.16: Experimental results of the proposed ANC system - pink noise as a noise source

3.4.3 Discussion

The results described in the previous section proved the viability of the ANC system and are coherent. Table 3.3 summarizes the ANC system's attenuation gain obtained from the results. An observed pattern was the system's superior performance to cancel the spectrum below 7 kHz. The signal's wavelength size and its relation with: i) the distance between the error microphones, and ii) the angle between the position of the secondary loudspeakers and the position of the error microphones helps explain this phenomenon. For example, the wavelength of a 7 kHz noise under the experiment's environmental conditions is approximately 4.9 cm. This value is in the same order of magnitude as the distance between the two error microphones, 4.3 cm. The ANC system can more effectively attenuate wavelengths greater than this distance because the phase difference among the error microphones is not so discrepant (i.e., greater than 120 degrees). In turn, the sound waves from both secondary loudspeakers destructively interfere with the noise at the two error microphones' positions. In the same line of thought, the system could not reduce the frequencies above 7 kHz, as the sound waves from the secondary loudspeakers will have a constructive interference with the noise at one error microphone position. In this case, a physically realistic solution, where both secondary loudspeakers can simultaneously create a destructive behaviour on both error microphones, is not possible. Aside from this discussion and relevantly, the sound intensity above 7 kHz is already too weak for the system to actuate.

Equations 3.7 and 3.8 calculate the maximum actuation frequency of the ANC system for the particular arrangement proposed in this thesis. Where d_{mics} is the distance between the two error microphones, d_{spks} is the distance between the two secondary loudspeakers, d_{spks_mics} is the distance between the secondary loudspeakers and the error microphones, d is the length used to calculate the maximum frequency, v_{sound} is the speed of sound and f_{max} is the maximum frequency. Figure 3.17 illustrates the geometric scenario used to deduce Equation 3.7, bearing in mind that the blue line is the wavefront.

Table 3.3: Results - average attenuation for each noise type

Noise type	Average attenuation
Classical music	9.45 dB
City ambient noise	9.09 dB
Crowded restaurant ambient noise	9.06 dB
Pink noise	6.34 dB

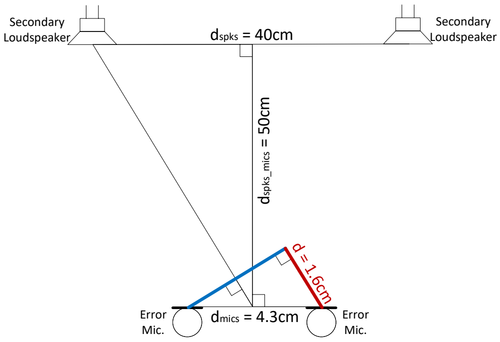

Figure 3.17: Geometry used to obtain the formula of Equation 3.7

$$d = cos\left[\frac{\pi}{2} - atan\left(\frac{d_{spks}}{2d_{spks\_mics}}\right)\right] d_{mics} \tag{3.7}$$

$$f_{max} = \frac{v_{sound}}{3d} \tag{3.8}$$

From equations 3.7 and 3.8, the maximum actuation frequency of the system (for the given geometry) is 7.16 kHz. This frequency supports the information obtained through the FFT graphics in Figures 3.13, 3.14, 3.15 and 3.16.

To conclude, in the first three experiments, the system has an average attenuation gain superior to 9 dB, whereas, for the pink noise, the attenuation was reduced to 6.34 dB. As explained, the system's ability to attenuate the lower part of the spectrum (lower than 7 kHz) was recurrent to all the processed noises. However, since the pink noise has a full spectrum content and high amplitude across all frequencies, it is reasonable to assume that the gain should be lower due to these characteristics since the ANC system was not designed to work effectively on the high frequencies (greater than 7 kHz).

3.5 Conclusion

This chapter has comprehensively discussed ANC systems, presenting an overview of the state-of-the-art research and examining both classical feedback ANC systems and the proposed hardware-accelerated approach. The proposed hardware-accelerated system's design and implementation were explored, providing detailed insights into its several components and FPGA-based implementation.

The automotive industry is a key application area for the proposed ANC system, with the potential to enhance passenger comfort by reducing unwanted noise within the vehicle cabin. The hardware-accelerated approach offers benefits in terms of system efficiency and processing power, which are critical for real-time noise cancellation in automotive environments.

To assess the performance of the proposed system, a test methodology was designed, and the results obtained were presented and analyzed. This evaluation led to a detailed discussion of the system's performance, highlighting its strengths and weaknesses.

In addressing the research questions and objectives, this chapter provided a comprehensive review of the state-of-the-art research on ANC systems (RQ1 and O1) and proposed a hardware-accelerated ANC system using spectral methods (RQ2 and O2). The successful implementation of the ANC prototype using an FPGA (O3) and its performance evaluation (O4) further contributed to the study's goals.

In conclusion, this chapter contributes to the understanding and development of ANC systems, particularly within the context of hardware-accelerated solutions for the automotive industry. The proposed system offers insights and serves as a foundation for ongoing research and innovation in the field of ANC systems. Further investigation and optimization will be essential to address the system's limitations and explore additional applications, both within the automotive industry and beyond.

Chapter 4

Electromagnetic waves application - Inductive position sensor design methodology

The increasing adoption of electric vehicles, the development of autonomous driving systems, and the need for cost reduction are driving the demand for low-cost, high-performance, reliable, and low-power sensors. Position sensors are among these devices, and their current leading technology relies on permanent magnets made from rare raw materials. However, due to the costs involved, there is a gradual shift towards using induction coils designed on Printed Circuit Board (PCB), which do not require an iron core.

Coupled coil technology, applied in position sensing applications (see Figure 4.1 as an example), depends on the variation of inductive coupling between excitation and receiver coils to determine the relative position of an electrically conductive target. The excitation coil generates a time-varying magnetic field, which induces Foucault currents in the conductive target. These Foucault currents, in turn, generate their own magnetic fields that oppose the original one. Both fields sum up together and interact with the receiver coils, placed on the same plane (PCB). By analyzing the induced voltage or current in the receiver coils,

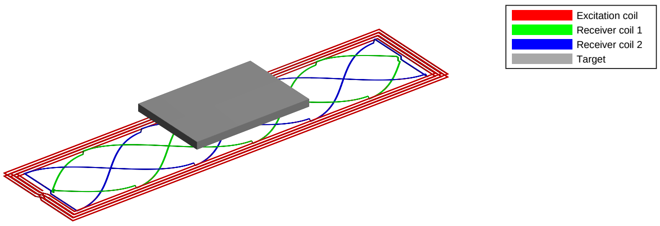

Figure 4.1: Inductive position sensor for linear displacement measurement

the system can infer the target's position, distance, or orientation.

This technology offers advantages such as robustness in harsh environments, resistance to external magnetic fields, contactless operation, low cost, and most importantly, the absence of rare raw elements in its material composition. These benefits make it suitable for various applications, including automotive systems, industrial automation, and medical devices. Despite its advantages, the performance of inductive position sensors is closely related to the shape of the sensor's coil, emphasizing the need for a dedicated optimization tool for the coil's design. To the best of the authors' knowledge, there are currently no such tools available in the market.

4.1 State-of-the-art

A position sensor measures a relative, linear or angular position concerning a reference. In most cases, this type of sensor is a transduction mechanism that converts physical quantities, for example, distance travelled, into electrical quantities. The market is filled with several position sensors designed to address specific requirements. They are widely used in robotics, mechatronics, automation, machine tools, automotive, avionics, aerospace, medical devices, and consumer electronics. The increasing demand for these sensors results in a market requirement for more reliability, higher performance, and lower power sensors. For applications in harsh environments, such as automotive or industrial applications, may limit technology choices. Usually, they require sensor robustness to various influential factors, such as temperature, mechanical vibrations, mechanical tolerances, and external magnetic fields. In addition to the above factors, the cost of manufacturing the position sensors must be kept competitive. Furthermore, the position sensors must meet strict specifications regarding resolution, accuracy, hysteresis, robustness and stability. The following sections describe several physical principles used in developing position sensors. These are classified into magnetic, optical, capacitive and inductive based. The magnetic category is further subdivided into individual technologies.

4.1.1 Magnetic-based position sensors

Magnetic-based position sensors are used primarily in the automotive industry due to their robustness, contactless, and non-destructive sensing. The two main operating principles of magnetic-based position sensors are Hall-effect, where a voltage is produced by magnetic deflection of current-carrying electrons, and magnetoresistance, where a change in resistance occurs in a material exposed to an external magnetic field. Magnetic-based position sensors are commonly found in applications with permanent-magnet machines (especially, Hall-effect sensors) like, Antilock Braking System (ABS), Traction Control System (TCS) or Electronic Stability Program (ESP) [81–84]. Among the most prominent manufacturers of this type of sensors are Bosch, Honeywell International, Inc., STMicroelectronics N.V., Infineon Technologies AG, and TDK Corporation.

A Hall-effect sensor is a transducer that measures a magnetic field based on the Hall-effect principle—discovered in 1879 by American physicist Edwin Herbert Hall [85]. It results from Lorentz's force, which deflects moving charge carriers in the presence of a magnetic field applied perpendicularly to the current flow. When a magnetic field B is applied in the direction parallel to the current flow, Lorentz force deflects the moving charge carrier towards the surface. Consequently, charges of opposite sign accumulate at two surfaces/edges orthogonal to the direction of current flow, resulting in a differential voltage between them. A critical parameter determining the sensitivity of Hall-effect sensors is their building materials' carrier mobility [86]. Hall-effect sensors present several advantages: simple device architecture, easy manufacturing, low cost, the possibility of scaling down, integration with Complementary Metal Oxide Semiconductor (CMOS) circuits, and can provide contactless measurement [87]. Nevertheless, Hall-effect sensors suffer from some drawbacks: i) the output signal is very weak compared to other technologies, namely magnetoresistive sensors, which require electronics to amplify the output signal; ii) the output signal drifts with temperature due to the thermal instability of the devices, which requires complex electronics to compensate the drift; iii) the sensitivity to external magnetic disturbances can cause undesired effects such as erroneous data measurement [87].

Magnetoresistance-based sensors, similar to the previously mentioned Hall-effect-based sensors, can also provide contactless measurements. Magnetoresistance-based sensors are sub-categorized into Tunnel Magnetoresistance (TMR), Anisotropic Magnetoresistance (AMR) and Giant Magnetoresistance (GMR). They all share a similar operational property, dependence of the electrical resistance on the angle between the electric current's direction and the direction of the magnetic field, but these have different structures [87].

Certain materials' resistance is influenced by the angle formed between the magnetization of the material and the applied current's direction [87]. This phenomenon, called AMR, was initially observed by William Thomson (Lord Kelvin) in 1856. At the time, he noted that the resistance is highest when the magnetization is parallel to the current and lowest when it is perpendicular [88].

AMR sensors have the disadvantage of being less sensitive than the other magnetoresistance technologies, such as GMR and TMR sensors. Nonetheless, they are much simpler to make, have more design flexibility regarding device shape and resistance, and perform better at low frequencies in terms of Signal-to-Noise Ratio (SNR) [89, 90]. Because of their robustness, AMR sensors are used in linear positioning systems [91], and an Angular Position Sensor (APS) is described in [92] using a quadruple permalloy layer AMR sensor.

The resistance of a thin-film structure composed of two ferromagnetic layers separated by a non-ferromagnetic spacer layer depends on the relative alignments of the magnetizations of the two ferromagnetic layers. This effect is known as the giant magnetoresistive effect, discovered independently by two scientists who were awarded the 2007 Nobel Prize in Physics for its discovery, Albert Fert and Peter Grunberg [93, 94]. One of the two ferromagnetic layers of a typical GMR sensor is manufactured to have a fixed direction of magnetization. This layer is known as the pinned (or reference) layer. The other one is the free layer, which is made of a soft magnetic substance that, under the effect of the applied magnetic field, has its magnetization direction rotates accordingly [87]. The GMR effect is a product of the spin-dependent scattering of electrons. For example, suppose the magnetization of the pinned layer is parallel to that of the free layer. In that case, the device's resistance is relatively small because electrons with a spin direction opposite to the magnetization are more weakly scattered. On the other hand, if the magnetization directions of the pinned and free layers are antiparallel to each other, the device's resistance increases substantially due to electrons with both up and down spin polarizations being strongly scattered [87]. Since the free layer rotates at an angle under the influence of the applied field, the resistance of the GMR device is proportional to the sine of that angle. The electrical resistance can be determined by running a continuous current through the device and measuring its voltage. Due to their excellent sensitivity, resolution, and low sensor resistance, GMR sensors are highly appealing [95]. This lower resistance also leads to higher operational bandwidth, lower power consumption for a given sensor current, and reduced noise levels [87].

Similar to the GMR sensor, a tunnelling magnetoresistance sensor comprises two ferromagnetic layers. However, instead of being separated by a conductor layer, it is separated by a tunnelling barrier (an extremely thin insulator, typically a few nanometers thick). If the insulating layer is thin enough, electrons can tunnel from one ferromagnet into the other. Since this process is forbidden in classical physics, the TMR is a strictly quantum mechanical phenomenon. Like the GMR sensor, the resistance relies on the magnetic vectors' relative alignment in the free and fixed layers, affecting the flow of conduction electrons between the layers. The parallel configuration results in minimum resistance, and the antiparallel configuration results in maximum resistance. The resistance is measured by passing a current through the layer structure and measuring its voltage. The concept behind the TMR effect was initially demonstrated in 1975 by Julliere. Julliere demonstrated that a junction of two ferromagnetic materials separated by a thin insulating film exhibits the TMR effect [96].

Similar to the GMR sensors, one of the ferromagnetic layers of a typical TMR sensor is free to rotate with the applied field. In contrast, the magnetization of the other layer is pinned. Like GMR sensors, the resistance of the TMR stack is proportional to the cosine of the angle between the free and pinned layers. Consequently, to create a TMR sensor with a linear response to an applied magnetic field, the magnetization of the reference layer must be pinned perpendicular to the free layer. TMR sensors have a higher sensitivity and resistance and consume less power than GMR sensors. However, they suffer from higher noise. TMR sensors are also more expensive and difficult to manufacture since they require a high-quality, pinhole-free, extremely thin tunnelling barrier.

4.1.2 Optical-based position sensor

Optical sensors have better resolution than Magnetoresistance-based sensors [97]. Although many structures may be applied, optical-based position sensor present immunity to external magnetic fields [97]. Conventionally, optic sensors are developed using either a shadowing effect or linear gratings. Conventional optic sensors are often discarded from most applications, despite high-resolution requirements, due to their high manufacturing cost from the production of lithographic patterns for encoders [97]. Diffractive optical sensors allow for a chosen distribution of light, and with Fourier diffractive optics, a similar resolution is obtained, but more resistant against vibrations and assembly tolerances [98]. The optical sensors require a full-proof enclosure. This is due to their sensibility to environmental pollution, and thus they are prone to be discarded in most industrial, and automotive applications [97].

4.1.3 Capacitive-based position sensors

Capacitive sensors are an alternative type of sensor that can be used to measure position. They can provide high-precision measurements in environments where magnetic fields may cause interference. In addition, capacitive position sensors have the advantages of simple design, small size, low cost, low power consumption [99–102], and superior accuracy compared to magnetoresistance-based sensors [103]. However, they are susceptible to environmental pollution and require special care when operating in dusty environments with moisture and grease [99].

As a general operational concept, these sensors use capacitance to detect displacement. They operate based on a principle similar to that of a parallel-plate capacitor. As one plate rotates/moves, the dielectric is modulated by the rotational movement causing a change in the capacity. Typically, capacitive position sensors employ an array of capacitors that transmit signals based on electric field coupling between fixed and moving plates [104–109]. Their basic structure allows contactless readings but is susceptible to condensation, and electrostatic build-up [103, 109]. In addition to their ability to work without a direct power connection, capacitive sensors typically exhibit lower power consumption than alternative sensors.

Although optical encoders are comparatively more accurate, position sensors made with capacitors can gather high-precision and long-range displacement measurements due to the absence of any inherent limitation in capacitor array length. Also, using the electrode planes as the sensing unit significantly reduces the accuracy requirements of the measurement mechanism [104]. Nevertheless, they are vulnerable to environmental conditions, such as moisture and temperature, and present more significant non-linearity due to the electric field bending effect and stray capacitance, affecting accuracy [103, 110–112]. Zhang et al. [113] proposed a new capacitive array absolute positioning system that provides two coarse and two fine orthogonal signals, allowing absolute positioning measurement. This intricate device, however, needs several electrical connections. As a result, many of the benefits of capacitive position sensors are lost in the design, which is also unsuitable for portability and downsizing, reducing its applicability in real-world situations.

4.1.4 Conclusions

This section reviewed several position sensor technologies, which are vital components in numerous industries such as automotive, robotics, mechatronics, automation, machine tools, avionics, aerospace, medical devices, and consumer electronics. The market demands sensors with higher reliability, performance, and lower power consumption while maintaining competitive manufacturing costs. Furthermore, position sensors must meet strict specifications regarding resolution, accuracy, hysteresis, robustness, and stability.

Magnetic-based position sensors, including Hall-effect and magnetoresistance-based sensors, are prevalent in the automotive industry due to their robustness, contactless, and non-destructive sensing. Optical-based position sensors offer high resolution and immunity to external magnetic fields, but their susceptibility to environmental pollution and higher manufacturing costs limit their applications in industrial and automotive sectors. Capacitive-based position sensors provide an alternative solution for environments where magnetic fields may cause interference, featuring simple design, small size, low cost, low power consumption, and superior accuracy compared to magnetoresistance-based sensors. However, they are sensitive to environmental conditions, such as moisture and temperature, and exhibit significant non-linearity due to the electric field bending effect and stray capacitance.

In conclusion, each position sensor technology has its advantages and disadvantages, making them suitable for specific applications and environments.

4.2 State-of-the-art in inductive-based position sensors

Inductive sensors are adaptable to a wide range of applications due to their extensive design options. Nevertheless, inductive sensors designed with planar coils stands out above the rest in terms of its application. This design opens the possibility of impressing the coils directly on PCBs or flexible materials, offering solutions with a lower weight, better mechanical stability, and a compact design when compared to solenoid-based [114–126]. Furthermore, since planar coils can be printed on PCBs, they are highly repeatable, predictable, and economically efficient, facilitating assembly and integration processes. Combining the production method with the high reliability of inductive-based technologies delivers robust solutions offering good thermal behaviour, flexible design, and high replication capability for various applications–including automotive, healthcare, robotics and electronics. In addition, PCB-based planar coils are well-suited for various sensing applications due to their device size (smaller for low-power applications), cost-effectiveness (more affordable), and harsh operational conditions (e.g. dust and oil) constraints. There are already devices on the market that utilize this technology in their transduction mechanisms, such as the IPS2200 magnet-free inductive position sensors from Renesas [127]. However, New designs continue to emerge. The remainder of this subsection is devoted to presenting some of these.

Anandan et al. [128] proposed a shaft angle sensor, Figure 4.2, which uses four identical flexible planar coils as excitation coils. These four coils, arranged in cylindrical quadrants, induce a voltage on a fifth coil

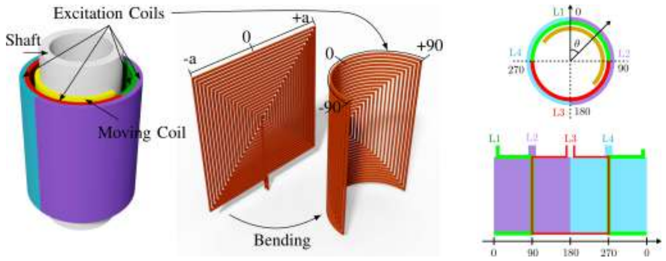

Figure 4.2: The flexible planar coil-based sensor for thru-axis angle detection proposed by Anandan et al.

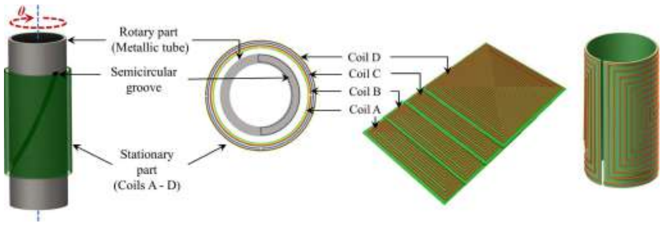

Figure 4.3: The schematization of the non-contact angle sensor based on the Foucault current proposed by Kumar et al.

placed next to them. This fifth coil, coupled to the shaft, is free to move and its induced voltage, related to its azimuthal angle, is measured and processed to determine the angle. In addition, in the processing phase, an algorithm is needed to identify the quadrant of the measured angle. According to the authors, the sensor has a maximum full-scale error of 1% (equivalent to 3.6°) and a resolution of 0.15°. The excitation coils are fed with a 10 kHz sinusoidal signal.

In [129], Kumar et al. proposed a different shaft angle sensor. The sensor consists of a conductive rotating shaft with a groove and a stationary part with four identical flexible coils (see Figure 4.3). The coils are fed with a 60 kHz sinusoidal signal, and there is a 3 mm air gap between the shaft and the coils. As a brief description of its operating principle, the groove modifies the inductance value of the stationary coils according to their position. Thus, these stationary coils, connected to a signal conditioning circuit, determine the circuit's output voltage, which is proportional to the coils' inductance change. The authors claim that the sensor has a resolution of 0.08°and a precision of 0.02%. The maximum non-linearity of the sensor is 0.25% for the entire circle range (0.9°).

Kumar proposes another shaft angle sensor in [130] (Figure 4.4). The working principle is the same as in the previous work. A surface groove introduced on the shaft changes the inductance of the stationary coils according to their angular position. The difference is the stationary part of the sensor that is composed of two layers of six flexible square-planar coils each. The idea is to use a successive approximation algorithm to determine the quadrant in which the surface groove is present. Then a fine measurement is done

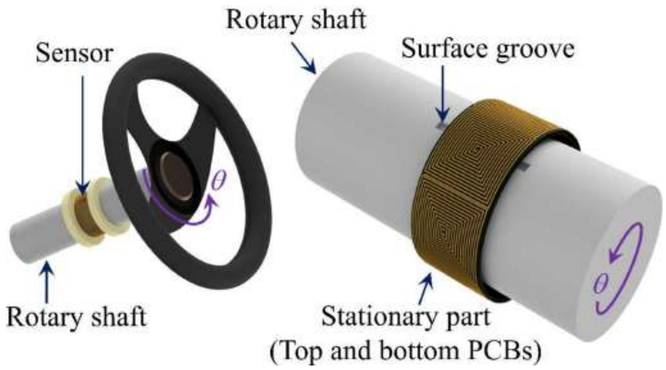

Figure 4.4: The Foucault current-based angle sensor proposed by Kumar et al.

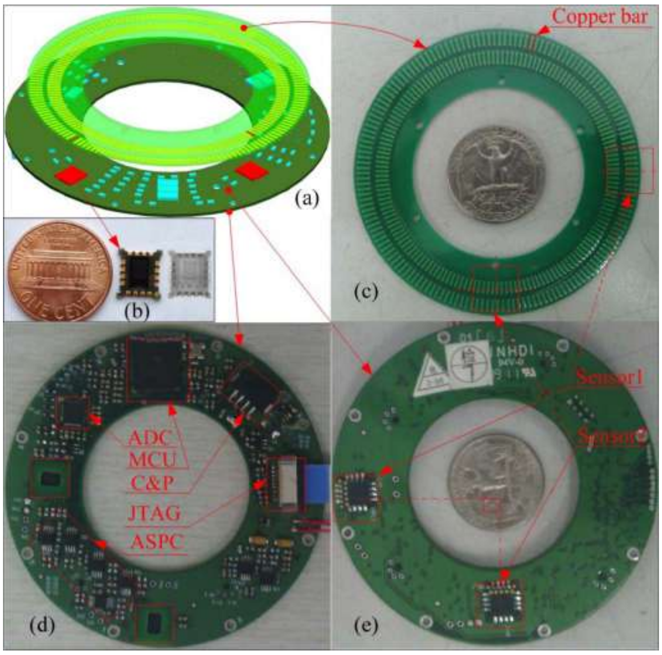

Figure 4.5: The absolute magnetic rotary sensor proposed by Zhang et al.

using the coils from the two layers that belong to that particular quadrant. The coils are fed with a 200 kHz sinusoidal signal, and there is a 0.5 mm air gap between the shaft and the coils. According to the authors, the sensor has a resolution of 0.1°and a non-linearity of 0.9%.

Zhang et al. [131, 132], proposed an angle sensor composed of two inductors and a code disc (Figures 4.5 and 4.6). Both inductors are embedded with a big planar spiral copper coil and four smaller copper coils using Microelectromechanical System (MEMS) technology (Figure 4.6). Two circles of regular copper sheets are listed on the surface of the code disc. The outer has 177 strips and the inner 176 strips. The excitation signal of the sensor is 4 MHz. According to the authors, the sensor's resolution is 0.5°.

In [133], Kumar proposed another angle sensor with an eccentric disc-shaped rotor and a stator in a PCB with four circular coils (see Figure 4.7). The rotor rotates off-centre such that the inductances of

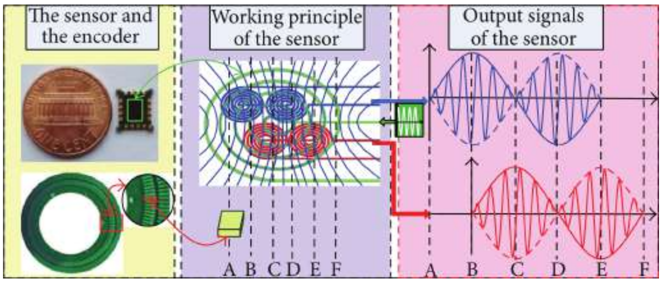

Figure 4.6: The working principle of the absolute magnetic rotary sensor proposed by Zhang et al.

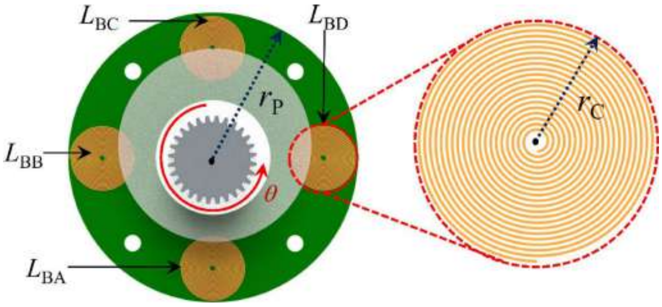

Figure 4.7: Angle sensor with an eccentric disc-shaped rotor proposed by Kumar et al.

the coils change as the angle changes. The air gap between the rotor and the stator is 0.5 mm. In this configuration, the authors claim that the sensor's resolution and worst-case non-linearity are 0.06°and 0.7%, respectively.

The design of a multiperiod bipolar inductive absolute angle sensor is proposed in [134]. The sensor structure comprises a stator and a rotor, where the last is a fan-shaped target with four outer blades and one inner blade, Figure 4.8. The receiving coils are on the stator, and there are two groups: the outer group and the inner group. The outer group comprises two orthogonal sinusoidal-shaped with four cycles that match the fan-shaped target at the outer edge. The inner group comprises two orthogonal sinusoidal-shaped with one cycle corresponding to the centre's fan-shaped target. The coil with more sinusoidal cycles provides high measurement accuracy, and the coil with a small number of sinusoidal cycles identifies the quadrant of measurement.

Additionally, on the stator, there is an excitation coil driven by a 4 MHz sinusoidal signal that induces the Foucault currents on the target sensed by the receiving coils. (As a side note, a more detailed description of its operation is provided in the following subchapter, as this sensor is similar to the ones described in the present work.) Zhang et al. state that the measurement error, the accuracy and the resolution of the sensor are 0.04°, 0.1°, and 0.005°, respectively, in the full range of 360°.

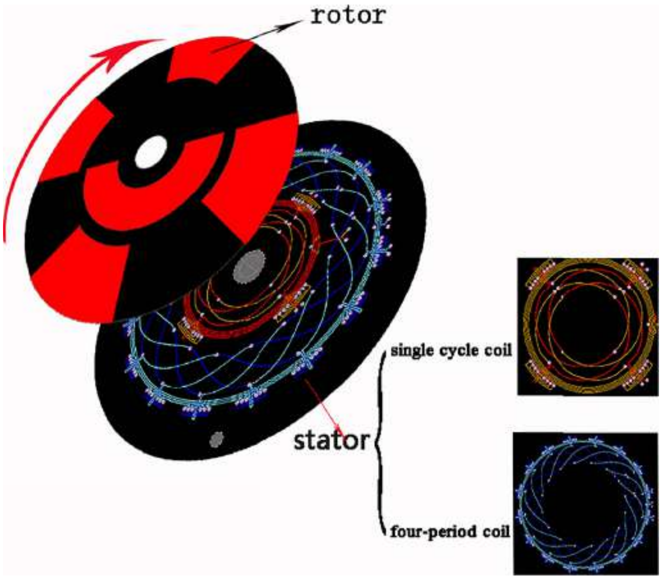

Figure 4.8: Multiperiod bipolar inductive absolute angle sensor proposed by Zhang et al.

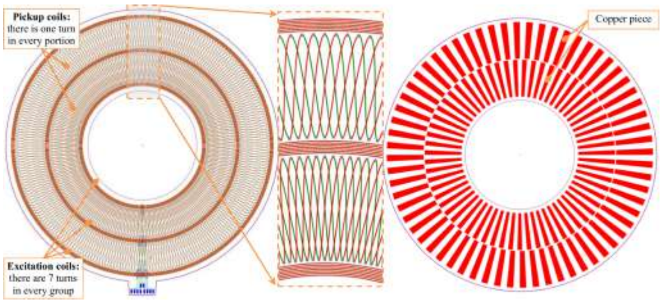

Figure 4.9: Planar inductive-based sensor proposed by Gao et al.

Goa et al. propose another planar inductive-based sensor in [135] similar to the previous work. In this work, the PCB stator consists of three circular excitation coils and two sets of two orthogonal sinusoidal-shaped receiver coils (see Figure 4.9). The rotor, printed on PCB, has two segmented copper circles that match the receiver's coils' position. There are 64 segments on the outer circle and 63 on the inner circle, the exact number of sinusoidal cycles in the respective receiver's coils. In this way, there are two fine sense channels that, together, make an absolute angle sensor. This absolute capability is achieved by representing the two sensing signals (the inner and the outer) with complex numbers where the real and imaginary parts are the values of the respective orthogonal receiver's coils. Multiplying these two complex numbers together results in a signal with one cycle per 360°, the same as if the sensor had just one sinusoidal cycle shape in the entire 360°, but with the precision of the 64/63 cycles. Exciting the excitation's coils at 125 kHz, the authors claim that the sensor has 0.000278°of full-range error.

In [136], Babu et al. proposed a LIPS using a U-shaped moving magnetic core as the target and stationary

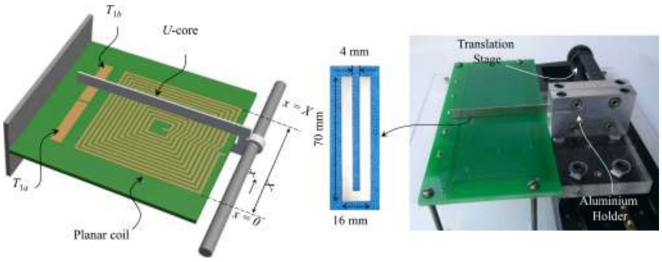

Figure 4.10: Linear Position Sensor (LIPS) using a U-shaped target proposed by Babu et al.

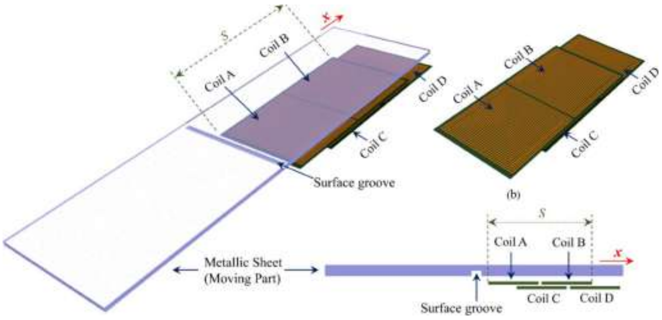

Figure 4.11: LIPS using a conductive sheet with a surface groove as the target proposed by Kumar et al.

spiral planar coils as the stator, Figure 4.10. They use the inductance of the planar coils to determine the position, as it varies depending on where the target is. According to the authors, the sensor with a range of 21.5 mm has a resolution of 6.5 µm and a worst-case error of 0.2%.

Kumar et al. in [137] present a LIPS based on the Foucault current sensing technique. In this work, the moving part of the sensor is a conductive sheet with a surface groove, Figure 4.11. The stationary part has two pairs of planar coils, whose inductances vary as a function of the moving part displacement. The authors claim that the sensor, which has a range of 80 mm, presents a maximum error of 1.65%.

In [138], Wu et al. proposed an absolute LIPS based on an orthogonal dual travelling wave magnetic field. The sensor consists of two PCBs, one fixed containing two groups of coils 90°apart that generate

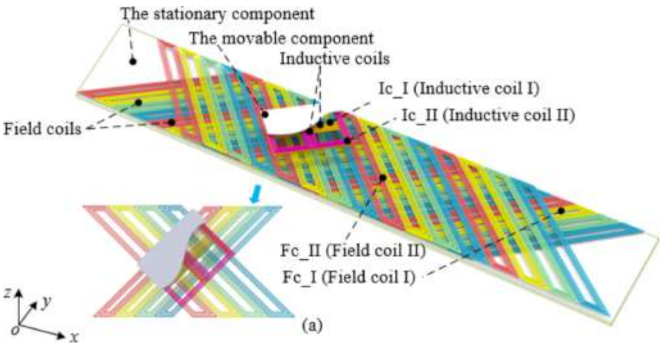

Figure 4.12: Absolute LIPS based on an orthogonal dual travelling wave proposed by Wu et al.

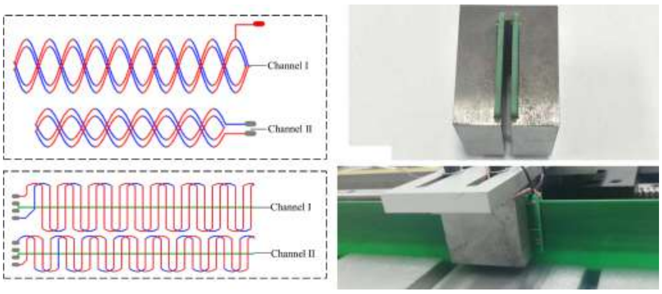

Figure 4.13: Inductive LIPS with two sensing units on each stator side proposed by Gu et al.

the field and the other movable that contains two coils 90°apart where an Electromotive Force (EMF) will be induced (see Figure 4.12). The fixed coils sourced at 10 kHz sinusoidal wave generates two travelling magnetic fields which move in orthogonal directions. Then the mixed magnetic field is then picked up by the movable PCB's coils. Absolute position measurement is realized by reading the induced EMF on the movable coils and comparing its phase differences. According to the authors, the measurement accuracy is 15 µm within the measurement range of 0-80 mm.

Gu et al. propose an inductive LIPS with two sensing units on each stator side in [139]. The sensor consists of a stator with excitation coils on both sides and two movers with pickup coils that work on both sides of the stator, Figure 4.13. The stator and movers' coils are all printed on PCBs. The excitation coils are fed with a 20 kHz sinusoidal wave. According to the authors, having two sensing units—one on either side of the stator—helps to reduce the impact that the gap change between the movers and stator has on the sensor's measurement performance. They argue that the two movers can maintain the sum of two side gaps constant and therefore reach good magnetic coupling with the stator. According to the authors, the sensor's accuracy is 15 µm with a precision of 7 µm and a resolution of 1.2 µm in the full range of the sensor, which is 288 mm.

In [140], Tang et al. propose an inductive LIPS based on PCB-printed planar coils. The sensor mainly consists of a ferromagnetic stator with the pickup coils' PCB on it and a ferromagnetic mover with several excitation coils' PCBs embedded in it (see Figure 4.14). Excitation coil-PCBs, excited by a 4 kHz sinusoidal wave, generate quadrature magnetic fields both in temporal and spatial domains. Pickup coil-PCB receives the magnetic fields and outputs a signal whose phase is proportional to the displacement of the mover. The authors claim that the sensor has a measurement error of 50 µm in the sensor's full range of 208 mm.

Zhao et al. propose an inductive LIPS with complementary resonant coupling units in [141]. The sensor

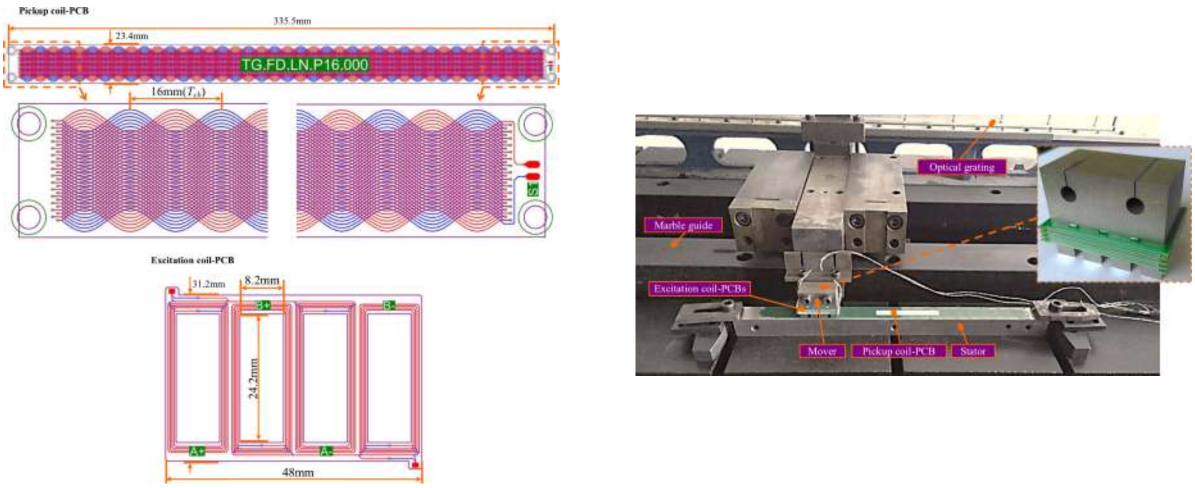

Figure 4.14: Inductive LIPS based on PCB-printed planar coils proposed by Tang et al.

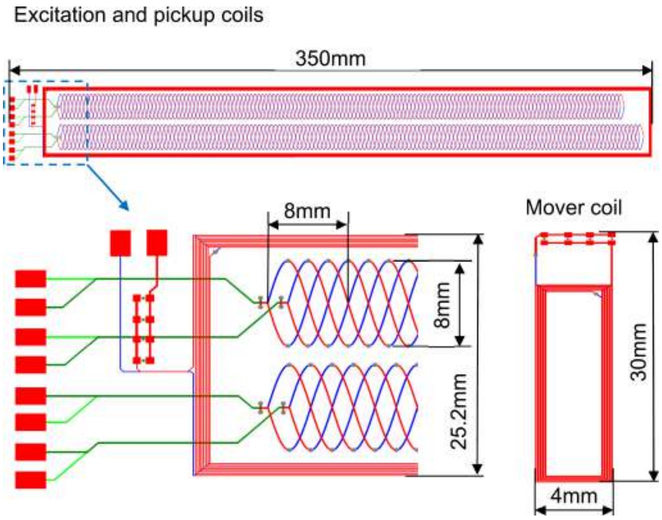

Figure 4.15: Inductive LIPS with complementary resonant coupling units proposed by Zhao et al.

mainly comprises a stator and two identical movers, Figure 4.15. The two movers are symmetrically arranged on both sides of the stator with an air gap of 1 mm. The stator contains excitation and receiving coils, which generate a magnetic field and output induction signals. A 2 MHz sinusoidal signal powers the excitation coil. The movers also contain a receiver's coils in series with resonance capacitors to generate a secondary magnetic field that interacts with the original one, modulating it. The modulated field induces an amplitude-modulated signal on the stator's receiver's coils that reflects the target's position. According to the authors, the measurement error of the sensor is 14 µm within the entire 300 mm range of the sensor.

Dauth et al. in [142] proposed a method to model and simulate the behaviour of inductive angle sensors

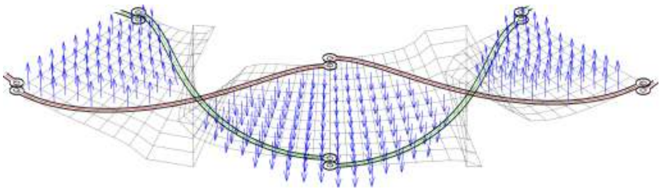

Figure 4.16: Magnetic field data used in the proposed method by Dauth et al. to model and simulate the behaviour of inductive angle sensors

based on coupled coils, where the information about the position angle is amplitude modulated in the receiver's induced voltage. Their method contains several steps, beginning with the parametrization of the sensor geometry: the receiver's coils' central radius; the receiver's coils' amplitude; the number of turns per layer of the excitation coil; the number of layers of the excitation coil; the air gap between the coils and the target; and the periodicity of the sensor. Where each parameter must be changed in increments for the regression model computations; for instance, the total number of simulations required will be the total number of increments per parameter at the power of the total number of parameters, which leads to a considerable number of simulations. In order to reduce the number of simulations, the authors chose to find a D-optimal design, which drastically reduces the number of simulations required. Furthermore, as the Finite Element Method (FEM) is used, they excluded the receiver's coils from the simulation model, reducing the number of simulations even more. Instead, the induced voltages on the receiver's coils are obtained by a numerical implementation of Faraday's law applied to the magnetic field data from the FEM simulations (Figure 4.16). Also, the entire electrical period is calculated by shifting the simulated magnetic field in the angular direction. Once the data are acquired, linear regression models are fitted by the least-squares method.

According to the authors, the deviation between the values predicted by the proposed method and the simulated ones is in the range of ±2% for the excitation coils' inductance, -17% to $+15\%$ for the receiver's coils' amplitude voltage, -23% to $+ 11\%$ for the 4th-order harmonic, and ±260% for the offset.

In [143], Hoxha et al. introduce a methodology to optimize the design of an angular inductive position sensor fabricated in PCB technology. The goal of the optimization is to reduce the sensor's linearity error and amplitude difference between the induced voltages on the two receiving coils. This is done by modifying only the receiver's coils' geometry to reproduce theoretical coil voltages as much as possible. By doing it, the non-linearity is automatically reduced. The design is modified by changing the radial distance of a certain number of points, which, when connected, form the geometry of the receiver's coils. The radial position of those points was obtained using the non-linear least-square solver, together with the

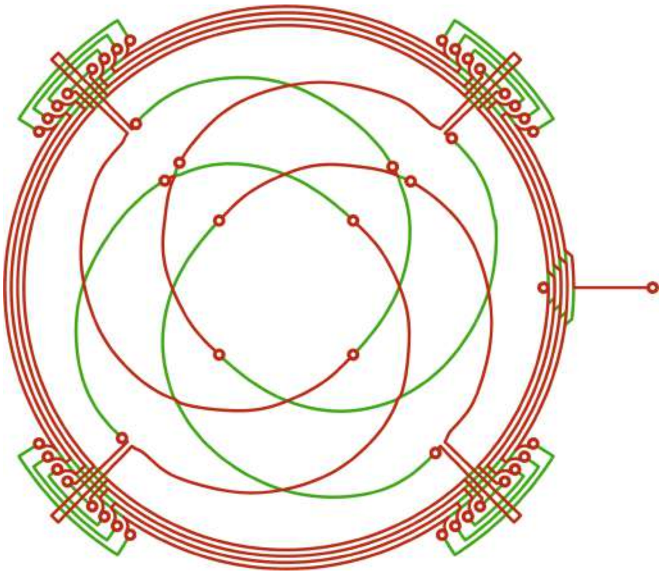

Figure 4.17: Angular inductive position sensor generated using the methodology proposed by Hoxha et al.

surface integral method for the sensor's simulations. The authors used this methodology to optimize an APS with a full range of 360°, Figure 4.17. They state that the optimized sensor exhibit a linearity error below 0.1% of the full scale without signal calibration or post-processing manipulation.

4.2.1 Conclusions

In this section, the state-of-the-art in inductive-based position sensors has been reviewed, with a focus on those employing planar coil designs. These sensors demonstrate high adaptability and versatility, finding applications in a wide range of industries such as automotive, healthcare, robotics, and electronics. The use of planar coils printed on PCBs offers several advantages, including lower weight, better mechanical stability, compactness, repeatability, predictability, and cost-effectiveness. As a result, they are well-suited for various sensing applications, particularly those with small device size, cost, and harsh operational environment constraints.

To conclude the review of the state-of-art, Tables 4.1 and 4.2 present an analysis of the most relevant recent research on inductive position sensors. These tables include the key elements of each previously mentioned sensor, provided by the authors.

Table 4.1: Comparison of different inductive position sensors

Inductive sensor	Displacement type	Range	Excitation frequency	Air gap
Anandan et al. [128]	Angular	360°	10 kHz	-
Kumar et al. [129]	Angular	360°	60 kHz	3 mm
Kumar et al. [130]	Angular	360°	200 kHz	0.5 mm
Zhang et al. [131]	Angular	360°	4 MHz	-
Kumar et al. [133]	Angular	360°	-	0.5 mm
Zhang et al. [134]	Angular	360°	4 MHz	-
Gao et al. [135]	Angular	360°	125 kHz	-
Babu et al. [136]	Angular	360°	473 kHz	-
Hoxha et al. [143]	Angular	360°	2.1 MHz	1 mm
Kumar et al. [137]	Linear	80 mm	60 kHz	1 mm
Wu et al. [138]	Linear	80 mm	10 kHz	-
Gu et al. [139]	Linear	288 mm	20 kHz	-
Tang et al. [140]	Linear	208 mm	4 kHz	-
Zhao et al. [141]	Linear	300 mm	2 MHz	1 mm

Table 4.2: Comparison of different inductive position sensors - results

Inductive sensor	Resolution	Error	Non-linearity	Accuracy	Precision
Anandan et al. [128]	0.15°	3.6°	-	-	-
Kumar et al. [129]	0.08°	-	0.9°	-	0.072°
Kumar et al. [130]	0.1°	-	3.24°	-	-
Zhang et al. [131]	-	-	-	-	0.5°
Kumar et al. [133]	0.06°	-	2.52°	-	-
Zhang et al. [134]	0.005°	0.04°	-	0.1°	-
Gao et al. [135]	-	0.000278°	-	-	-
Babu et al. [136]	6.5 µm	0.72°	-	-	-
Hoxha et al. [143]	-	0.36°	-	-	-
Kumar et al. [137]	-	1.32 mm	-	-	-
Wu et al. [138]	-	-	-	15 µm	-
Gu et al. [139]	1.2 µm	-	-	15 µm	7 µm
Tang et al. [140]	-	50 µm	-	-	-
Zhao et al. [141]	-	14 µm	-	-	-

4.3 Designing inductive-based position sensors

Several works have been carried out in recent years to obtain a better performance in the main characteristics of the position sensors, such as safety, reliability, sensitivity, resolution, stability, thermal compensation, energy consumption and size [110, 131, 144–151]. The position sensors are typically divided into five main groups: optical [152], capacitive [144, 152], magnetic [144, 152], and inductive [144, 152]. A wide variety of position sensors are currently available on the market. Depending on the application, they can indirectly measure other physical quantities converted into motion [153]. The application range of position sensors goes from the automotive industry, robotics, control applications, medical equipment, instrumentation, and military applications to the aerospace industry [131, 144, 145]. This section only covers the inductive sensors based on Foucault currents since linear and angular optimized position sensors were designed in this thesis.

Foucault currents are closed circuits of induced electric current that circulate in a conductive target, usually perpendicular to the magnetic flux (time-varying). In their simplest form, Foucault currents concentrate near the adjacent surface of the excitation coil, and their density decreases with depth. Being Lenz's law, the principle of operation of Foucault's current sensors [154].

There are two main versions of Foucault's current-based sensors for position measurement, frequency-based and amplitude-based (see Figures 4.18a and 4.18b, respectively). The frequency-based version has an oscillator circuit connected to the sensor coils (Figure 4.19), where the frequency of this oscillator is used for the target's position calculation. Figure 4.20 depict the block diagram of the amplitude-based version. This version includes an excitation coil that generates the magnetic field and receiver coils connected to an Amplitude Modulation (AM) demodulator circuit. The target's position dictates the amplitude

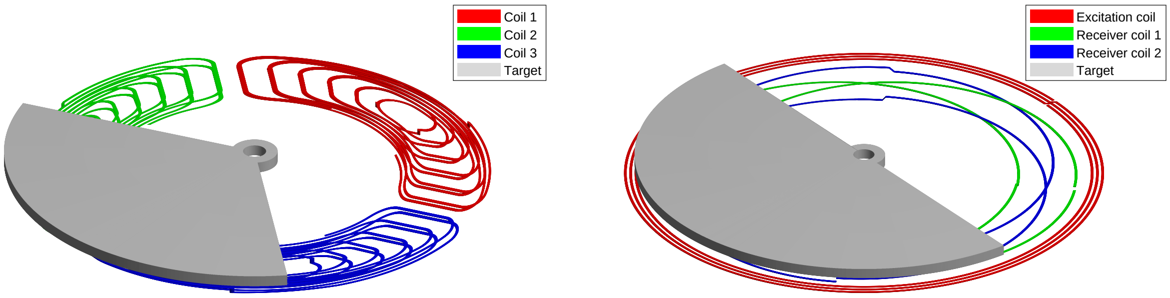

(a) Frequency-based **(b)** Amplitude-based

Figure 4.18: Angular position sensor

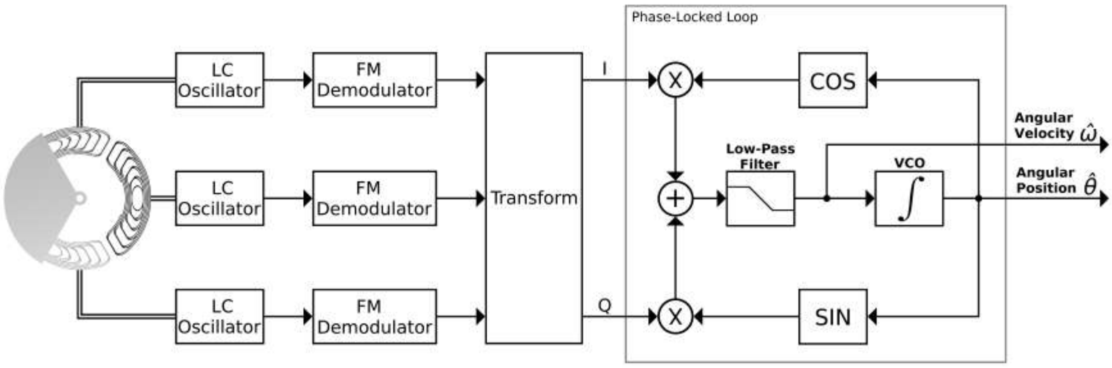

Figure 4.19: Frequency-based APS block diagram

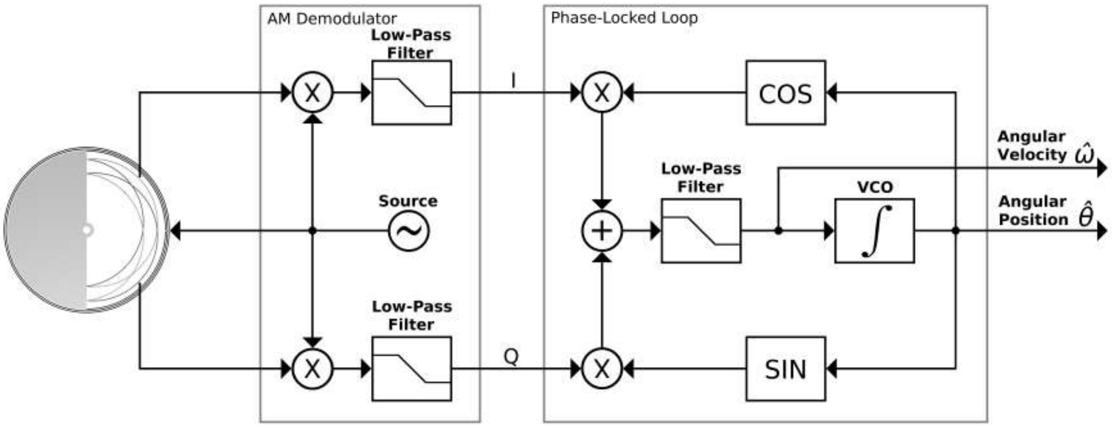

Figure 4.20: Amplitude-based APS block diagram

of these AM signals. Both versions of Foucault's current-based sensors have a coil energized by an alternating current, facing a conductive target. This alternating current generates an alternating magnetic field perpendicular to the direction of the electric current, which in turn induces currents in the conducting metal target, known as Foucault currents. These Foucault currents, also alternating currents, generate a new magnetic field that adds to the original one. The difference between the two types of sensors starts here. In the case of the Foucault current-based sensor version with the oscillator circuit (frequency-based version), the interaction between the two magnetic fields will change the coil's impedance value [153, 155]. In turn, this coil is a passive component of an electronic oscillator circuit, in which the oscillation frequency is related to the inductance value. Thus, by knowing the oscillating frequency, it is possible to calculate the inductance value of the coil. Moreover, since this inductance value is related to the relative position between the coil and the metal target [145, 147, 153, 154, 156], it is possible, as well, to calculate the displacement of the sensor. In the case of the amplitude-based version, which has dedicated receiver coils, the interaction between the two magnetic fields (the field generated by the excitation coil and the field generated by the Foucault currents on the target) dictates the induced signal amplitude on the receiver coils. Consequently, by knowing the amplitude of the induced signal related to the relative position between the coil and the metal target, it is possible to calculate the displacement of the sensor.

The sensors based on Foucault currents provide a non-contact measurement system, are immune to external magnetic fields, have high performance even in hostile environments, and are robust [147, 153, 157, 158]. With the increasing number of sensors in a single application, compact, low-cost, and low-power solutions are gaining relevance [110, 145, 153]. However, the skin effect limits high-frequency Foucault's current-based sensor's resolution and stability [150], their usual compact shape and insensitivity to the environment have become very attractive for industrial applications [159–161], leading to their deployment in several automotive systems.

4.4 Proposed methodology for inductive position sensor design

This section proposes and describes an automatic geometry generator for inductive position sensors that optimizes the sensor's coils for high induced current while simultaneously reducing the overall sensor's non-linearity. Finding the best coils' geometry configuration is required to accomplish these goals. The automatic geometry generator tool optimizes the sensor's coils' geometry for those two goals (more can be added) by performing two optimizations independently. In the first optimization iteration, the tool searches for one possible design that maximizes the induced current in the receiver's coils and fulfils the user constraints. Typically, those constraints are related to the selected PCB (e.g., stack size and the number of layers), the sensor's maximum allowed size and operating frequency. Those constraints could be imposed (e.g., the operating frequency), or an allowed range could be given (e.g., the sensor's coils' minimum and maximum permitted dimensions, including the target coil). In the second optimization iteration, the automatic geometry generator picks the optimized geometry from the first optimization iteration and harmonically deforms the two receiver coils to minimize the sensor's non-linearity. This is done by searching the amplitudes and phases of added harmonics components to the receiver's coils' forms (this is one of the main contributions of this thesis).

The automatic geometry generator tool utilizes a global search algorithm, the Real-Coded Genetic Algorithm (RCGA), and an electromagnetic field simulator to optimize the geometry of the sensor's coils. In

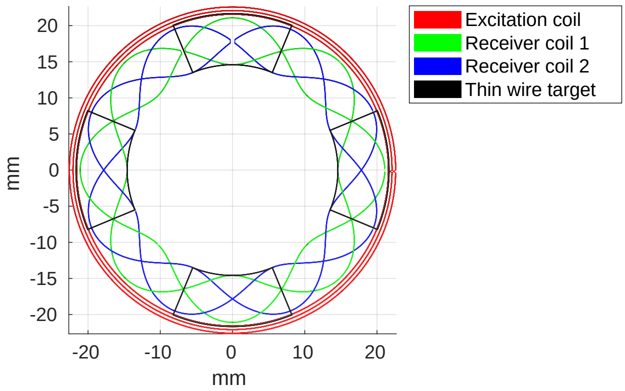

(a) Angular position sensor

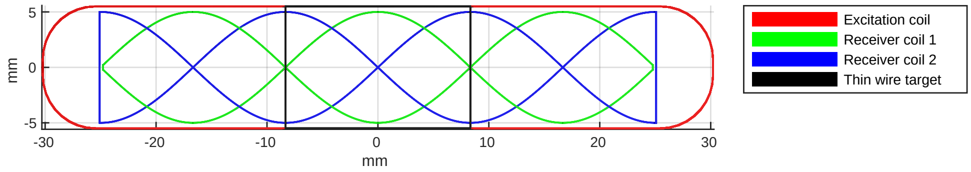

(b) Linear position sensor

Figure 4.21: Examples of position sensor geometries

the implemented RCGA, a population of individuals, each containing a single chromosome, evolves over a predetermined number of generations. Each chromosome consists of multiple genes, where the entire chromosome represents a sensor coil's geometry and each gene corresponds to one optimizable parameter. For the electromagnetic field simulator, three methods were implemented: the Method of Moments (MoM), a modified version of the MoM named Fast Harmonic Method (FHM) (detailed in Section 4.5), and the Multilevel Fast Multipole Method (MLFMM). Among these three methods, only one is employed throughout the entire optimization process, with the selecting being made during the tool's configuration phase.

The tool was primarily designed for linear and angular inductive position sensors, Figures 4.21a and 4.21b, respectively. It optimizes the sensor's geometry (excitation, receivers, and target coils) to achieve higher induced current on the receiver's coils and lower the sensor's non-linearity. However, it is not intended to limit the scope of the tool's applicability. It could be easily extended to other types of inductive sensors and other optimization goals like flux maximization and mechanic tolerances.

The flowchart of Figure 4.22 overviews how the automatic geometry generator tool operates. The process begins with collecting the user's input settings that define the non-optimizable parameters and their respective fixed values. Correspondingly, the tool prompts the user to specify the optimizable ones and their limits. As an option, the user can provide an initial geometry. If provided, it is incorporated into the Genetic Algorithm (GA)'s first generation as an individual. This option allows for improving an existing

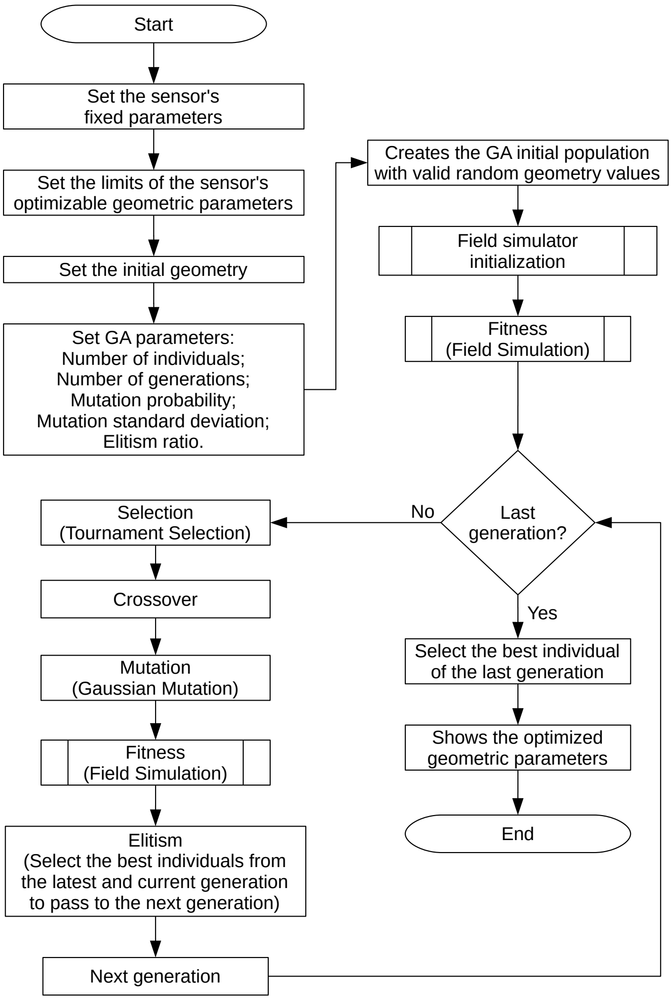

Figure 4.22: Optimization algorithm flowchart

geometry. Lastly, the last settings before the optimization process begins are the GA's settings. These are the number of individuals (geometries) that compose the population, the maximum number of generations that the population will be able to evolve, how often a mutation occurs (mutation probability) and its non-normalized standard deviation, and the elitism ratio that defines the ratio of individuals from the previews generation that will be part of the next one.

With this configuration as input, the automatic geometry generator tool creates the first generation of

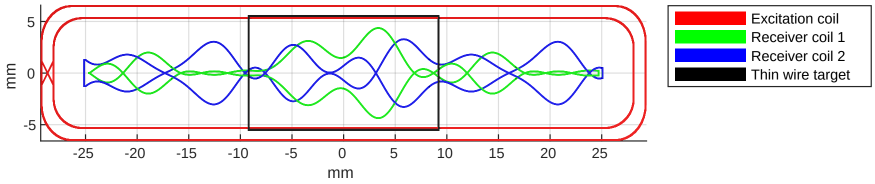

Figure 4.23: Geometry generated in the first generation

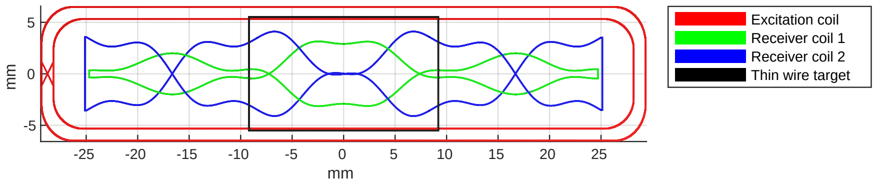

Figure 4.24: Geometry generated by the optimization tool

Table 4.3: Example of fixed and optimizable parameters for induced current maximization

Fixed parameters		
Description	**Value**	
PCB trace width	165.000 μm	
PCB copper thickness	18.000 μm	
Thickness between PCB layers 1 and 2	70.000 μm	
Thickness between PCB layers 2 and 3	320.000 μm	
Thickness between PCB layers 3 and 4	70.000 μm	
Receiver coils' lenght	50.000 mm	
Receiver coils' width	10.000 mm	
Target airgap	2.000 mm	
Frequency of the excitation coil's power source	10.700 MHz	
Voltage of the excitation coil's power source	707.107 mV$_{RMS}$	
Maximum current of the excitation coil's power source	7.071 mA$_{RMS}$	
Optimizable parameters		
Description	**Minimum**	**Maximum**
Turns in the excitation coil	1	3
Layers in the excitation coil	1	4
Gap between turns of excitation coil	165.000 μm	1.000 mm
Excitation coil inner lenght	50.660 mm	101.320 mm
Excitation coil inner width	10.660 mm	21.320 mm
Target lenght	1.000 mm	50.000 mm
Target width	1.000 mm	21.320 mm

induced position sensors' geometries (individuals). If the user supplies an initial geometry as a starting point, it is inserted as the first individual in the first generation, and the remaining individuals are generated randomly. If not, the first individual is also generated randomly. All randomly generated individuals are valid designs (e.g., all geometries where the receiver's coils invade the excitation coil area and geometries outside the limits of the user-defined optimizable parameters are not allowed). As a curiosity, Figure 4.23 depicts an example of a random geometry generated in the first generation in the second iteration (low non-linearity goal).

As an example of a valid use case, the geometry illustrated in Figure 4.24 was achieved through a series of parameters set. In this example, the fixed parameters in the first optimizing iteration (high induced

Table 4.4: Example of fixed and optimizable parameters for non-linearity minimization

	Receiver coil	Harmonic	Minimum	Maximum
Amplitudes	1	0	-5.000 mm	5.000 mm
		2	-5.000 mm	5.000 mm
		3	-5.000 mm	5.000 mm
		4	-5.000 mm	5.000 mm
		5	-5.000 mm	5.000 mm
	2	0	-5.000 mm	5.000 mm
		2	-5.000 mm	5.000 mm
		3	-5.000 mm	5.000 mm
		4	-5.000 mm	5.000 mm
		5	-5.000 mm	5.000 mm
Phases	1	2	-90°	90°
		3	-90°	90°
		4	-90°	90°
		5	-90°	90°
	2	2	-90°	90°
		3	-90°	90°
		4	-90°	90°
		5	-90°	90°

current goal) were: the PCB trace width, the PCB copper and layers' thickness, the receiver's coils' length and width, the target airgap (airgap space between the receiver's coils plane and target coil plane), the frequency and voltage of the excitation coil's power source, and the maximum current allowed in the excitation coil. The optimizable parameters were: the total number of turns in the excitation coil in each layer, the total number of layers that compose the excitation coil, the gap between the excitation coil's turns' traces, the excitation coil's inner length and width (the length and width of the innermost turn), and the length and width of the target's coil. All of them and their respective values are summarised in Table 4.3. Also, in this example, the optimization tool was fed with an initial geometry, the geometry depicted in Figure 4.21b. In the second optimization iteration (low non-linearity goal), the tool is fed with the geometry generated in the first iteration as initial geometry. This time the optimizable parameters are the amplitudes and phases of the harmonics components to be physically added to the receiver's coils. These components are the continuous component and all harmonics from 2 through 5. Table 4.4 summarizes the optimizable parameters and depicts their respective limits. As a side note, the fundamental harmonic amplitude is adjusted accordingly to avoid superposition over the excitation coil.

As stated before, the global search algorithm implemented is the RCGA to search through all possible solutions for optimal design. In essence, the RCGA algorithm evolves a population of candidate designs, where every individual has a chromosome that encodes the optimizable parameters in several genes. These parameters are evaluated against the desired objective of higher induced current or lower non-linearity, where a fitness function gives a score. Any potential offspring from a pair of parents would inherit their parent's genes and any new gene they acquired during the evolution process. If the proposed solution did not fit the goal, it will not produce offspring and eventually will die out. The individuals that survived would pass on their genes to further generations. In addition, a mutation may occur. The algorithm continues until it comes across a solution that has met the criteria. Essentially, the RCGA is composed of genetic operators (selection, crossover and mutation) that generate a series of populations (sensor's coils' geometries) whose individuals will have evolved to satisfy a particular propose (higher induced current or lower non-linearity). A more detailed description of the GA is presented in Section 2.3.3.

The first evolutionary operator applied to the population is the *Selection*, as shown in the flowchart in Figure 4.22. The primary objective of this operator is to probabilistically advance the most suitable solutions to the next generation, while discarding the less optimal ones. There are various strategies available for selection, one of which is tournament selection. In the implemented tournament selection algorithm, the chromosomes, representing the sensor's geometries, are randomly reordered into two distinct arrays, each containing the entire population in a different sequence. Chromosomes in corresponding positions within the arrays compete with each other, and the winner is the one with the highest fitness value. This process is repeated for all positions within the arrays.

The second evolutionary operator to be applied is the *crossover*. This operator is the primary search tool for GAs since it combines chromosomes with relevant genetic information, creating a new population. The implemented crossover algorithm randomly selects the genes (optimizable parameters) from parent one (sensor's geometry) to be inherited by offspring one (crossed sensor's geometry). At the same time, the remains come from parent two. In turn, offspring two inherits both parents' rejected genes. Parent one and two are randomly selected from the population and removed to ensure they are not selected again. This process repeats until all chromosomes (sensor's geometries) have been crossed.

The subsequent evolutionary operator is *mutation*. As described in Section 2.3.3, it is introduced to prevent early convergence and to ensure diversity. The implemented version of this operator modifies the offspring genes (optimizable parameters) randomly by altering their value in compliance with a unidimensional gaussian curve, resulting in a new individual (sensor's geometry). The user-specified mutation standard deviation value determines the gaussian curve, and the mutation probability, which is also user-specified, dictates how frequently this mutation can occur.

The *elitism* operator guarantees that the best preview individuals (sensor geometries) are included in the following generation. This operator is necessary for the most refined individual of the previous generation to be present in the next. The ratio of the individuals of the prior generation and the current generation that will be part of the next generation is given by the elitism ratio (user-specified), and the best individuals from both generations (previous and current) are selected.

With the next generation formed, the process repeats until a limited number of generations is achieved (see Figure 4.22). When this occurs, the best individual from the last generation is selected and presented as the optimized sensor geometry.

4.4.1 Fitness function

As mentioned previously, the optimization tool has three methods to solve the field equations, the MoM, a modified version of the MoM named FHM (detailed in Section 4.5), and the MLFMM. Each of them is called in the fitness function.

The flowchart in Figure 4.25 depicts the implementation of the fitness function that employs the MoM to solve the field equations. This function begins by generating the geometry encoded in the individual's chromosomal genes, followed by the discretization using perfectly conducting thin wires. After that, it generates the system of linear equations to be solved, as described in Section 2.2.2. The system of linear equations is then solved, using the Generalized Minimum Residue (GMRES) method solver, and stored. Depending on the optimization objective, increasing the induced current in the receiver's coils or reducing the sensor's non-linearity, the sensor's coils' geometry must be simulated with different target positions. To minimize non-linearity, the sensor must be simulated with the target at several positions to know the sensor's non-linearity overall the target excursion (linear and angular). Thus, after each simulation, the target is repositioned, and the simulation process is repeated, ending when the target reaches the final position. Finally, the fitness score is calculated according to the optimization objective through the knowledge of the current $[i]$ distribution for different target positions.

The flowchart of the fitness function that implements the FHM is depicted in Figure 4.26. Similar to the MoM's fitness function, this function starts by generating the geometry encoded in the individual's

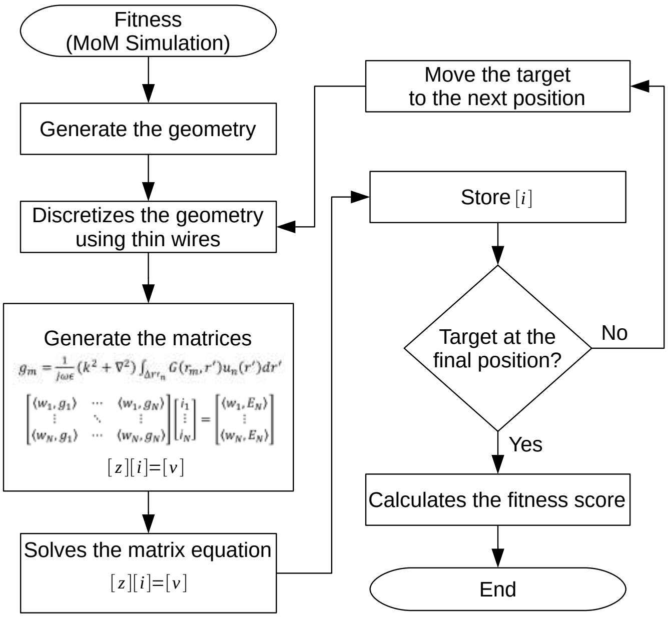

Figure 4.25: MoM simulation algorithm flowchart

chromosomal genes, followed by the discretization using perfectly conducting thin wires. After, it generates the system of linear equations in the same way as in the MoM, the only difference being that the impedance matrix $[z]$ and the source matrix $[v]$ are converted to the frequency domain. In this new domain, the higher frequencies are removed to reduce the size of the matrices and, therefore, the processing time needed to solve the system of linear equations. This reduction is only possible because inductive position sensors are typically much smaller than the operating wavelength. The system of linear equations in the frequency domain is then solved using the GMRES solver, and the current $[i]$ is converted back to the original domain and stored. A similar way as in the MoM's fitness function, the target is also moved to the next position, and the simulation process is repeated until it reaches the last position. Finally, the fitness score is calculated.

The last fitness function employs the MLFMM algorithm to solve the field equations. Figures 4.27 and 4.28 show the algorithm's initialization and the fitness function flowcharts, respectively.

The MLFMM initialization algorithm initializes the octal tree structure and related matrices. As the structure of the octal tree and the matrices related to it are independent of the sensor geometry, they only need to be computed once. In this way, all matrices that meet these criteria are initialized in the Figure 4.27 flowchart. These are the radially oriented unit vectors on the sphere ($\hat{k}$), the interpolation matrices (W), and the transfer functions (H) of all possible combinations of distinct values of $\hat{k}$ and $\vec{r}_{ab}$. All transfer

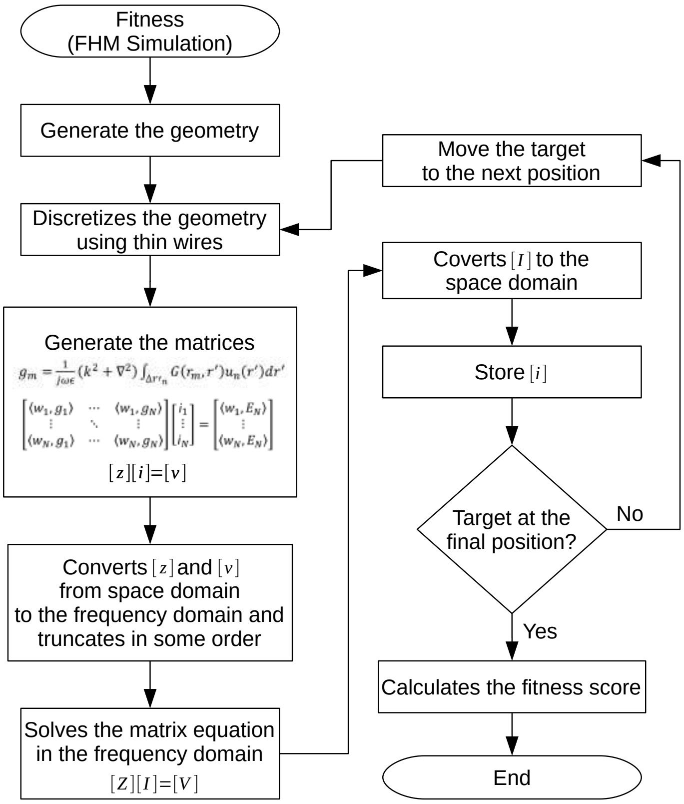

Figure 4.26: FHM simulation algorithm flowchart

functions are computed using Equation 2.104, and the interpolation matrices are formed employing Lagrange Polynomials, with weights calculated using Equation 2.110. More details about the octal structure and mentioned matrices can be found in Section 2.2.3.

The fitness function algorithm depicted in Figure 4.28 begins similarly to the other two fitness functions by generating the geometry encoded in the individual's chromosomal genes, followed by discretization using perfectly conducting thin wires. Alongside that, it generates the impedance matrix $[z^{near}]$ in the same way as MoM. The only difference is that the generated matrix is sparse because it only considers the near-thin-wire elements. The following two steps compute the radiation functions, T, used to translate the source and field waves from the thin-wire elements to the respective box's centre and the receiver functions, R, used to translate back from the box's centre to the respective thin-wire elements. The implemented algorithm is based on the theoretical background covered in Section 2.2.3.

The Fast Multipole Method (FMM) algorithm solves the far interactions on the fly, requiring an iterative method. For this task, GMRES was selected, and incomplete Lower–Upper (LU) factorization of the sparse matrix $[z^{near}]$ was used as a preconditioner to reduce the number of convergence iterations. In each

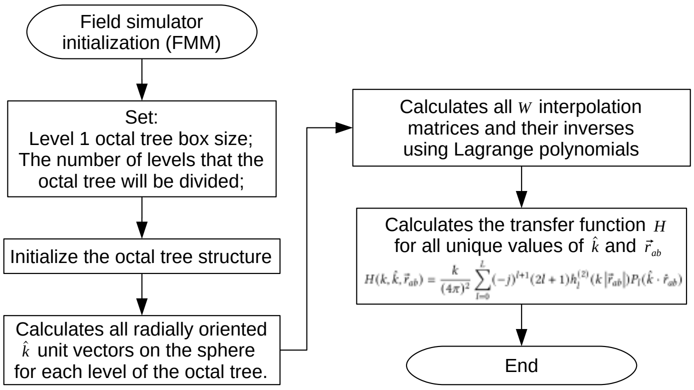

Figure 4.27: MLFMM initialization algorithm flowchart

iteration, the GMRES algorithm guesses $[i]$, and $[v]^{near}$, $[v^{near}] = [z^{near}]\,[i]$, is solved straight-forward. The $[v]^{far}$ is computed during the aggregation, translation and disaggregation phases (see Algorithm 1), and the source $[v] = [v^{near}] + \left[v^{far}\right]$. The algorithm then compares the calculated values of the source $[v]$ with its actual value. If the difference exceeds a predetermined threshold set during the GMRES configuration, $[i]$ is considered to have not enough accuracy, and a new iteration is started. If not, the iterative method stops, and $[i]$ is stored.

Similar to the others two fitness functions, the target is moved to the next position, and the simulation process is repeated until it reaches the last position. In the last step, the fitness score is calculated and stored.

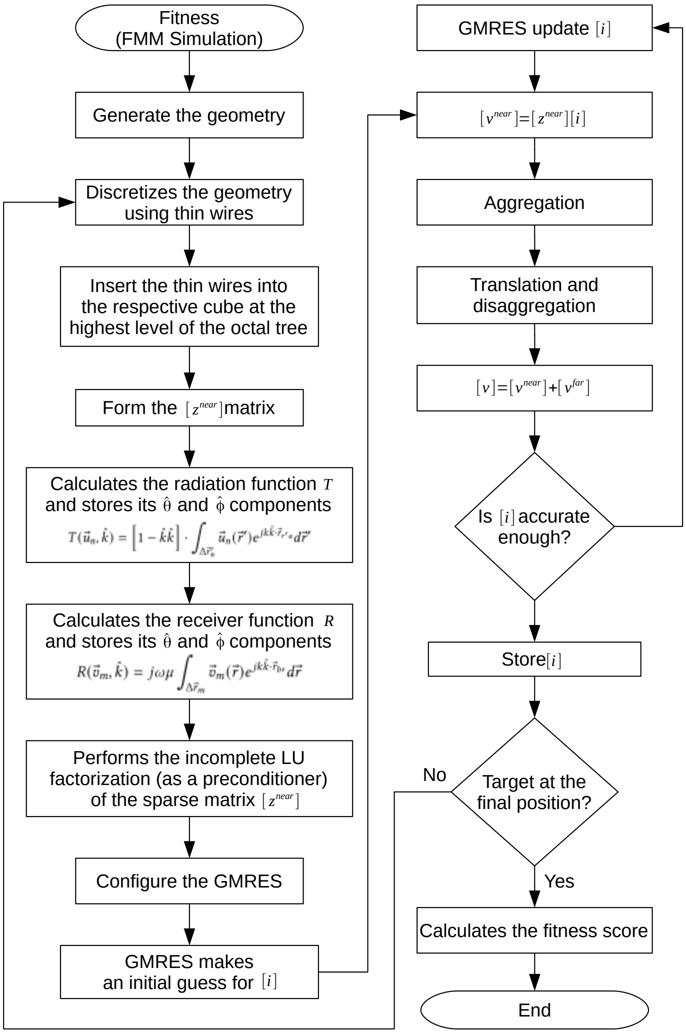

Figure 4.28: MLFMM simulation algorithm flowchart

4.5 Fast harmonic method

The FHM aims to reduce the size of the matrices formed by the MoM (Subsection 2.2.2). It seems suitable for thin-wire low-frequency problems where the device's size is much smaller than the wavelength, and thin-wire elements can be used to discretize it, which is the case of inductive sensors. This method assumes that the current flowing through the device's wires does not vary significantly from one thin-wire element to the next. It can be used to reduce the MoM's matrices sizes, consequently reducing the memory consumption and processing time to solve MoM's matrix equation.

To simplify the explanation and infer the equations used by this method, it is first assumed that the device is made up of only one long thin wire. Later in this section, the use of FHM with multi-wire devices is described.

$$[z]\,[i] = [v] \tag{4.1a}$$

$$\sum_{m=1}^{M}\sum_{n=1}^{N} z_{mn} i_n e^{-j2\pi(p-1)\frac{m-1}{M}} = \sum_{m=1}^{M} v_m e^{-j2\pi(p-1)\frac{m-1}{M}} \quad , \ p \in \mathbb{N} : p < M \tag{4.1b}$$

$$\sum_{m=1}^{M}\sum_{n=1}^{N} z_{mn} \sum_{q=1}^{N} I_q e^{j2\pi(n-1)\frac{q-1}{N}} e^{-j2\pi(p-1)\frac{m-1}{M}} = \sum_{m=1}^{M} v_m e^{-j2\pi(p-1)\frac{m-1}{M}} \quad , \ p \in \mathbb{N} : p < M \tag{4.1c}$$

$$\sum_{q=1}^{N} I_q \sum_{m=1}^{M}\sum_{n=1}^{N} z_{mn} e^{j2\pi(q-1)\frac{n-1}{N}} e^{-j2\pi(p-1)\frac{m-1}{M}} = \sum_{m=1}^{M} v_m e^{-j2\pi(p-1)\frac{m-1}{M}} \quad , \ p \in \mathbb{N} : p < M \tag{4.1d}$$

$$\sum_{q=1}^{N} I_q Z_{pq} = V_p \ , \ p \in \mathbb{N} : p < M \tag{4.1e}$$

$$[Z]\,[I] = [V] \tag{4.1f}$$

It begins with the matrix Equation 4.1a, formed by the MoM. Analyzing this equation, it is possible to see that each side of the equation has one column vector, $[z]\,[i]$ on the left and $[v]$ on the right. $[z]\,[i]$ can be written as $\sum_{n=1}^{N} z_{mn} i_n$, where N represents the total number of columns in the $[z]$ square matrix. Applying the Discrete Fourier Transform (DFT) to both sides of the equality yields Equation 4.1b, where M is the total number of lines of matrices $[z]$, $[i]$ and $[v]$, $j^2 = -1$, and p is the frequency domain coefficient index. In Equation 4.1b i_n can be replaced with the frequency domain coefficients I_q and the Inverse Discrete Fourier Transform (IDFT) can be applied on those coefficients to preserve the equality ($i_n = \sum_{q=1}^{N} I_q e^{j2\pi(n-1)\frac{q-1}{N}}$). By doing it, Equation 4.1c is obtained, where q is the frequency domain coefficient index of $[I]$. By annalizing Equation 4.1c, one can determine that the term I_q is not dependent on m and n, so it can be taken out (Equation 4.1d). By observing Equation 4.1d, the right side can be simplified by substituting it with the frequency domain coefficients V_p. On the left side of Equation 4.1d, please note that the DFT is being applied along the second dimension of the matrix $[z]$ and the IDFT along the first dimension. For simplicity, it was substituted by the Z_{pq} coefficients. Those replacements result in Equation 4.1e, which can be written more compactly, as shown in Equation 4.1f.

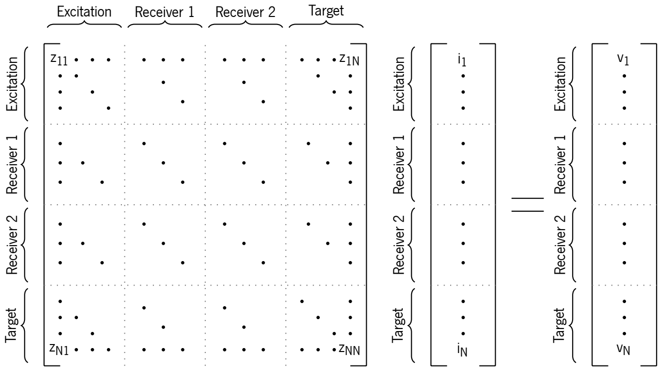

Figure 4.29: Matrices regions division

Throughout this deduction, the size of the matrices was not reduced, or the problem simplified. The problem's domain was simply changed to the frequency domain. By doing this and with the assumption that the current flowing through the device's wires does not vary significantly from one thin-wire element to the next, the possibility of truncating the coefficients to some order is now open, and in that way, the possibility to reduce the MoM's matrices size. This procedure works because when the device's size is much smaller than the operating wavelength, the higher frequency domain coefficients are very near to zero and thus can be discarded without significantly compromising the overall simulation's result. After the truncation, the matrix equation depicted in Equation 4.1f is solved in the same manner as in the MoM. This gives the coefficient values of I_q truncated at some level. The final step is to perform an IDFT to the coefficients $[I]$ to get the current distribution, $[i]$, over the wire.

Everything stated here works perfectly for the case of a single-wire device. In the circumstance of multi-wire devices, e.g. position sensors with an excitation coil, two receiver's coils and one target coil, the matrices should be partitioned into smaller regions, and each region should be translated to the frequency domain independently. Figure 4.29 depicts it, with the three matrices, $[z]$, $[i]$, and $[v]$, partitioned based on their association with thin wire coils, representing the target, excitation and receiver coils. The way Figure 4.29 is presented may lead to the misconception that the number of thin-wire elements in each coil must be the same to ensure that all sub-matrices are all square, but this is not the case. Under typical conditions, the number of thin-wire elements in each coil differs, resulting in non-square sub-matrices. To work with non-square matrices, the limits of the indices m and n in Equations 4.1a to 4.1d are differentiated using distinct letters, M and N.

After translating all sub-matrices from matrices, $[z]$ and $[v]$ to the frequency domain, the matrix equation is solved in the same manner as in the MoM. This gives the current distribution over the thin wire's coils in the frequency domain. The final step, as stated before, is to perform an IDFT and obtain the current distribution in the space domain. Once more, the column matrix $[I]$ is partitioned into smaller regions, and each region should be translated to the space domain independently to obtain the matrix $[i]$.

4.6 Inductive sensor optimization methodology

This section starts with the description of the methodology used to evaluate the automatic geometry generator tool presented in this thesis. Next, the results obtained are presented, and the section finishes with a brief discussion.

4.6.1 Methodology

As described in 4.4, the electromagnetic simulator and the global optimizer are the two major building blocks of the automatic geometry generator tool for inductive sensor. The global optimizer block has a implementation of a GA. The electromagnetic simulator block relies in three different implementations. Opening three different possibilities for the tool. The first one implements the MoM to solve the field equations, the second uses FHM, and the third the MLFMM.

To evaluate the different implementations of the optimization tool, two custom sensor geometries, an APS and a LIPS (both based on real automotive designs), were used to evaluate the different implementations of the optimization tool. The first implementation, which employed the MoM, was used to optimize the APS sensor. In contrast, the second implementation, which incorporated the FHM, was applied to optimize the LIPS sensor. As the different implementations uses the exact same RCGA and the FHM implementation employs the MoM to construct the matrix equation to be solved, the only difference lies in the strategy employed to reduce the equation matrix size without compromising the overall simulation results (the discrepancies between the MoM and the FHM in the results simulations are negligible). As a result, it was decided to implement one method to optimize an angular sensor and another method to optimize a linear sensor, since both simulators yield similar results with negligible differences. Finally, for the third version using the MLFMM implementation, only the electromagnetic simulator block was tested. The reason for this decision is explained in the section dedicated to the MLFMM test.

In order to optimize both inductive position sensors, APS and LIPS, the tool was employed through two separate iterations. The first iteration aimed at maximizing the induced current in the receiver's coils.

Subsequently, in the second iteration, the optimized geometry from the first iteration was used as the starting point. Furthermore, the second iteration was performed independently twice, each time with different objectives. The first objective aimed to minimize the sensor's non-linearity, while the second one focused on reducing the harmonic content. Again, both objectives used the optimized geometry from the first iteration. Further details are discussed in the following sections.

Since three electromagnetic simulators were developed, the remaining of this section describes the results obtained with each one.

4.6.2 Optimization using the MoM

This section summarizes the main results obtained with the optimization tool implemented with the MoM to solve the electromagnetic field equations. The optimization tool was used to optimize the geometry of an APS, consisting of an excitation coil, two receiving coils and one target coil, with a measurement range of 360°. The excitation coil and both receiver coils were printed on the same PCB, defined as the stator, while the target coil was printed on a separate PCB identified as the rotor. The goals were to maximize the induced current in both receivers' coils and minimize the APS non-linearity. To accomplish this, the optimization procedure was divided into two iterations. The first iteration used the optimization tool to optimize the sensor's geometry to obtain a maximization of the induced current on both receivers' coils. The second iteration takes the optimized geometry obtained in the first iteration, and uses it as the starting point to minimize the sensor's non-linearity, using the same optimization tool. In addition, the second iteration was repeated 14 times, with different fitness functions and GA parameters. The goal was to determine which fitness functions and GA parameters best fit the objective in terms of convergence and geometric solution. A diagram of the optimization procedure can be seen in Figure 4.30. *Geometry 1*, depicted in Figure 4.31, is the initial human-made geometry most suitable for producing acceptable results. This geometry was the starting point to maximize the induced current, and *Geometry 2* results from geometry optimization. *Geometry 3* is the optimized version of *Geometry 2* when maximum non-linearity is used as a fitness parameter to be optimized.

Geometry 4.x (*Geometry 4.x* refers to 12 geometry optimizations, from *Geometry 4.1* through *Geometry 4.12*, that employ the same fitness function but different GA parameters) and *5* begin with the same geometry as *Geometry 3* but with extra optimizable parameters. As in *Geometry 3*, the maximum sensor non-linearity is the fitness parameter for *Geometry 4.x*. However, rather than the maximum non-linearity of

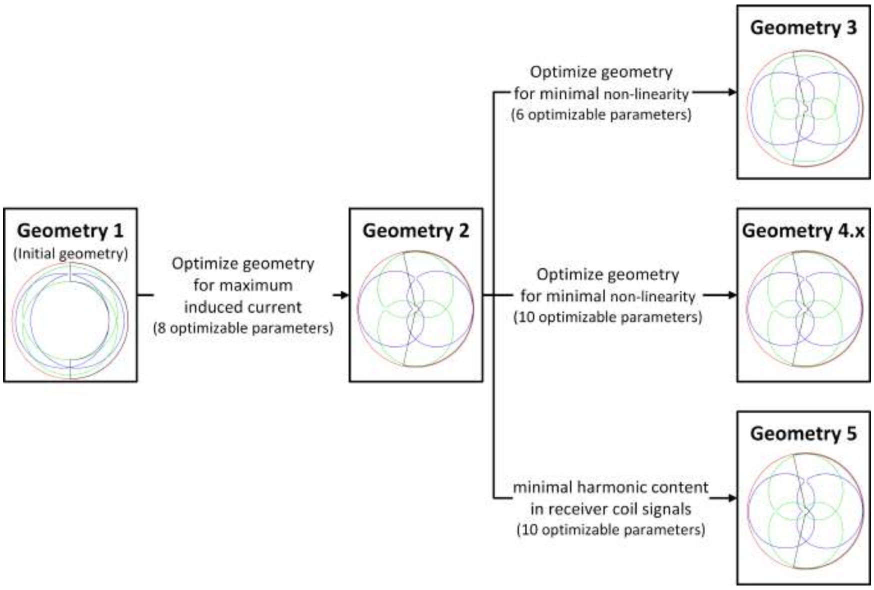

Figure 4.30: Optimization flowchart

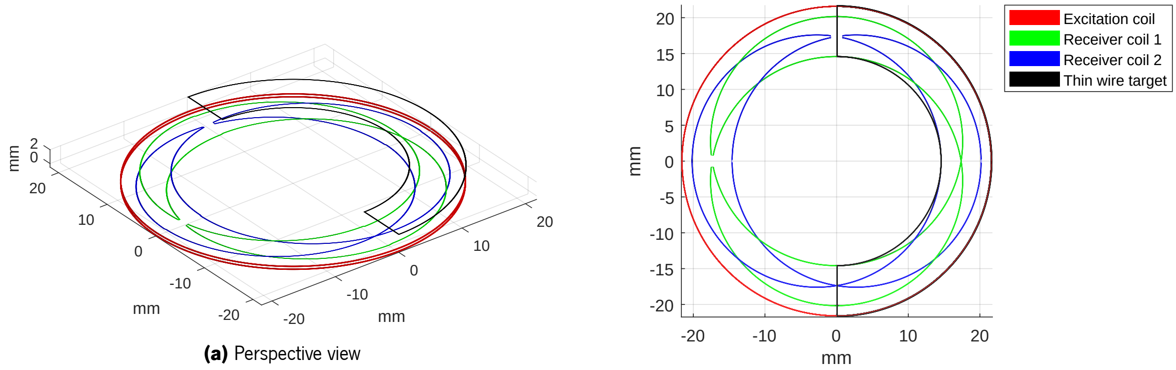

(a) Perspective view

(b) Top view

Figure 4.31: APS initial geometry - Geometry 1

eight equally spaced angular positions, like in *Geometry 3*, *Geometry 4.x* has 16. Finally, *Geometry 5* has the same optimizable parameters as *Geometry 4.x*. The only difference is the fitness parameter, which is the harmonic content in the two receivers' coils signals. The goal is to reduce the harmonic content and, consequently, the non-linearity. A more detailed description of each optimization and respective results are given in the following subsections, one for each optimization.

4.6.2.1 APS peak-to-peak induced current optimization

This subsection describes the use of the optimization tool to generate a geometry that maximizes the induced current in the sensor receiver's coils. As previously stated, this process begins with *Geometry 1* as a starting point. It is necessary to select which geometric parameters will be fixed and which will

Table 4.5: APS optimization using MoM - Limits and initial parameters for induced current maximization

<table>
<tr><th colspan="5">Fixed parameters</th></tr>
<tr><th>Description</th><th colspan="4">Value</th></tr>
<tr><td>PCB trace width</td><td colspan="4">165.000 µm</td></tr>
<tr><td>PCB copper thickness</td><td colspan="4">18.000 µm</td></tr>
<tr><td>Thickness between PCB layers 1 and 2</td><td colspan="4">70.000 µm</td></tr>
<tr><td>Thickness between PCB layers 2 and 3</td><td colspan="4">320.000 µm</td></tr>
<tr><td>Thickness between PCB layers 3 and 4</td><td colspan="4">70.000 µm</td></tr>
<tr><td>Receiver coils’ outermost radius</td><td colspan="4">20.250 mm</td></tr>
<tr><td>Target airgap</td><td colspan="4">2.000 mm</td></tr>
<tr><td>Frequency of the excitation coil’s power source</td><td colspan="4">10.700 MHz</td></tr>
<tr><td>Voltage of the excitation coil’s power source</td><td colspan="4">707.107 mV$_{RMS}$</td></tr>
<tr><td>Maximum current of the excitation coil’s power source</td><td colspan="4">7.071 mA$_{RMS}$</td></tr>
<tr><th colspan="5">Optimizable parameters</th></tr>
<tr><th>Description</th><th>Initial Geometry 1</th><th>Minimum</th><th>Maximum</th><th>Optimized Geometry 2</th></tr>
<tr><td>Turns in the excitation coil</td><td>1</td><td>1</td><td>3</td><td>1</td></tr>
<tr><td>Layers in the excitation coil</td><td>4</td><td>1</td><td>4</td><td>4</td></tr>
<tr><td>Gap between turns of excitation coil</td><td>335.000 µm</td><td>165.000 µm</td><td>1.000 mm</td><td>732.212 µm</td></tr>
<tr><td>Excitation coil inner radius</td><td>21.500 mm</td><td>1.000 mm</td><td>50.000 mm</td><td>20.428 mm</td></tr>
<tr><td>Receiver coils’ innermost radius</td><td>14.500 mm</td><td>1.000 mm</td><td>50.000 mm</td><td>1.000 mm</td></tr>
<tr><td>Target inner radius</td><td>14.500 mm</td><td>1.000 mm</td><td>50.000 mm</td><td>1.000 mm</td></tr>
<tr><td>Target outer radius</td><td>21.750 mm</td><td>1.000 mm</td><td>50.000 mm</td><td>20.320 mm</td></tr>
<tr><td>Target angular wing size</td><td>180.000°</td><td>0.000°</td><td>360.000°</td><td>205.363°</td></tr>
</table>

be optimizable, as well as their upper and lower limits in the case of the optimizable parameters. As fixed geometric parameters, the PCB trace width, the PCB copper thickness, the PCB layers stack, the receiver's coils' outermost radius and the conductive target airgap (airgap between the *stator* and *rotor* PCBs) were imported to the tool. Some were selected for obvious reasons, such as copper thickness and PCB layers' stack, resulting from PCB fabrication constraints. Others are due to mechanical constraints, such as the receiver's coils' outermost radius and the target airgap. For optimizable parameters, eight parameters were selected: the total number of turns in the excitation coil in each layer, the total number of layers that compose the excitation coil, the gap between the excitation coil's turns' traces, the excitation coil's inner radius (the radius of the innermost turn), the receivers coils' innermost radius (the shortest distance that receiver's coils' traces has to the sensor's centre), the inner and outer radius of the target's coil, and the angular size of the target. Table 4.5 summarizes these parameters and shows the upper and lower limits, as well as the initial values of the optimizable parameters used in *Geometry 1* (initial geometry).

After selecting and configuring the fixed and optimizable parameters, the fitness function and GA parameters must also be coded and configured, respectively. The fitness function is made up of MoM simulations, in which the APS's coils (the excitation coil together with the two receiver coils and the target coil) are all immersed in a medium with a relative electrical permittivity and a relative magnetic permeability of one. Also, the excitation coil is powered by a differential potential of 0.7071 V_{RMS} at 10.7 MHz, being the maximum induced current on the receiver's coils used as a fitness value. For this, two MoM simulations were performed, being the target positioned 180° apart in the two areas where the induced current is maximum. The fitness value is calculated by adding those two maximums values (peak-to-peak). Also, the fitness function sets the fitness value to zero if the optimizable geometric parameters yield a physically impossible geometry or if the excitation current exceeds a threshold value, which was set to 7.071 mA_{RMS}.

Finally, the GA parameters are configured to produce a population of 100 individuals that will evolve over 100 generations with a mutation probability of 1/8. This implyes that, on average, one gene per chromosome will be mutated, as there are a total of eight genes per chromosome (eight configurable parameters per individual or geometry). The non-dimensionalized standard deviation mutation is 1/30, and the elitism ratio is 1/2. This value indicates that half of the individuals from the previous generation, the best ones, will be part of the next generation.

Being the optimization tool fully configured as described, the optimization procedure took approximately

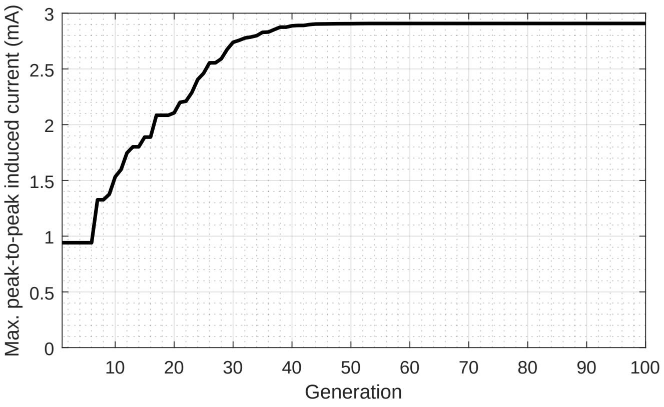

Figure 4.32: APS optimized for maximum induced current - Convergence curve

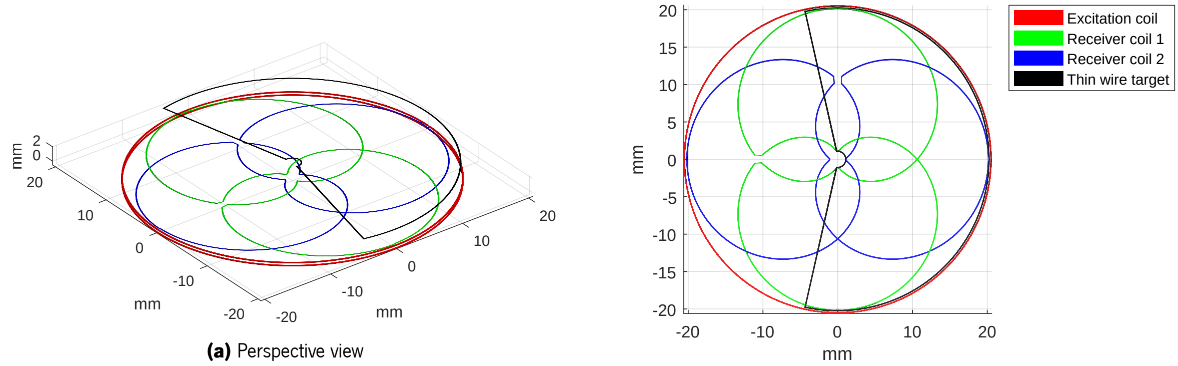

(a) Perspective view

(b) Top view

Figure 4.33: APS optimized for maximum induced current - Geometry 2

14 wall time hours to optimize *Geometry 1* and get *Geometry 2* on a high-end 2014 workstation with 64 GB of Random-Access Memory (RAM). Figure 4.32 shows the convergence curve, which depicts the evolution of the best individual's fitness value (highest peak-to-peak induced current) over 100 generations, and Figure 4.33 illustrates the optimized geometry, *Geometry 2*. *Geometry 2* reached a fitness value of 2.908 mA (peak-to-peak), whereas *Geometry 1* has 0.941 mA (peak-to-peak), indicating that *Geometry 2* has approximately a three times stronger induction current than *Geometry 1*.

4.6.2.2 APS non-linearity optimization (amplitudes)

The next step is to reduce *Geometry 2*'s maximum non-linearity after optimizing the induced current in the receiver's coils. *Geometry 2*, with a maximum non-linearity of 0.663°, is used as the starting point. The goal is to see if the optimization tool can discover a solution that considerably reduces sensor non-linearity by introducing some harmonic distortion into the receiver's coils design. Because the receiver's coil's signals had a significant harmonic amplitude in the continuous component and the third and fifth harmonics, those components were employed to generate the geometric harmonic distortion. In other

Table 4.6: APS optimization using MoM - Limits, initial and optimized parameters for non-linearity optimization (amplitudes)

	Receiver coil	**Harmonic**	**Initial Geometry 2**	**Minimum**	**Maximum**	**Optimized value (Geometry 3)**
Amplitudes	1	0	0.000 mm	-19.250 mm	19.250 mm	0.000 mm
		1	19.250 mm	-	-	16.576 mm
		3	0.000 mm	-19.250 mm	19.250 mm	1.140 mm
		5	0.000 mm	-19.250 mm	19.250 mm	-1.534 mm
	2	0	0.000 mm	-19.250 mm	19.250 mm	-0.007 mm
		1	19.250 mm	-	-	17.762 mm
		3	0.000 mm	-19.250 mm	19.250 mm	0.115 mm
		5	0.000 mm	-19.250 mm	19.250 mm	-1.366 mm

words, a geometric harmonic distortion was created in the continuous component and in third and fifth harmonics to counterbalance the presence of those on the receiver's coil signal. Table 4.6 depicts the optimization parameters, including their initial values as well as their upper and lower limits. It is worth noting that the fundamental harmonic amplitude is lowered proportionally to accommodate the existence of the additional harmonics and avoid geometric constraints.

The maximum non-linearity that the sensor can have in a single complete turn was used as fitness value. For this, eight MoM simulations were executed in the fitness function, being the target position in each of them angularly equally separated. The angle detected by the sensor is calculated using Equation 4.2, where α is the measured angle, and x and y are the amplitude signals from receiver coils 1 and 2, respectively. The non-linearity is defined as the difference between the true angular target position and the measured angle, with the fitness value (the maximum non-linearity) being the highest of the eight non-linearities. It is also important to note that the sensor's zero location was chosen such that the maximum non-linearity was as minimal as feasible. This was accomplished by subtracting the average non-linearity value from all non-linearity values.

$$\alpha = \begin{cases} \tan^{-1}\left(\frac{y}{x}\right) & , if\ x > 0 \\ \tan^{-1}\left(\frac{y}{x}\right) + \pi & , if\ x < 0\ and\ y \geq 0 \\ \tan^{-1}\left(\frac{y}{x}\right) - \pi & , if\ x < 0\ and\ y < 0 \\ +\frac{\pi}{2} & , if\ x = 0\ and\ y > 0 \\ -\frac{\pi}{2} & , if\ x = 0\ and\ y < 0 \end{cases} \tag{4.2}$$

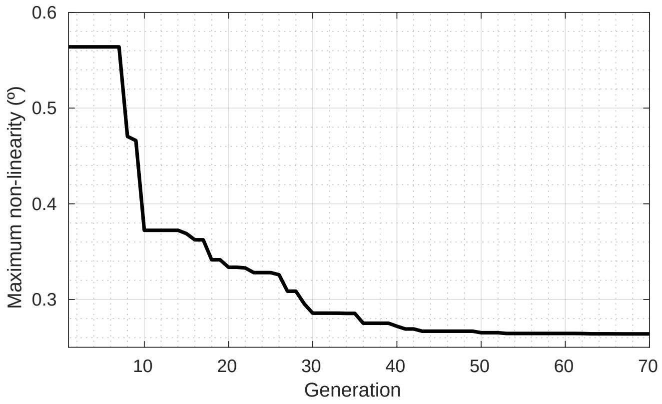

Figure 4.34: APS optimized for minimal non-linearity - Convergence curve

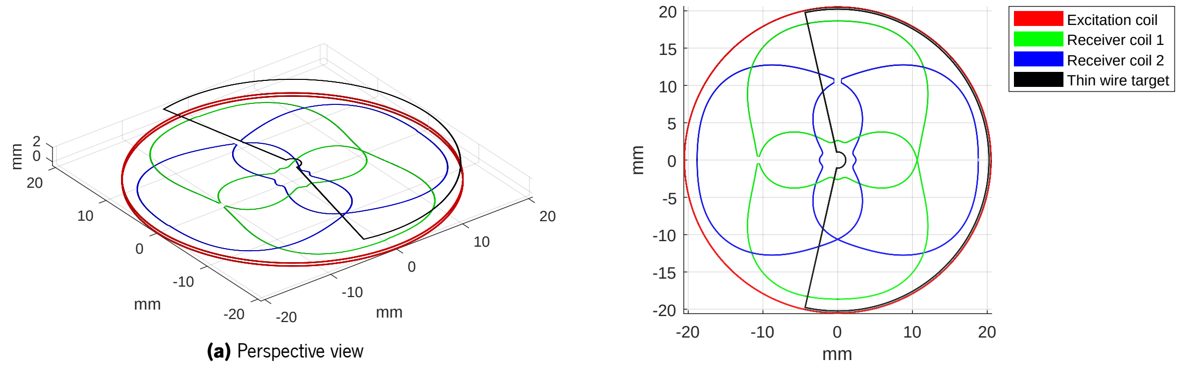

(a) Perspective view

(b) Top view

Figure 4.35: APS optimized for minimal non-linearity - Geometry 3

For the settings chosen for each GA parameter, the GA population, like the receiver's coils induced current optimization, consists of 100 individuals who will evolve over 70 generations. The non-dimensionalized standard deviation mutation and elitism ratio are again adjusted at $1/30$ and $1/2$, respectively. The only difference is that the mutation probability is set to $1/6$. This ensures that on average, one gene per chromosome gets modified since there are six genes per chromosome (six optimizable parameters per individual or geometry).

The optimization tool took approximately 142 wall time hours on the same workstation used to optimize *Geometry 2*, and *Geometry 3* with the specifications mentioned in this subsection was obtained. Figure 4.34 depicts the convergence curve, which shows the evolution of the best individual's fitness value (highest non-linearity) over 70 generations, and Figure 4.35 depicts the optimized geometry, *Geometry 3*. Figure 4.35 shows that an unexpected geometry, a more *"squared"* geometry, was achieved. Despite being more *"squared"*, *Geometry 3* has less than half the non-linearity of *Geometry 2*. *Geometry 2* had a maximum non-linearity of 0.663°, while *Geometry 3* had a maximum non-linearity of 0.283°. Note that the convergence curve employs the maximum value among the eight MoM simulations performed within

Table 4.7: APS non-linearity optimization (amplitudes and phases) - GA parameters

Geometry	Population	Mutation Probability	Non-dimensionalized standard deviation mutation
4.1	50	1/10	1/30
4.2	100	1/10	1/30
4.3	150	1/10	1/30
4.4	50	1/100	1/30
4.5	100	1/100	1/30
4.6	150	1/100	1/30
4.7	50	1/1000	1/30
4.8	100	1/1000	1/30
4.9	150	1/1000	1/30
4.10	50	1/1000	1/10
4.11	100	1/1000	1/10
4.12	150	1/1000	1/10

the fitness function. The non-linearity values shown here are the true maximum values. This explains the discrepancy between the non-linearity of the convergence curve and the non-linearity presented here. The same goes for the following subsections.

4.6.2.3 APS non-linearity optimization (amplitudes and phases)

This subsection discusses another optimization that takes the same geometry, *Geometry 2*, as a starting point and the same fitness parameter, the sensor's maximum non-linearity. The only changes in the fitness function are the total number of MoM simulations performed for each fitness function execution, which is 16 instead of the eight used in *Geometry 3*, and the addition of four more optimizable parameters. This allows the adjustment of the initial phase of the receiver's coils' third and fifth harmonics. By introducing those changes, the four additional optimizable parameters and twice the MoM simulations extend the optimization processing time. However, as demonstrated later, it can discover a better solution with a substantially smaller maximum non-linearity. Along with those changes, and differently from the previous section, there are 12 specific optimizations named *Geometry 4.1* to *Geometry 4.12*. These optimizations have the same fitness function but different GA parameters, namely mutation probability, non-dimensionalized standard deviation mutation and population. The other two GA parameters, the elitism ratio and the total number of generations that the population will evolve, are the same across all optimizations, and they are set to 1/2 and 100, respectively. Briefly stated, Table 4.7 contains all GA parameters for all geometric optimizations.

Table 4.8: APS optimization using MoM - Limits, initial and optimized parameters for non-linearity optimization (amplitudes and phases)

	Receiver coil	Harmonic	Initial Geometry 2	Minimum	Maximum	Optimized Geometry 4.2
Amplitudes	1	0	0.000 mm	-19.250 mm	19.250 mm	0.003 mm
		1	19.250 mm	-	-	18.695 mm
		3	0.000 mm	-19.250 mm	19.250 mm	0.232 mm
		5	0.000 mm	-19.250 mm	19.250 mm	-0.154 mm
	2	0	0.000 mm	-19.250 mm	19.250 mm	-0.003 mm
		1	19.250 mm	-	-	18.379 mm
		3	0.000 mm	-19.250 mm	19.250 mm	0.570 mm
		5	0.000 mm	-19.250 mm	19.250 mm	-0.133 mm
Phases	1	3	0°	-90°	90°	7.440°
		5	0°	-90°	90°	-4.131°
	2	3	0°	-90°	90°	4.732°
		5	0°	-90°	90°	13.301°

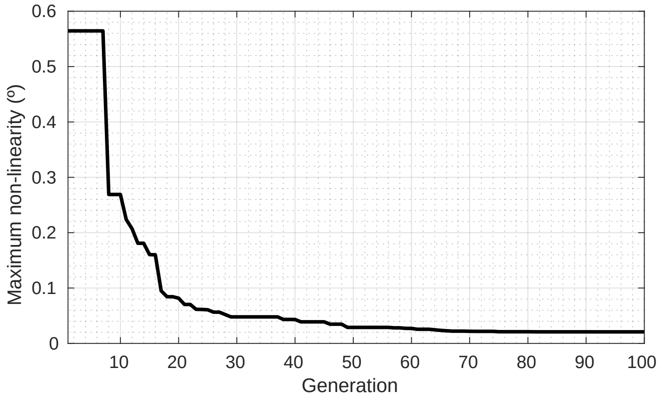

Figure 4.36: APS optimized for minimal non-linearity - Convergence curve

The optimization tool required approximately an average of 107, 213 and 321 wall time hours to work with a population of 50, 100 and 150, respectively, on a high-end 2020 workstation with 128 GB of RAM to optimize *Geometry 2*, and obtain the respective optimized geometry with the specifications listed in this subsection. Figure 4.36 depicts the convergence curve of the best geometric optimization, *Geometry 4.2*, among the 12, which shows the evolution of the best individual's fitness value (highest non-linearity) over 100 generations. Figure 4.37 depicts the respective optimized geometry. As a result, *Geometry 4.2* achieved 0.021° of maximum non-linearity, saying that *Geometry 4.2* has non-linearity reduced by 32 times when compared to *Geometry 2*, which has 0.663° of maximum non-linearity. Table A.1 in Appendix A shows the geometric results (the values of the optimizable parameters) for all 12 optimized geometries, and the non-linearity values are depicted in Table A.2.

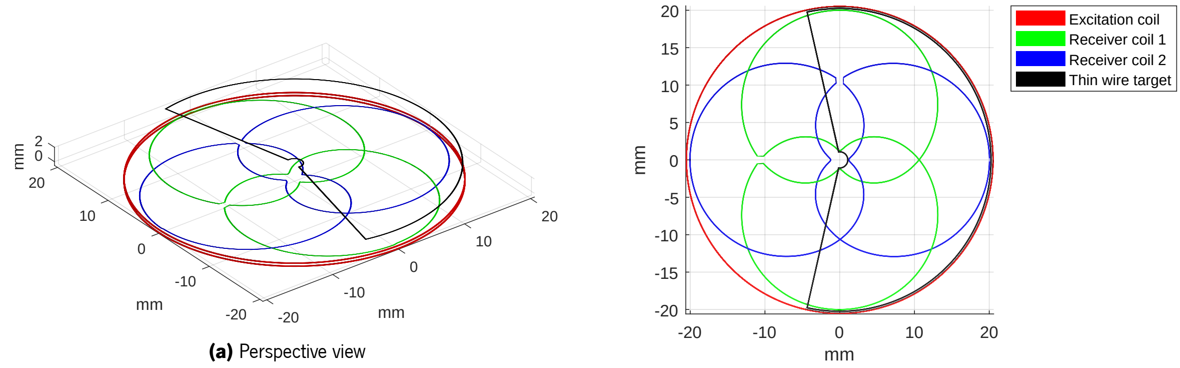

(a) Perspective view

(b) Top view

Figure 4.37: APS optimized for minimal non-linearity - Geometry 4.2

Table 4.9: APS optimization using MoM - Limits, initial and optimized parameters for harmonic content optimization

	Receiver coil	**Harmonic**	**Initial Geometry 2**	**Minimum**	**Maximum**	**Optimized Geometry 5**
Amplitudes	1	0	0.000 mm	-19.250 mm	19.250 mm	0.002 mm
		1	19.250 mm	-	-	18.629 mm
		3	0.000 mm	-19.250 mm	19.250 mm	0.350 mm
		5	0.000 mm	-19.250 mm	19.250 mm	0.105 mm
	2	0	0.000 mm	-19.250 mm	19.250 mm	-0.003 mm
		1	19.250 mm	-	-	18.611 mm
		3	0.000 mm	-19.250 mm	19.250 mm	0.333 mm
		5	0.000 mm	-19.250 mm	19.250 mm	-0.138 mm
Phases	1	3	0°	-90°	90°	3.462°
		5	0°	-90°	90°	-18.951°
	2	3	0°	-90°	90°	3.330°
		5	0°	-90°	90°	89.994°

4.6.2.4 APS harmonic content optimization

Another strategy to minimize the sensor non-linearity involves reducing the amplitude of the harmonics present in the receiver coils' signals. Essentially, this approach uses the same initial geometry (*Geometry 2*) the same optimizable parameters, upper and lower limits values, and GA configurations as *Geometry 4.2*. The only difference is the fitness function that uses the harmonic content instant of maximum non-linearity as a fitness value. In this optimization, the fitness value is calculated by adding the continuous component and the third and fifth harmonics amplitudes of the two receiver's coils signals together. As previously stated, the goal is to reduce the continuous component and the third and fifth harmonics amplitudes in the receiver's coils' signals and, consequently, the sensor's non-linearity.

Using the same workstation, the optimization procedure took around 394 wall time hours. Figure 4.38

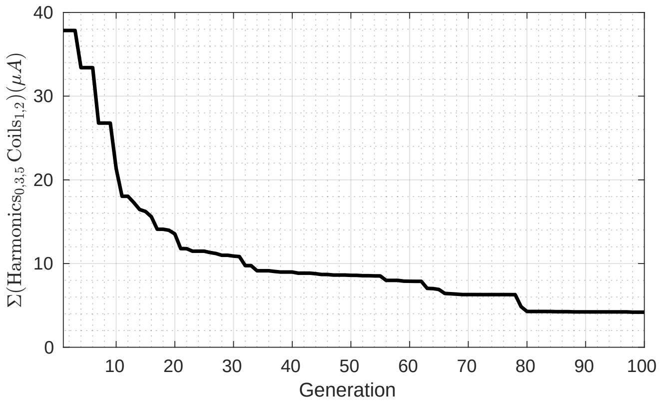

Figure 4.38: APS optimized for minimal harmonic content - Convergence curve

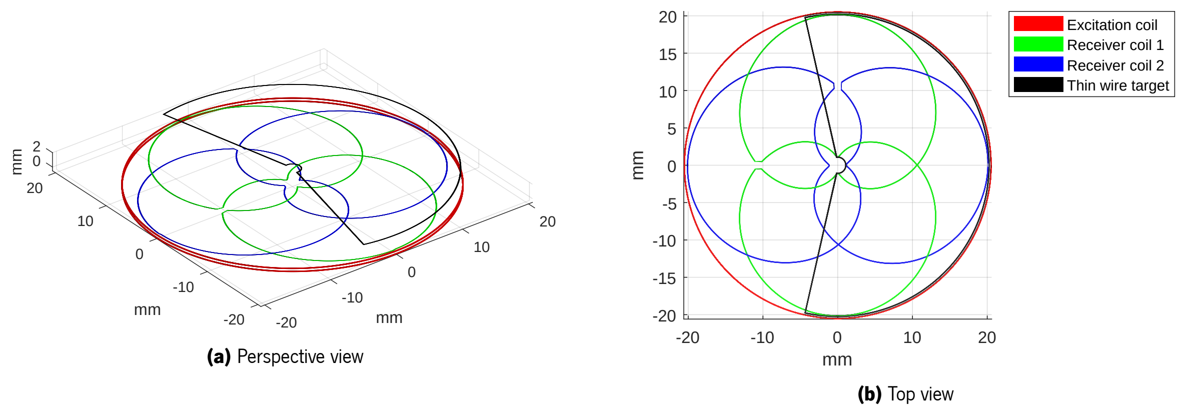

(a) Perspective view

(b) Top view

Figure 4.39: APS optimized for minimal harmonic content - Geometry 5

depicts the convergence curve, which illustrates the best individual's fitness value (harmonic content) evolution over 100 generations, and Figure 4.39 depicts the optimized geometry, *Geometry 5*. As a result, *Geometry 5* achieved 0.130° of maximum non-linearity, suggesting that *Geometry 5* has five times less than *Geometry 2*, which has 0.663° of maximum non-linearity.

4.6.2.5 APS coil's geometry comparison

The APS sensor's optimization results are compared in this subsection. Figure 4.40 depicts the non-linearity curves for *Geometries 1*, *2*, *3*, *4.2* and *5* in a single graph. It is clear that the geometry with the lowest non-linearity is *Geometry 4.2*. Knowing that *Geometries 4.2* and *5* have the same GA settings and optimizable parameters, being the only difference in the fitness parameter, it can be concluded that using the maximum non-linearity value as fitness is more advantageous than using harmonic content, as utilized in obtaining *Geometry 5*.

Figures 4.41a and 4.41b display geometry distortion by illustrating the geometry of the receiver's coils 1

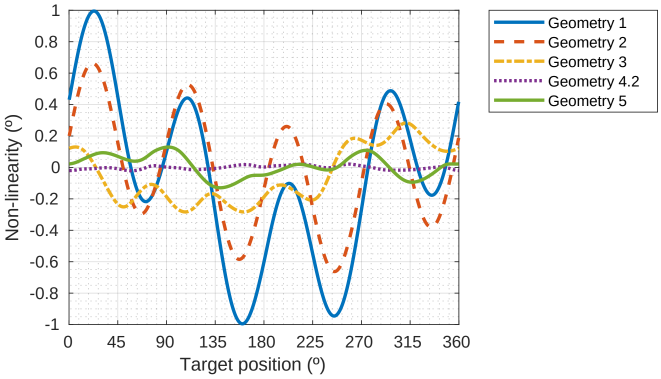

Figure 4.40: Non-linearity

and 2 in a straight line (by opening the circle), respectively. Figures 4.41c and 4.41d depict the geometric harmonic content of the receiver's coils 1 and 2 designs. Observing it and relating it with the non-linearity results from Figure 4.40 revealed that including harmonic distortion into the receiver's coil design can lower the sensor's non-linearity. Also, in the same figures, the geometry with the highest harmonic distortion is *Geometry 3*. However, even with this distortion, *Geometry 3* presents significantly less non-linearity than sensors from *Geometries 1* and *2*.

Figure 4.42 illustrates the signals from the receiver's coils from *Geometries 1*, *2*, *3*, *4.2* and *5* and their corresponding harmonics content. Figures 4.42a and 4.42b are the induced current over the angular target position for the receiver's coils 1 and 2. Figures 4.42c and 4.42d are their respective harmonic content. Looking at Figures 4.42c and 4.42d, it is clear that while *Geometry 5* has the lowest harmonic content, *Geometry 4.2* has the lowest non-linearity.

In this inductive sensor type, it is common to apply some correction to the signals coming from the receiver's coils to reduce the sensor's non-linearity. Usually, these corrections consist of continuous component removal, normalization and orthogonality correction of the receiver coil signals. Figure 4.43 depicts the non-linearity after applying these three corrections to *Geometries 1*, *2*, *3*, *4.2* and *5*. By observing it, *Geometries 3* and *4.2* are the only ones whose corrections have the opposite effect. Their non-linearity increases, which was also unexpected. This non-linearity increase means that the unique combination of these harmonics in terms of amplitude and phase reduces non-linearity, implying that any change could increase non-linearity, even if the changes are a harmonic amplitude reduction. Analyzing Figure 4.43, the geometry with the lowest non-linearity after applying these corrections is *Geometry 5*, which is not surprising given that the optimization goal was to reduce the continuous component and the third and fifth harmonics. These corrections only helped reduce the non-linearity by further reducing the

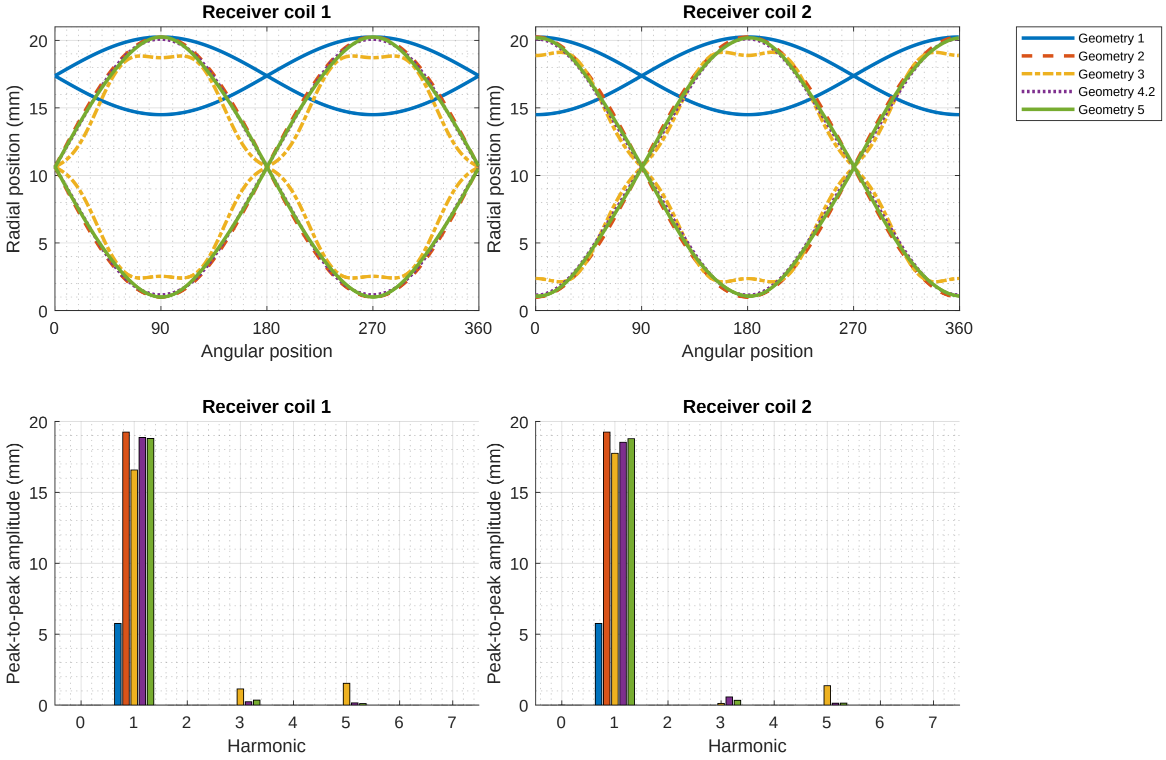

Figure 4.41: Geometric deformation

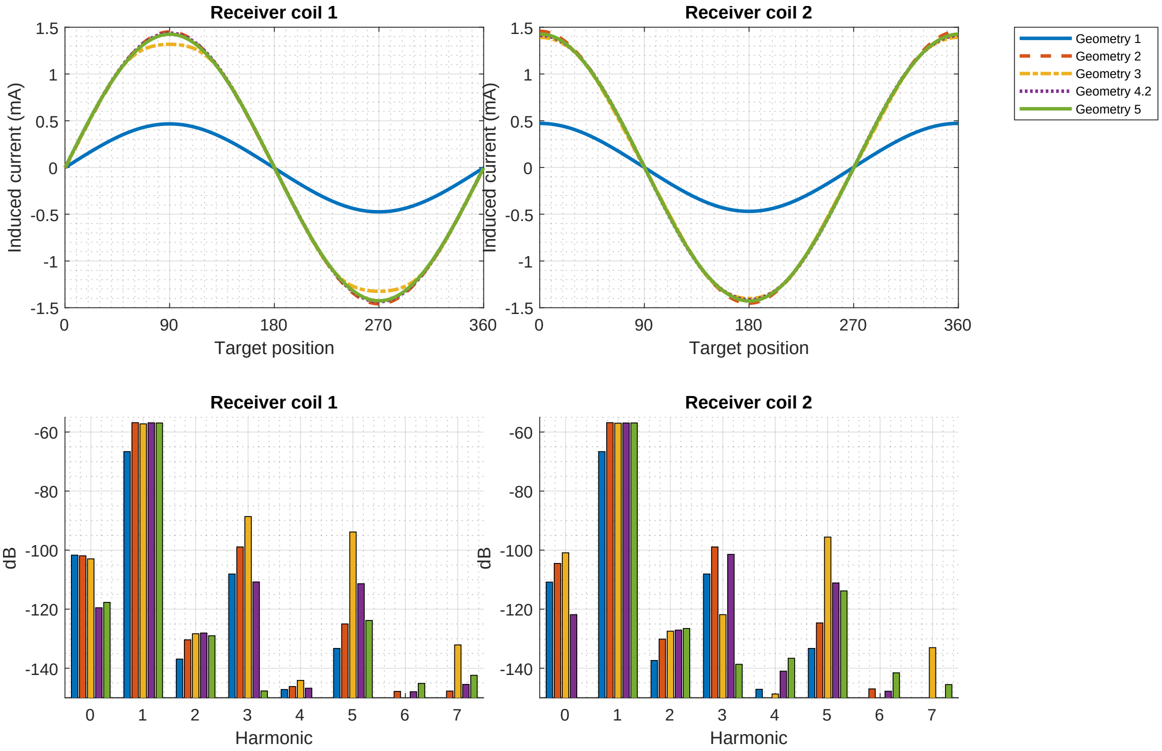

Figure 4.42: Induced current

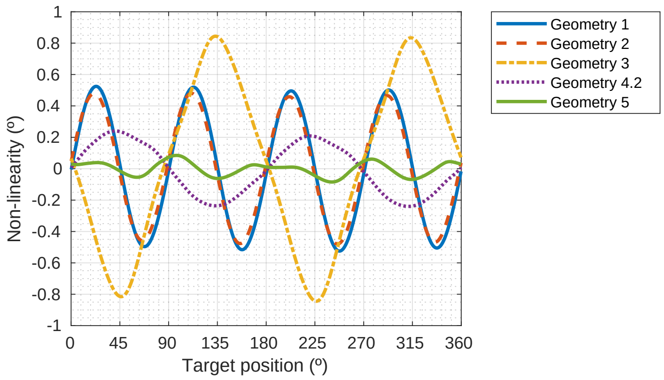

Figure 4.43: Non-linearity after applying continuous component removal, amplitude normalization and orthogonality correction to both receiver's coils' signals

continuous component.

Table A.2 resumes all the results obtained by combining the essential data from all 14 geometries, namely, the highest peak-to-peak induced current, the maximum sensor non-linearity with and without receiver's coils' signals corrections, and the amplitude of the continuous and fundamental components as well as the third and fifth harmonics. By observing this table, it is clear that *Geometry 5* has less harmonic content than *Geometry 4.2* in its receiver's coils' signals. However, *Geometry 4.2*, even having a considerable harmonic content, is the geometry that presents the lowest non-linearity of all geometries. On the other hand, *Geometry 5* has the lowest non-linearity when the continuous component removal, normalization, and orthogonality correction are applied to both receiver's coils' signals.

4.6.3 Optimization using the FHM

This section presents a summary of the key results achieved using the optimization tool implemented with the FHM to solve electromagnetic field equations, the optimization tool developed in this thesis. Initially, the optimization tool was employed to optimize the same APS sensor used in the previous section (Section 4.6.2). This was done to compare the results derived from both the MoM and the FHM methods, thereby facilitating a direct comparison. Subsequently, the optimization tool implementing the FHM was employed to optimize a LIPS sensor.

As previously stated, this new suggested tool employs the GA in conjunction with a FHM to solve field equations and improve the sensor's coil design. As an example of its performance, on a 2018 laptop with 8 GB of RAM, the FHM took 26 seconds to run 256 successive simulations of a geometry composed of four coils (one excitation coil, two receiver's coils and one target coil), making a total of 2537 thin-wire

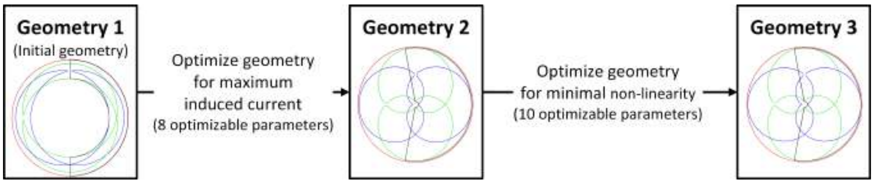

Figure 4.44: Optimization flowchart

elements. On the other hand, the MoM to do the same simulations took 299 seconds, which means that the FHM was at least 11 times faster than MoM under these conditions. It is essential to mention that the FHM was truncated at the twelve harmonic reducing the impedance matrix Z from 2537×2537 to 100×100 elements. Nevertheless, with this configuration, the maximum discrepancy of the receiver's coils induced current of the FHM compared with the MoM was approximately 0.16%.

As a side note, all simulations described in this section using the FHM were truncated at the twelve harmonic. The detailed description and individual results of each optimization are provided in the following subsections.

4.6.3.1 APS

This section focuses on evaluating the results obtained by applying the FHM-based optimization tool to the APS sensor. The tool was employed to optimize the geometry from Section 4.6.2 (Figure 4.31), which consists of an excitation coil, two receiving coils, and a target coil, with a 360°measurement range. The primary objectives remained the same: to maximize the induced current in both receiver coils and minimize the APS non-linearity. To achieve this, the optimization process was again divided into two iterations.

The first iteration used the optimization tool to optimize the sensor's geometry, aiming to maximize the induced current in both receiver coils. In the second iteration, the optimized geometry from the first iteration was used as a starting point to minimize the sensor's non-linearity with the same optimization tool. Figure 4.44 provides an illustration of the optimization procedure.

Geometry 1, depicted in Figure 4.31, represents the initial human-made geometry (the same as in Section 4.6.2) used as a starting point for maximizing induced current. *Geometry 2* is the outcome of the geometry optimization process, and *Geometry 3* is the optimized version of *Geometry 2* when maximum non-linearity is utilized as a fitness parameter to be optimized.

Table 4.10: APS optimization using FHM - Limits and initial parameters for induced current maximization

Optimizable parameters				
Description	**Initial Geometry 1**	**Minimum**	**Maximum**	**Optimized Geometry 2**
Turns in the excitation coil	1	1	3	1
Layers in the excitation coil	4	1	4	4
Gap between turns of excitation coil	335.000 µm	165.000 µm	1.000 mm	587.096 µm
Excitation coil inner radius	21.500 mm	1.000 mm	50.000 mm	20.433 mm
Receiver coils' innermost radius	14.500 mm	1.000 mm	50.000 mm	1.000 mm
Target inner radius	14.500 mm	1.000 mm	50.000 mm	1.000 mm
Target outer radius	21.750 mm	1.000 mm	50.000 mm	20.205 mm
Target angular wing size	180.000°	0.000°	360.000°	201.362°

4.6.3.2 APS peak-to-peak induced current optimization

This subsection details the use of the optimization tool to generate a geometry that maximizes the induced current in the sensor receiver coils. As mentioned earlier, this process starts with *Geometry 1* as the initial point, followed by the selection of geometric parameters that will be fixed and those that will be optimizable, along with their upper and lower limits for the optimizable parameters. Similar to Section 4.6.3.2, the fixed geometric parameters include the PCB trace width, copper thickness, layers stack, receiver coils' outermost radius, and the conductive target airgap.

The optimizable parameters consist of eight elements: the total number of turns in the excitation coil in each layer, the total number of layers composing the excitation coil, the gap between the excitation coil's turns' traces, the excitation coil's inner radius, the receiver coils' innermost radius, the target coil's inner and outer radius, and the target's angular size. Table 4.5 summarizes these parameters and presents the upper and lower limits, along with the initial values of the optimizable parameters used in *Geometry 1*. Note that the fixed and optimizable parameters are all the same as in Section 4.6.3.2.

The fitness function comprises FHM simulations, wherein the APS's coils are immersed in a medium with a relative electrical permittivity and relative magnetic permeability of one, as in Section 4.6.3.2. The excitation coil is powered by a differential potential of 0.7071 V_{RMS} at 10.7 MHz, with the maximum induced current in the receiver coils serving as the fitness value. Two FHM simulations were performed, positioning the target 180° apart in the two areas where the induced current is maximum. The fitness value is calculated by adding the two maximum values (peak-to-peak). Additionally, the fitness function sets the value to zero if the optimizable geometric parameters result in an impossible geometry or if the

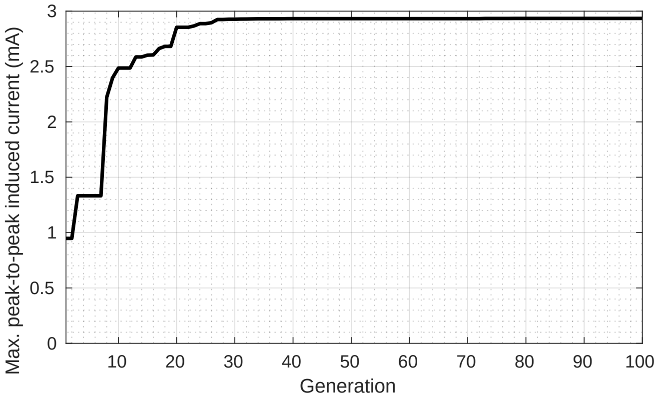

Figure 4.45: APS optimized for maximum induced current - Convergence curve

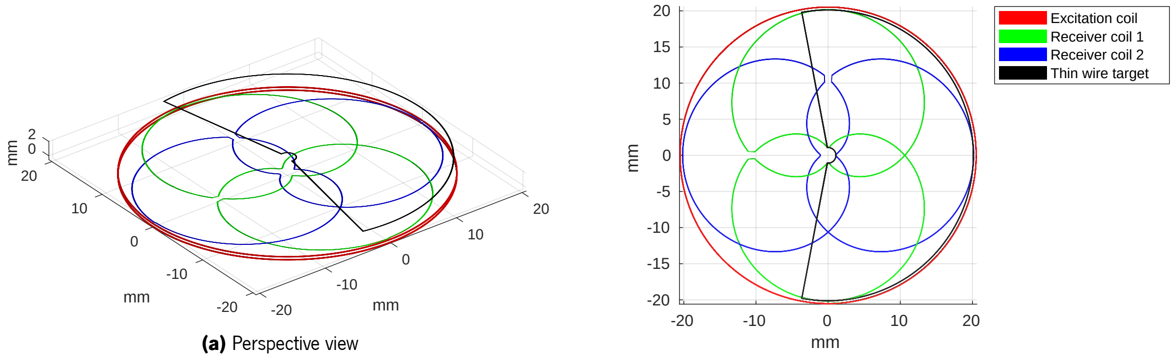

(a) Perspective view

(b) Top view

Figure 4.46: APS optimized for maximum induced current - Geometry 2

excitation current exceeds a threshold value, which was set to 7.071 mA$_{RMS}$.

Finally, the GA parameters are configured for a population of 100 individuals that will evolve over 100 generations with a mutation probability of $1/8$. The non-dimensionalized standard deviation mutation is $1/30$, and the elitism ratio is $1/2$, with the exact same parameters as in Section 4.6.3.2.

With the optimization tool fully configured as described, the optimization process took approximately 2.4 wall time hours to optimize *Geometry 1* and obtain *Geometry 2* on a high-end 2014 workstation with 64 GB of RAM. Figure 4.45 displays the convergence curve, which illustrates the evolution of the best individual's fitness value (highest peak-to-peak induced current) over 100 generations, and Figure 4.46 shows the optimized geometry, *Geometry 2*.

Geometry 2 achieved a fitness value of 2.934 mA (peak-to-peak), while *Geometry 1* reached 0.941 mA (peak-to-peak), indicating that *Geometry 2* has approximately three times stronger induction current than *Geometry 1*. Furthermore, when compared with the optimization using the MoM (Section 4.6.3.2), where the initial geometry, GA configurations, and all fixed and optimizable parameters are identical (including

Table 4.11: APS optimization using FHM - Limits, initial and optimized parameters for non-linearity optimization (amplitudes and phases)

	Receiver coil	**Harmonic**	**Initial Geometry 2**	**Minimum**	**Maximum**	**Optimized Geometry 3**
Amplitudes	1	0	0.000 mm	-19.250 mm	19.250 mm	0.000 mm
		1	19.250 mm	-	-	18.627 mm
		3	0.000 mm	-19.250 mm	19.250 mm	0.458 mm
		5	0.000 mm	-19.250 mm	19.250 mm	0.000 mm
	2	0	0.000 mm	-19.250 mm	19.250 mm	0.000 mm
		1	19.250 mm	-	-	18.637 mm
		3	0.000 mm	-19.250 mm	19.250 mm	0.448 mm
		5	0.000 mm	-19.250 mm	19.250 mm	0.000 mm
Phases	1	3	0°	-90°	90°	6.235°
		5	0°	-90°	90°	6.998°
	2	3	0°	-90°	90°	6.289°
		5	0°	-90°	90°	-14.089°

the upper and lower limits for optimizable parameters), the obtained maximum peak-to-peak induced current values were similar. In Section 4.6.3.2, the maximum peak-to-peak induced current was 2.908 mA, and in this section, it was 2.934 mA.

However, the optimization using the MoM took approximately 14 wall time hours, while the FHM took around 2.4 wall time hours, making it almost six times faster. This significant reduction in optimization time highlights the efficiency of the FHM in comparison to the MoM for this specific application. Consequently, the results demonstrate that FHM-based optimization is a highly effective and time-saving approach for designing APS sensors with enhanced performance.

4.6.3.3 APS non-linearity optimization (amplitudes and phases)

In this section, the main objective was to minimize the maximum non-linearity in *Geometry 2* subsequent to the optimization of the induced current in the receiver coils. The starting point was *Geometry 2*, which exhibits a maximum non-linearity of 0.593°. Like in the Section 4.6.3.3, a geometric harmonic distortion was created in the continuous component and in third and fifth harmonics to counterbalance the presence of those on the receiver's coil signal. Table 4.11 delineates the optimization parameters, including their initial values and upper and lower limits. It is worth noting that the fundamental harmonic amplitude was lowered proportionally to accommodate the existence of the additional harmonics and avoid geometric constraints.

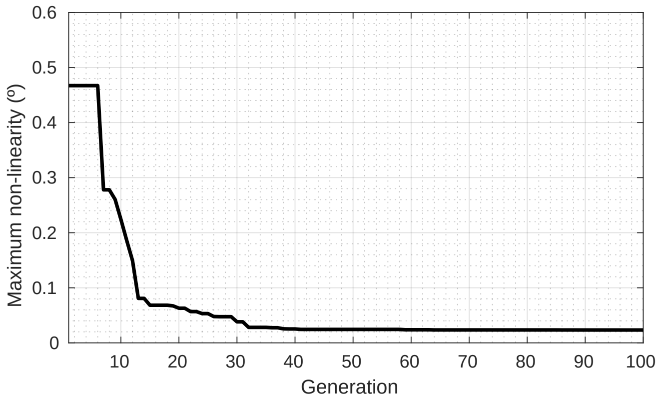

Figure 4.47: APS optimized for minimal non-linearity - Convergence curve

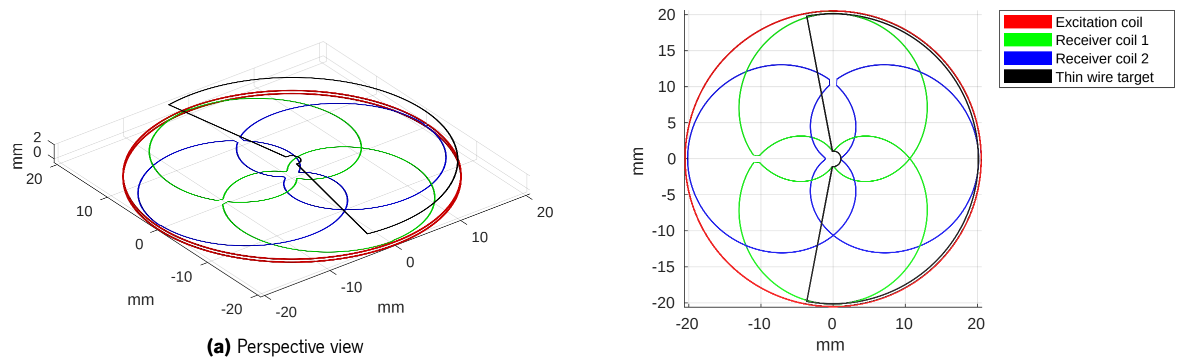

(a) Perspective view

(b) Top view

Figure 4.48: APS optimized for minimal non-linearity - Geometry 3

For the fitness value, the maximum non-linearity that the sensor can display in a single complete turn was employed. The fitness function involves the execution of 16 FHM simulations, with each simulation featuring an angularly equidistant target position. It is also important to note that the sensor's zero location was chosen such that the maximum non-linearity was as minimal as feasible. This was accomplished by subtracting the average non-linearity value from all non-linearity values.

The GA population, akin to the receiver coils induced current optimization, comprises 100 individuals who evolve over 100 generations. The non-dimensionalized standard deviation mutation and elitism ratio were set to $1/30$ and $1/2$, respectively, with a mutation probability of $1/6$.

The optimization process took approximately 19 wall time hours on a high-end 2020 workstation equipped with 128 GB of RAM. The convergence curve of the best geometric optimization, *Geometry 3*, is illustrated in Figure 4.47, which presents the evolution of the best individual's fitness value (lowest non-linearity) across 100 generations. Figure 4.48 portrays the optimized geometry. As a result, *Geometry 3* achieved a maximum non-linearity of 0.023°, representing a 26-fold reduction when compared to *Geometry 2*'s

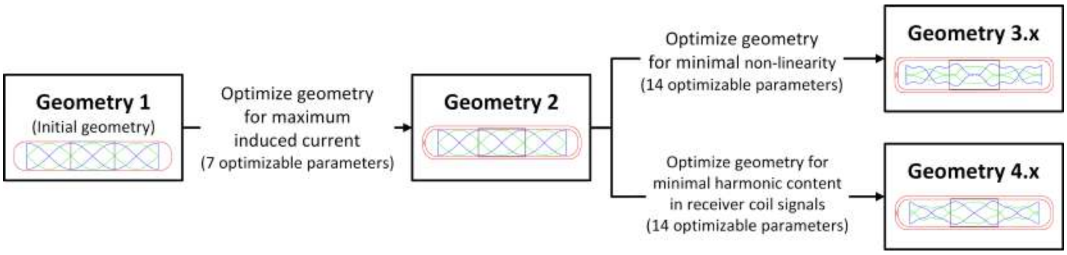

Figure 4.49: Optimization flowchart

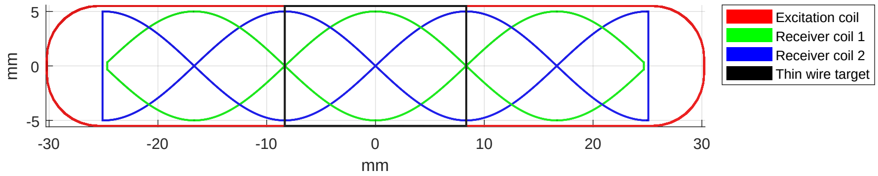

Figure 4.50: Linear position sensor initial geometry - Geometry 1

0.593°. In comparison with the MoM implementation (Section 4.6.3.3), the maximum non-linearity values were similars. Using the MoM, the maximum non-linearity reached 0.021°, while the FHM achieved 0.023°. However, the MoM implementation required 213 wall time hours, whereas the FHM implementation took only 19 wall time hours, rendering it eleven times faster. Note that the initial geometry, GA configurations, and all fixed and optimizable parameters are identical (including the upper and lower limits for optimizable parameters).

4.6.3.4 LIPS

This section focuses on the study of the results obtained from the application of the FHM to the LIPS sensor. The optimization tool was used to optimize the geometry of a full-scale linear position sensor (LIPS) with a measurement range of 33.3 mm, consisting of one excitation coil, two receiver coils, and one target coil. The excitation coil and both receiver coils are printed on the same PCB, defined as the *stator*, while the target coil is printed on a different PCB identified as the *target*. The goals were to optimize the induced current in both receiver coils while minimizing the sensor's non-linearity. To accomplish this, the optimization process was divided into two iterations. The first iteration employs the FHM tool to adjust the sensor's coils design to maximize the induced current in both receiver coils. The second iteration uses the same optimization tool to decrease the sensor's non-linearity, taking the optimized geometry from the previous iteration as a starting point. Furthermore, the second iteration was performed 28 times with different fitness functions and GA parameters. These multiple optimizations aim to find which fitness functions and GA parameters best match the objective in terms of convergence and geometric solutions.

The optimization procedure described here is schematized in Figure 4.49, where *Geometry 1* is the initial human-made geometry suitable for producing acceptable results. Its geometry is depicted in Figure 4.50 and is used as the starting point for induced current optimization. After running the optimization, *Geometry 2* was obtained. *Geometries 3.1* through *3.12* are optimized versions of *Geometry 2*, where the maximum non-linearity was used as a fitness parameter to be optimized. The maximum non-linearity fitness value is calculated by selecting the highest value from the 32 induced current simulations, one for each equally spaced target position. This fitness function was used for all 12 geometries. The only change is the GA parameters applied to each one of the geometries.

Geometries 4.1 to *4.12* start with the same geometry and optimizable parameters as *Geometries 3.x*. Once again, the GA settings follow the same rule as in *Geometries 3.x* (all 12 geometries have different GA settings). The only change is the fitness parameter, which is the harmonic content of the two receivers' coil signals. The aim is to minimize the harmonic content and, consequently, the sensor non-linearity.

4.6.3.5 LIPS peak-to-peak induced current optimization

The optimization tool is used in this subsection to design a geometry that maximizes the induced current in the sensor receiver's coils. As previously indicated, *Geometry 1* serves as the starting point for this process, in which it is required to choose which geometric parameters will be fixed and which will be optimizable. Correspondingly, their upper and lower limits for the case of optimizable parameters. As in the previous section, the PCB trace width, PCB copper thickness, PCB layers stack, receiver coil length and width, and target airgap (airgap space between the sensor and target PCBs) were chosen as fixed geometric characteristics. Seven parameters were chosen to be optimized: the total number of turns in the excitation coil in each layer, the total number of layers that comprise the excitation coil, the gap between the traces of the excitation coil's turns, the length and width of the excitation coil (the length and width of the innermost turn), and the length and width of the target's coil. Table 4.12 resumes these parameters and includes the upper and lower limits of each one, as well as the initial values of the optimizable parameters employed in *Geometry 1* (initial geometry).

In addition to selecting and setting the fixed and optimizable parameters, the fitness function and GA parameters must be coded and configured. The fitness function performs field simulations where the coils of the LIPS (the excitation coil, the two receiver coils, and the target coil) are submerged in a medium with a relative electrical permittivity and a relative magnetic permeability of one. In addition, the excitation

Table 4.12: LIPS optimization using FHM - Limits and initial parameters for induced current maximization

Fixed parameters	
Description	**Value**
PCB trace width	165.000 μm
PCB copper thickness	18.000 μm
Thickness between PCB layers 1 and 2	70.000 μm
Thickness between PCB layers 2 and 3	320.000 μm
Thickness between PCB layers 3 and 4	70.000 μm
Receiver coils' lenght	50.000 mm
Receiver coils' width	10.000 mm
Target airgap	2.000 mm
Frequency of the excitation coil's power source	10.700 MHz
Voltage of the excitation coil's power source	707.107 mV$_{RMS}$
Maximum current of the excitation coil's power source	7.071 mA$_{RMS}$

Optimizable parameters				
Description	**Initial Geometry 1**	**Minimum**	**Maximum**	**Optimized Geometry 2**
Turns in the excitation coil	1	1	3	2
Layers in the excitation coil	4	1	4	2
Gap between turns of excitation coil	335.000 μm	165.000 μm	1.000 mm	1.000 μm
Excitation coil inner lenght	51.000 mm	50.660 mm	101.320 mm	50.660 mm
Excitation coil inner width	11.000 mm	10.660 mm	21.320 mm	10.660 mm
Target lenght	16.667 mm	1.000 mm	50.000 mm	18.386 mm
Target width	11.000 mm	1.000 mm	21.320 mm	11.042 mm

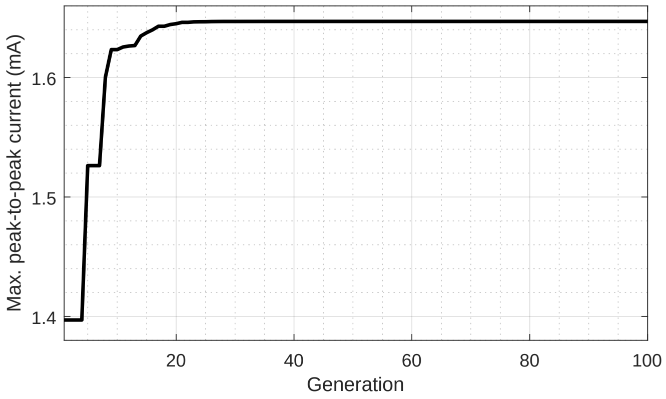

Figure 4.51: Linear position sensor optimized for maximum induced current - Convergence curve

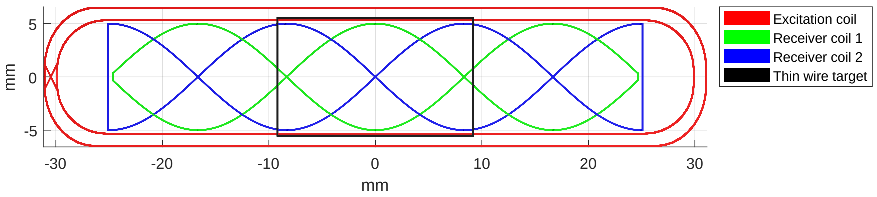

Figure 4.52: Linear position sensor optimized for maximum induced current - Geometry 2

coil is driven by an alternate current at 10.7 MHz with a differential potential of 0.7071 V_{RMS}, being the highest induced current on the receiver's coils used to compute the fitness value. This highest induced current is taken by placing the target in the two locations where its induced current difference is maximum, which are separated by 16.67 mm. The fitness value is then calculated by summing the two maximum values (peak-to-peak). Also, the fitness function sets the fitness value to zero if the optimizable geometric parameters result in a physically impossible geometry or if the excitation current crosses the threshold value of 7.071 mA_{RMS}.

Finally, the GA parameters are set to generate a population of 100 individuals that will evolve over 100 generations with a mutation probability of 1/7. This setting implies that on average one gene per chromosome will be modified, as there are a total of seven genes per chromosome, which represent seven optimizable parameters per individual or geometry. The non-dimensionalized standard deviation mutation is set to 1/30, and the elitism ratio is set to 1/2. This 1/2 elitism ratio indicates that half of the previous generation's top individuals will be part of the next generation.

On a high-end 2020 workstation with 128 GB of RAM, the optimization procedure took approximately 1.40 wall time hours to optimize *Geometry 1* and obtain *Geometry 2*. Figure 4.51 depicts the optimization convergence curve, which shows the evolution of the best individual's fitness value (highest peak-to-peak induced current) over 100 generations, and Figure 4.52 illustrates the optimized geometry, *Geometry*

Table 4.13: LIPS optimization using FHM - Limits, initial and optimizable parameters for non-linearity optimization (amplitudes and phases)

	Receiver coil	**Harmonic**	**Initial Geometry 2**	**Minimum**	**Maximum**	**Optimized Geometry 3.5**
Amplitudes	1	0	0.000 mm	-5.000 mm	5.000 mm	-1.250 mm
		1	10.000 mm	-	-	5.790 mm
		2	0.000 mm	-5.000 mm	5.000 mm	-0.989 mm
		3	0.000 mm	-5.000 mm	5.000 mm	0.605 mm
		4	0.000 mm	-5.000 mm	5.000 mm	1.052 mm
		5	0.000 mm	-5.000 mm	5.000 mm	-0.312 mm
	2	0	0.000 mm	-5.000 mm	5.000 mm	0.000 mm
		1	10.000 mm	-	-	7.420 mm
		2	0.000 mm	-5.000 mm	5.000 mm	0.629 mm
		3	0.000 mm	-5.000 mm	5.000 mm	-0.142 mm
		4	0.000 mm	-5.000 mm	5.000 mm	-1.758 mm
		5	0.000 mm	-5.000 mm	5.000 mm	-0.050 mm
Phases	1	2	0°	-90°	90°	5.114°
		3	0°	-90°	90°	9.639°
		4	0°	-90°	90°	0.767°
		5	0°	-90°	90°	11.539°
	2	2	0°	-90°	90°	89.761°
		3	0°	-90°	90°	-8.418°
		4	0°	-90°	90°	85.046°
		5	0°	-90°	90°	34.794°

2. The optimized geometry, *Geometry 2*, achieved a fitness value of 1.647 mA (peak-to-peak), whereas *Geometry 1* presents 1.397 mA (peak-to-peak), indicating that *Geometry 2* has a slightly stronger induction current than *Geometry 1*.

4.6.3.6 LIPS non-linearity optimization

After optimizing the induced current in the receiver's coils, the next iteration is to lower the sensors' maximum non-linearity. As a starting point, *Geometry 2*, with a maximum non-linearity of 16.47 mm, is used. The aim is to determine if the optimization tool can find a solution that significantly minimizes sensor non-linearity by inserting some harmonic distortion into the design of the receiver's coils and modifying the curvature of the excitation coil. Because the signals from the receiver's coil had a considerable harmonic amplitude in the continuous component and the first harmonics, the geometric harmonic distortion was constructed by using the continuous component and the second to fifth harmonics. With this, a geometric harmonic distortion to counterbalance the presence of some harmonics on the receiver's coil signal was created. In addition, the fundamental component of the two receiver's coil geometries is also a set of parameters to be modified by the optimizer tool. It allows for rectifying the amplitudes discrepancy between the two induced signals. It is worth mentioning that the optimizable parameters are amplitudes of the continuous and fundamental components, amplitudes and phases of the second to fifth harmonics, and the curvature of the excitation coil. Table 4.13 shows the parameters, including their initial values as well as their upper and lower limits.

The maximum non-linearity the LIPS sensor can have in a single passage was used as the fitness value. For this, 32 simulations in the fitness function were executed, with the target position in each equally separated. The sensor's linear position was computed using Equation 4.3, where r is the computed position, S is the maximum distance that the target can move on one of the sensor's sides, and α is supplied by Equation 4.4. Where, in Equation 4.4, x and y are the amplitude signals from receiver coils 1 and 2, respectively. The difference between the actual target position and the computed position is characterized as the non-linearity, with the fitness value being the highest non-linearity of the 32 computed positions.

$$r = \frac{S\alpha}{\pi} \tag{4.3}$$

$$\alpha = \begin{cases} \tan^{-1}\left(\frac{y}{x}\right) & , if\ x > 0 \\ \tan^{-1}\left(\frac{y}{x}\right) + \pi & , if\ x < 0\ and\ y \geq 0 \\ \tan^{-1}\left(\frac{y}{x}\right) - \pi & , if\ x < 0\ and\ y < 0 \\ +\frac{\pi}{2} & , if\ x = 0\ and\ y > 0 \\ -\frac{\pi}{2} & , if\ x = 0\ and\ y < 0 \end{cases} \tag{4.4}$$

As previews stated, this iteration was performed 12 times, each with different GA parameters but using the fitness function described above. The optimized geometries were labelled from *Geometry 3.1* to *Geometry 3.12*, and the GA parameters applied in each one are listed in Table 4.14. Where the elitism ratio and the total number of generations that the population will evolve are set to 1/2 and 100, respectively. The other three parameters, mutation probability, non-dimensionalized standard deviation mutation and population, have distinct settings across all optimizations.

Table 4.14: LIPS non-linearity optimization (amplitudes and phases) - GA parameters

Geometry	Population	Mutation Probability	Non-dimensionalized standard deviation mutation
3.1	100	1/20	1/30
3.2	100	1/100	1/30
3.3	100	1/1000	1/30
3.4	100	1/1000	1/10
3.5	200	1/20	1/30
3.6	200	1/100	1/30
3.7	200	1/1000	1/30
3.8	200	1/1000	1/10
3.9	400	1/20	1/30
3.10	400	1/100	1/30
3.11	400	1/1000	1/30
3.12	400	1/1000	1/10

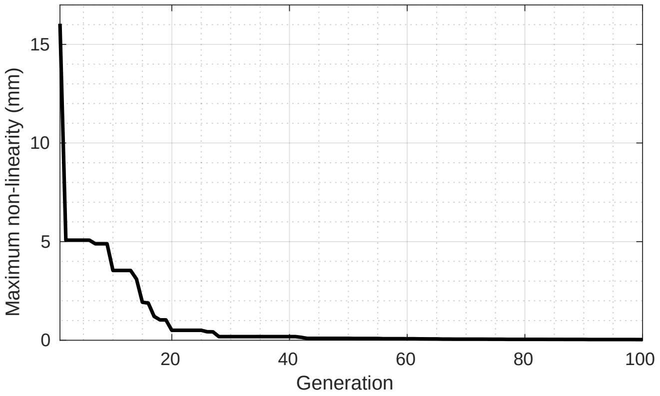

Figure 4.53: Linear position sensor optimized for minimal non-linearity - Convergence curve

With the specifications listed in this subsection, the optimization tool required an average of 9, 18 and 36 wall time hours to work with a population of 100, 200, and 400 individuals, respectively, on a high-end 2020 workstation with 128 GB of RAM to optimize *Geometry 2* and obtain the respective optimized geometry. The convergence curve of the best geometric optimization, *Geometry 3.5*, among the 12, is depicted in Figure 4.53, which displays the evolution of the best individual's fitness value (maximum non-linearity across all 32 simulations) over 100 generations. The optimized geometry is depicted in Figure 4.54. In conclusion, *Geometry 3.5* obtained a maximum non-linearity of 122 µm, which is over 135 times smaller than *Geometry 2*, which has a maximum non-linearity of 16.570 mm. The geometric results (the values of the optimizable parameters) for all 12 optimized geometries are shown in Table A.4 in Appendix A, and the non-linearity values are shown in Table A.6.

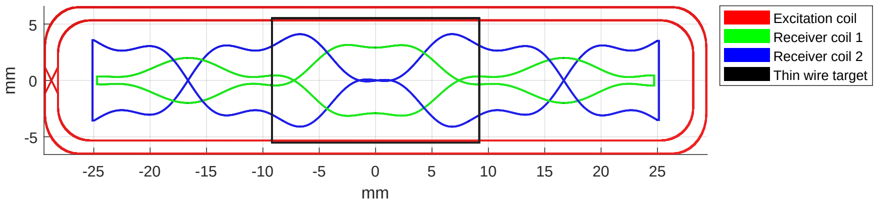

Figure 4.54: Linear position sensor optimized for minimal non-linearity - Geometry 3.5

Table 4.15: LIPS harmonic content optimization - GA parameters

Geometry	Population	Mutation Probability	Non-dimensionalized standard deviation mutation
4.1	100	1/20	1/30
4.2	100	1/100	1/30
4.3	100	1/1000	1/30
4.4	100	1/1000	1/10
4.5	200	1/20	1/30
4.6	200	1/100	1/30
4.7	200	1/1000	1/30
4.8	200	1/1000	1/10
4.9	400	1/20	1/30
4.10	400	1/100	1/30
4.11	400	1/1000	1/30
4.12	400	1/1000	1/10

4.6.3.7 LIPS harmonic content optimization

Another strategy for minimizing sensor non-linearity is described in this subsection. Essentially, this approach uses the same geometry to optimize (*Geometry 2*) the same optimizable parameters, upper and lower limits values, and GA settings as in *Geometries 3.x*. The only difference is the fitness function that uses the harmonic content instead of the maximum non-linearity as a fitness value. In this strategy, the fitness value is calculated by adding the continuous component amplitudes, the second to fifteenth harmonics amplitudes, and the difference between the fundamental components amplitudes of the two receiver's signals together. As previously stated, the goal is to reduce harmonic content in the receiver's coils' signals and, consequently, the sensor's non-linearity.

The optimization process consumed approximately the same amount of wall time hours on the same workstation as the previous optimization (4.6.3.6), which was 9, 18, and 36 hours, to operate with populations of 100, 200, and 400 individuals, respectively. Figure 4.55 depicts the convergence curve of the best geometric optimization, *Geometry 4.5*, among the 12, which illustrates the best individual's fitness

Table 4.16: LIPS optimization using FHM - Limits, initial and optimizable parameters for harmonic content optimization

	Receiver coil	**Harmonic**	**Initial Geometry 2**	**Minimum**	**Maximum**	**Optimized Geometry 4.5**
Amplitudes	1	0	0.000 mm	-5.000 mm	5.000 mm	-1.455 mm
		1	10.000 mm	-	-	6.822 mm
		2	0.000 mm	-5.000 mm	5.000 mm	-0.150 mm
		3	0.000 mm	-5.000 mm	5.000 mm	-0.165 mm
		4	0.000 mm	-5.000 mm	5.000 mm	-0.630 mm
		5	0.000 mm	-5.000 mm	5.000 mm	-0.779 mm
	2	0	0.000 mm	-5.000 mm	5.000 mm	0.014 mm
		1	10.000 mm	-	-	8.010 mm
		2	0.000 mm	-5.000 mm	5.000 mm	-0.714 mm
		3	0.000 mm	-5.000 mm	5.000 mm	0.365 mm
		4	0.000 mm	-5.000 mm	5.000 mm	-0.582 mm
		5	0.000 mm	-5.000 mm	5.000 mm	0.316 mm
Phases	1	2	0°	-90°	90°	-34.179°
		3	0°	-90°	90°	-15.550°
		4	0°	-90°	90°	-7.363°
		5	0°	-90°	90°	6.914°
	2	2	0°	-90°	90°	87.614°
		3	0°	-90°	90°	1.718°
		4	0°	-90°	90°	80.060°
		5	0°	-90°	90°	27.849°

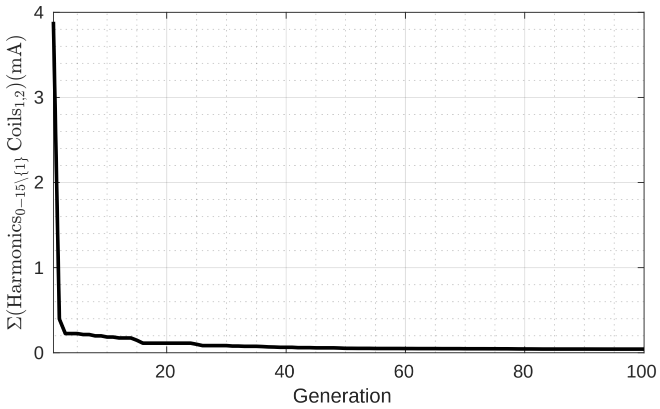

Figure 4.55: Linear position sensor optimized for minimal harmonic content - Convergence curve

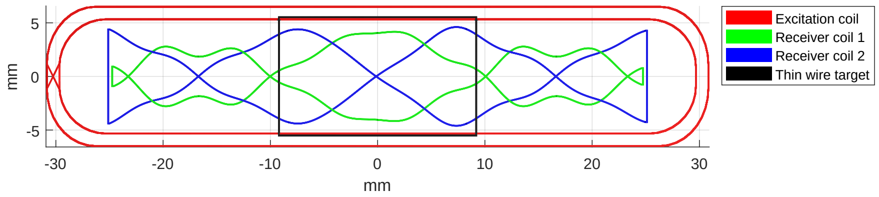

Figure 4.56: Linear position sensor optimized for minimal harmonic content - Geometry 4.5

value (harmonic content) evolution over 100 generations, and Figure 4.56 depicts the optimized geometry, *Geometry 4.5*. As a result, *Geometry 4.5* achieved 162 µm of maximum non-linearity, implying that *Geometry 4.5* has 102 times less than *Geometry 2*, which has 16.570 mm of maximum non-linearity. Table A.5 in Appendix A shows the geometric results (the values of the optimizable parameters) for all 12 optimized geometries, and the respective non-linearity values are depicted in Table A.6.

4.6.3.8 LIPS coil's geometry comparison

The LIPS sensor's optimization results are compared in this subsection. Figure 4.57 depicts the non-linearity curves for the LIPS sensor corresponding to *Geometries 1*, *2*, *3.5*, and *4.5*. These figures shows

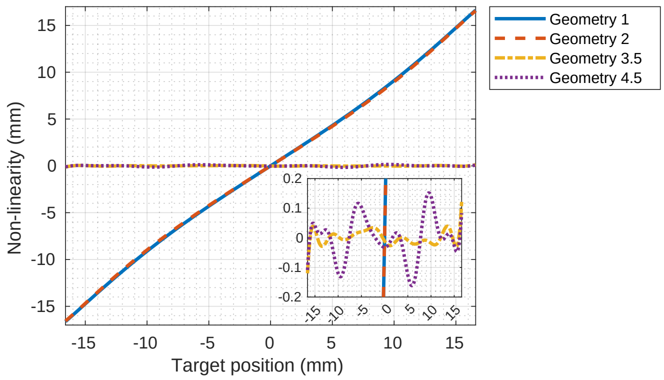

Figure 4.57: Error of geometries 1, 2, 3.5 and 4.5

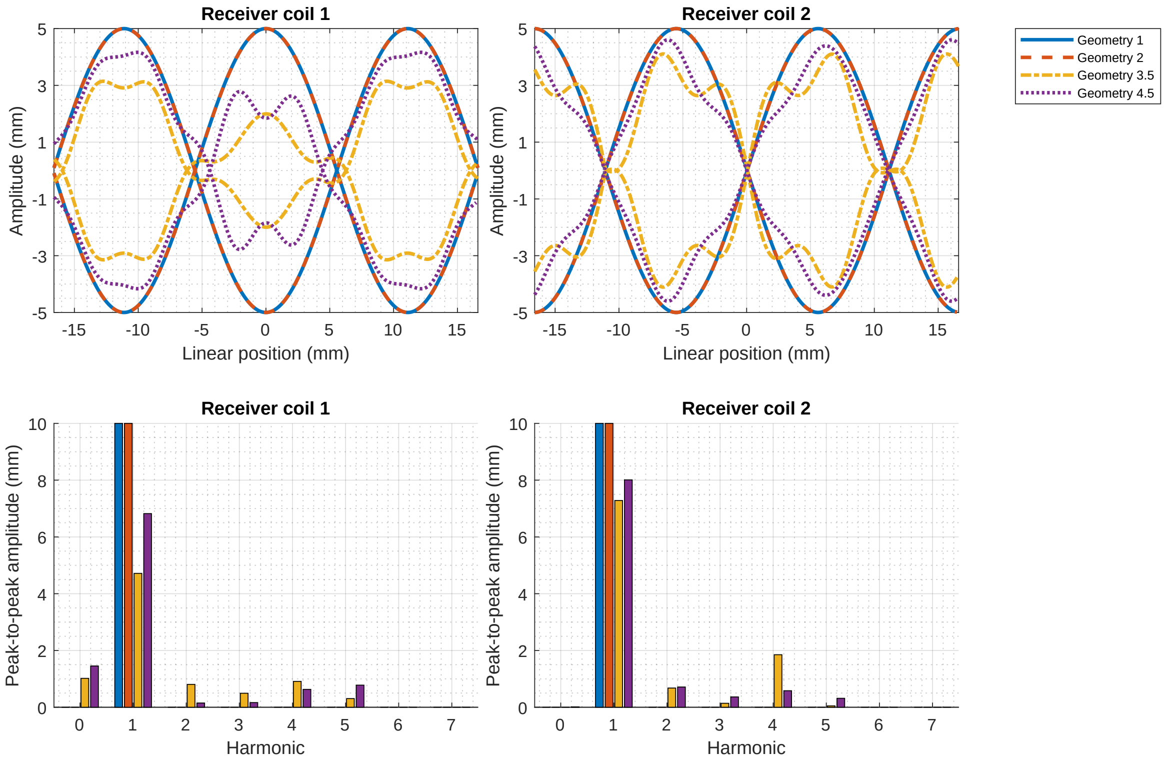

Figure 4.58: Geometric deformation

that the geometry with the lowest non-linearity is *Geometry 3.5*. This suggests, given that *Geometries 3.5* and *4.5* have the exact GA settings and optimizable parameters with the only change being the fitness parameter, that using the maximum non-linearity value as the fitness parameter is more advantageous than using the harmonic contents.

Figures 4.58a and 4.58b compare geometry distortion by depicting the geometry of the receiver's coils 1 and 2 from *Geometries 1*, *2*, *3.5*, and *4.5* on the same graph. The geometric harmonic content of the receiver's coils 1 and 2 is depicted in figures 4.58c and 4.58d. Observing and comparing them to the non-linearity results shown in Figure 4.57 demonstrates that including harmonic distortion into the receiver's coil design can reduce the sensor non-linearity significantly.

The receiver's coils induced signals from *Geometries 1*, *2*, *3.5*, and *4.5* are shown in Figure 4.59 together with their respective harmonic content. Figures 4.59a and 4.59b display the induced current over the linear target location for receiver's coils 1 and 2, respectively. The harmonic content is depicted in figures 4.59c and 4.59d.

It is usual with this type of inductive sensor to apply some correction to the signals induced in the receiver's coils in order to lessen the sensor's non-linearity. These adjustments often include continuous

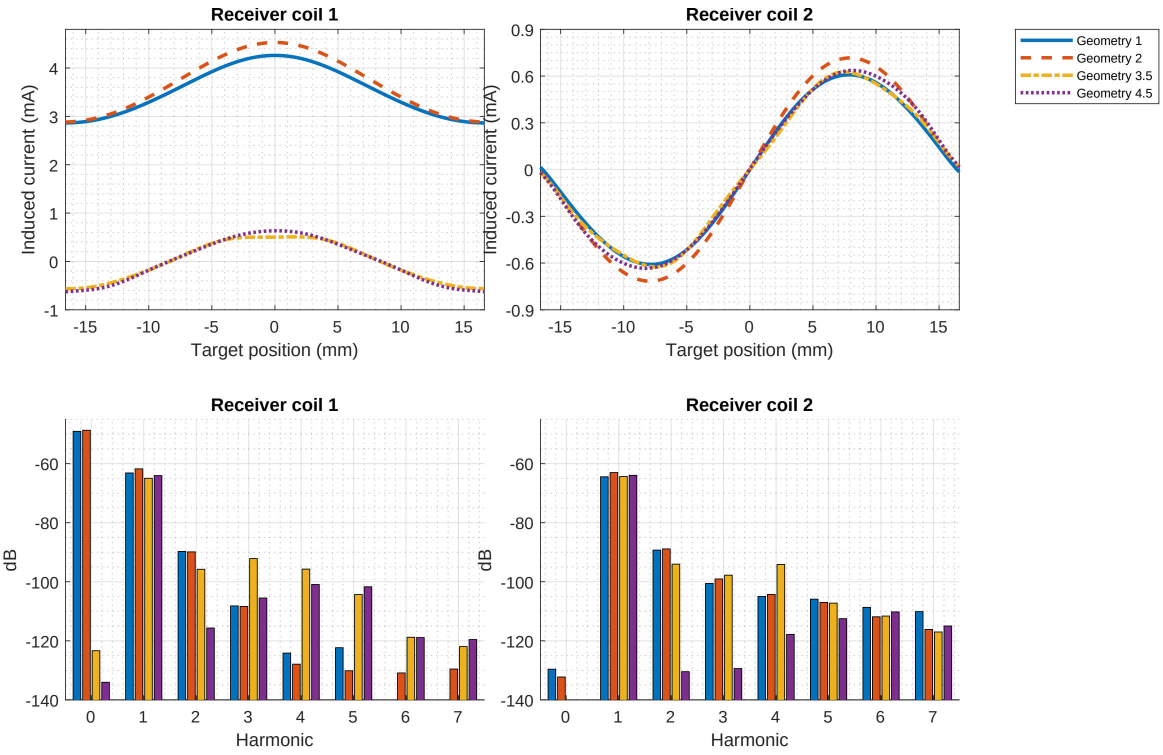

Figure 4.59: Induced current

component removal, normalization, and orthogonality correction. The non-linearity after applying these three adjustments to *Geometries 1*, *2*, *3.5*, and *4.5* is depicted in Figure 4.60.

Table A.6 summarizes the relevant data from all 26 geometries, namely the maximum peak-to-peak induced current, the maximum sensor non-linearity with and without receiver coil signal corrections, and the amplitude of the continuous and fundamental components, as well as the second to fifth harmonics.

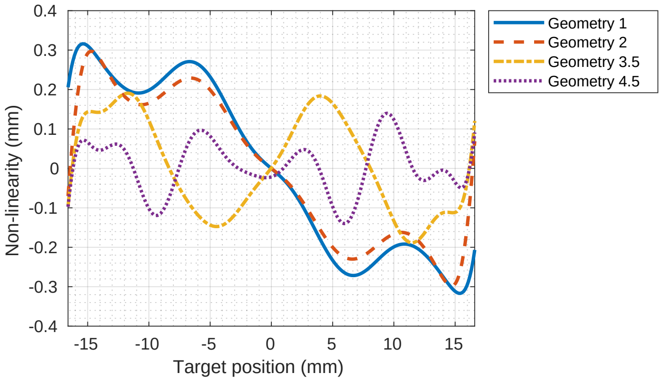

Figure 4.60: Error when applying continuous component removal, amplitude normalization and orthogonality correction to both receiver's coils' signals

4.6.4 Optimization using the FMM

As previously mentioned, the GA requires tens of thousands of electromagnetic simulations to converge to a solution. This clearly highlights the need for a quick numerical approach to solving field equations. In Section 4.6.2, the MoM was applied. This method took almost nine days to optimize the non-linearity of an angular position sensor where a population of 100 individuals evolved over 100 generations. In Section 4.6.3, a different approach was applied, the FHM. Using FHM the optimization took nearly 9 hours to optimize the non-linearity of a LIPS where a population of 100 individuals evolved over 100 generations. Although the sensors are different, it is evident that the FHM was significantly faster than the MoM.

This thesis next research challenge was to try to reduce further the time required by the simulation process to achieve an even faster optimization tool. To tackle this challenge the well-known FMM was used to solve the field equations. The FMM exploits the fact that the amplitude of the interaction between the basis (radiated field) and testing (received field) functions diminish quickly over distance. This can be accomplished by dividing the MoM matrix equation into two sparse matrices, the $\left[z^{near}\right]\left[i^{near}\right]=\left[v^{near}\right]$ and the $\left[z^{far}\right]\left[i^{far}\right]=\left[v^{far}\right]$. The near equation deals with the nearby interactions, and the far equation deals with the far interactions. Both equations are solved independently, with the near region equation explicitly solved, as in the MoM, and the far region equation solved differently on the fly, as described in Section 2.2.3.

Due to the wavelength of the source that feeds the excitation coil being vastly higher than the sensor's dimensions, this method may be ineffective because the near equation will solve all interactions. To assess it, an optimized version of the APS obtained in Section 4.6.2 was simulated (Figure 4.37). This simulation uses the MLFMM with four levels, where the first level is a cube with a 42 mm edge (large enough to accommodate the inductive sensor). The large wavelength when compared to the sensor's dimensions requires a higher number of multipoles, which might theoretically cause the Hankel function of the second kind to generate enormous numbers (see Equation 2.98 in Section 2.2.3). This becomes a problem later in the desegregation phase due to the lack of resolution necessary to overcome this. Like with all other simulations in this document, a double-precision floating-point format was used for this simulation. The resolution necessary to overcome the lack of resolution is higher than what a double-precision floating-point can provide. As a result, this could limit the use of the FMM in inductive position sensors.

To evaluate the usefulness of the MLFMM algorithm applied to inductive position sensors, the algorithm

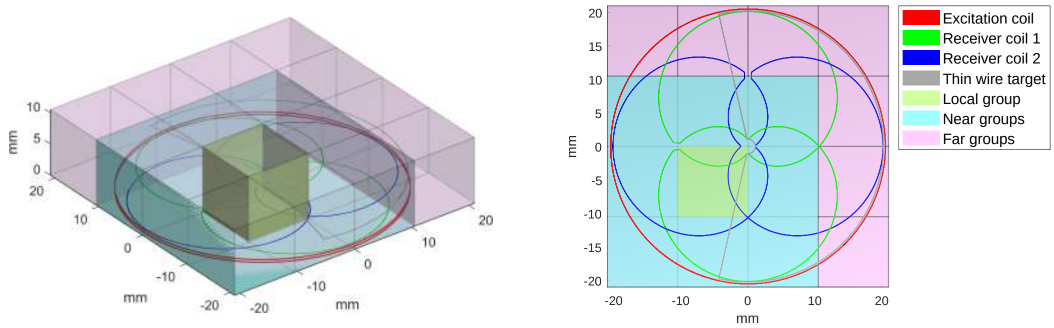

(a) Perspective view

(b) Top view

Figure 4.61: APS on octree level 3

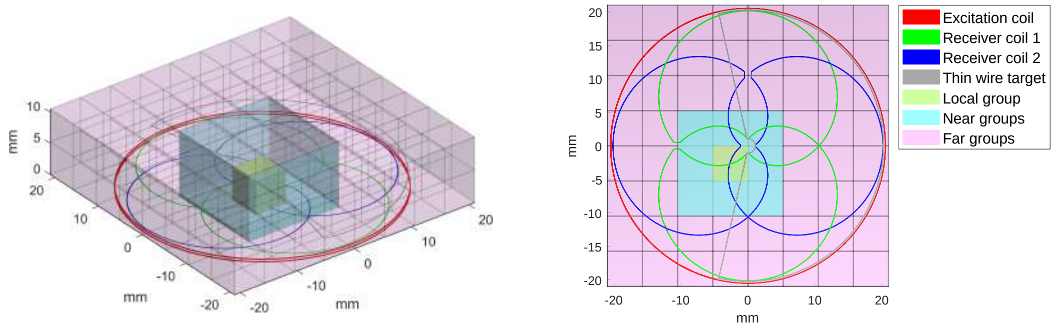

(a) Perspective view

(b) Top view

Figure 4.62: APS on octree level 4

was used to simulate the Figure 4.37's sensor. To accomplish this, the sensor was inserted into an octree with four levels, where levels three and four are depicted in Figures 4.61 and 4.62, respectively. In Figure 4.63, for this particular arrangement, all elements of the impedance matrix $[z^{near}]$ that differ from zero are represented by white squares. Since the $[z^{near}]$ matrix is highly sparse, there is a higher number of interactions solved by the MLFMM far algorithm through the multipole expansion. Otherwise, with a low $[z^{near}]$ sparse matrix, which can be achieved by increasing the first level octree cube size, most of the interactions are solved by the MoM itself, and the MLFMM method becomes useless. However, with this highly sparse matrix, the MLFMM method can be assessed and compared to the other methods used.

The test consists of several simulations in which the frequency of the excitation coil's source and the number of multipoles employed in the MLFMM algorithm are changed. The idea is to start at the optimized sensor frequency, determine the maximum number of multipoles allowed at this specific frequency, and then assess if this maximum is enough for an acceptable simulation. If an acceptable simulation cannot be produced, the process is repeated at a higher frequency until a satisfactory result is obtained. The goal of this procedure is to determine whether the MLFMM is effective at the sensor's optimized frequency and, if not, at what frequency it becomes effective.

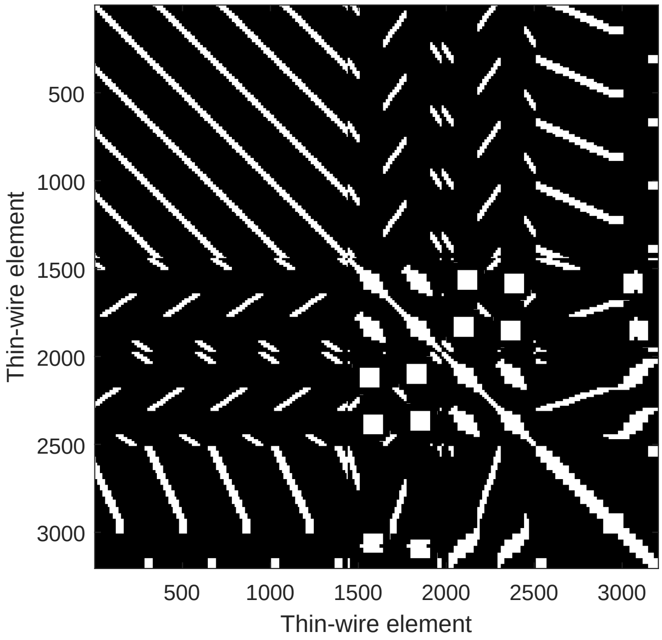

Figure 4.63: APS on octree Z_{near} mask (white square means 1 and black square means 0)

The maximum number of multipoles was determined by first solving the equation $[z]\,[i] = [v]$ using the MoM to determine the current distribution $[i]$ when the excitation coil is powered with a 1 V peak sine wave. Then, this current distribution is inserted in the MLFMM that multiplies it by the $[z^{near}]$, and $\left[z^{far}\right]$ to get the $[v^{near}]$, and $\left[v^{far}\right]$. The $[v^{near}]$ is calculated in a straightway, $[v^{near}] = [z^{near}]\,[i^{near}]$, the $\left[v^{far}\right]$ is computed on the fly using the MLFMM algorithm.

Figure 4.65 depicts the results obtained using the above process to determine the maximum number of multipoles allowed at the optimized sensor frequency, 10.7 MHz. After analysis, it is clear that the maximum number of multipoles allowed is five. With six multipoles, the $[v]^{far}$ becomes highly oscillatory. Also, as expected, as the number of multipoles increases, $[v^{near}] + \left[v^{far}\right]$ approaches $[u]$ until six multipoles are reached. Figure 4.66 displays the current distribution $[i]$ obtained by applying MLFMM (blue curve) and by applying the MoM (red curve). Comparing both curves reveals that the MLFMM fails due to the wavelength being large when compared to the sensor's dimensions, requiring a higher number of multipoles (above five).

Since the MLFMM failed at 10.7 MHz, the goal is to determine the frequency from which MLFMM produces results. Figure 4.67 depicts the same test to determine the maximum number of multipoles before $\left[v^{far}\right]$ becomes highly oscillatory. This time, the excitation coil is fed with a 100 MHz sine wave. Observing Figure 4.67, the maximum number of multipoles is again five, but this time $[v^{near}] + \left[v^{far}\right]$ is significantly closer to the excitation vector $[u]$ than the 10.7 MHz case. The current distribution $[i]$ computed through the

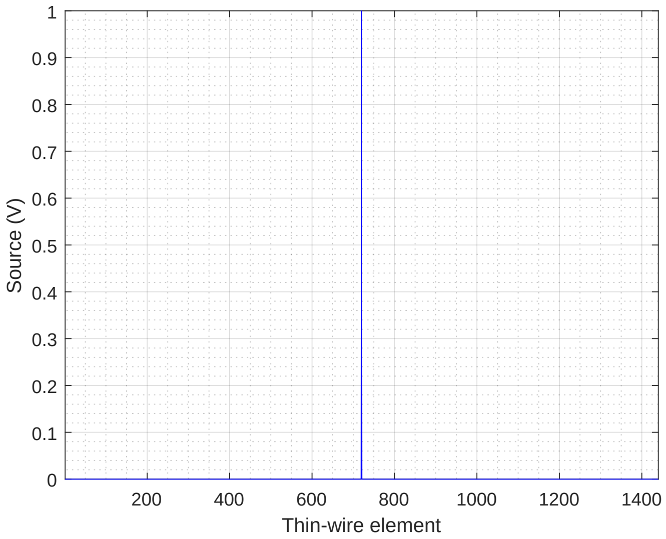

Figure 4.64: Excitation vector $[u]$ with one non-zero element at the segment that support the coil terminals (delta-gap)

MLFMM and the MoM is depicted in Figure 4.68. Although the distance between the two curves is smaller than in Figure 4.66, there is still a noticeable difference.

Figures 4.69 and 4.70 depict the results at 1 GHz. This time $[v^{near}] + [v^{far}]$ is significantly closer to the excitation vector $[u]$, especially in the six multipole case, which is the maximum allowed. Correspondingly, the current distribution computed through the MLFMM with six multipoles is identical to that computed through the MoM.

Based on the research described in this section, it is concluded that the MLFMM is not an attractive simulation method for inductive position sensors when the working wavelength is significantly larger than the sensor's dimensions. In this case, the FHM is more suited. The MLFMM begins to be attractive at 1 GHz, where the wavelength has an order of magnitude closer to the sensor dimensions.

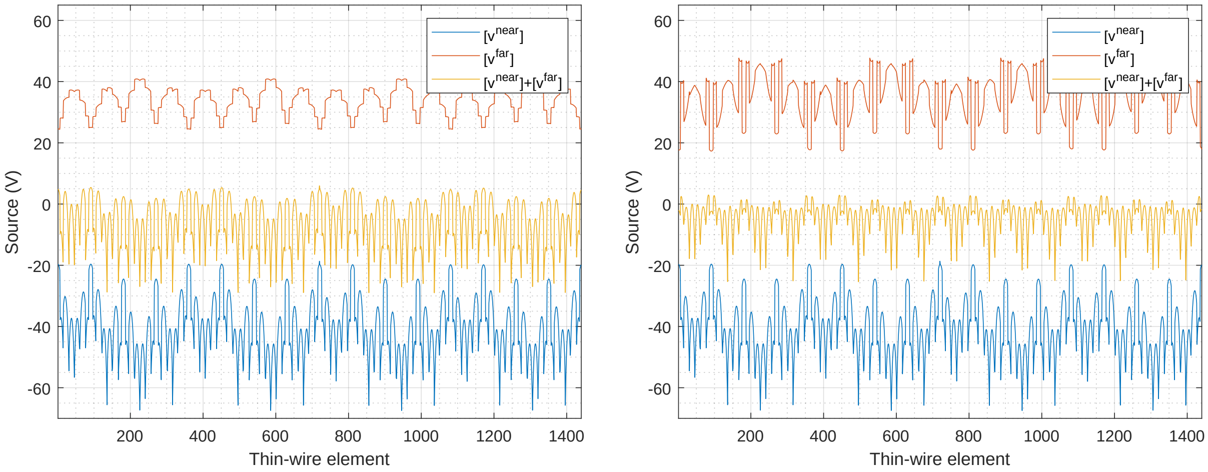

(a) 2 multipoles

(b) 3 multipoles

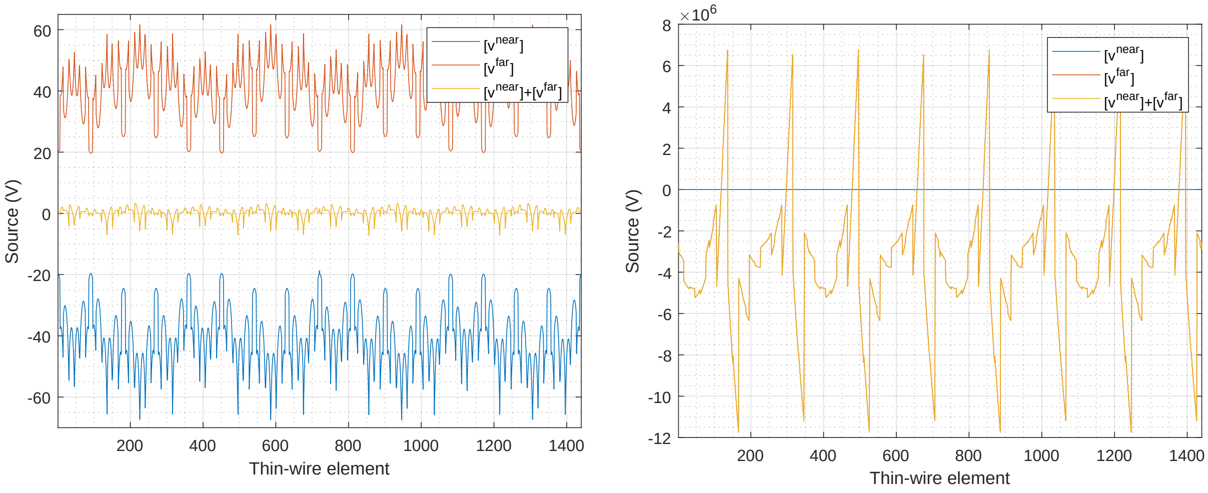

(c) 5 multipoles

(d) 6 multipoles

Figure 4.65: FMM vs MoM - Excitation coil v_{far} and v_{near} at 10.7 MHz

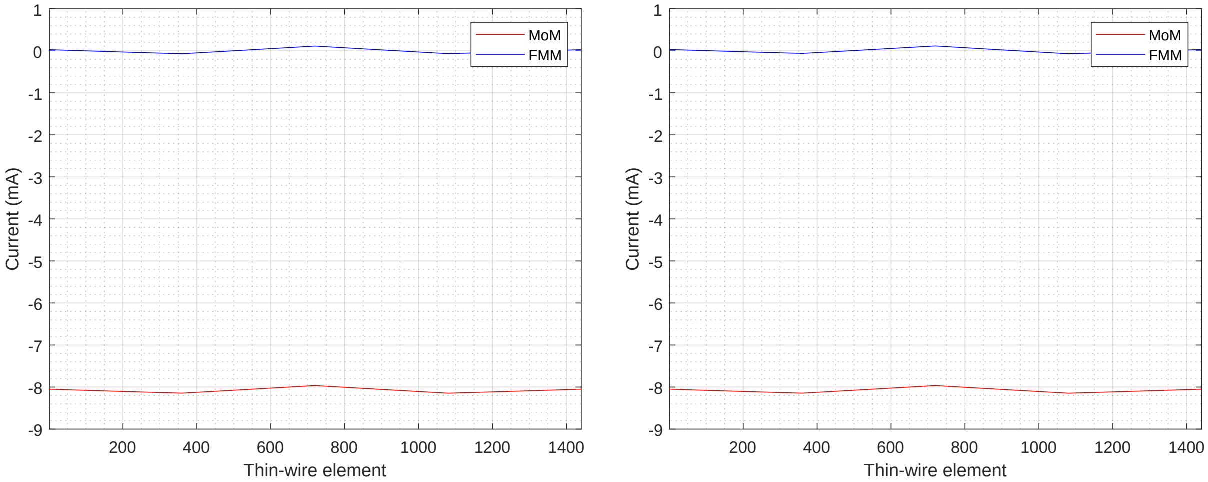

(a) 2 multipoles **(b)** 3 multipoles

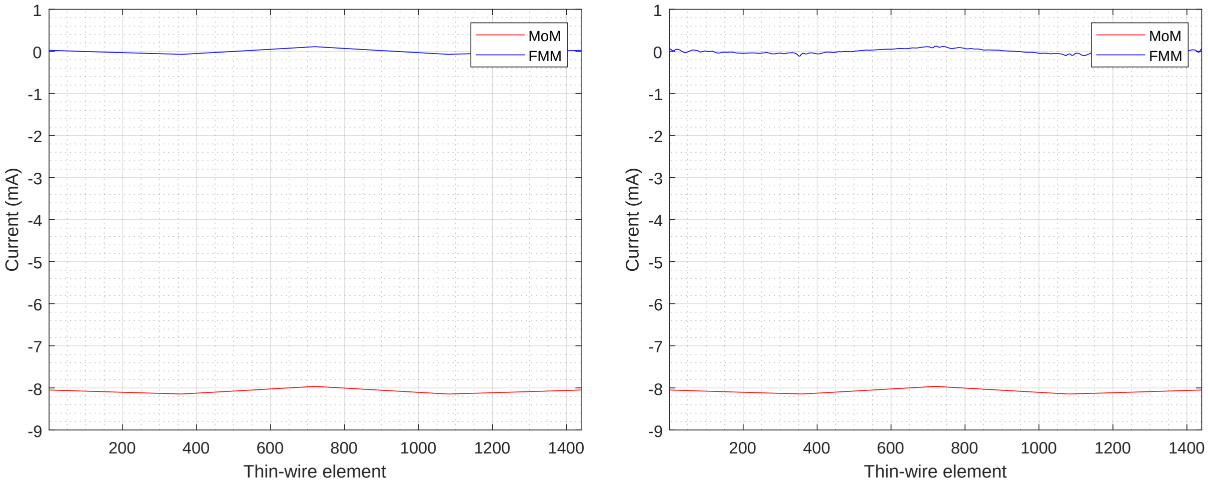

(c) 5 multipoles **(d)** 6 multipoles

Figure 4.66: FMM vs MoM - Excitation coil current distribution at 10.7 MHz

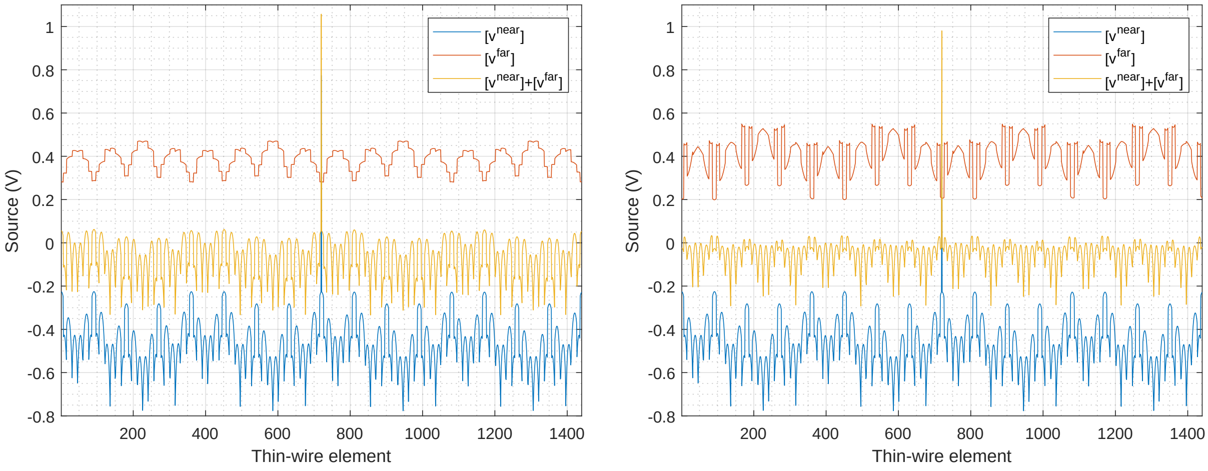

(a) 2 multipoles

(b) 3 multipoles

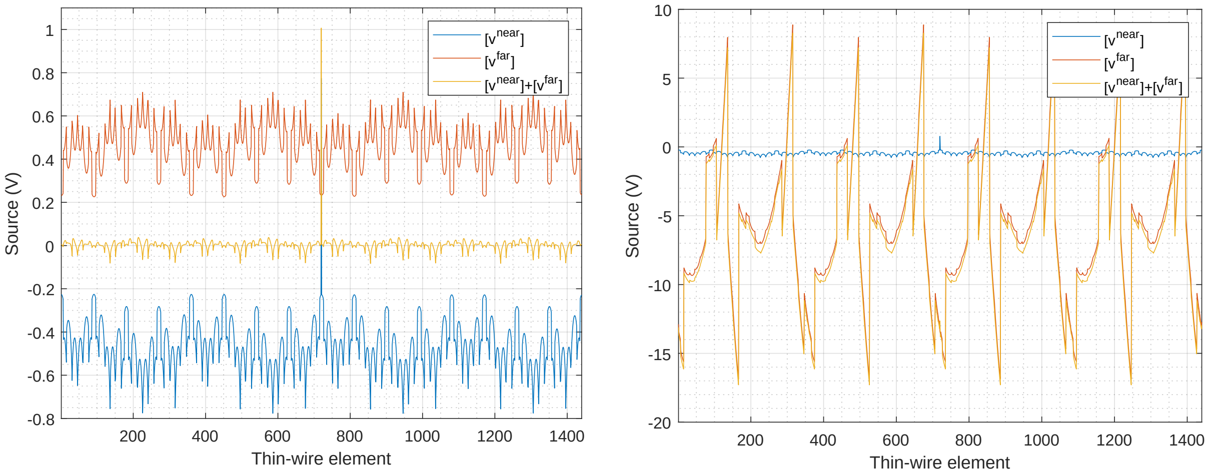

(c) 5 multipoles

(d) 6 multipoles

Figure 4.67: FMM vs MoM - Excitation coil v_{far} and v_{near} at 100 MHz

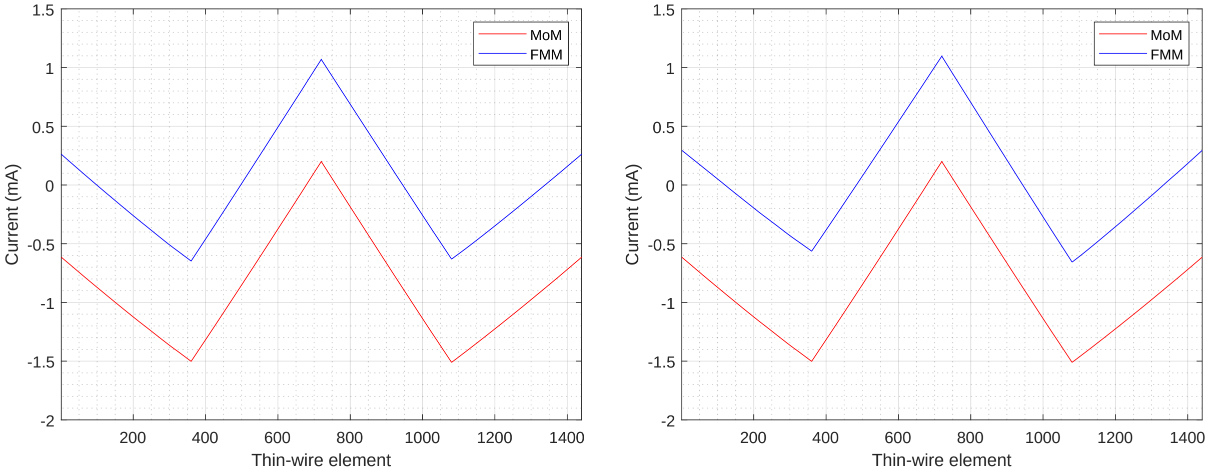

(a) 2 multipoles

(b) 3 multipoles

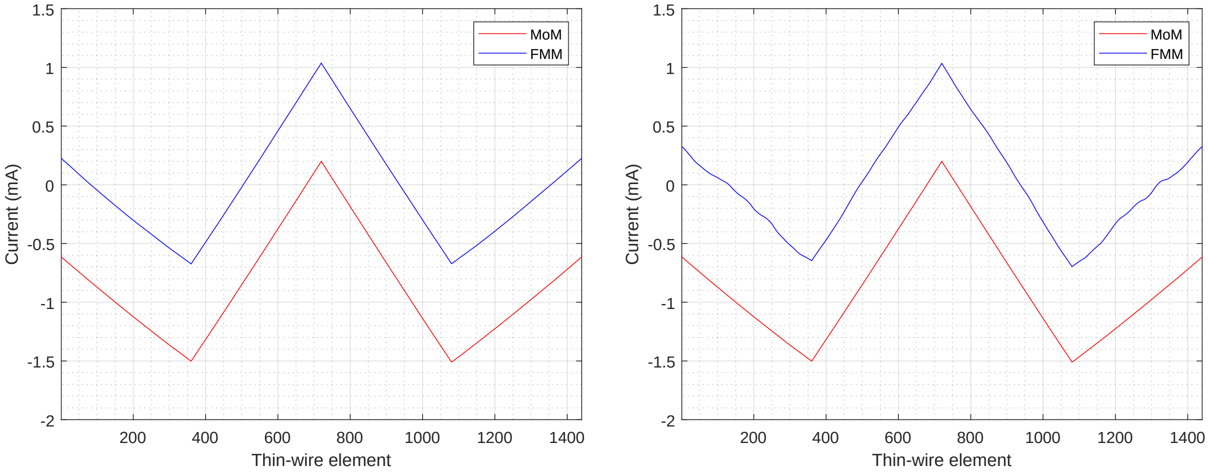

(c) 5 multipoles

(d) 6 multipoles

Figure 4.68: FMM vs MoM - Excitation coil current distribution at 100 MHz

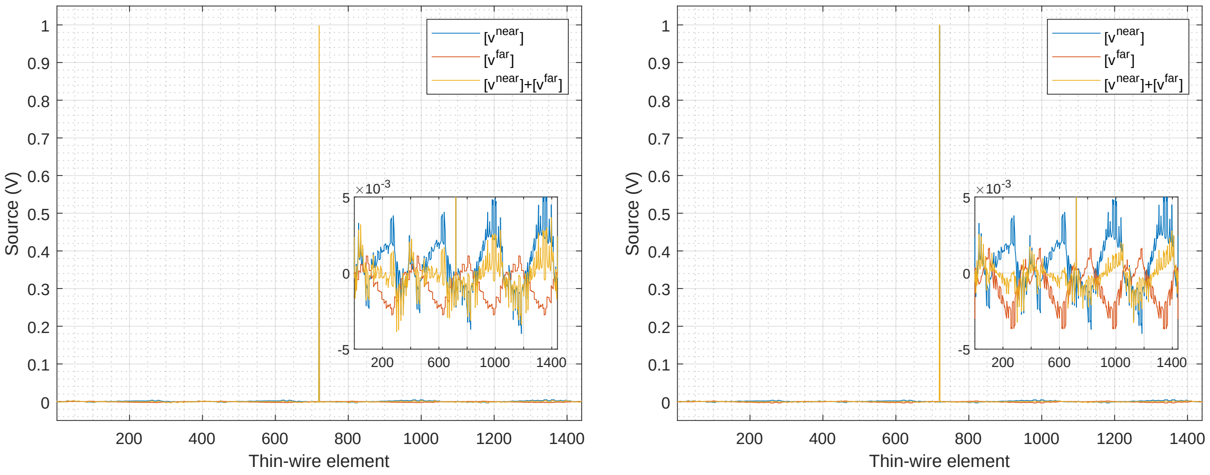

(a) 2 multipoles

(b) 3 multipoles

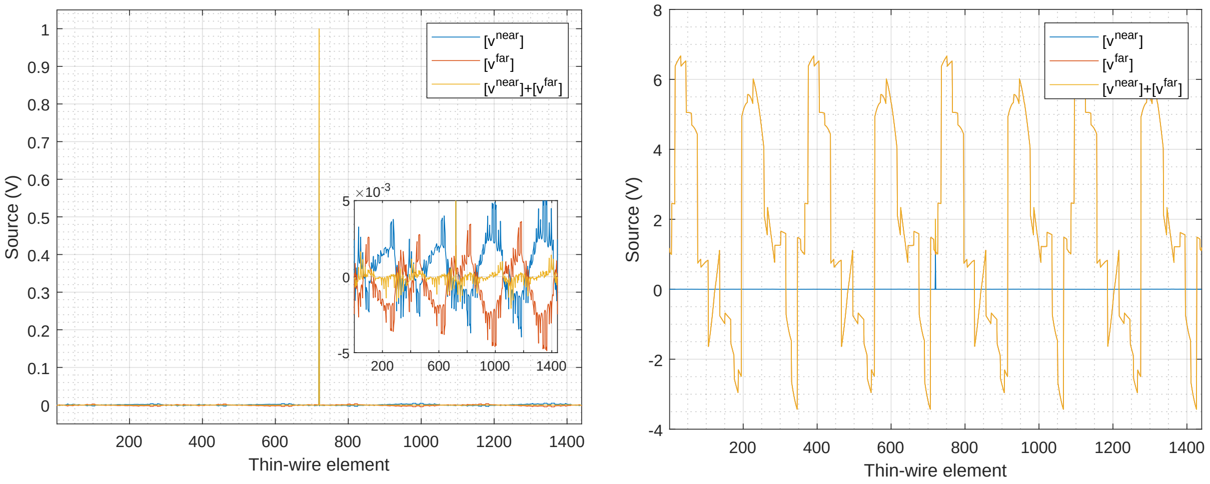

(c) 6 multipoles

(d) 7 multipoles

Figure 4.69: FMM vs MoM - Excitation coil v_{far} and v_{near} at 1 GHz

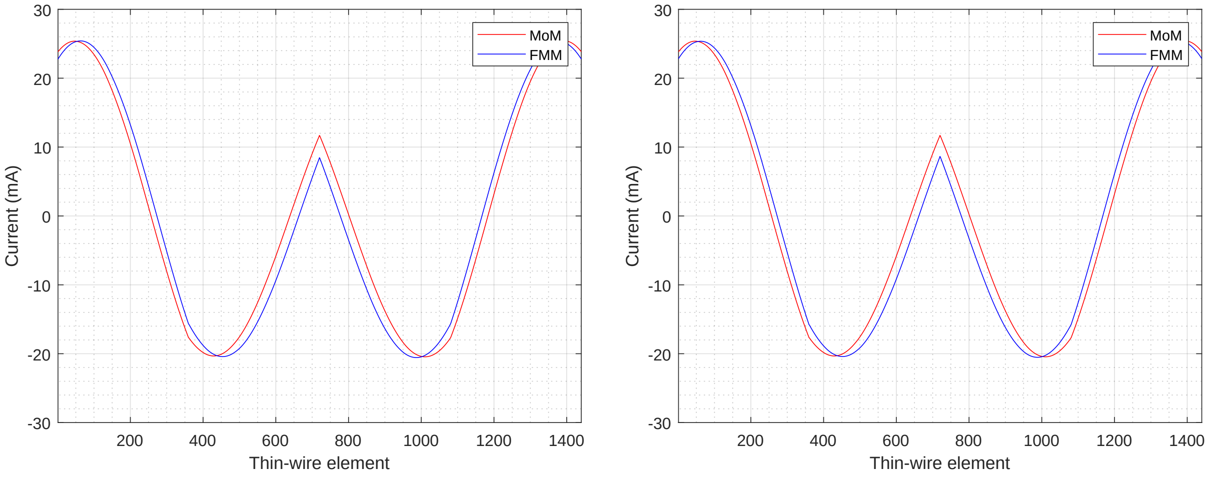

(a) 2 multipoles **(b)** 3 multipoles

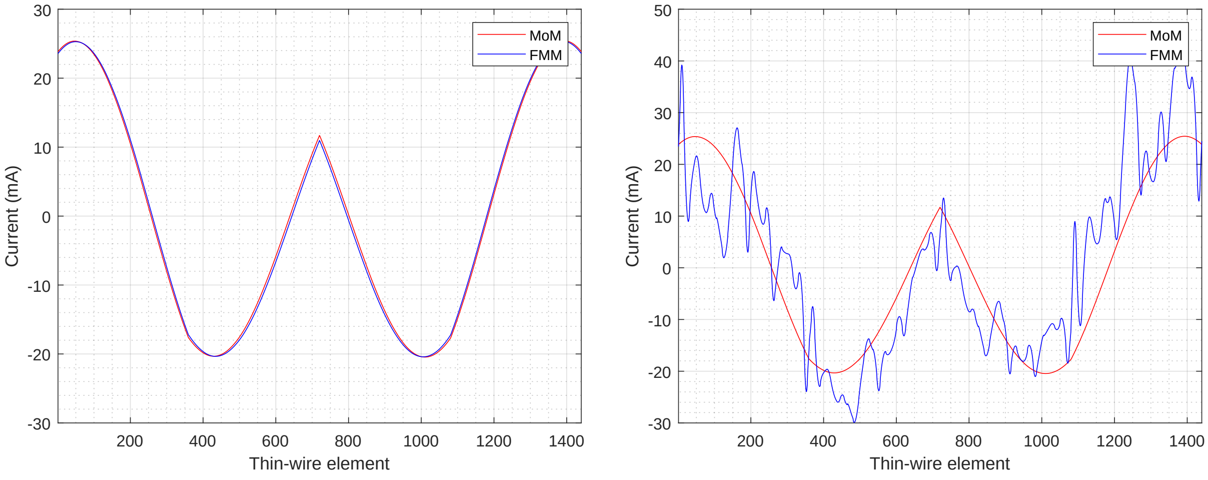

(c) 6 multipoles **(d)** 7 multipoles

Figure 4.70: FMM vs MoM - Excitation coil current distribution at 1 GHz

4.6.5 Discussion

In this section, the proposed methodology for improving the design of inductive position sensors was evaluated. A combination of an electromagnetic simulator and a global optimizer, specifically a GA algorithm, was used to optimize the coils of sensors printed directly on a PCB. The proposed methodology was applied to optimize two different sensor geometries, an APS and a LIPS. Furthermore, three different implementations of the electromagnetic simulator, MoM, FHM, and MLFMM were assessed. MoM and FHM were used as electromagnetic simulators to optimize the APS and LIPS.

The optimization methodology starts by finding the most efficient coil geometry for maximum induced current on the receiver coils of both the APS and LIPS sensors. Using the optimized geometry for maximum induced current as a starting point, two additional optimized geometries for each sensor were then generated. The first optimized geometry aimed for minimum non-linearity, while the second focused on minimizing harmonic content in the receiver coils' signals.

The evaluation results showed that the optimization methodology was effective in optimizing the design of both sensors (APS and LIPS). Additionally, the FHM implementation of the electromagnetic simulator was significantly faster than the MoM implementation. The MoM implementation took almost 213 wall time hours to optimize the APS sensor for minimum non-linearity, while the FHM implementation took only 9 wall time hours to optimize the LIPS sensor for the same metric on the same machine. The best optimization for the APS sensor (Geometry 4.2) resulted in a maximum non-linearity of 0.021°, a significant improvement of 32 times compared to the initial geometry (Geometry 2), which had a maximum non-linearity of 0.663°. Similarly, the best optimization for the LIPS sensor (Geometry 3.5) resulted in a maximum non-linearity of 122 µm, a significant improvement of 135 times when compared to the initial geometry (Geometry 2), which had a maximum non-linearity of 16.570 mm. It is important to note that the non-linearity values presented above were calculated without any signal corrections applied to the signals received by the coils. Meaning that the continuous component was not removed, no amplitude normalization was made, nor orthogonality correction was performed. The only processing applied was a four-quadrant inverse tangent function on the two modulator signals.

Additionally, a third implementation of the electromagnetic simulator, the MLFMM, was also tested, for simulating the APS sensor. The results showed that the MLFMM is not an ideal simulation method for inductive position sensors when the working wavelength is significantly larger than the sensor's dimensions. In this cases, the FHM method was deemed more appropriate. However, at a frequency of 1 GHz, where the wavelength is closer to the sensor's dimensions, the MLFMM becomes a more viable option.

4.7 Conclusions

This chapter has comprehensively explored the design and optimization of inductive position sensors. It provided a detailed analysis of the state-of-the-art in position sensors, including magnetic, optical, and capacitive-based technologies, and emphasized their respective strengths and weaknesses. A more in-depth examination of the state-of-the-art was conducted specifically for inductive-based position sensors, reflecting the primary focus of this chapter. The presentation of a proposed methodology for inductive position sensors design followed this analysis.

The proposed methodology integrated an electromagnetic simulator and a global optimizer, specifically a GA algorithm. It aimed to optimize the coils of sensors printed directly on a PCB. The approach was applied to two distinct sensor geometries, an APS and a LIPS. The performance of three different implementations of the electromagnetic simulator (MoM, FHM, and MLFMM) was assessed.

A range of optimization scenarios were investigated, including peak-to-peak induced current optimization, non-linearity optimization, and harmonic content optimization. The optimized coil geometries demonstrated enhanced performance compared to non-optimized configurations.

Addressing the research questions and objectives, this chapter presented a thorough review of current advancements in inductive position sensors (RQ1 and O1). By introducing a design methodology that merges an electromagnetic simulator and a global optimizer, the chapter also responded to RQ2. The viability and effectiveness of the proposed methodology (RQ3) were demonstrated by applying it to the optimization of two different sensor geometries and evaluating multiple optimization scenarios (O5 and O6).

In conclusion, this chapter contributes to the broader knowledge of inductive position sensor design by proposing a methodology that delivers enhanced performance. The insights provided in this chapter, particularly the proposed optimization methodology for inductive-based position sensors, open new opportunities for future research and practical applications in the domain of inductive position sensor design.

Chapter 5

Conclusions and future work

This thesis addressed two current engineering challenges facing the automotive industry: creating an Active Noise Cancellation (ANC) system that can effectively reduce non-stationary signals inside a vehicle's passenger compartment, and developing a methodology for designing reliable inductive position sensors without using a magnet. The proposed solutions for both challenges were based on spectral methods.

In the case of the ANC system, spectral methods were used to identify the frequency components of the non-stationary signals, which enabled the development of a control algorithm that effectively reduced these components of the noise signal.

Chapter 3 discussed a novel ANC solution. This proposed solution was implemented in an Field Programmable Gate Array (FPGA), and field tests were conducted to verify its efficiency. The field tests showed that the system could reduce non-stationary noise in an open and uncontrolled acoustic space environment by up to 9 dB [162]. This was achieved by using a unique combination of various approaches:

i) the arrangement of the anti-phase speakers and microphones allowed us to anticipate the undesired noise in the specific place where the reduction was wanted;

ii) the use of wavelets allowed for the decomposition of broadband noise and error signals from microphones into multiple straightforward signals;

iii) the Undecimated Wavelet Packet Transform (UWPT) proved to be the best option, as its high output rate (all output decomposition has the same rate as the input signal) is easier to process by the Filtered-x Least Mean Square (FxLMS) algorithm. It also enables the normalization of the noise signal independently in each wavelet decomposition that arrives at the Least Mean Square (LMS)

Figure 5.1: Hardware accelerated ANC system board

coefficient update algorithm, making all decomposition error signals converge to zero at almost the same rate, regardless of the decomposed signal's power.

The use of the Haar wavelet and different implementation strategies allowed to simplify and made it possible to place the entire ANC system in an FPGA (embedded system). Some of these simplification strategies have been described in Chapter 3. Based on these findings, an ANC based on Haar wavelets is a promising method for reducing undesired ambient noise in an open and uncontrolled acoustic space environment.

However, the proposed ANC system can be improved. Currently, the system is based on injecting an anti-phase signal at the loudspeakers, which cancels the noise at the error microphone's position. However, from the listeners' perspective, as they are on a medium that was not evaluated, and the noise and correction evolve with different wavevectors, this may not be the case. An improved system implementing a constellation of error microphones and anti-phase loudspeakers may be able to solve this challenge.

For the inductive position sensor, spectral methods were used in conjunction with a Genetic Algorithm (GA) to determine the optimal design parameters, such as the number of excitation coil turns, the size of the coils, and the amplitude and phase of the appropriate harmonics added to the receiver's coils geometry. Thus, helping to achieve the sensor's desired performance.

Chapter 4 presented, described, and tested a novel methodology for optimizing inductive position sensors, which are used to optimize the coils' geometry of the sensor.

The full assessment made revealed that the developed methodology was significantly helpful in developing these novel inductive sensors. It is based on a GA for global optimization and an electromagnetic

(a) APS coils' PCB

(b) APS target's PCB

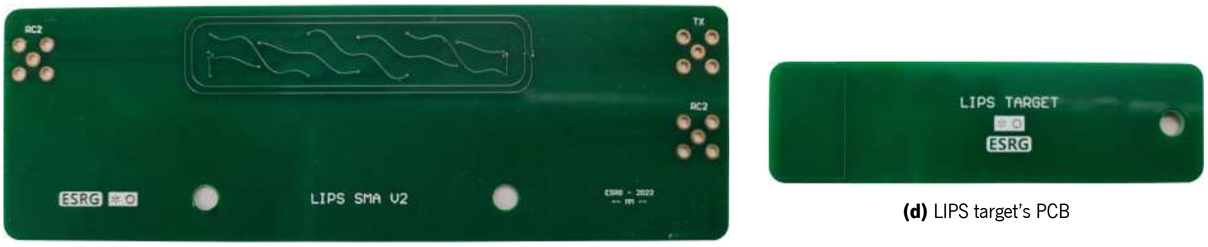

(c) LIPS coils' PCB

(d) LIPS target's PCB

Figure 5.2: Manufactured inductive position sensors' PCB featuring the optimized geometries

field simulator. Furthermore, it simplifies the sensor's coil geometry for electromagnetic simulations by decomposing it with perfectly conducting thin wires, simplifying the electromagnetic problem and making all processes less time-consuming. The tests revealed that this tool could maximize the induced current on an inductive sensor's receiver coils by fine-tuning the geometry of the sensor's coils. In addition to induced current optimization, the non-linearity in the inductive position sensor measurements was minimized using the same optimization tool described in this thesis. Essentially, after the induced current optimization, a second optimization was performed in which the optimization tool handles the geometry of the coils from the previous optimization and optimizes it by adding some harmonic distortion to the coils' geometry to achieve better non-linearity results. This novel idea was submitted in a patent request [163].

Based on these findings, the proposed inductive position sensor optimization methodology based on the GA and the Method of Moments (MoM) proved to be an efficient method for optimizing inductive sensors. This methodology maximizes the induced current on the receiver's coils and minimizes the sensor's error by fine-tuning the geometry of the sensor's coils. Furthermore, it speeds up and simplifies

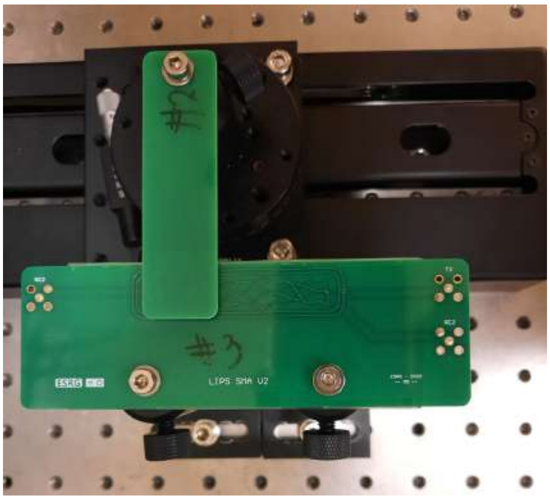

(a) Setup

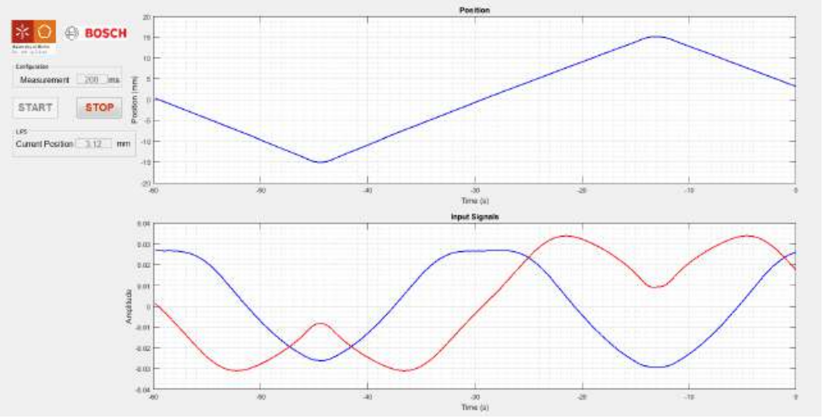

Configuration
Measurement 200 ms
LPS
Current Position 3.12 mm

(b) Graphical interface

Figure 5.3: LIPS sensor test setup

the inductive sensor design process, assisting in the transition from permanent magnet-based to inductive-based sensors.

However, the proposed inductive position sensors' optimization methodology is far from perfect, as it can be improved even further. It can be improved by enhancing the coding of the numerical method used to solve the field equations or looking for a potential new method to speed up the simulation process without compromising simulation reliability. The effectiveness of GA can be further improved by combining it with Artificial Intelligence (AI) techniques, which can help to identify more suitable configurations for faster convergence with fewer generations. However, it is important to exercise caution and ensure that this enhancement does not significantly increase the likelihood of the solution being trapped in a local maximum, rather than achieving a global maximum. These enhancements can speed up the optimization process, allowing for more complex optimization schemes such as increasing the number of variables that can be optimized or enabling the possibility of using a machine with fewer computational resources.

Additionally, this could potentially lead to further improvements in the optimization of inductive position sensors, making them even more advantageous for use in the automotive industry.

References

[1] I. R. Sinclair, *Sensors and Transducers*, 3rd ed. Newnes, 2001.

[2] A. V. Oppenheim, A. S. Willsky, and S. H. Nawab, *Signals & Systems*, 2nd ed. Pearson, 1996.

[3] F. V. Grilo, A. Casimiro, J. C. Lopes, and J. Azevedo, *Teoria do Sinal e suas aplicações*. Escolar Editora, 2010.

[4] S. Mallat, *A Wavelet Tour of Signal Processing: The Sparse Way*, 3rd ed. Academic Press, 2008.

[5] I. Daubechies, "Orthonormal bases of compactly supported wavelets," *Communications on Pure and Applied Mathematics*, vol. 41, no. 7, pp. 909–996, 1988. [Online]. Available: https://onlinelibrary.wiley.com/doi/abs/10.1002/cpa.3160410705

[6] M. Smith and T. Barnwell, "A procedure for designing exact reconstruction filter banks for tree-structured subband coders," in *ICASSP '84. IEEE International Conference on Acoustics, Speech, and Signal Processing*, vol. 9, 1984, pp. 421–424.

[7] M. Vetterli, "Filter banks allowing perfect reconstruction," *Signal Processing*, vol. 10, pp. 219–244, 1986.

[8] P. Vaidyanathan, "Quadrature mirror filter banks, M-band extensions and perfect-reconstruction techniques," *IEEE ASSP Magazine*, vol. 4, no. 3, pp. 4–20, 1987.

[9] M. J. Shensa, "The discrete wavelet transform: wedding the a trous and Mallat algorithms," *IEEE Transactions on Signal Processing*, vol. 40, no. 10, pp. 2464–2482, 1992.

[10] P. Sumithra and T. Dhanasingh, "Review on Computational Electromagnetics," *Advanced Electromagnetics*, vol. 6, p. 42, mar 2017.

[11] D. Tayli, "Computational Tools for Antenna Analysis and Design," Ph.D. dissertation, Department of Electrical and Information Technology, 2018.

[12] A. Reineix and B. Jecko, “Analysis of microstrip patch antennas using finite difference time domain method,” *IEEE Transactions on Antennas and Propagation*, vol. 37, no. 11, pp. 1361–1369, nov 1989.

[13] J. G. Maloney, G. S. Smith, and W. R. Scott, “Accurate computation of the radiation from simple antennas using the finite-difference time-domain method,” *Digest on Antennas and Propagation Society International Symposium*, pp. 42–45 vol.1, 1989.

[14] P. A. Tirkas and C. A. Balanis, “Finite-difference time-domain method for antenna radiation,” *IEEE Transactions on Antennas and Propagation*, vol. 40, pp. 334–340, 1992.

[15] Z. Lou and J.-M. Jin, “Modeling and simulation of broad-band antennas using the time-domain finite element method,” *IEEE Transactions on Antennas and Propagation*, vol. 53, no. 12, pp. 4099–4110, 2005.

[16] E. M. Purcell, *Electricity and Magnetism (Berkeley Physics Course, Volume 2)*, 2nd ed. Cambridge University Press, 2011.

[17] J.-M. Jin, *The Finite Element Method in Electromagnetics*, 3rd ed. Wiley-IEEE Press, 2014.

[18] V. M. Machado, *Simulação Computacional em Eletromagnetismo*. IST Press, 2018.

[19] W. C. Gibson, *The Method of Moments in Electromagnetics*, 3rd ed. CRC Press, 2021.

[20] R. F. Harrington, *Field Computation by Moment Methods*, reprint ed ed. Wiley-IEEE Press, 1993.

[21] G. J. Burke, A. J. Poggio, J. C. Logan, and J. W. Rockway, “Numerical Electromagnetic Code (NEC),” in *1979 IEEE International Symposium on Electromagnetic Compatibility*, 1979, pp. 1–3.

[22] F.-G. Hu, J. Song, and M. Yang, “Errors in Projection of Plane Waves Using Various Basis Functions,” *Antennas and Propagation Magazine, IEEE*, vol. 51, pp. 86–98, may 2009.

[23] M. A. Echeverri Bautista, M. A. Francavilla, F. Vipiana, and G. Vecchi, “A Hierarchical Fast Solver for EFIE-MoM Analysis of Multiscale Structures at Very Low Frequencies,” *IEEE Transactions on Antennas and Propagation*, vol. 62, no. 3, pp. 1523–1528, 2014.

[24] B. Carpentieri, “Preconditioning for Large-Scale Boundary Integral Equations in Electromagnetics [Open Problems in CEM],” *IEEE Antennas and Propagation Magazine*, vol. 56, no. 6, pp. 338–345, 2014.

[25] J. Barnes and P. Hut, “A hierarchical O(N log N) force-calculation algorithm,” *Nature*, vol. 324, no. 6096, pp. 446–449, 1986.

[26] L. Greengard and V. Rokhlin, “A fast algorithm for particle simulations,” *Journal of Computational Physics*, vol. 73, no. 2, pp. 325–348, 1987. [Online]. Available: https://www.sciencedirect.com/science/article/pii/0021999187901409

[27] J. Song, C.-C. Lu, and W. C. Chew, “Multilevel fast multipole algorithm for electromagnetic scattering by large complex objects,” *IEEE Transactions on Antennas and Propagation*, vol. 45, no. 10, pp. 1488–1493, 1997.

[28] B. Bramas, “Optimization and parallelization of the boundary element method for the wave equation in time domain,” Ph.D. dissertation, 2016.

[29] P. Salamon, P. Sibani, and R. Frost, *Facts, Conjectures, and Improvements for Simulated Annealing*. SIAM, 2002.

[30] A. Lazinica, *Particle Swarm Optimization*. Intechopen, 2009.

[31] S. Sivanandam and S. N. Deepa, *Introduction to Genetic Algorithms*. Springer, 2008.

[32] S. Kirkpatrick, C. Gelatt, and M. Vecchi, “Optimization by Simulated Annealing,” *Science (New York, N.Y.)*, vol. 220, pp. 671–680, 1983.

[33] R. Eberhart and J. Kennedy, “A new optimizer using particle swarm theory,” in *MHS’95. Proceedings of the Sixth International Symposium on Micro Machine and Human Science*, 1995, pp. 39–43.

[34] J. Kennedy and R. Eberhart, “Particle swarm optimization,” in *Proceedings of ICNN’95 - International Conference on Neural Networks*, vol. 4, nov 1995, pp. 1942–1948 vol.4.

[35] J. Kennedy and R. C. Eberhart, *Swarm Intelligence*, 1st ed. Morgan Kaufmann, 2001.

[36] ——, “A discrete binary version of the particle swarm algorithm,” in *1997 IEEE International Conference on Systems, Man, and Cybernetics. Computational Cybernetics and Simulation*, vol. 5, 1997, pp. 4104–4108 vol.5.

[37] C. Darwin and W. F. Bynum, *On the Origin of Species*, revised ed ed. Oxford University Press, 2009.

[38] T. Back, D. B. Fogel, and Z. Michalewicz, *Handbook of Evolutionary Computation*, 1st ed. CRC Press, 1997.

[39] D. S. Weile and E. Michielssen, "Genetic algorithm optimization applied to electromagnetics: a review," *IEEE Transactions on Antennas and Propagation*, vol. 45, no. 3, pp. 343–353, 1997.

[40] J. M. Johnson and V. Rahmat-Samii, "Genetic algorithms in engineering electromagnetics," *IEEE Antennas and Propagation Magazine*, vol. 39, no. 4, pp. 7–21, 1997.

[41] A. Hoorfar, "Evolutionary Programming in Electromagnetic Optimization: A Review," *IEEE Transactions on Antennas and Propagation*, vol. 55, no. 3, pp. 523–537, 2007.

[42] L. Eshelman and J. Schaffer, "Real-Coded Genetic Algorithms and Interval-Schema," vol. 2, 1992.

[43] D. Goldberg, "Real-coded Genetic Algorithms, Virtual Alphabets, and Blocking," *Complex Systems*, vol. 5, 1995.

[44] A. Wright, "Genetic Algorithms for Real Parameter Optimization," *Foundations of Genetic Algorithms*, vol. 1, 1999.

[45] K. Deb and D. Deb, "Analysing mutation schemes for real-parameter genetic algorithms," *International Journal of Artificial Intelligence and Soft Computing*, vol. 4, pp. 1–28, 2014.

[46] B. Widrow, J. Glover, J. McCool, J. Kaunitz, C. Williams, R. Hearn, J. R. Zeidler, J. Dong, and R. Goodlin, "Adaptive Noise Cancelling: Principles and Applications," *Proceedings of the IEEE*, vol. 63, pp. 1692–1716, 1976.

[47] L. Y. L. Ang, Y. Koh, and H. Lee, "The performance of active noise-canceling headphones in different noise environments," *Applied Acoustics*, vol. 122, pp. 16–22, 2017.

[48] N. Zafeiropoulos, J. Zollner, and V. Rajan, *State-of-the-art digital road noise cancellation by Harman*, 2019, pp. 59–74.

[49] M. Porghove, K. Shirazi, A. Messia, and E. Yildizdag, "A PSO-based computational framework to design active noise cancelation systems for smart vehicle enclosures," *Mathematics and Mechanics of Solids*, vol. 27, 2022.

[50] Y. Jiang, S. Chen, F. Gu, H. Meng, and Y. Cao, "A modified feedforward hybrid active noise control system for vehicle," *Applied Acoustics*, vol. 175, p. 107816, 2021.

[51] Y. Wang, S. Zhang, H. Guo, X. Wang, C. Yang, and N. Liu, “Hybrid time–frequency algorithm for active sound quality control of vehicle interior noise based on stationary discrete wavelet transform,” *Applied Acoustics*, vol. 171, p. 107561, 2021.

[52] Y. Wang, H. Guo, Y. R. Li, N. Liu, and C. Yang, “Active control for vehicle interior noise based on DWT-FxLMS algorithm using a piezoelectric feedback system,” *Applied Acoustics*, vol. 167, p. 107409, 2020.

[53] H. Guo, Y. Wang, C. Yang, X. Wang, N. Liu, and Z. J. Xu, “Vehicle interior noise active control based on piezoelectric ceramic materials and improved fuzzy control algorithm,” *Applied Acoustics*, vol. 150, pp. 216–226, 2019.

[54] S. Zhang, Y. Wang, H. Guo, C. Yang, X. Wang, and N. Liu, “A normalized frequency-domain block filtered-x LMS algorithm for active vehicle interior noise control,” *Mechanical Systems and Signal Processing*, vol. 120, pp. 150–165, 2019.

[55] D. Schubert, R. Henneberger, S. Hecker, S. Sentpali, and S. Marburg, “Active Noise Cancellation in Passenger Cars using the Electrical Power Steering Motor,” 2017.

[56] B. Widrow, D. Shur, and S. Shaffer, “On adaptlve inverse control,” in *15th Asilomar Conf. Circuits, Systems, and Components*, 1981, pp. 185–189.

[57] N. JI and A. Noda, “A Learning Method for System Identification,” *Automatic Control, IEEE Transactions on*, vol. AC-12, pp. 282–287, 1967.

[58] R. Nitzberg, “Application of the normalized LMS algorithm to MSLC,” *Aerospace and Electronic Systems, IEEE Transactions on*, vol. AES-21, pp. 79–91, 1985.

[59] T. Padhi, M. Chandra, and D. A. Kar, “Performance evaluation of hybrid active noise control system with online secondary path modeling,” *Applied Acoustics*, vol. 133, pp. 215–226, 2018.

[60] Y. Cheng, R. Zhang, and S. Chen, “Wavelet packet transform applied to active noise control system for mixed noise in nonlinear environment,” *Digital Signal Processing*, vol. 133, p. 103860, 2022.

[61] S. Wen, W.-S. Gan, and D. Shi, “An Improved Selective Active Noise Control Algorithm Based on Empirical Wavelet Transform,” in *ICASSP 2020 - 2020 IEEE International Conference on Acoustics, Speech and Signal Processing (ICASSP)*, 2020, pp. 1633–1637.

[62] L. Luo, J. Sun, and B. Huang, “A novel feedback active noise control for broadband chaotic noise and random noise,” *Applied Acoustics*, vol. 116, 2017.

[63] M. Akraminia and M. J. Mahjoob, “Adaptive feedback active noise control using wavelet frames: simulation and experimental results,” *Journal of Vibration and Control*, vol. 22, no. 7, pp. 1895–1912, 2016. [Online]. Available: https://doi.org/10.1177/1077546314545835

[64] M. Rakhshan, E. Moula, F. Shabani-nia, B. Safarinejadian, and S. Khorshidi, “Active noise control using wavelet function and network approach,” *Journal of Low Frequency Noise, Vibration and Active Control*, vol. 35, 2016.

[65] Z. Qiu, C.-R. Lee, Z. H. Xu, and L. N. Sui, “A multi-resolution filtered-x LMS algorithm based on discrete wavelet transform for active noise control,” *Mechanical Systems and Signal Processing*, vol. 66, 2015.

[66] S. Attallah, “The wavelet transform-domain LMS algorithm: a more practical approach,” *IEEE Transactions on Circuits and Systems II: Analog and Digital Signal Processing*, vol. 47, no. 3, pp. 209–213, 2000.

[67] D. C. Le, J. Zhang, and D. Li, “Hierarchical partial update generalized functional link artificial neural network filter for nonlinear active noise control,” *Digital Signal Processing*, vol. 93, 2019.

[68] D. C. Le, D. Li, and J. Zhang, “M-max partial update leaky bilinear filter-error least mean square algorithm for nonlinear active noise control,” *Applied Acoustics*, vol. 156, pp. 158–165, 2019.

[69] D. C. Le, J. Zhang, D. Li, and S. Zhang, “A generalized exponential functional link artificial neural networks filter with channel-reduced diagonal structure for nonlinear active noise control,” *Applied Acoustics*, vol. 139, pp. 174–181, 2018.

[70] H. Zhao, X. Zeng, Z. He, Z. Cao, S. Yu, and B. D. Chen, “Improved functional link artificial neural network via convex combination for nonlinear active noise control,” *Applied Soft Computing*, vol. 42, 2016.

[71] S. Behera, D. Das, and N. Rout, “Nonlinear feedback active noise control for broadband chaotic noise,” *Applied Soft Computing*, vol. 15, pp. 80–87, 2014.

[72] S. K. Behera, D. P. Das, and B. Subudhi, “Functional link artificial neural network applied to active noise control of a mixture of tonal and chaotic noise,” *Applied Soft Computing*,

vol. 23, pp. 51–60, 2014. [Online]. Available: https://www.sciencedirect.com/science/article/pii/S1568494614002701

[73] T. Padhi, M. Chandra, D. A. Kar, and M. Swamy, “Design and analysis of an improved hybrid active noise control system,” *Applied Acoustics*, vol. 127, pp. 260–269, 2017.

[74] J. Zhang, T. Abhayapala, W. Zhang, P. Samarasinghe, and S. Jiang, “Active Noise Control Over Space: A Wave Domain Approach,” *IEEE/ACM Transactions on Audio, Speech, and Language Processing*, vol. PP, p. 1, 2018.

[75] G. Long, Y. Wang, and T. Lim, “Optimal parametric design of delayless subband active noise control system based on genetic algorithm optimization,” *Journal of Vibration and Control*, vol. 28, p. 107754632110016, 2021.

[76] B. Widrow and M. E. Hoff, “Adaptive Switching Circuits,” in *1960 IRE WESCON Convention Record, Part 4*, Institute of Radio Engineers. New York: Institute of Radio Engineers, 1960, pp. 96–104. [Online]. Available: http://www-isl.stanford.edu/{~}widrow/papers/c1960adaptiveswitching.pdf

[77] B. Widrow, J. McCool, and M. Ball, “The complex LMS algorithm,” *Proceedings of the IEEE*, vol. 63, pp. 719–720, 1975.

[78] B. Widrow and D. S. Stearns, *Adaptive Signal Processing*. Englewood Cliffs, New Jersey: Prentice-Hall, 1985.

[79] S. Haykin and B. Widrow, *Least-Mean-Square Adaptive Filters*, 1st ed. Wiley-Interscience, 2003.

[80] S. Haykin, *Adaptive Filter Theory*, 5th ed. Hamilton, Ontario, Canada: Pearson, 2013.

[81] K. Kapser, M. Weinberger, W. Granig, and P. Slama, “GMR sensors in automotive applications,” in *Smart Sensors, Measurement and Instrumentation*. Springer International Publishing, 2013, vol. 6, pp. 133–156.

[82] M. Grönefeld, “Permanent Magnets: Sensor Applications,” in *Encyclopedia of Materials: Science and Technology*. Elsevier, 2001, pp. 6822–6825.

[83] G. Rieger, K. Ludwig, J. Hauch, and W. Clemens, “GMR sensors for contactless position detection,” *Sensors and Actuators, A: Physical*, vol. 91, no. 1-2, pp. 7–11, jun 2001.

[84] C. P. Treutler, “Magnetic sensors for automotive applications,” *Sensors and Actuators, A: Physical*, vol. 91, no. 1-2, pp. 2–6, jun 2001.

[85] E. Hall, “On a New Action of the Magnet on Electric Currents,” *Nature*, vol. 21, p. 361, 1880.

[86] E. Ramsden, *Hall-Effect Sensors: Theory and Application*, 2nd ed. Newnes, 2006.

[87] M. A. Khan, J. Sun, B. Li, A. Przybysz, and J. Kosel, “Magnetic sensors – A review and recent technologies,” *Engineering Research Express*, vol. 3, 2021.

[88] W. Thomson, “On the ElectroDynamic Qualities of Metals:Effects of Magnetization on the Electric Conductivity of Nickel and of Iron,” *Proceedings of The Royal Society of London*, vol. 8, pp. 546–550, 1856.

[89] A. Grosz, V. Mor, E. Paperno, S. Amrusi, I. Faivinov, M. Schultz, and L. Klein, “Planar Hall Effect Sensors With Subnanotesla Resolution,” *Magnetics Letters, IEEE*, vol. 4, p. 6500104, 2013.

[90] A. Grosz, V. Mor, S. Amrusi, I. Faivinov, E. Paperno, and L. Klein, “A High Resolution Planar Hall Effect Magnetometer for Ultra-Low Frequencies,” *IEEE Sensors Journal*, vol. 16, p. 1, 2016.

[91] P. Dimitrova, S. Andreev, and L. Popova, “Thin film integrated AMR sensor for linear position measurements,” *Sensors and Actuators A-physical - SENSOR ACTUATOR A-PHYS*, vol. 147, pp. 387–390, 2008.

[92] Y. Guo, Y. Deng, and S. Wang, “Multilayer Anisotropic Magnetoresistive Angle Sensor,” *Sensors and Actuators A: Physical*, vol. 263, 2017.

[93] M. Baibich, J.-M. Broto, A. F. Fert, N. F, F. Petroff, P. E. Etienne, G. Creuzet, A. Friederich, and J. Chazelas, “Giant Magnetoresistance of (001)Fe/(001)Cr Magnetic Superlattices,” *Physical review letters*, vol. 61, pp. 2472–2475, 1988.

[94] G. Binasch, P. Grünberg, F. Saurenbach, and W. Zinn, “Enhanced Magnetoresistance in Layered Magnetic Structures with Antiferromagnetic Interlayer Exchange,” *Physical review. B, Condensed matter*, vol. 39, pp. 4828–4830, 1989.

[95] A. Guedes, G. Jaramillo, C. Buffa, G. Vigevani, P. Freitas, D. Horsley, D. Leitao, and S. Cardoso, “Towards picotesla magnetic field detection using a GMR-MEMS hybrid device,” *IEEE Transactions on Magnetics*, vol. 48, p. 4115, 2012.

[96] M. Julliere, "Tunneling Between Ferromagnetic Films," *Physics Letters A*, vol. 54, pp. 225–226, 1975.

[97] S. Das and B. Chakraborty, "Design and Realization of an Optical Rotary Sensor," *IEEE Sensors Journal*, vol. 18, no. 7, pp. 2675–2681, 2018.

[98] S. Alvarez-Rodríguez, F. Peña, M. Briones, M. Helguera, and N. Alcalá-Ochoa, "Low-cost non-concentric diffraction-based encoder," *Optics & Laser Technology*, vol. 138, p. 106836, 2021.

[99] A. S., B. George, and S. C. Mukhopadhyay, "Technologies and Applications of Angle Sensors: A Review," *IEEE Sensors Journal*, vol. 21, pp. 7195–7206, 2021.

[100] F. Wei, C. Mei, J. Huaxue, and W. Yin, "Multi-layer concentric ring differential capacitance displacement sensor," *Measurement*, vol. 136, 2019.

[101] X. Rimpault, E. Bitar-Nehme, M. Balazinski, and R. Mayer, "Online monitoring and failure detection of capacitive displacement sensor in a Capball device using fractal analysis," *Measurement*, vol. 118, 2018.

[102] A. Fleming, "A review of nanometer resolution position sensors: Operation and performance," *Sensors and Actuators A: Physical*, vol. 190, pp. 106–126, 2013.

[103] M. Gasulla, X. Li, G. C. M. Meijer, L. Van der Ham, and J. W. Spronck, "A contactless capacitive angular-position sensor," *IEEE Sensors Journal*, vol. 3, no. 5, pp. 607–614, 2003.

[104] X. Liu, R. Huang, Z. Yu, K. Peng, and H. Pu, "A High-Accuracy Capacitive Absolute Time-Grating Linear Displacement Sensor Based On a Multi-Stage Composite Method," *IEEE Sensors Journal*, vol. PP, p. 1, 2021.

[105] H. Wang, K. Peng, X. Liu, Z. Yu, and Z. Chen, "Design and Realization of a Compact High-Precision Capacitive Absolute Angular Position Sensor Based on Time Grating," *IEEE Transactions on Industrial Electronics*, vol. PP, p. 1, 2020.

[106] X. Fan, Z. Yu, K. Peng, Z. Chen, and X. Liu, "A Compact and High-Precision Capacitive Absolute Angular Displacement Sensor," *IEEE Sensors Journal*, vol. PP, p. 1, 2020.

[107] bo Hou, C. Li, Z. Gao, Q. Wei, B. Zhou, and R. Zhang, "Design, Optimization, and Compensation of High-precision Single-excitation Absolute-capacitive Rotary Encoder with Nonlinearity Error of Up

To ± 4”,” *IEEE Transactions on Industrial Electronics*, vol. PP, p. 1, 2018.

[108] Z. Yu, K. Peng, X. Liu, Z. Chen, and Y. Huang, “A High-Precision Absolute Angular-Displacement Capacitive Sensor Using Three-Stage Time-Grating in Conjunction With a Remodulation Scheme,” *IEEE Transactions on Industrial Electronics*, vol. PP, p. 1, 2018.

[109] D. Zheng, S. Zhang, S. Wang, C. Hu, and X. Zhao, “A capacitive rotary encoder based on quadrature modulation and demodulation,” *IEEE Transactions on Instrumentation and Measurement*, vol. 64, no. 1, pp. 143–153, jan 2015.

[110] B. George, Z. Tan, and S. Nihtianov, “Advances in Capacitive, Eddy Current, and Magnetic Displacement Sensors and Corresponding Interfaces,” *IEEE Transactions on Industrial Electronics*, vol. 64, no. 12, pp. 9595–9607, 2017.

[111] Y. Bai, Y. Lu, P. Hu, G. Wang, J. Xu, T. Zeng, Z. Li, Z. Zhang, and J. Tan, “Absolute Position Sensing Based on a Robust Differential Capacitive Sensor with a Grounded Shield Window,” *Sensors*, vol. 16, p. 680, 2016.

[112] D. Kang and W. Moon, “Electrode configuration method with surface profile effect in a contact-type area-varying capacitive displacement sensor,” *Sensors and Actuators A: Physical*, vol. 189, pp. 33–44, 2013.

[113] D. Zhang, Z. Shuji, Q. Zheng, and L. Li, “Absolute Capacitive Grating Displacement Measuring System with Both High-Precision and Long-Range,” *Sensors and Actuators A: Physical*, vol. 295, 2019.

[114] A. Danisi, A. Masi, R. Losito, and Y. Perriard, “Modeling of High-Frequency Electromagnetic Effects on an Ironless Inductive Position Sensor,” *Sensors Journal, IEEE*, vol. 13, pp. 4663–4670, 2013.

[115] S. Li, Q. He, Z. Zhang, B. Han, Z. Li, and J. Lan, “Simple eddy current sensor for small angle measurement,” *CPEM Digest (Conference on Precision Electromagnetic Measurements)*, pp. 496–497, 2012.

[116] W. Li, J. Hu, Z. Su, and D. Wang, “Analysis and Design of Axial Inductive Displacement Sensor,” *Measurement*, vol. 187, p. 110159, 2021.

[117] ——, “Radial Displacement Detection Using Sensing Coils Weakly Coupled With Magnetic Bearing,” *IEEE Sensors Journal*, vol. PP, p. 1, 2022.

[118] P. Luo, Q. Tang, H. Jing, and X. Chen, “Design and Development of a Self-Calibration- Based Inductive Absolute Angular Position Sensor,” *IEEE Sensors Journal*, vol. PP, p. 1, 2019.

[119] M. Mirzaei, P. Ripka, A. Chirtsov, and J. Vyhnanek, “Eddy Current Linear Speed Sensor,” *IEEE Transactions on Magnetics*, vol. PP, pp. 1–4, 2018.

[120] M. Mirzaei, P. Ripka, J. Vyhnanek, A. Chirtsov, and V. Grim, “Rotational Eddy Current Speed Sensor,” *IEEE Transactions on Magnetics*, vol. PP, pp. 1–10, 2019.

[121] M. Mirzaei, P. Ripka, A. Chirtsov, J. Vyhnanek, and V. Grim, “Design and Modeling of a Linear Speed Sensor with a Flat Type Structure and Air Coils,” *Journal of Magnetism and Magnetic Materials*, vol. 495, p. 165834, 2019.

[122] M. Mirzaei, P. Ripka, and V. Grim, “A Novel Position Sensor with Conical Iron Core,” *IEEE Transactions on Instrumentation and Measurement*, vol. PP, p. 1, 2020.

[123] F. Poltschak and P. Grundhammer, “Non-contact position sensing of five axes for linear motor systems,” pp. 1–6, 2021.

[124] P. Ripka, J. Blazek, M. Mirzaei, P. Lipovský, M. Šmelko, and K. Draganová, “Inductive Position and Speed Sensors,” *Sensors*, vol. 20, p. 65, 2019.

[125] S. Sun, Z. Lv, Y. Han, Z. He, and J. Zhang, “A novel inductive angular displacement sensor based on based on time-grating,” *Measurement Science and Technology*, vol. 33, 2022.

[126] Y. Wang, Y. Qin, X. Chen, Q. Tang, T. Zhang, and L. Wu, “Absolute Inductive Angular Displacement Sensor for Position Detection of YRT Turntable Bearing,” *IEEE Transactions on Industrial Electronics*, vol. 69, p. 1, 2022.

[127] Renesas, “IPS2200 INDUCTIVE POSITION SENSORS A New Era in Motor Commutation.” [Online]. Available: https://www2.renesas.cn/cn/en/document/ovr/ips2200-family-overview?language=en

[128] N. Anandan, A. Varma, and B. George, “A Flexible, Planar-Coil-Based Sensor for Through-Shaft Angle Sensing,” *IEEE Sensors Journal*, vol. PP, p. 1, 2018.

[129] A. S. and B. George, “A Non-Contact Angle Sensor Based on Eddy Current Technique,” *IEEE Transactions on Instrumentation and Measurement*, vol. PP, p. 1, 2019.

[130] A. S., B. George, and S. C. Mukhopadhyay, "An Eddy-Current-Based Angle Sensor With a Minimally Modified Shaft as a Sensing Element," *IEEE Open Journal of Instrumentation and Measurement*, vol. PP, 2022.

[131] Z. Zhang, F. L. Ni, Y. Dong, C. Guo, J. Minghe, and H. Liu, *A Novel Absolute Magnetic Rotary Sensor*, jul 2015, vol. 62.

[132] Z. Zhang, Y. Dong, F. L. Ni, J. Minghe, and H. Liu, "A Method for Measurement of Absolute Angular Position and Application in a Novel Electromagnetic Encoder System," *Journal of Sensors*, vol. 2015, pp. 1–10, 2015.

[133] B. George, S. C. Mukhopadhyay, and A. S., "Design and Development of a Variable Reluctance Based Thin Planar Angle Sensor," *IEEE Transactions on Industrial Electronics*, vol. PP, 2022.

[134] B. Zhang, X. Chen, X. Sun, Y. Jiang, X. Wen, and J. Li, "Study on the Multiperiod Bipolar Inductive Absolute Angle Sensor," *IEEE Sensors Journal*, vol. PP, p. 1, 2022.

[135] W. Gao, H. Shi, and Q. Tang, "A Contactless Planar Inductive Sensor for Absolute Angular Displacement Measurement," *IEEE Access*, vol. PP, p. 1, 2021.

[136] A. Babu and B. George, "Design and Development of a New Non-Contact Inductive Displacement Sensor," *IEEE Sensors Journal*, vol. PP, p. 1, 2017.

[137] A. S., B. George, and S. C. Mukhopadhyay, "An Eddy Current Based Non-contact Displacement Sensor," pp. 1–6, 2020.

[138] L. Wu, P. Tong, X. Wang, Y. A, and R. Su, "An Absolute Linear Displacement Sensor Based on Orthogonal Dual Traveling Wave Magnetic Field," *IEEE Sensors Journal*, vol. 22, p. 1, 2022.

[139] X. Gu, Q. Tang, D. Peng, and D. Weng, "An Inductive Linear Displacement Sensor With Bilateral Sensing Units," *IEEE Sensors Journal*, vol. PP, p. 1, 2020.

[140] Q. Tang, L. Wu, X. Chen, and D. Peng, "An Inductive Linear Displacement Sensor Based on Planar Coils," *IEEE Sensors Journal*, vol. PP, p. 1, 2018.

[141] J. Zhao, M. Li, S. Peng, Y. Guo, and Q. Tang, "An Inductive Linear Displacement Sensor With Complementary Resonant Coupling Units," *IEEE Sensors Journal*, vol. 21, p. 1, 2021.

[142] R. Dauth, G. Gerlach, and S. Fella, “An Effective Method to Model and Simulate the Behavior of Inductive Angle Encoders,” *Sensors*, vol. 22, p. 7804, 2022.

[143] A. Hoxha, M. Passarotto, G. Qama, and R. Specogna, “Design Optimization of PCB-Based Rotary-Inductive Position Sensors,” *Sensors*, vol. 22, 2022.

[144] E. Szelitzky, J. Kuklyte, D. Mândru, and N. O’Connor, “Low Cost Angular Displacement Sensors for Biomechanical Applications - A Review,” *Journal of Biomedical Engineering and Technology*, vol. 2, no. 2, pp. 21–28, 2014. [Online]. Available: http://pubs.sciepub.com/jbet/2/2/3/index.html

[145] S. Wang, Z. Wu, D. Peng, W. Li, S. Chen, and S. Liu, “An angle displacement sensor using a simple gear,” *Sensors and Actuators, A: Physical*, vol. 270, pp. 245–251, 2018. [Online]. Available: https://www.sciencedirect.com/science/article/abs/pii/S0924424717312797

[146] M. Reza Nabavi and S. Nihtianov, *Eddy-Current Sensor Interface for Advanced Industrial Applications*, 2011, vol. 58.

[147] P. Ragunathan and L. Edeswaran, *Design and Fabrication of Low Cost Eddy Current Sensor for Position Control Applications*, nov 2016, vol. 9.

[148] Q. Feng, Z. Weimin, C. Guolong, and G. Xuanyi, “A New Differential Excitation Eddy Current Sensor Used for Micro-defects on Metal Surface,” in *2015 Sixth International Conference on Intelligent Systems Design and Engineering Applications (ISDEA)*, 2015, pp. 37–39.

[149] Q. Tang, D. Peng, L. Wu, and X. Chen, “An Inductive Angular Displacement Sensor Based on Planar Coil and Contrate Rotor,” *IEEE Sensors Journal*, vol. 15, no. 7, pp. 3947–3954, 2015.

[150] V. Chaturvedi, M. R. Nabavi, J. Vogel, K. A. A. Makinwa, and S. Nihtianov, “9.9 A 0.6nm resolution 19.8mW eddy-current displacement sensor interface with 126MHz excitation,” in *2017 IEEE International Solid-State Circuits Conference (ISSCC)*, 2017, pp. 174–175.

[151] Y. Zheng, J. Wu, and Y. Yang, *Temperature compensation of eddy current sensor based on temperature-voltage model*, jun 2016.

[152] J. Gächter, J. Fabian, M. Hirz, A. Schmidhofer, and H. Lanzenberger, *Evaluation of Angular Sensor Systems for Rotor Position Sensing of Automotive Electric Drive*, jun 2014.

[153] M. R. Nabavi and S. N. Nihtianov, “Design Strategies for Eddy-Current Displacement Sensor Systems: Review and Recommendations,” *IEEE Sensors Journal*, vol. 12, no. 12, pp. 3346–3355, 2012.

[154] M. Reza Nabavi and S. Nihtianov, *A Novel Interface for Eddy Current Displacement Sensors*, jun 2009, vol. 58.

[155] C. Tai, “Advanced eddy-current methods for quantitative NDE,” 1997.

[156] M. R. Nabavi, M. A. P. Pertijs, and S. Nihtianov, “An Interface for Eddy-Current Displacement Sensors With 15-bit Resolution and 20 MHz Excitation,” *IEEE Journal of Solid-State Circuits*, vol. 48, no. 11, pp. 2868–2881, 2013.

[157] A. Fekri, M. Nabavi, N. Radeljić-Jakić, Z. Chang, M. Pertijs, and S. Nihtianov, “An eddy-current displacement-to-digital converter based on a ratio-metric delta-sigma ADC,” in *ESSCIRC 2014 - 40th European Solid State Circuits Conference (ESSCIRC)*, 2014, pp. 403–406.

[158] M. R Nabavi and S. Nihtianov, *A survey of eddy current displacement sensors: Imperfections and signal conditioning methods*, mar 2007.

[159] H. Wang and Z. Feng, *Ultrastable and highly sensitive eddy current displacement sensor using self-temperature compensation*, 2013, vol. 203.

[160] H. Nguyen, J. Grundy, and M. Almorsy, *Ontology-based automated support for goal–use case model analysis*, jun 2015, vol. 24.

[161] J. Vogel and S. Nihtianov, “Modelling the inductance of a novel eddy-current position sensor for high-precision applications,” in *2016 IEEE Sensors Applications Symposium (SAS)*, 2016, pp. 1–6.

[162] P. Santos, E. Mendes, J. Carvalho, F. Alves, J. Azevedo, and J. Cabral, “Hardware Accelerated Active Noise Cancellation System using Haar Wavelets,” *Microprocessors and Microsystems, In review*, 2023.

[163] P. Santos, J. Carvalho, and J. Cabral, “Inductive position sensor and obtaining process thereof,” 2023.

Appendix A

Data from all optimizations

Table A.1: *APS* Geometric optimization - Error measurement minimization

		Coil	**Harmonic**			
			0	**1**	**3**	**5**
Geom. 4.1	**Ampl.**	1	0.004 mm	18.186 mm	0.761 mm	-0.134 mm
		2	-0.002 mm	18.982 mm	-0.019 mm	-0.082 mm
	Phase	1	0.000°	0.000°	-2.460°	-85.648°
		2	0.000°	0.000°	-52.047°	-79.192°
Geom. 4.2	**Ampl.**	1	0.003 mm	18.695 mm	0.232 mm	-0.154 mm
		2	-0.003 mm	18.379 mm	0.570 mm	-0.133 mm
	Phase	1	0.000°	0.000°	7.440°	-4.131°
		2	0.000°	0.000°	4.732°	13.301°
Geom. 4.3	**Ampl.**	1	0.003 mm	18.961 mm	-0.051 mm	-0.070 mm
		2	-0.001 mm	18.196 mm	0.759 mm	-0.130 mm
	Phase	1	0.000°	0.000°	-79.576°	11.355°
		2	0.000°	0.000°	-0.423°	-71.837°
Geom. 4.4	**Ampl.**	1	0.000 mm	18.260 mm	0.772 mm	0.053 mm
		2	0.000 mm	19.060 mm	0.016 mm	0.009 mm
	Phase	1	0.000°	0.000°	0.288°	-10.300°
		2	0.000°	0.000°	82.923°	35.722°

Continued on next page

Table A.1: *APS* Geometric optimization - Error measurement minimization

Continued from previous page

		Coil	**Harmonic**			
			0	**1**	**3**	**5**
Geom. 4.5	**Ampl.**	1	0.002 mm	18.889 mm	0.194 mm	0.000 mm
		2	-0.002 mm	18.483 mm	0.591 mm	0.009 mm
	Phase	1	0.000°	0.000°	11.738°	6.382°
		2	0.000°	0.000°	3.459°	-9.039°
Geom. 4.6	**Ampl.**	1	0.003 mm	18.206 mm	0.724 mm	-0.153 mm
		2	0.000 mm	18.734 mm	0.071 mm	-0.280 mm
	Phase	1	0.000°	0.000°	0.000°	-44.216°
		2	0.000°	0.000°	-3.700°	-41.635°
Geom. 4.7	**Ampl.**	1	0.000 mm	18.648 mm	0.437 mm	0.000 mm
		2	0.000 mm	18.723 mm	0.306 mm	-0.056 mm
	Phase	1	0.000°	0.000°	0.000°	-56.735°
		2	0.000°	0.000°	-8.939°	-3.279°
Geom. 4.8	**Ampl.**	1	0.000 mm	18.668 mm	0.399 mm	0.018 mm
		2	0.000 mm	18.510 mm	0.345 mm	-0.230 mm
	Phase	1	0.000°	0.000°	8.456°	-10.135°
		2	0.000°	0.000°	-1.353°	-61.396°
Geom. 4.9	**Ampl.**	1	0.000 mm	18.551 mm	0.525 mm	0.009 mm
		2	0.000 mm	18.826 mm	0.259 mm	0.000 mm
	Phase	1	0.000°	0.000°	5.632°	-20.587°
		2	0.000°	0.000°	7.296°	17.413°
Geom. 4.10	**Ampl.**	1	0.000 mm	18.925 mm	0.000 mm	0.160 mm
		2	0.000 mm	18.220 mm	0.715 mm	-0.150 mm
	Phase	1	0.000°	0.000°	37.053°	-88.968°
		2	0.000°	0.000°	0.000°	51.990°

Continued on next page

Table A.1: *APS* Geometric optimization - Error measurement minimization

Continued from previous page

		Coil	**Harmonic**			
			0	**1**	**3**	**5**
Geom. 4.11	**Ampl.**	1	0.002 mm	18.889 mm	0.194 mm	0.000 mm
		2	0.000 mm	18.587 mm	0.367 mm	-0.131 mm
	Phase	1	0.000°	0.000°	0.000°	33.737°
		2	0.000°	0.000°	0.000°	-18.494°
Geom. 4.12	**Ampl.**	1	0.003 mm	18.206 mm	0.724 mm	-0.153 mm
		2	0.000 mm	18.849 mm	0.000 mm	-0.236 mm
	Phase	1	0.000°	0.000°	3.199°	0.000°
		2	0.000°	0.000°	0.000°	-8.971°

Table A.2: *APS* main results

Geometry	**Receiver coil**	**Maximum peak-to-peak induced current**	**Maximum non-linearity**	**Maximum non-linearity with signal corrections**
1	**1**	0.941 mA	0.995°	0.524°
	2	0.941 mA		
2	**1**	2.908 mA	0.663°	0.480°
	2	2.908 mA		
3	**1**	2.642 mA	0.283°	0.844°
	2	2.793 mA		
4.1	**1**	2.796 mA	0.044°	0.556°
	2	2.903 mA		
4.2	**1**	2.873 mA	0.021°	0.240°
	2	2.828 mA		

Continued on next page

Table A.2: *APS* main results

Continued from previous page				
Geometry	**Receiver coil**	**Maximum peak-to-peak induced current**	**Maximum non-linearity**	**Maximum non-linearity with signal corrections**
4.3	**1**	2.903 mA	0.049°	0.549°
	2	2.798 mA		
4.4	**1**	2.799 mA	0.207°	0.538°
	2	2.906 mA		
4.5	**1**	2.883 mA	0.052°	0.286°
	2	2.828 mA		
4.6	**1**	2.804 mA	0.092°	0.432°
	2	2.886 mA		
4.7	**1**	2.850 mA	0.227°	0.146°
	2	2.867 mA		
4.8	**1**	2.854 mA	0.181°	0.092°
	2	2.850 mA		
4.9	**1**	2.838 mA	0.193°	0.192°
	2	2.874 mA		
4.10	**1**	2.898 mA	0.226°	0.532°
	2	2.805 mA		
4.11	**1**	2.849 mA	0.202°	0.073°
	2	2.855 mA		
4.12	**1**	2.804 mA	0.218°	0.467°
	2	2.900 mA		
5	**1**	2.851 mA	0.130°	0.085°
	2	2.855 mA		

Table A.3: Signal components' amplitudes of the *APS* sensors' receiver coils

Geometry	**Receiver coil**	**Continuous component**	**Fundamental component**	**3rd harmonic**	**5th harmonic**
1	**1**	-102 dB	-66.6 dB	-108 dB	-133 dB
	2	-111 dB	-66.6 dB	-108 dB	-133 dB
2	**1**	-102 dB	-56.8 dB	-98.9 dB	-125 dB
	2	-105 dB	-56.8 dB	-98.9 dB	-125 dB
3	**1**	-103 dB	-57.2 dB	-88.6 dB	-93.9 dB
	2	-101 dB	-57.0 dB	-122 dB	-95.6 dB
4.1	**1**	-114 dB	-57.0 dB	-96.6 dB	-114 dB
	2	-143 dB	-56.8 dB	-98.5 dB	-119 dB
4.2	**1**	-120 dB	-56.9 dB	-111 dB	-111 dB
	2	-122 dB	-56.9 dB	-101 dB	-111 dB
4.3	**1**	-137 dB	-56.8 dB	-98.8 dB	-116 dB
	2	-136 dB	-57.0 dB	-96.6 dB	-114 dB
4.4	**1**	-103 dB	-57.0 dB	-96.9 dB	-121 dB
	2	-104 dB	-56.8 dB	-98.4 dB	-121 dB
4.5	**1**	-115 dB	-56.9 dB	-105 dB	-119 dB
	2	-135 dB	-56.9 dB	-102 dB	-118 dB
4.6	**1**	-154 dB	-57.0 dB	-97.2 dB	-111 dB
	2	-110 dB	-56.8 dB	-102 dB	-109 dB
4.7	**1**	-102 dB	-56.9 dB	-111 dB	-118 dB
	2	-106 dB	-56.9 dB	-112 dB	-115 dB
4.8	**1**	-103 dB	-56.9 dB	-117 dB	-119 dB
	2	-111 dB	-56.9 dB	-114 dB	-111 dB
4.9	**1**	-103 dB	-56.9 dB	-105 dB	-118 dB
	2	-104 dB	-56.9 dB	-109 dB	-118 dB

Continued on next page

Table A.3: Signal components' amplitudes of the *APS* sensors' receiver coils

Continued from previous page

Geometry	**Receiver coil**	**Continuous component**	**Fundamental component**	**3rd harmonic**	**5th harmonic**
4.10	**1**	-104 dB	-56.8 dB	-99.1 dB	-114 dB
	2	-104 dB	-57.0 dB	-97.4 dB	-111 dB
4.11	**1**	-102 dB	-56.9 dB	-111 dB	-117 dB
	2	-106 dB	-56.9 dB	-115 dB	-112 dB
4.12	**1**	-103 dB	-57.0 dB	-97.0 dB	-116 dB
	2	-105 dB	-56.8 dB	-100 dB	-110 dB
5	**1**	-118 dB	-56.9 dB	-148 dB	-124 dB
	2	-152 dB	-56.9 dB	-139 dB	-114 dB

Table A.4: *LIPS* geometric optimization - Error measurement minimization

		Coil	**Harmonic**					
			0	**1**	**2**	**3**	**4**	**5**
Geom. 3.1	**Ampl.**	1	-1.369 mm	5.239 mm	0.000 mm	-0.821 mm	-0.034 mm	2.537 mm
		2	0.000 mm	6.502 mm	0.000 mm	-0.554 mm	0.000 mm	2.944 mm
	Phase	1	0.000°	0.000°	-0.196°	0.000°	2.126°	-0.062°
		2	0.000°	0.000°	-86.795°	0.000°	13.124°	0.000°
Geom. 3.2	**Ampl.**	1	-0.732 mm	4.100 mm	-1.675 mm	1.313 mm	0.860 mm	-1.320 mm
		2	0.000 mm	6.282 mm	-0.597 mm	-0.911 mm	1.477 mm	0.734 mm
	Phase	1	0.000°	0.000°	-10.101°	2.899°	-24.202°	14.718°
		2	0.000°	0.000°	78.180°	-8.579°	-88.150°	-35.394°

Continued on next page

Table A.4: *LIPS* geometric optimization - Error measurement minimization

Continued from previous page

		Coil	**Harmonic**					
			0	**1**	**2**	**3**	**4**	**5**
Geom. 3.3	**Ampl.**	1	-1.576 mm	6.517 mm	0.517 mm	-0.921 mm	0.469 mm	0.000 mm
		2	0.000 mm	7.313 mm	1.964 mm	-0.258 mm	-0.127 mm	0.338 mm
	Phase	1	0.000°	0.000°	-49.134°	25.445°	8.774°	-30.955°
		2	0.000°	0.000°	85.267°	0.000°	-60.527°	-75.968°
Geom. 3.4	**Ampl.**	1	-1.212 mm	4.582 mm	1.388 mm	-1.404 mm	0.837 mm	0.576 mm
		2	-0.050 mm	5.078 mm	-1.142 mm	0.900 mm	2.123 mm	0.706 mm
	Phase	1	0.000°	0.000°	-64.904°	33.737°	0.165°	52.039°
		2	0.000°	0.000°	-71.476°	86.337°	-70.353°	-47.633°
Geom. 3.5	**Ampl.**	1	-1.234 mm	5.716 mm	-0.976 mm	0.598 mm	1.105 mm	-0.370 mm
		2	0.000 mm	7.283 mm	0.677 mm	-0.140 mm	-1.851 mm	-0.049 mm
	Phase	1	0.000°	0.000°	0.454°	6.570°	0.000°	9.745°
		2	0.000°	0.000°	89.883°	0.000°	88.323°	16.211°
Geom. 3.6	**Ampl.**	1	-0.628 mm	3.672 mm	-1.498 mm	1.383 mm	1.133 mm	-1.686 mm
		2	0.021 mm	5.370 mm	-0.681 mm	-0.331 mm	2.325 mm	1.272 mm
	Phase	1	0.000°	0.000°	-10.346°	-16.563°	1.343°	-10.415°
		2	0.000°	0.000°	56.032°	38.146°	-72.478°	69.215°
Geom. 3.7	**Ampl.**	1	-1.705 mm	7.659 mm	0.385 mm	0.211 mm	0.000 mm	0.041 mm
		2	0.000 mm	8.806 mm	0.000 mm	0.088 mm	-0.456 mm	0.651 mm
	Phase	1	0.000°	0.000°	-42.371°	-6.897°	0.000°	-20.857°
		2	0.000°	0.000°	0.000°	0.000°	89.551°	0.000°
Geom. 3.8	**Ampl.**	1	-0.791 mm	4.426 mm	0.000 mm	1.812 mm	1.061 mm	-1.910 mm
		2	0.000 mm	5.553 mm	1.709 mm	-0.753 mm	-1.587 mm	0.398 mm
	Phase	1	0.000°	0.000°	-33.176°	-0.644°	7.573°	-27.338°
		2	0.000°	0.000°	78.521°	11.557°	78.777°	79.885°

Continued on next page

Table A.4: *LIPS* geometric optimization - Error measurement minimization

		Continued from previous page						
		Coil	**Harmonic**					
			0	**1**	**2**	**3**	**4**	**5**
Geom. 3.9	**Ampl.**	1	-1.433 mm	6.287 mm	-1.302 mm	0.000 mm	0.881 mm	-0.098 mm
		2	0.000 mm	6.999 mm	-0.203 mm	0.489 mm	2.023 mm	-0.285 mm
	Phase	1	0.000°	0.000°	0.357°	35.787°	1.438°	34.951°
		2	0.000°	0.000°	-89.986°	-2.486°	-89.963°	-5.322°
Geom. 3.10	**Ampl.**	1	-1.378 mm	4.683 mm	-0.566 mm	-1.070 mm	0.079 mm	2.224 mm
		2	-0.024 mm	5.405 mm	1.195 mm	-0.524 mm	0.168 mm	2.684 mm
	Phase	1	0.000°	0.000°	-19.728°	16.475°	-39.624°	7.855°
		2	0.000°	0.000°	-89.475°	9.807°	-83.998°	11.186°
Geom. 3.11	**Ampl.**	1	-1.409 mm	6.069 mm	-1.825 mm	0.047 mm	-0.542 mm	-0.109 mm
		2	-0.121 mm	6.757 mm	1.943 mm	0.000 mm	0.406 mm	0.773 mm
	Phase	1	0.000°	0.000°	64.406°	-56.702°	-73.861°	-10.835°
		2	0.000°	0.000°	-63.590°	72.559°	-81.000°	16.152°
Geom. 3.12	**Ampl.**	1	-1.380 mm	6.053 mm	1.069 mm	0.906 mm	-0.385 mm	-0.206 mm
		2	-0.019 mm	7.155 mm	1.318 mm	-0.497 mm	1.011 mm	0.000 mm
	Phase	1	0.000°	0.000°	-42.670°	-16.760°	-77.912°	-62.062°
		2	0.000°	0.000°	-86.840°	0.000°	33.782°	-14.605°

Table A.5: *LIPS* geometric optimization - Harmonic content minimization

		Coil	**Harmonic**					
			0	**1**	**2**	**3**	**4**	**5**
Geom. 4.1	**Ampl.**	1	-1.341 mm	5.885 mm	0.123 mm	-0.007 mm	-1.275 mm	-1.370 mm
		2	-0.019 mm	7.946 mm	-0.577 mm	0.363 mm	0.394 mm	0.701 mm
	Phase	1	0.000°	0.000°	37.683°	89.188°	31.944°	46.149°
		2	0.000°	0.000°	89.920°	-3.028°	-88.577°	72.743°
Geom. 4.2	**Ampl.**	1	-1.063 mm	3.967 mm	-1.122 mm	0.297 mm	1.766 mm	1.784 mm
		2	0.258 mm	4.646 mm	-1.350 mm	-0.113 mm	-1.776 mm	1.857 mm
	Phase	1	0.000°	0.000°	22.532°	49.824°	16.081°	37.546°
		2	0.000°	0.000°	1.342°	-83.182°	13.073°	-87.360°
Geom. 4.3	**Ampl.**	1	-1.183 mm	5.040 mm	0.535 mm	-0.113 mm	-2.051 mm	-1.078 mm
		2	0.078 mm	6.895 mm	-0.585 mm	-0.362 mm	0.025 mm	2.056 mm
	Phase	1	0.000°	0.000°	66.397°	-20.533°	-8.556°	42.235°
		2	0.000°	0.000°	83.990°	-47.231°	61.156°	-60.910°
Geom. 4.4	**Ampl.**	1	-1.387 mm	6.100 mm	0.000 mm	0.000 mm	-1.351 mm	-1.163 mm
		2	0.000 mm	8.325 mm	0.000 mm	0.363 mm	0.362 mm	0.950 mm
	Phase	1	0.000°	0.000°	-56.604°	-25.641°	63.306°	57.179°
		2	0.000°	0.000°	5.388°	-36.022°	-47.246°	-26.652°
Geom. 4.5	**Ampl.**	1	-1.455 mm	6.822 mm	-0.150 mm	-0.165 mm	-0.630 mm	-0.779 mm
		2	0.014 mm	8.010 mm	-0.714 mm	0.365 mm	-0.582 mm	0.316 mm
	Phase	1	0.000°	0.000°	-34.179°	-15.550°	-7.363°	6.914°
		2	0.000°	0.000°	87.614°	1.718°	80.060°	27.849°
Geom. 4.6	**Ampl.**	1	-1.488 mm	6.681 mm	-0.213 mm	-0.024 mm	0.646 mm	0.948 mm
		2	0.087 mm	7.587 mm	-0.367 mm	0.150 mm	-1.709 mm	0.100 mm
	Phase	1	0.000°	0.000°	-16.751°	-62.096°	-43.330°	-41.659°
		2	0.000°	0.000°	88.140°	-0.317°	-16.495°	48.739°

Continued on next page

Table A.5: *LIPS* geometric optimization - Harmonic content minimization

Continued from previous page

		Coil	**Harmonic**					
			0	**1**	**2**	**3**	**4**	**5**
Geom. 4.7	**Ampl.**	1	-0.978 mm	4.086 mm	-1.783 mm	-0.322 mm	-1.282 mm	-1.549 mm
		2	-0.016 mm	5.915 mm	0.558 mm	0.265 mm	-2.119 mm	-1.126 mm
	Phase	1	0.000°	0.000°	81.620°	86.893°	-37.864°	-66.710°
		2	0.000°	0.000°	-37.390°	-23.933°	-18.758°	22.808°
Geom. 4.8	**Ampl.**	1	-1.466 mm	6.749 mm	0.524 mm	0.088 mm	-0.783 mm	-0.390 mm
		2	0.035 mm	6.074 mm	-1.071 mm	-0.121 mm	0.817 mm	1.883 mm
	Phase	1	0.000°	0.000°	-70.757°	-73.745°	-19.580°	15.648°
		2	0.000°	0.000°	85.423°	87.535°	-87.819°	-33.683°
Geom. 4.9	**Ampl.**	1	-1.432 mm	5.885 mm	-0.025 mm	-0.051 mm	0.490 mm	2.117 mm
		2	0.068 mm	8.218 mm	-0.795 mm	0.408 mm	-0.489 mm	-0.021 mm
	Phase	1	0.000°	0.000°	-72.782°	-12.032°	-26.971°	3.894°
		2	0.000°	0.000°	67.827°	0.815°	89.978°	37.685°
Geom. 4.10	**Ampl.**	1	-1.533 mm	6.904 mm	0.748 mm	0.001 mm	0.070 mm	0.743 mm
		2	0.006 mm	7.976 mm	0.696 mm	0.382 mm	-0.502 mm	0.439 mm
	Phase	1	0.000°	0.000°	75.358°	-9.154°	-31.526°	2.701°
		2	0.000°	0.000°	-89.714°	-14.027°	87.479°	-6.813°
Geom. 4.11	**Ampl.**	1	-1.461 mm	7.192 mm	-0.421 mm	-0.134 mm	-0.722 mm	-0.069 mm
		2	0.112 mm	7.580 mm	-0.735 mm	0.309 mm	-0.462 mm	0.802 mm
	Phase	1	0.000°	0.000°	-21.738°	-47.792°	77.363°	12.920°
		2	0.000°	0.000°	41.649°	2.576°	84.223°	3.455°
Geom. 4.12	**Ampl.**	1	-1.554 mm	6.833 mm	0.701 mm	-0.038 mm	-0.725 mm	0.149 mm
		2	0.016 mm	8.431 mm	0.028 mm	0.292 mm	-0.649 mm	0.585 mm
	Phase	1	0.000°	0.000°	1.445°	-25.789°	57.669°	-43.550°
		2	0.000°	0.000°	-48.605°	8.687°	77.414°	-31.129°

Table A.6: *LIPS* main results

Geometry	Receiver coil	Maximum peak-to-peak induced current	Maximum error	Maximum error with signal corrections
1	**1**	1.397 mA	16.855 mm	0.317 mm
	2	1.217 mA		
2	**1**	1.646 mA	16.570 mm	0.298 mm
	2	1.433 mA		
3.1	**1**	1.039 mA	0.169 mm	0.171 mm
	2	0.978 mA		
3.2	**1**	0.818 mA	0.183 mm	0.694 mm
	2	1.103 mA		
3.3	**1**	1.189 mA	0.332 mm	0.532 mm
	2	1.202 mA		
3.4	**1**	1.102 mA	0.375 mm	0.818 mm
	2	0.949 mA		
3.5	**1**	1.072 mA	0.121 mm	0.191 mm
	2	1.251 mA		
3.6	**1**	0.776 mA	0.300 mm	0.958 mm
	2	0.967 mA		
3.7	**1**	1.252 mA	0.142 mm	0.210 mm
	2	1.308 mA		
3.8	**1**	0.705 mA	0.248 mm	0.909 mm
	2	1.006 mA		
3.9	**1**	1.226 mA	0.127 mm	0.126 mm
	2	1.234 mA		
3.10	**1**	1.099 mA	0.133 mm	0.317 mm
	2	0.998 mA		

Continued on next page

Table A.6: *LIPS* main results

Continued from previous page

Geometry	**Receiver coil**	**Maximum peak-to-peak induced current**	**Maximum error**	**Maximum error with signal corrections**
3.11	**1**	1.180 mA	0.130 mm	0.425 mm
	2	1.239 mA		
3.12	**1**	1.131 mA	0.149 mm	0.395 mm
	2	1.342 mA		
4.1	**1**	1.109 mA	0.837 mm	0.782 mm
	2	1.341 mA		
4.2	**1**	0.798 mA	0.993 mm	1.348 mm
	2	0.875 mA		
4.3	**1**	0.882 mA	0.904 mm	0.645 mm
	2	1.102 mA		
4.4	**1**	1.159 mA	0.490 mm	0.274 mm
	2	1.315 mA		
4.5	**1**	1.260 mA	0.162 mm	0.140 mm
	2	1.270 mA		
4.6	**1**	1.339 mA	0.545 mm	0.680 mm
	2	1.224 mA		
4.7	**1**	0.832 mA	1.127 mm	1.318 mm
	2	0.975 mA		
4.8	**1**	1.251 mA	0.910 mm	0.423 mm
	2	1.013 mA		
4.9	**1**	1.127 mA	0.828 mm	0.371 mm
	2	1.297 mA		

Continued on next page

Table A.6: *LIPS* main results

Continued from previous page

Geometry	**Receiver coil**	**Maximum peak-to-peak induced current**	**Maximum error**	**Maximum error with signal corrections**
4.10	**1** **2**	1.343 mA 1.262 mA	0.322 mm	0.278 mm
4.11	**1** **2**	1.373 mA 1.200 mA	0.399 mm	0.188 mm
4.12	**1** **2**	1.283 mA 1.283 mA	0.282 mm	0.278 mm

Table A.7: Signal components' amplitudes of the *LIPS* sensors' receiver coils

Geometry	**Receiver coil**	**Cont. comp.**	**Fund. comp.**	**2nd harm.**	**3rd harm.**	**4th harm.**	**5th harm.**
1	**1**	-49.0 dB	-63.2 dB	-89.7 dB	-108 dB	-124 dB	-122 dB
	2	-130 dB	-64.4 dB	-89.3 dB	-101 dB	-105 dB	-106 dB
2	**1**	-48.7 dB	-61.7 dB	-89.9 dB	-108 dB	-128 dB	-130 dB
	2	-132 dB	-63.0 dB	-88.9 dB	-99.0 dB	-104 dB	-107 dB
3.1	**1**	-108 dB	-66.9 dB	-110 dB	-91.5 dB	-118 dB	-90.2 dB
	2	-138 dB	-67.0 dB	-104 dB	-93.9 dB	-109 dB	-92.5 dB
3.2	**1**	-97.9 dB	-67.3 dB	-90.0 dB	-85.4 dB	-98.8 dB	-93.6 dB
	2	-104 dB	-65.9 dB	-115 dB	-89.0 dB	-97.3 dB	-106 dB
3.3	**1**	-97.4 dB	-65.0 dB	-99.4 dB	-91.1 dB	-102 dB	-118 dB
	2	-115 dB	-64.6 dB	-88.8 dB	-97.3 dB	-106 dB	-109 dB

Continued on next page

Table A.7: Signal components' amplitudes of the *LIPS* sensors' receiver coils

Continued from previous page

Geometry	**Receiver coil**	**Cont. comp.**	**Fund. comp.**	**2nd harm.**	**3rd harm.**	**4th harm.**	**5th harm.**
3.4	**1**	-96.3 dB	-66.3 dB	-91.7 dB	-85.8 dB	-96.2 dB	-100 dB
	2	-105 dB	-67.0 dB	-92.5 dB	-92.0 dB	-91.3 dB	-103 dB
3.5	**1**	-123 dB	-65.0 dB	-95.8 dB	-92.2 dB	-95.7 dB	-104 dB
	2	-197 dB	-64.4 dB	-94.0 dB	-97.8 dB	-94.1 dB	-107 dB
3.6	**1**	-93.6 dB	-68.2 dB	-90.9 dB	-85.0 dB	-96.2 dB	-91.5 dB
	2	-112 dB	-66.9 dB	-103 dB	-95.4 dB	-91.3 dB	-97.2 dB
3.7	**1**	-99.4 dB	-64.1 dB	-101 dB	-103 dB	-123 dB	-116 dB
	2	-122 dB	-63.9 dB	-99.7 dB	-101 dB	-123 dB	-115 dB
3.8	**1**	-92.7 dB	-68.4 dB	-114 dB	-84.7 dB	-97.7 dB	-92.9 dB
	2	-106 dB	-66.7 dB	-89.4 dB	-91.0 dB	-94.8 dB	-107 dB
3.9	**1**	-106 dB	-64.2 dB	-92.4 dB	-115 dB	-97.4 dB	-114 dB
	2	-137 dB	-64.2 dB	-98.6 dB	-103 dB	-92.6 dB	-103 dB
3.10	**1**	-99.0 dB	-66.6 dB	-99.8 dB	-87.8 dB	-110 dB	-90.0 dB
	2	-116 dB	-66.9 dB	-97.5 dB	-93.1 dB	-113 dB	-91.7 dB
3.11	**1**	-95.7 dB	-64.7 dB	-90.1 dB	-115 dB	-103 dB	-116 dB
	2	-93.2 dB	-64.4 dB	-92.0 dB	-99.8 dB	-117 dB	-108 dB
3.12	**1**	-127 dB	-64.6 dB	-94.2 dB	-90.2 dB	-106 dB	-115 dB
	2	-104 dB	-63.8 dB	-96.9 dB	-91.8 dB	-94.0 dB	-106 dB
4.1	**1**	-134 dB	-65.2 dB	-116 dB	-124 dB	-94.7 dB	-96.4 dB
	2	-146 dB	-63.5 dB	-138 dB	-118 dB	-120 dB	-104 dB
4.2	**1**	-168 dB	-68.2 dB	-95.4 dB	-98.6 dB	-92.0 dB	-93.7 dB
	2	-133 dB	-67.4 dB	-93.4 dB	-103 dB	-92.8 dB	-94.1 dB

Continued on next page

Table A.7: Signal components' amplitudes of the *LIPS* sensors' receiver coils

Continued from previous page

Geometry	**Receiver coil**	**Cont. comp.**	**Fund. comp.**	**2nd harm.**	**3rd harm.**	**4th harm.**	**5th harm.**
4.3	**1**	-139 dB	-67.2 dB	-101 dB	-107 dB	-91.2 dB	-100 dB
	2	-154 dB	-65.7 dB	-123 dB	-95.5 dB	-105 dB	-94.7 dB
4.4	**1**	-125 dB	-64.8 dB	-116 dB	-123 dB	-93.7 dB	-97.2 dB
	2	-127 dB	-63.7 dB	-101 dB	-104 dB	-109 dB	-104 dB
4.5	**1**	-134 dB	-64.0 dB	-116 dB	-106 dB	-101 dB	-102 dB
	2	-147 dB	-63.9 dB	-130 dB	-129 dB	-118 dB	-112 dB
4.6	**1**	-145 dB	-63.7 dB	-133 dB	-130 dB	-101 dB	-98.0 dB
	2	-151 dB	-64.3 dB	-109 dB	-107 dB	-92.7 dB	-109 dB
4.7	**1**	-147 dB	-68.1 dB	-90.7 dB	-101 dB	-95.9 dB	-95.6 dB
	2	-185 dB	-66.1 dB	-102 dB	-112 dB	-90.7 dB	-97.2 dB
4.8	**1**	-133 dB	-64.1 dB	-99.8 dB	-115 dB	-99.3 dB	-111 dB
	2	-133 dB	-66.3 dB	-102 dB	-101 dB	-105 dB	-95.7 dB
4.9	**1**	-125 dB	-65.5 dB	-110 dB	-119 dB	-102 dB	-91.6 dB
	2	-122 dB	-63.7 dB	-107 dB	-130 dB	-121 dB	-106 dB
4.10	**1**	-142 dB	-63.7 dB	-96.8 dB	-122 dB	-114 dB	-99.5 dB
	2	-132 dB	-64.0 dB	-142 dB	-112 dB	-127 dB	-128 dB
4.11	**1**	-151 dB	-63.4 dB	-109 dB	-108 dB	-99.5 dB	-133 dB
	2	-130 dB	-64.5 dB	-102 dB	-121 dB	-137 dB	-108 dB
4.12	**1**	-143 dB	-64.0 dB	-96.1 dB	-116 dB	-99.9 dB	-109 dB
	2	-143 dB	-63.9 dB	-100 dB	-110 dB	-112 dB	-111 dB